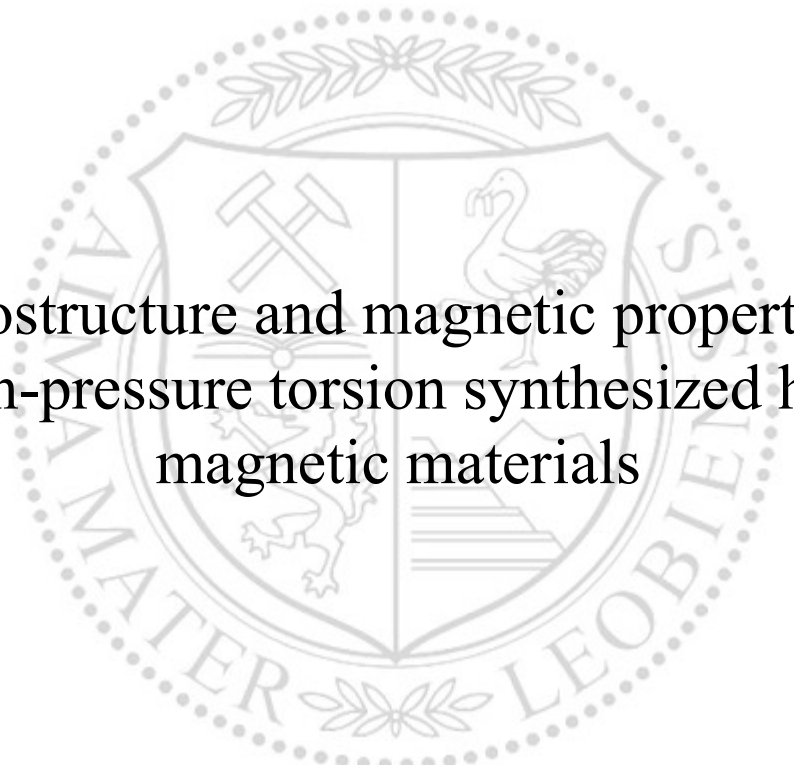Chair of Materials Physics
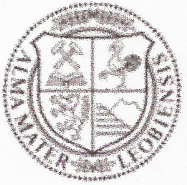
Doctoral Thesis

Microstructure and magnetic properties of high-pressure torsion synthesized hard magnetic materials

Dipl.-Ing. Lukas Emanuel Weissitsch

November 2023

AFFIDAVIT

I declare on oath that I wrote this thesis independently, did not use other than the specified sources and aids, and did not otherwise use any unauthorized aids.

I declare that I have read, understood, and complied with the guidelines of the senate of the Montanuniversität Leoben for "Good Scientific Practice".

Furthermore, I declare that the electronic and printed version of the submitted thesis are identical, both, formally and with regard to content.

Date 26.11.2023

Signature Author
Lukas Emanuel Weissitsch

DOI: 10.34901/mul.pub.2023.177

Erich Schmid Institute of Materials Science
Austrian Academy of Sciences
Jahnstraße 12
A-8700 Leoben

CC BY 4.0

Abstract

The rising public awareness of green technologies manifests itself in the increasing demand for renewable energy and electric mobility, leading to an annually raising production of permanent magnets. Performance and efficiency of generators, motors and electric components, rely on the use of high-performance permanent magnets, which contain a significant amount of cobalt or rare-earth elements. However, their production is associated with questionable working conditions and environmental problems related to mining and the availability of these materials is subject to a monopolistic situation. Supply shortages, already recognized by international institutions, represent a critical bottleneck for modern economic and social development.

This work is dedicated to the search of alternatives regarding hard-magnetic materials. Herein, the focus is on two main approaches. First, the utilization of magnetic coupling effects, namely 'exchange bias' and 'exchange coupling', to reduce the amount of critical elements. Second, the formation of a rare-earth free ferro-magnetic phase, in particular α-MnBi. For material processing, severe plastic deformation by high-pressure torsion is conducted, which allows for the application of a high, tunable amount of strain. Using phases with different magnetic properties, this top-down technique results in both, microstructural refinement and strongly refined composite structures, all while maintaining bulk sized samples.

In the pursuit of achieving an exchange bias, extensive microstructural processing and characterization of the Fe-Cr material system are performed. An observed co-deformation of powders limits a sufficient refinement for exchange bias due to a significant hardness increase. The deformation behavior is improved by using

arc-melted Fe-Cr ingots as starting material, leading to a refined solid solution. A remarkable temperature stability is reported, hindering a decomposition into finely dispersed Fe and Cr phases. This holds true for both increased annealing temperatures and prolonged annealing times. A multi-sector 2-stage high-pressure torsion process is developed to refine the phases and simultaneously prevent intermixing of Fe and Cr. Despite promising results, no exchange bias is achieved within this material system.

$SmCo_5$ is deformed by high-pressure torsion and serves as a hard magnetic phase for an exchange coupled spring magnet. The coupling is demonstrated across a broad variation of chemical compositions. A change in the operating temperature allows switching between a coupled spring magnet and the uncoupled state. The influence of a high-pressure torsion deformation induced textured microstructure results in the formation of an anisotropic permanent magnet.

In obtaining bulk sized samples, the successful processing of the rare-earth free α-MnBi phase is emphasized. The high microstructural defect density induced by high-pressure torsion enhances the α-MnBi phase formation during a subsequent annealing procedure. A deformation at 2 GPa is preferred over 5 GPa, as well as a higher amount of applied strain. The thermal treatment is improved by applying vacuum conditions and an external magnetic field during annealing. The formed α-MnBi phase is studied and an influence of the sample's shear texture with respect to the applied field direction during annealing is found. This allows to tune the magnetic properties between an isotropic and anisotropic behavior.

Kurzfassung

Das steigende Bewusstsein der Öffentlichkeit für grüne Technologien spiegelt sich in der zunehmenden Nachfrage nach erneuerbarer Energie und Elektromobilität wieder. Dies führt zu einer jährlich steigenden Produktion von Permanentmagneten. Die Leistung und Effizienz von Generatoren, Motoren und elektrischen Komponenten hängt von den gewählten Hochleistungsmagneten ab, die eine erhebliche Menge an Kobalt oder Seltenerdmetallen enthalten. Jedoch stehen die Produktion mit fragwürdigen Arbeitsbedingungen und Umweltproblemen im Zusammenhang, und die Verfügbarkeit dieser Materialien unterliegt einer monopolistischen Situation. Lieferengpässe, welche bereits von internationalen Institutionen erkannt wurden, stellen einen kritischen Engpass für die moderne wirtschaftliche und soziale Entwicklung dar.

Diese Arbeit widmet sich der Suche nach Alternativen im Bereich der hartmagnetischen Materialien. Dabei liegt der Fokus auf zwei fundamentalen Ansätzen. Einerseits wird die Nutzung magnetischer Kopplungseffekte, bekannt unter den Begriffen „exchange coupling" und „exchange bias", zur Reduzierung des Anteils kritischer Elemente ausgenützt. Andererseits wird die Herstellung einer Seltenenerdmetall-freien ferromagnetischen Phase, konkret der α-MnBi Phase, betrachtet. Für die Materialverarbeitung wird eine starke plastische Verformung durch Hochdrucktorsionsumformung angewendet, die es ermöglicht eine hohe und einstellbare Dehnung aufzubringen. Durch die Verwendung von Phasen mit unterschiedlichen magnetischen Eigenschaften führt diese Top-Down-Technik sowohl zu einer Verfeinerung der Mikrostruktur als auch zu stark verfeinerten Verbundstrukturen, wobei die makroskopischen Proben-Abmessungen erhalten bleiben.

Um einen exchange bias zu erreichen, werden umfangreiche mikrostrukturelle Herstellungswege und Charakterisierungen des Fe-Cr Materialsystems durchgeführt. Eine beobachtete gleichzeitige Verformung von Pulvern resultiert in einer nicht ausreichenden Verfeinerung für einen exchange bias, aufgrund einer signifikanten Steigerung der Härte. Das Verformungsverhalten wird verbessert, indem umgeschmolzenes Fe-Cr als Ausgangsmaterial verwendet werden, welches zu einem Mischkristall mit starker Kronfeinung führt. Eine bemerkenswerte Temperaturstabilität wird beschrieben, die eine Zersetzung in fein verteilte Fe- und Cr-Phasen verhindert. Dies gilt sowohl für erhöhte Glühtemperaturen als auch für verlängerte Glühzeiten. Ein mehrsektoraler 2-stufiger Hochdrucktorsions-Prozess wird entwickelt, um die Phasen zu verfeinern und gleichzeitig eine Vermischung von Fe und Cr zu verhindern. Trotz vielversprechender Ergebnisse wird innerhalb dieses Materialsystems kein exchange bias beobachtet.

$SmCo_5$ wird durch Hochdrucktorsiuonsumformung plastisch verformt und dient als harte magnetische Phase für einen „exchange coupled Spring-Magneten". Die Kopplung wird über eine breite Variation chemischer Zusammensetzungen nachgewiesen. Eine Änderung der Betriebstemperatur ermöglicht die Einstellung zwischen dem exchange coupled Magneten und dem entkoppelten Zustand. Der Einfluss einer durch Hochdrucktorsionsumformung verursachten texturierten Mikrostruktur führt zur Bildung eines anisotropen Dauermagneten.

Im Bezug auf die Herstellung von makroskopischen Proben ist die erfolgreiche Herstellung der Seltenerdmetall-freien MnBi-Phase hervorzuheben . Die hohe mikrostrukturelle Defektdichte, die durch Hochdrucktorsionsumformung verursacht wird, verstärkt die Bildung der α-MnBi-Phase während eines anschließenden Glühverfahrens. Eine Verformung bei 2 GPa wird gegenüber 5 GPa bevorzugt, ebenso wie eine höhere aufgebrachte Dehnung. Die thermische Behandlung wird durch Bereitstellung von Vakuumbedingungen und eines externen Magnetfeldes während des Glühens maßgeblich verbessert. Die gebildete α-MnBi-Phase wird untersucht und ein Einfluss der Scherstruktur der Probe in Bezug auf die angelegte Feldrichtung während des Glühens wurde festgestellt. Dadurch können die magnetischen Eigenschaften zwischen einem isotropen und einem anisotropen Verhalten eingestellt werden.

Acknowledgment

At this point, I would like to thank everyone, who accompanied and supported me in a professional or personal way during the past years.

First and foremost, I would like to express my appreciation to my supervisors **Prof. Dr. Reinhard Pippan** and **Priv. Doz. Dr. Andrea Bachmaier**. Their scientific point of view encouraged me to always find new ideas and their open-minded attitude to my suggestions allowed to perform a multitude of tasks. At that point, I want to thank for the opportunity to work in such an environment, for countless discussions and a constant support.

I sincerely thank **Prof. Dr. Roland Würschum**, his supervision during my master's thesis at the Technische Universität Graz still guides me and I am glad he contributed as my mentor for this doctoral thesis.

The 'man behind everything' definitely is **Dr. Stefan Wurster**. His always friendly, diplomatic and profound way to help during experiments, coffee breaks or proof-reading is an important encouragement and will guide me beyond this phD-time.

Very special thanks are dedicated to **Dr. Martin Stückler**, **Michael Pegritz** and **David Gebhart**. Their endless patience and support could not be more diverse and more important to me.

I am extremely grateful to **Prof. Dr. Heinz Krenn** who introduced me into SQUID magnetometry. I owe him a lot for many time-consuming discussions and data interpretations, his enthusiasm for magnetic measurements is still inspiring. Furthermore, I would like to extend my sincere thank to **Prof. Peter Knoll**, for our discussions and some different points of view to our scientific collaboration.

List of Abbreviations

AM arc melting

APT atom probe tomography

BM ball milling

BSE backscattered electrons

DMI Dzyaloshinskii–Moriya interaction

EDS energy dispersive X-ray spectroscopy

FC field cooling

HEXRD high energy X-ray diffraction

HPT high-pressure torsion

MVA magnetic field assisted vacuum annealing

PM permanent magnet

REE rare-earth element

RT room temperature

RKKY Ruderman-Kittel-Kasuya-Yosida

SAD selective area diffraction

SEM scanning electron microscopy

SPD severe plastic deformation

SQUID superconducting quantum interference device

TEM transmission electron microscopy

TKD transmission Kikuchi diffraction

XRD X-ray diffraction

ZFC zero field cooling

Contents

Contents

1

Motivation and Aim

Independent of the potential users perception, magnetic materials are constantly present in our nowadays lives and mandatory in a wide range of daily used devices. Magnets feature a broad range of sizes and applications spanning from data storage technologies, sensors and loudspeakers to electric-magnetic energy converters, e.g., power transformers, actuators, motors or generators [1]. The development of magnetic materials is an important task in the sense of a competitive market and product optimization. Depending on their implementation, the materials are chosen based on their magnetic properties, which on a rough basis are divided into soft- and hard-magnetic.

In Figure 1.1 the historic development of hard-magnetic material systems, which are used as permanent magnets (PMs) is shown. The maximum energy product $(BH)_{\mathrm{max}}$, an important figure of merit for PMs, is improved after the first steel magnets are initially reported about a century ago [2]. Ever since, the $(BH)_{\mathrm{max}}$ is increased trough improvement of the respective magnetic material class and especially by discovering novel material systems. Simultaneously the required magnetic material volume is reduced, while still obtaining a similar strength of the magnets' stray field. This is beneficial for two main points of view. First, less material is used and second, less mass is required. Both have an essential impact on considerations related to the growing topics of supply chains, sustainability, recycling and green energy transition.

A combination of all topics, is in particular important for the considerable growing interest in electric mobility, where cost and weight efficiency is crucial. In addition, the globally increasing energy consumption and simultaneous demand for renewable energy (e.g. attempts of fulfilling the Paris Climate Accords or the European Green Deal)
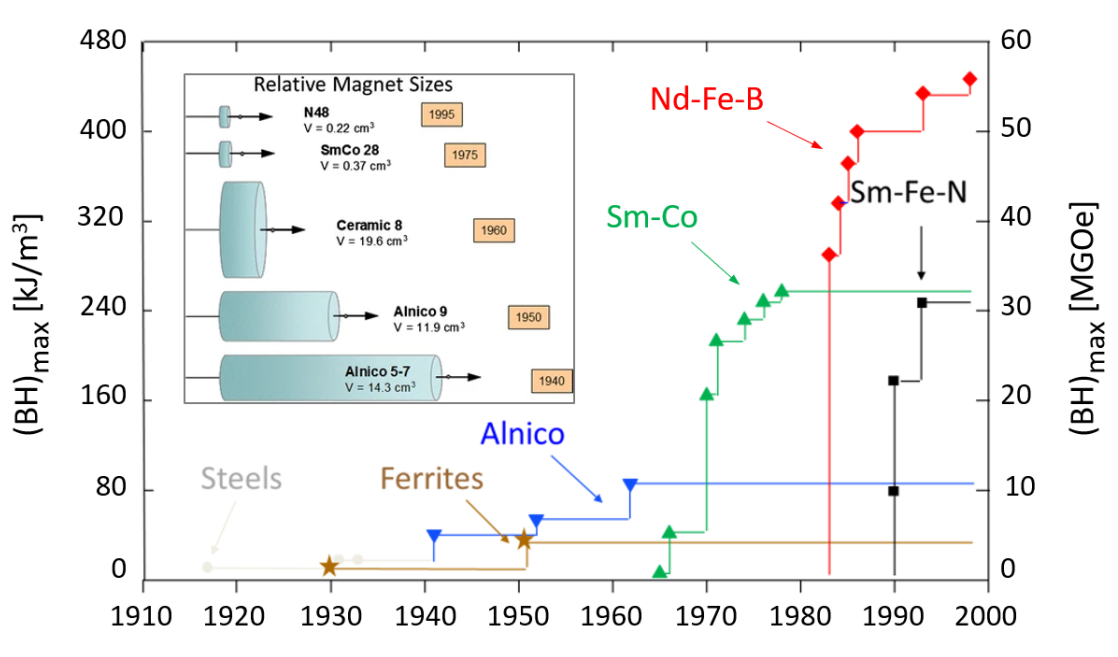
Figure 1.1.: Historic development of most relevant PM material systems. The inset shows a comparison of magnet volumes for different material types but the same energy density. Adapted from [3, 4]

require a substantially increasing amount of PMs [4, 5]. The problems coming along with the green energy transition lay in the consumption of certain elements required to manufacture high performing PMs. As can be seen in Figure 1.1, nowadays these PMs are based on rare-earth elements (REEs) such as Sm or Nd. Moreover, Dy or Tb (both heavy REEs) are additionally added to enhance the materials magnetocrystalline anisotropy and thus the operating temperature of the PM [6]. Rare-earth oxides however, are almost exclusively mined in China thus leading to a monopolistic situation which resulted in an artificial global price increase on REEs back in 2011 and meanwhile referred to as the 'rare-earth crisis' [7]. Supply shortages of REEs, often correlated to politic instabilities, would be a crucial problem for the economic and social development. Thus, an increasing awareness on such so called 'critical materials' of international and governmental institutions, inter alia, the U.S. Department of Energy or the European Commission is present [8–10].

Besides growing efforts to recycle materials containing REEs [11], scientifically motivated attempts are being made to reduce the content of REEs, seek for a novel ultra-high-performance PM material or broaden the diversity of PM material systems to easily substitute rarely available elements [12]. This thesis addresses the latter point by

meshing the unique microstructures obtained through severe plastic deformation (SPD) and magnetic coupling mechanisms. In particular, high-pressure torsion (HPT) is utilized, to extract and screen physical properties to form a basis for possible novel manufacturing routes. Materials treated by SPD show microstructural feature sizes of the same order as magnetic interactions take place. This aims towards the tunability of magnetic properties while large scaled bulk materials are obtained, featuring one of the beneficial special characteristics of SPD methods. The general goal of this thesis is the fabrication of specific microstructures aiming at tunable magnetic properties by utilizing magnetic coupling mechanisms as well as manufacturing processes and understanding the underlying physical phenomena.

The present cumulative thesis is structured as followed. Chapter 2 gives an introduction on SPD, PMs and its correlations. Chapter 3 shows selected results and is divided in three main topics. The first subsection deals with the microstructure of SPD-synthesized FeCr based alloys, which have been intended for a strong exchange biased PM. In the following two subsections, the findings to Fe-SmCo$_5$ exchange coupled spring magnets are presented as well as the results obtained on the formation of REE free MnBi based PMs. In Chapter 4 considerations for pursuing attractive experiments are outlined and in Chapter 5 major findings of this thesis are reviewed. An overview on the appended publications, written in the context of the thesis working objective, is listed in Chapter 7. Directly after, these six peer-reviewed publications (A-F) are presented.

2

Theoretical Background

In this chapter a brief overview of the main topics of this thesis is presented. First an introduction on SPD is given, with a focus on the formation of different microstructures by HPT. The second part is addressed to PMs, its nowadays increasing importance and future challenges. Further, the interplay between both topics is discussed which is related to the published review-article (Publication E). The necessity for state of the art methodologies to characterize magnetic nanostructures and selected innovative synthesis techniques are reviewed as well.

2.1. Microstructural Development by Severe Plastic Deformation

Since ancient times, at least since the chalcolithic period, plastic deformation of metals is established and used to increase its strength [13]. Nowadays, material scientists also understand the main underlying mechanisms, which are mainly referred to grain refinement and an increasing dislocation density within the material. But due to the strength-ductility trade-off mechanical material properties cannot be ever improved and thus, a reduced materials ductility and brittle material behaviour frequently accompanies strongly refined microstructures [14]. Nevertheless, high amounts of applied plastic deformation allow to generate and enhance mechanical and functional properties [13, 15]. Processing techniques utilizing such high amounts of plastic deformation are represented by the collective term 'severe plastic deformation (SPD)'. A wide range of SPD-methods are known, e.g., Accumulative Roll Bonding (ARB), Equal Angular Channel Extrusion/Pressing (ECAE/ECAP), Repetitive Corrugating

2. Theoretical Background

and Straightening (RCS) or multi-axial forging [16–19]. However, there is no other technique than HPT applying higher amounts of strain to the material.
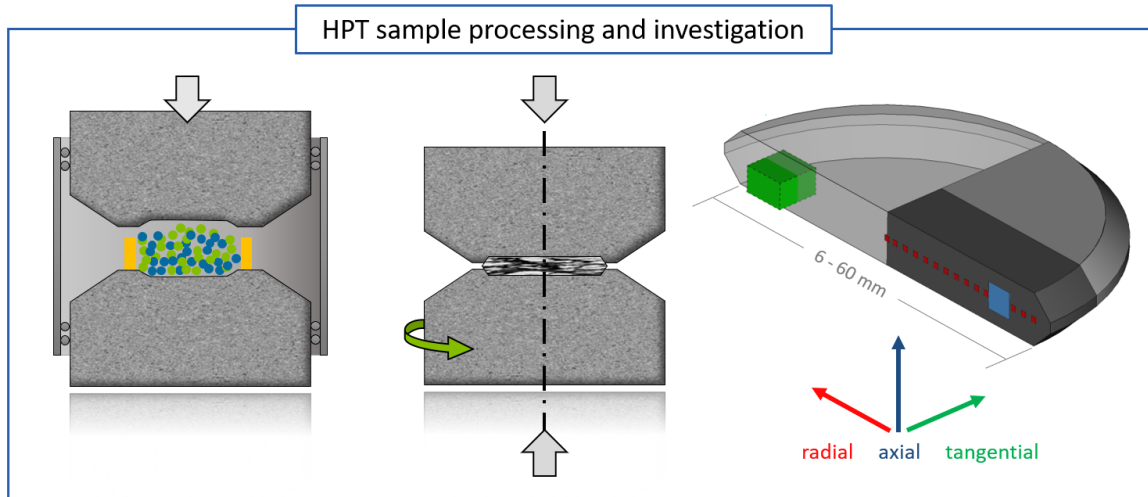
Figure 2.1.: Schematic representation of a powder-based HPT process typically used in this thesis. Using a custom made encapsulation device, allows to perform the powder compaction step in an inert gas atmosphere preventing the particles from oxidation (left image). In a subsequent step, the pellet is severely deformed by HPT. The resulting cylindrically shaped sample is utilized for further investigation techniques considering the respective HPT-disc directions and processing parameters.

For sample preparation in the framework of this doctoral thesis, HPT is conducted. In general, this technique uses two anvils, where the sample is placed in between as described in Figure 2.1. One anvil is fixed and the other one is rotated, while simultaneously a pressure is applied along the rotation axis. Several variations of this technique exists. The most common modification used at the Erich Schmid Institute is the so called constrained HPT set-up. For this purpose, the anvils are equipped with a cylindrical cavity accommodating the sample which significantly increases the high hydrostatic pressure in the processing zone during deformation. Currently, three different sizes of HPT devices are available at the Erich Schmid Institute. The maximum load spans from 400 kN and 4000 kN up to 10000 kN for the largest device. Using a larger HPT equipment, results in larger sample sizes, demonstrating the scalability of this process [20]. As a result, sample diameters up to 60 mm can be reached (Figure 2.1). Simultaneously, technical processing constraints are present, exemplified by the required torque for deformation, which scales with the cube of the sample diameter. An advantage of HPT is the adjustability of several processing parameters, inter alia, the applied pressure, rotation frequency, deformation

temperature and of course the number of rotations, which primarily defines the amount of applied shear strain. For the idealized unconstrained HPT-process the shear strain γ can be calculated by [19]

$$\gamma = \frac{2\pi n r}{t} \tag{2.1}$$

where n denotes the number of applied turns, r is the radius and t is the sample thickness. To compare the strain to other deformation techniques, γ often is converted to the equivalent strain according to the 'von Mises criterion'

$$\epsilon_{vM} = \frac{\gamma}{\sqrt{3}}. \tag{2.2}$$

In real HPT-experiments the thickness of the sample is reduced during the deformation through a material flow towards the sample's edge, thus underestimating the calculated values [19, 20]. With regard to this thesis, another aspect is of great relevance. Equation 2.1 implies a linear change of the strain between the maximum radius $r_{max} = \gamma_{max}$ and the center of the HPT-disc, where theoretically no deformation by torsion is applied and $\gamma(r = 0) = 0$ is valid. As a consequence, this leads to a deformation gradient within the sample, which allows to study functional properties as a function of γ within one sample as demonstrated in Publication C. In reality, a $\gamma = 0$ will never be the case after HPT, while a strain gradient still exists. However, if the number of rotations is largely increased, the resulting microstructure does not scale by γ anymore and a steady state is achieved. This steady state regime allows the processing of a homogeneous microstructure for a broad range of HPT-disc radii [21].

The deformation behavior is more complex for multi-phase materials compared to single phase materials. Alongside other factors, the material properties of one, several or all components, such as the hardness, crystal structure or yield stress are important and could limit a proper co-deformation process [22, 23]. If HPT-deformation succeeds, the resulting microstructure varies from a simple homogenisation and refinement of the phase distribution without intermixing (thus retaining a composite), a fragmentation of one phase to the formation of a supersaturated solid solution [24]. Supersaturated alloys or even metastable phases can also be obtained by HPT, if the initial material phases are immiscible in the thermodynamic equilibrium.

HPT allows a variety of starting materials. Usually disc shaped bulk materials, which could be a single- or multi-phase, are used. Also ribbons [25], obtained by melt-spinning, or just mechanically crushed ingots, leading to mm-sized granules are

possible [26, 27]. Powder mixtures can also serve as a starting material. It is possible to consolidate any kind of powders or powder mixtures, which is done by a simple compaction step within the HPT-device forming a pellet. Afterwards, the obtained pellet is handled similar to a bulk material and deformed by HPT. Powders are especially convenient, if powder blends e.g. of different phases are in the experimental focus, as chemical compositions are easily adjusted by mixing the powders. However, a materials tendency to chemical reactions like oxidation increases with the surface to volume ratio. Thus, the influence of forming oxides that impede the investigation of high-purity samples, have to be considered when using extremely fine powder particles. For storing and handling such critical powders, glove-boxes filled with an inert-gas such as argon, are used. To maintain this atmosphere during a transportation of the powder blend to the HPT-device for consolidation, a custom made encapsulation device is used as schematically shown in Figure 2.1 [28].

2.2. Important Aspects of Magnetism

There exists several attempts to describe the magnetic behavior of materials. The difficulty of doing so lies in its complexity. Results usually either suffer from simplifications or from immense computational expenses. In a general way, ferro-magnetism originates from an exchange coupling between the spins of the atoms, the spin-spin interaction. Additionally, the interaction of the electron orbitals with the potential energy of the hosting crystal lattice is defined by the magnetocrystalline energy (so called spin-orbit coupling). This approach implies a quantum mechanical behavior and can be described by the Heisenberg Hamiltonian:

$$\mathcal{H} = \sum_{i<j} J_{ij} s_i s_j - K \sum_i (S_{zi})^2 \qquad (2.3)$$

where s_i and s_j denotes atomic spins at different neighbouring sites, J_{ij} is the exchange coefficient and K is the magnetocrystalline anisotropy constant [29, 30]. The first term describes the spin-spin interaction and thus the alignment of atomic magnetic moments. For ferromagnetic materials J_{ij} is positive and aligns the spins parallel. This is graphically shown by the Bethe-Slater curve as depicted in Figure 2.2a). This term describes an energy, thus if an external energy, e.g., thermal energy ($k_B T$) exceeds the coupling energy, the material looses its ferromagnetic behavior. This point is called the Curie-Temperature T_C, following a similar behavior with respect to the atomic

number (Figure 2.2b) [31].
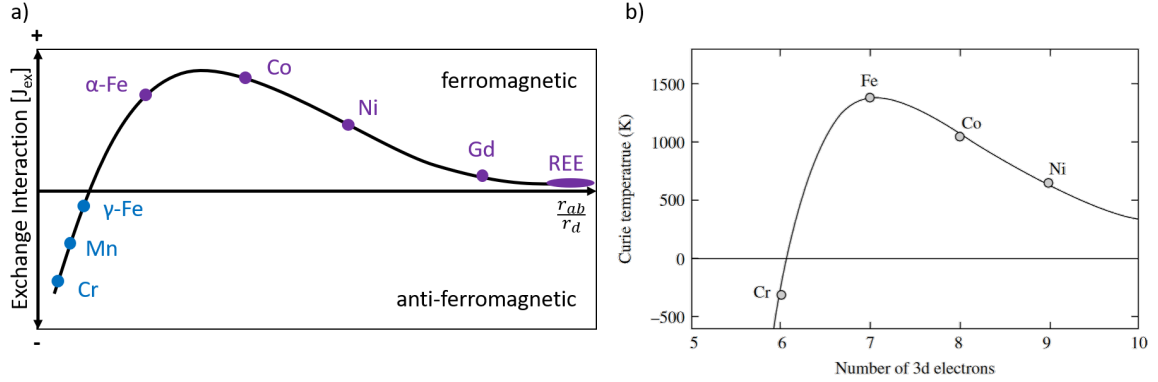
Figure 2.2.: **a)** Schematic Bethe-Slater curve with corresponding positions of important elements. Depending on the sign of the exchange interaction J_{ex} the spin orientation of the elements results in a ferro- or antiferro-magnetic behavior. The variation of J_{ex} scales with the interatomic spacing r_{ab} and the radius of the unfilled d-shell r_d. The REEs are located on the right side of the curve. Adapted from [29]. **b)** Bethe-Slater-Néel curve showing the dependence of the Curie-Temperature T_C on the atomic number. Image reprinted from [31].

The second term of equation 2.3 describes the spin-orbit interaction, here exemplarily for an uniaxial cubic system. The magnetocrystalline anisotropy is an intrinsic property, determining by which strength the magnetization is bound to the crystal lattice. For nearly every technological application comprising magnetic materials, material engineers have to consider this contribution. This term describes a directional dependent energy, the anisotropy energy (E_A). In Figure 2.3 it is shown for different elements exhibiting different crystal structures. The direction pointing towards a low value for E_A is called the 'easy axis' while high values are called the 'hard axis'. If a crystal is magnetized in any other direction than the easy axis, the additional contribution of E_A has to be surpassed to completely reach a saturating magnetization. This is seen by the different saturation behavior in magnetization measurements with respect to different crystal axis in the bottom row of Figure 2.3. Taking the uniaxial crystal system as an example, E_A is approximated by a power series

$$E_A = \sum_n K_n sin^{2n}(\theta) \tag{2.4}$$

where the n-th direction of the uniaxial anisotropy constant is K_n and θ is the angle between the vector of the applied magnetizing field and the easy axis [32]. Comparing to Figure 2.3, the easy axis points into the [0001] direction, as further recognized

by the fast saturation behavior of the corresponding magnetization measurement. Tilting the applied field of $\theta=90°$ leads to the maximum values of E_A, thus it requires very high external fields to magnetize the material completely. Besides the technical relevance of a reduced symmetry, the difficulty of magnetizing or in the sense of an application, the demagnetizing of an magnetic material, is the main reason why most of the high performing PMs exhibit a hexagonal, rhombohedral or tetragonal crystal structure [33].
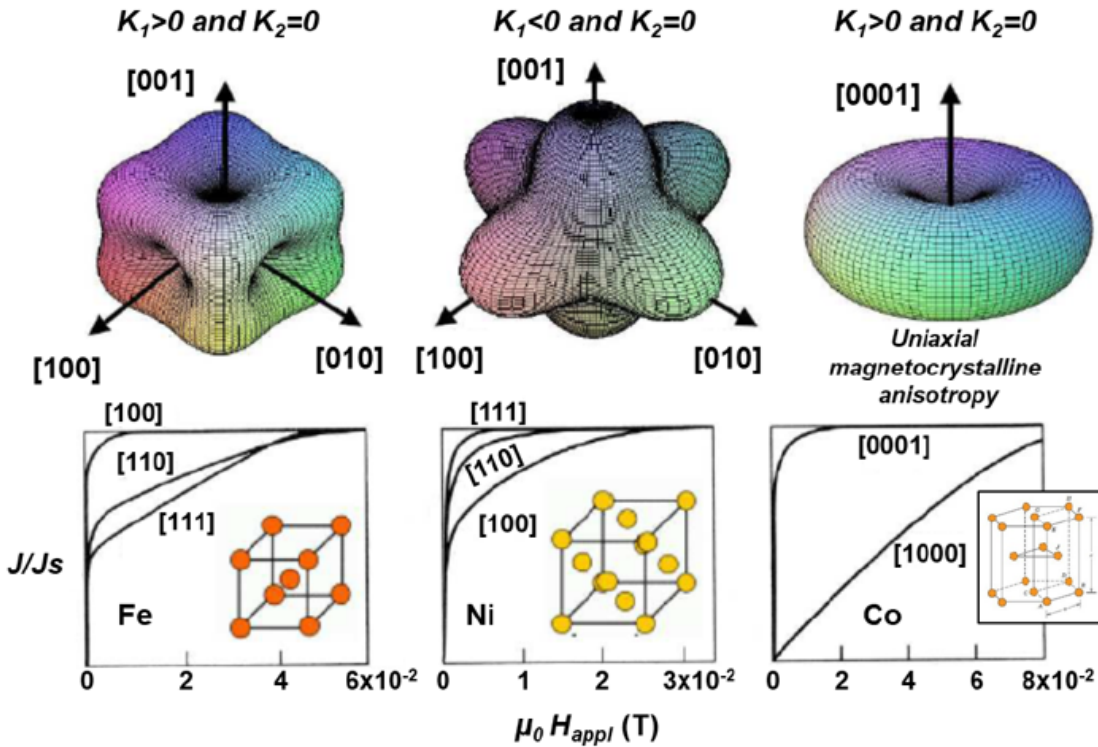
Figure 2.3.: Anisotropy energy distribution for body centered cubic Fe (left), face centred cubic Ni (middle) and hexagonal Co (right). Corresponding magnetization measurements along different crystallographic axes are shown in the bottom row. Reprinted from [34].

If we now consider larger structures comprising of a multitude of atoms, the magnetostatic energy strongly increases. Following the natures principle of energy minimization, this is an unfavourable state. Therefore the ordering of the spins within the material breaks up into numerous smaller volumes - so called domains - rearranging the direction of their atomic spins. As a result, the macroscopic material does not show any significant global magnetization in order to minimize the stray field contribution [30, 35]. These magnetic domains are separated by domain walls, which thickness

inversely scales with the magnetocrystalline anisotropy. As domain walls can move under the influence of an external magnetic field, thus one domain can grow in size in expense of other domains. The concept of domains is usually used to explain the appearance of hysteresis measurements [36].
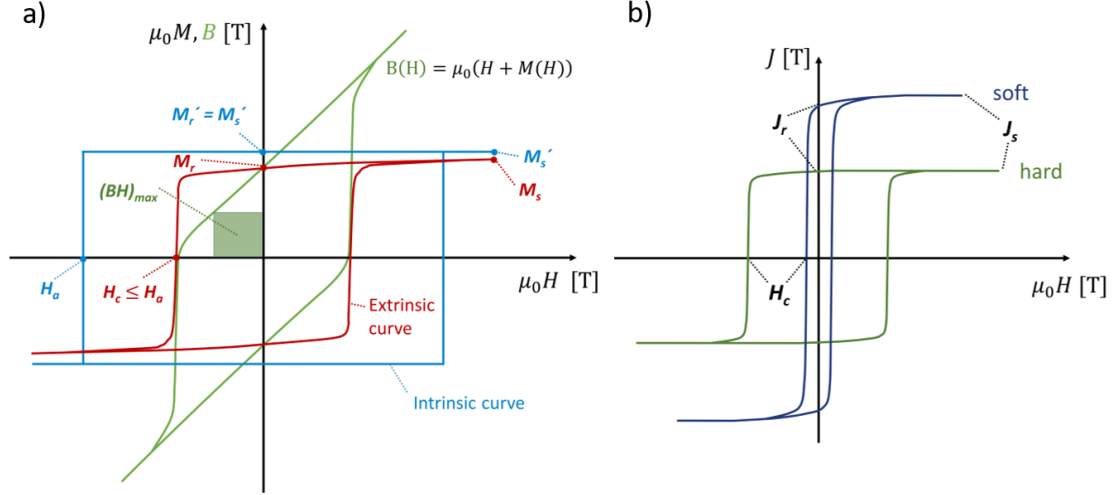
Figure 2.4.: **a)** Hysteresis loop drawn for an idealized and theoretical Stoner-Wohlfarth particle (blue, intrinsic curve) and a scheme for a realistic hysteresis loop (red, extrinsic curve). The $(BH)_{\mathrm{max}}$ is determined using the corresponding $B - H$ curve (green curve). **b)** Schematic representation of hysteresis measurements of a soft- and hard magnetic material (blue and green, respectively). Reprinted from [37].

The idealized magnetic hysteresis measurement and thus theoretical upper limit of achievable magnetic properties is represented in Figure 2.4a). This so called 'intrinsic curve' relies on the Stoner-Wohlfarth model for defect free single-domain particles. Therein, the completely magnetized material keeps the saturation magnetization (M_{s}) upon an external applied demagnetizing field until the anisotropy field H_{a}

$$H_{\mathrm{a}} = \frac{2K}{\mu_0 M_s} \tag{2.5}$$

is reached [6]. At that point, all spins simultaneously change their polarization. Because of already discussed reasons, this is a theoretical consideration and does not represent a real measurement. The extrinsic curve in Figure 2.4a) however, represents such a realistic experiment. M_{s} is only reached if an extremely high magnetic field $\mu_0 H$ is applied to align all spins in one direction. If this field is removed, already some domains are formed and the macroscopic materials shows a reduced magnetic

moment, called the remanence (M_r). Compared to the intrinsic curve, a much lower field, known as the coercivity (H_c), is required to demagnetize the material. The Brown's Paradox describes this discrepancy and includes any kind of imperfections, such as material defects or misaligned spins in domain walls [38]. Typical values for H_c adhere to the relation $H_c \leq \alpha_K H_a$ using the Kronmüller factor α_K, which is typically about 0.3 [39].

Magnetic materials are usually classified and characterized by parameters obtained from a magnetic hysteresis measurement. The most relevant division is done between soft- and hard-magnetic. A soft magnetic material exhibits a high M_s and a low H_c as depicted by the blue hysteresis in Figure 2.4 b). The area inside the loop corresponds to the energy needed for a rotation of the polarization. This is especially important for high frequency dependent applications, e.g. current transformers, which is why soft-magnetic materials feature minimized H_c [40]. On the other hand, a hard-magnetic material is recognized by a large H_c and when compared to soft-magnets, by a reduced M_s. Therein, again the area of the hysteresis loop represents an energy, namely the energy the material can store and provide in form of a stray field. However, the shape of the loop, hence the materials demagnetization behavior is of high importance. As a consequence, there exist several definitions to compare magnetic materials among each other and can be used as a figure of merit. The most common one is the maximum energy product $(BH)_{max}$, which is defined by the maximized area of an inscribed square of B and H on the recoil branch of the $B - H$ curve. An example is given by the green square of the corresponding hysteresis in Figure 2.4a).

2.3. Correlation of Microstructure and Magnetic Performance

The origin of magnetism, intrinsically bounded to the interacting spins of electrons on an atomic level was already discussed and the formation of magnetic domains for larger magnetic material volumes was mentioned. However, if we would like to design a PM, which probably is used in a wind turbine for power supply or an electric motor, the resulting product exhibits macroscopic dimensions although we have to understand the physical interactions taking place at smaller length scales. This is similar for macroscopic objects not related to magnetism, where the quality of a product is determined by material properties, hence its microstructure and atomic

arrangement. Large PMs exhibit a complex microstructure comprising phase, grain or grain boundary arrangement thus determining its magnetic performance. In Figure 2.5 the similarity of microstructure and magnetic features of underlying effects and interactions are related to the length scale. This length scale usually is divided into different regions (macroscopic-, mesoscopic-, nanometer- and atomic-scale), where the design of an underlying scale is capable to change the properties of the overlying ones.
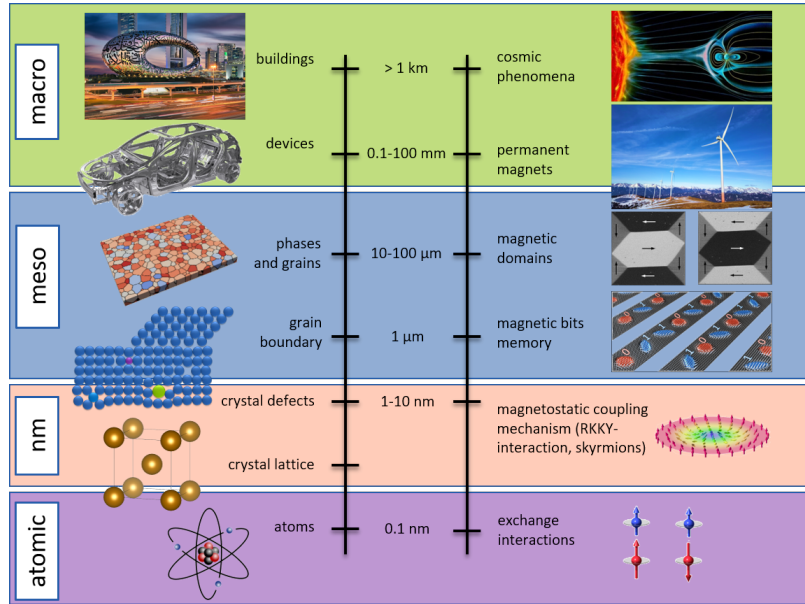
Figure 2.5.: Demonstration of typical length scales for microstructural (left) and magnetic (right) features. The properties of macroscopic applications usually rely on effects obtained at lower length scales. Inset images reprinted from [41–49].

Two distinct examples are summarized in Figure 2.6. The Herzer plot, which shows H_c as a function of the grain size for soft-magnetic materials, is one traditional representation for the correlation of magnetic properties and microstructure. In Figure 2.6a) a similar characteristics is found, but representing the H_c behavior for hard-magnetic materials. An increasing H_c with decreasing grain size is drawn. A maximum is reached for particles without any domain walls, so called single-domain particles. For such particle sizes it is energetically favourable to maintain a higher stray field than capture the energy which is stored within a domain wall. Because of other microstructural influences the curve characteristics do not allow a strict prediction, as it is known for Herzer's relation [50]. If the single-domain particles are further reduced in size, H_c is again reduced. Once more, several microstructural influences co-exist and different resulting states can be achieved. However, exemplary drawn

is a 'worst case scenario' for hard magnetic materials. When the particles are small enough the material could reach a super-paramagnetic state. This means, the spins directly align to an external applied field but if no field is present, thermal energies ensure a complete disorder and hence a vanishing H_c.
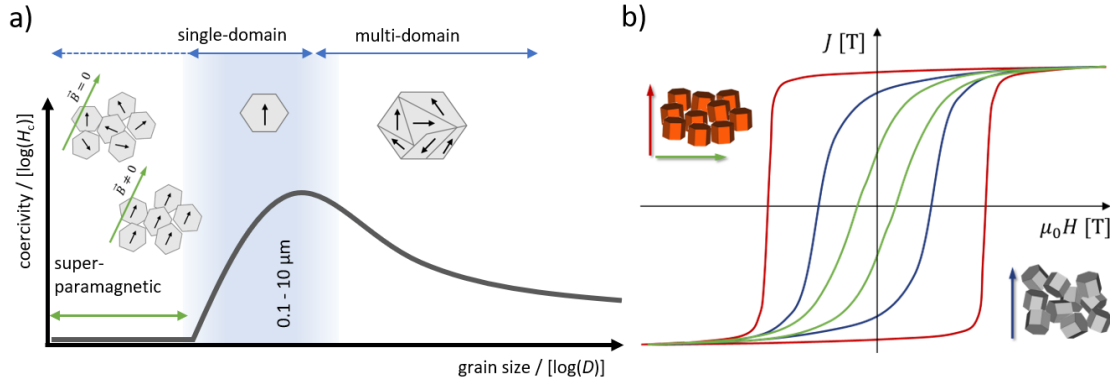
Figure 2.6.: **a)** Schematic representation for the H_c with changing particle sizes for a hard magnetic material. Adapted from [37]. **b)** Schematic representation of hysteresis loops of a hard magnetic material. The loop characteristics changes if the measurement field is applied parallel or perpendicular to the textured material (red and green curve) or if the materials crystals are randomly distributed.

Another important aspect is the influence of texture on PM materials, represented in Figure 2.6b) and further discussed in Publication D. A PM exhibits a textured microstructure, when there is a preferred orientation of crystallites. In the case of a hexagonal structure as depicted in the inset of Figure 2.6b), the measured hysteresis loop strongly differs when the applied measurement field is applied along the easy axis (red curve) or the hard axis (green curve). If the magnet has an isotropic microstructure, the resulting hysteresis loop (blue curve) could be understood best as a superposition of separated hysteresis measurements of every single crystallite, thus a mixture between easy and hard axes. For applications, anisotropic PMs are of high importance due to its orientation-dependent and thus enhanced magnetic performance.

In terms of magnetic microstructure design for hard-magnetic materials a classification in several types is convenient. Figure 2.7 summarizes such basic schematic types of microstructures and corresponding characteristic hysteresis loops. Type one (blue) represents aligned single domain particles, separated by a sufficient thick non magnetic grain boundary to ensure no multi-domain structure can form. Such a microstructure

would lead to the highest values for H_c. If particles or grains are of a similar size, but the non-magnetic boundary is absent, the spins can exchange couple with their surroundings (type II, red curve). The vectorial alignment will not be perfect but due to the absence of the second (non magnetic) phase the M_s is higher for the same volume.
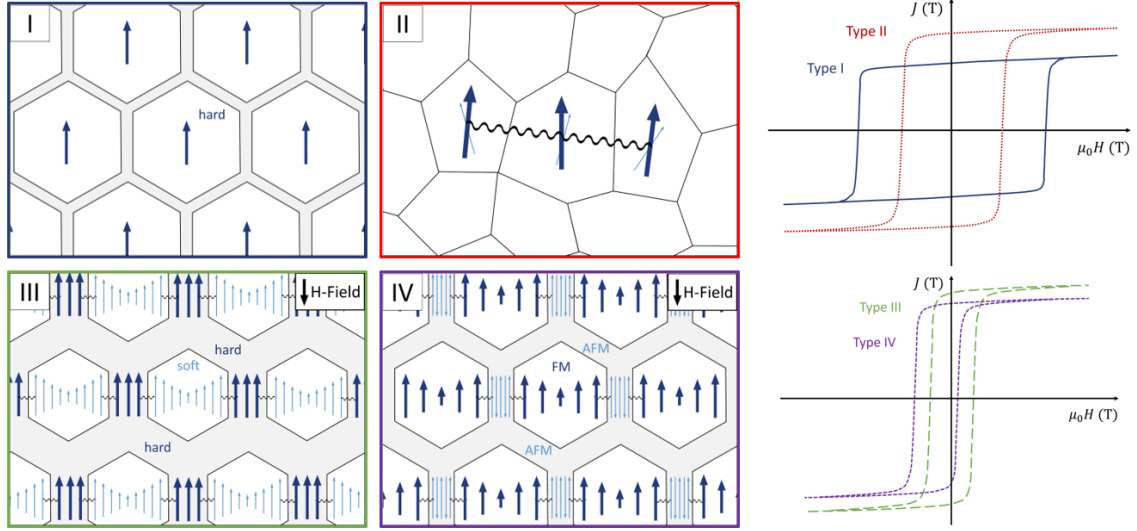
Figure 2.7.: Classified idealized microstructures relevant for nucleation-type PMs. Corresponding typical hysteresis characteristics are shown on the right side. Adapted from [37].

Type III (green) is a very promising technique for future PMs. Here, a composite combining the high magnetic moment and remanence of a soft-magnetic material and the high coercivity of a hard-magnetic material is used. This type is called exchange-spring magnet and was first introduced by Kneller and Hawig [51] in 1991. It is crucial to have the dimensions of the soft-magnetic phase distances in the same regime as the exchange length of the hard magnetic-phase. Then, the high crystal anisotropy of the hard-magnetic phase couples to the soft-magnetic spins and prevent them against a magnetization reversal of an external applied magnetic field. As a result, the area within the hysteresis as well as $(BH)_{max}$ increases. Using the Fe-SmCo$_5$ material system this Type III is further considered in Publication C and D. Another hetero-phase structure but using ferro- and anti-ferromagnetic materials results in type IV (purple). This concept requires a Curie-Temperature (T$_C$) of the ferromagnetic phase which is higher than the Néel-Temperature (T$_N$) of the anti-ferromagnetic phase, and an additional temperature treatment within a magnetic field. If an external applied magnetic field is applied when cooling through T$_N$, a magnetic measurement

results in a shifted hysteresis along the field axis of field cooling. This phenomenon is called exchange bias and was first reported for Co-CoO nanoparticles by Meiklejohn and Bean [52] in 1956. The anti-ferromagnetic (AFM) coupling is extremely strong, thus the alignment during field cooling allows a ferromagnetic spin exchange coupling on the FM-AFM interface. The shift of the hysteresis depends on the amount of pinned surface spins.
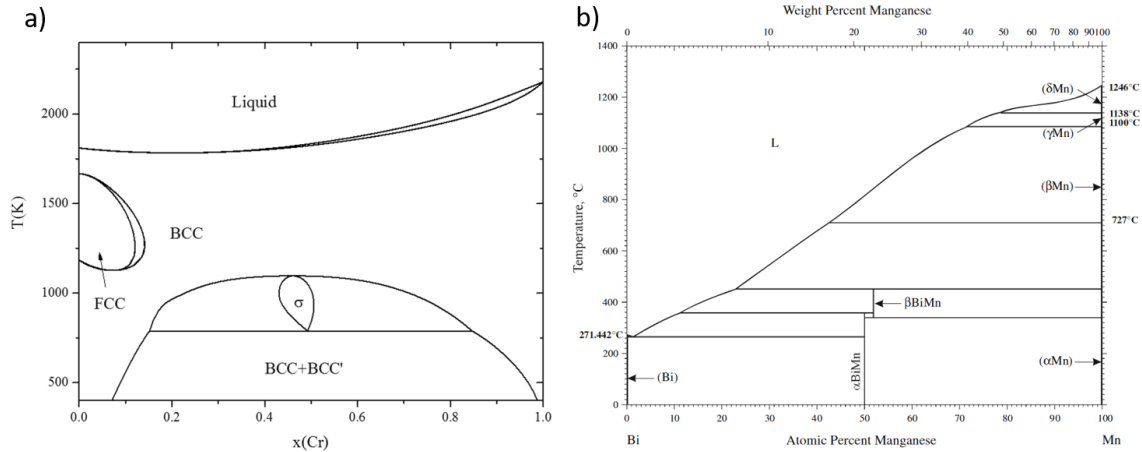
Figure 2.8.: Phase diagrams of **a)** Fe-Cr (reprinted from [53]) and **b)** MnBi (reprinted from [54]). The Fe-Cr system shows a pronounced miscibility gap. For the Mn-Bi system the α-MnBi phase at an equiatomic ratio is of interest.

These schematic microstructures with resulting magnetic characteristics can be directly processed by HPT as shown in the appended review (Publication E). In particular a focus is given on powders used as starting materials. However, another intended processing route to nanostructured materials is to use 'non-equilibrium processing'. It is already mentioned, that HPT-deformation allows the formation of supersaturated solid solutions. Thus, the processing of alloys, which can not be manufactured by standard methods (e.g. melting metallurgy), is achievable. This is the case for example for the Fe-Cr alloy (see Publication A and B). The associated phase diagram shown in Figure 2.8a) reveals a pronounced miscibility gap in the thermodynamic equilibrium at lower temperatures. When such a metastable material is exposed to a thermal treatment, the solid soulution phase is likely to change its local chemical composition. For the Fe-Cr system a spinodal decomposition is reported [53]. Because of the different magnetic properties of Fe (ferromagnetic) and Cr (anti-ferromagnetic) an annealing treatment of HPT-deformed FeCr could lead to a microstructure aiming type IV.

Standard alloy manufacturing often uses a melting approach, where the required elements are brought into the liquid phase to perfectly mix and then, is cooled down to room temperature. Depending on the material system, this method could be accompanied by segregating phases. In the case of the Mn-Bi system the α-MnBi phase which exists at an equiatomic ratio at temperatures below $\sim$271°C is of great interest for hard-magnetic applications. Cooling from a liquid phase is accompanied by the formation of several phases as can be seen in the phase diagram presented in Figure 2.8b). By using extremely high cooling rates (e.g. melt-spinning) the intended phase can be achieved yet, lower cooling rates would lead to the formation of undesired phases. However, HPT allows processing at low temperatures, e.g., directly at room temperature as demonstrated in Publication F. Therefore, this processing route completely avoids regions of other phases within the phase diagram, hence no adverse segregations are expectable when deforming Mn and Bi.

Results and Discussion

Three different material systems, namely FeCr, Fe-SmCo$_5$ and MnBi, were chosen to obtain the desired microstructures with respect to hard magnetic properties. Each system is presented separately in the following subsections. However, the choice of method for sample preparation within this thesis was primarily based on high-pressure torsion (HPT). Therefore, regardless of their material system, all obtained samples appeared as cylindrical discs. Thus, microstructural characterizations on these samples were performed as depicted in Figure 2.1. In general, the HPT-disc was halved along the diameter but due to the radial dependence on strain and microstructural variations, a further cutting of the sample material could have been required. Electron microscopy analysis as well as hardness measurements were performed in tangential viewing direction on the polished cut surface, if not stated otherwise. Synchrotron based XRD and magnetic experiments were not only resolving radial differences but were further sensitive to direction depended measurements. Accordingly, the coordinate system illustrated in Figure 2.1 applies to all experiments with respect to the HPT-disc.

3.1. Microstructural Tuning Aiming for Exchange-Biased FeCr

Single phase Fe exhibits a ferromagnetic and Cr an anti-ferromagnetic ordering. A combination of both phases could be expected to form a type IV microstructure (c.f. Figure 2.7) resulting in a shifted hysteresis after field cooling.

3. Results and Discussion

Starting with powder blends of commercially available Fe and Cr, HPT-deformation led to a two-phase microstructure. The phase distances were refined with increasing strain, but the deformation of the material was limited due to an enormous increase in hardness. Figures 3.1a)-d) show backscattered electrons (BSE) images of a binary Fe_xCr_{100-x} composite with a nominal equal atomic distribution (x=50). The Fe phase (bright contrast) and Cr phase (dark contrast) are clearly visible at low deformation grades (Figure 3.1a); r=0 mm) and are refined if the applied strain is increased (Figure 3.1b); r=1 mm). A co-deformation of both phases is present and leads to small phase distances (Figure 3.1c)-d); r=3 mm) but also to an embrittlement and crack formation. This strain induced microstructural refinement leads to a hardness increase, which is stronger pronounced for chemical compositions with higher Cr content as depicted in Figure 3.1e). The microhardness at the edge of the HPT-disc samples exceeds 800 HV, thus approaching the strength of the HPT anvils leading to a processing limit. For functional properties a further phase refinement into the nanometre range was envisaged, either directly by HPT-deformation or if the formation of a supersaturated solid solution could not be circumvented, by a subsequent annealing induced decomposition. Following this goal, the processing procedure was adapted, but the variation of pressure or temperature during deformation emerged as non-successful techniques.
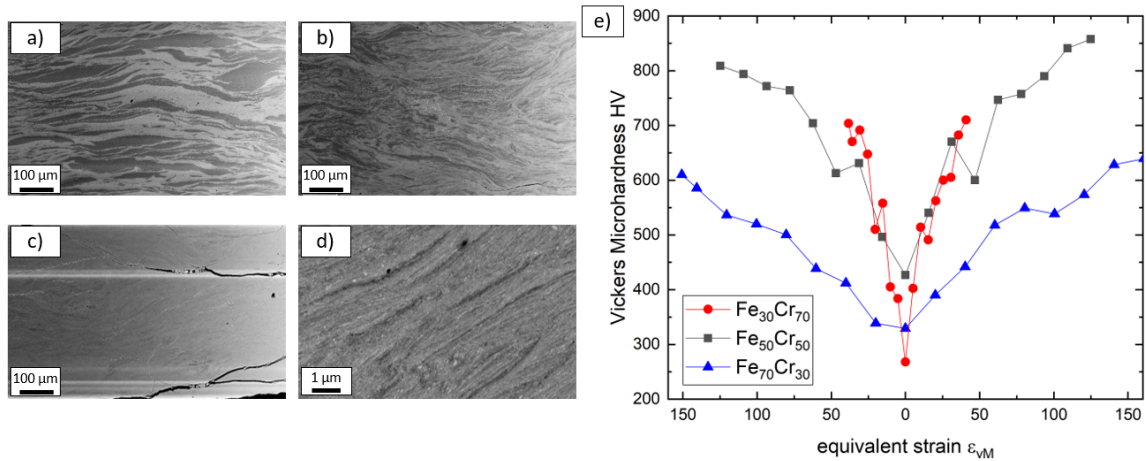
Figure 3.1.: BSE images of an HPT-deformed binary powder blend consisting of nominal 50 at.% Fe and 50 at.% Cr at **a)** r=0 mm, **b)** r=1 mm and **c)-d)** r=3 mm. **e)** Microhardness measurements for three different samples with chemical variations.

Therefore, the starting material was changed to separate the mixing process from the microstructural refinement by HPT. In a first attempt, ball milling (BM) was

conducted to powder blends of similar nominal chemical composition. The milling process, as well as powder handling in general, was performed in Ar-atmosphere. In total, the powders were milled for 20 h, already after 15 h of milling time energy dispersive X-ray spectroscopy (EDS) measurements could not resolve separated phases. Thus, the chemistry was at least homogeneous on a micrometer scale. The obtained powder blend was conducted to HPT consolidation and deformation. However, deformation at room temperature (RT) was again limited. The powder particles already contained a significant amount of microstructural defects and thus, a high hardness of the starting material was expected. HPT-deformation resulted in a slipping between the sample and anvil, already after a few rotations and the initial boundaries of powder particles were still visible in BSE-images (Figure 3.2a)). The deformation behavior was improved if the deformation temperature was increased to 250°C or 400°C (Figure 3.2b)). However, a pronounced crack formation upon HPT-deformation was not suppressed, especially for a higher Cr-content.
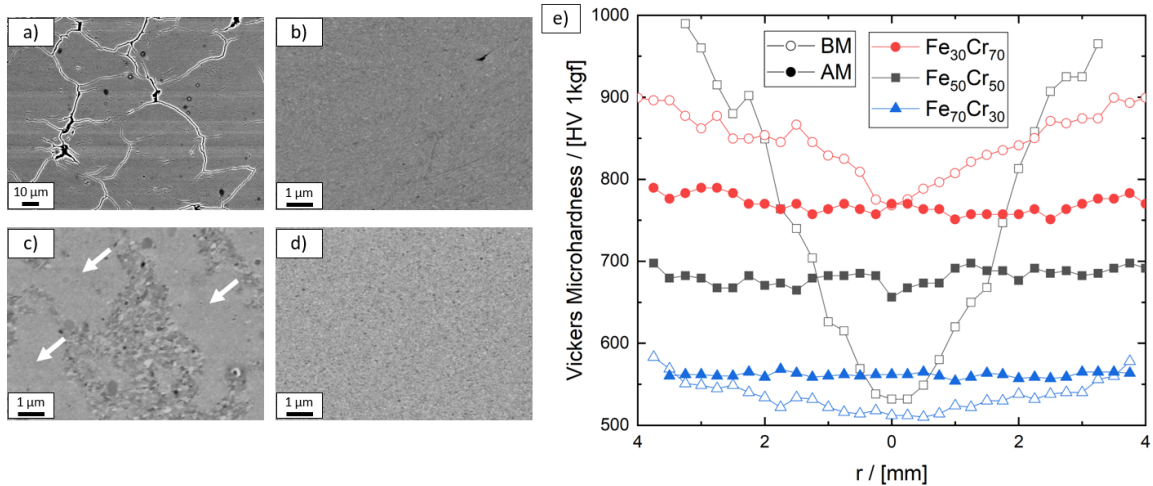
Figure 3.2.: BSE images of HPT-deformed samples consisting of nominal 50 at.% Fe and 50 at.% Cr. **a)** BM-powder as starting material at a low deformation rate at RT. The particle interfaces are still visible. **b)** BM-powder deformed at 400°C. **c)** BM-powder deformed after an intermediate annealing step. Areas with formation of the σ-phase (white arrows) are visible. **d)** AM-ingot served as starting material, micrograph taken after RT-deformation. **e)** Microhardness measurements for three chemical compositions for samples manufactured from BM-powders and intermediate annealing (open symbols) and from AM-ingots (filled symbols).

To circumvent this processing limitation, using the BM-powder as starting material, the HPT-compacted discs were annealed prior HPT-deformation to soften the material.

3. Results and Discussion

The samples were annealed at 1000°C for 2 h in vacuum conditions to avoid the formation of oxides or nitrides. A subsequent deformation at 400°C, was successful for the $Fe_{30}Cr_{70}$ and $Fe_{70}Cr_{30}$ samples. BSE-images showed a homogeneous microstructure and hardness measurements (Figure 3.2e) open symbols) revealed an almost constant value with respect to the sample radius. Therefore, a microstructure close to the steady state regime was reached. Nevertheless, for the $Fe_{50}Cr_{50}$ sample, an inhomogeneous microstructure as depicted in Figure 3.2c) was found. Referring to the phase diagram of Figure 2.8a) the mechanically unwanted σ-phase was found for medium compositions of FeCr. In the literature, cold rolling is reported to enhance the σ-phase formation [55, 56]. This σ-phase formation is correlated to the introduced material defects and are in strong accordance to the HPT experiments, where the hardness values in Figure 3.2e) radially increase.

However, for exchange bias coupling an equal distribution of closely spaced ferromagnetic and anti-ferromagnetic phases is intended and the σ-phase should be evaded. Therefore, the processing route was again changed. The elemental mixing was performed in the liquid phase, thus AM was applied to form FeCr ingots. The ingot was cut into discs by electrical discharge machining, to suite for HPT-deformation. Exemplarily, Figure 3.2d) shows a BSE-image of a RT-deformed $Fe_{50}Cr_{50}$ sample featuring a highly homogeneous and refined microstructure. The hardness measurements depicted in Figure 3.2e) show constant values (filled symbols) across the radius for all three chemical compositions. The hardness value increased with increasing Cr-content but for all compositions a steady state regime was found.

The constant hardness values already indicate the formation of a homogeneous microstructure (composite or solid solution), however, for the exchange bias coupling it is crucial to know about the elemental distribution on the small scale. Therefore, the following experiments were limited to the $Fe_{50}Cr_{50}$ composition with the AM material forming the HPT starting material. For this composition, the influence of an enhanced deformation temperature applied during HPT-deformation was studied. In Figure 3.3a)-c) and d)-f) electron microscopy images of a RT-deformed and a 400°C-deformed sample (7.5 GPa, 25 revolutions) are presented, respectively. The BSE images in Figure 3.3a) and d) are representative for the complete cross-section of the samples and show a highly homogeneous microstructure. The transmission electron microscopy (TEM) images in Figure 3.3b) and e) as well as the transmission Kikuchi diffraction (TKD) pattern of Figure 3.3c) and f) indicate a nanocrystalline structure. The inset in the TEM-images display corresponding selective area diffraction (SAD)

22
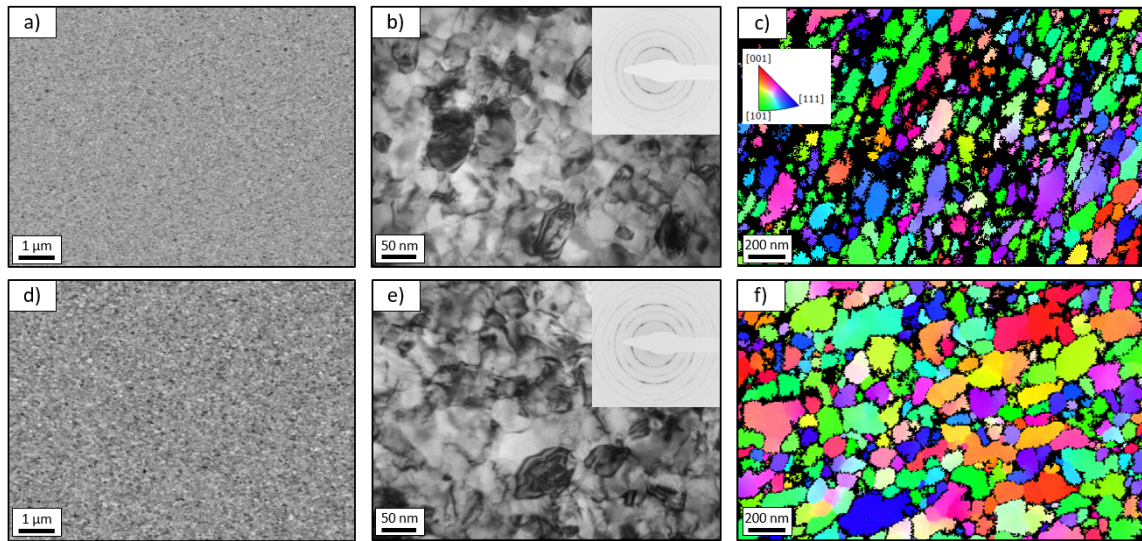
Figure 3.3.: Electron microscopy analysis for AM-samples after RT-deformation **a)-c)** and deformation at 400°C **d)-f)**. **a)** and **d)** show BSE-images, **b)** and **e)** show TEM-images with corresponding SAD-pattern and **c)** and **f)** show crystal orientation maps recorded by TKD.

pattern. No amorphous areas were found and within the TEM-resolution no diffraction peaks which would belong to separated Fe or Cr grains were recorded. Therefore, the formation of a supersaturated solid solution is presumed. Several TKD-scan were recorded and analyzed by fitting a log-normal distribution resulting in a median grain size of 102 nm and 158 nm for the RT and 400°C-deformed sample, respectively.

To further broaden our understanding on the HPT-deformation and phase distribution of Fe and Cr, atom probe tomography (APT) was conducted. The data presented in Figure 3.4a) and b) again belong to the samples deformed at RT and 400°C, respectively. The APT-tip representation shows the 50 at.% isosurfaces for Fe (blue) and Cr (green). For both samples the intended equal chemical composition of the used powder blend is in good agreement with the global APT-tips. The grey box indicates a selected region of interest (ROI), which is used to analyze the localized Fe and Cr concentration. The chemical composition varies only slightly within the ROI of the RT-deformed sample. For the 400°C-deformed sample the behavior is similar although the isosurfaces are larger in size. Thus, slight changes in chemical concentration are stronger localized for the RT-deformed sample. No distinct volumes containing mainly Fe or Cr were found within the tip. In summary, the two APT tips showed that the material formed a solid solution after HPT.

3. Results and Discussion
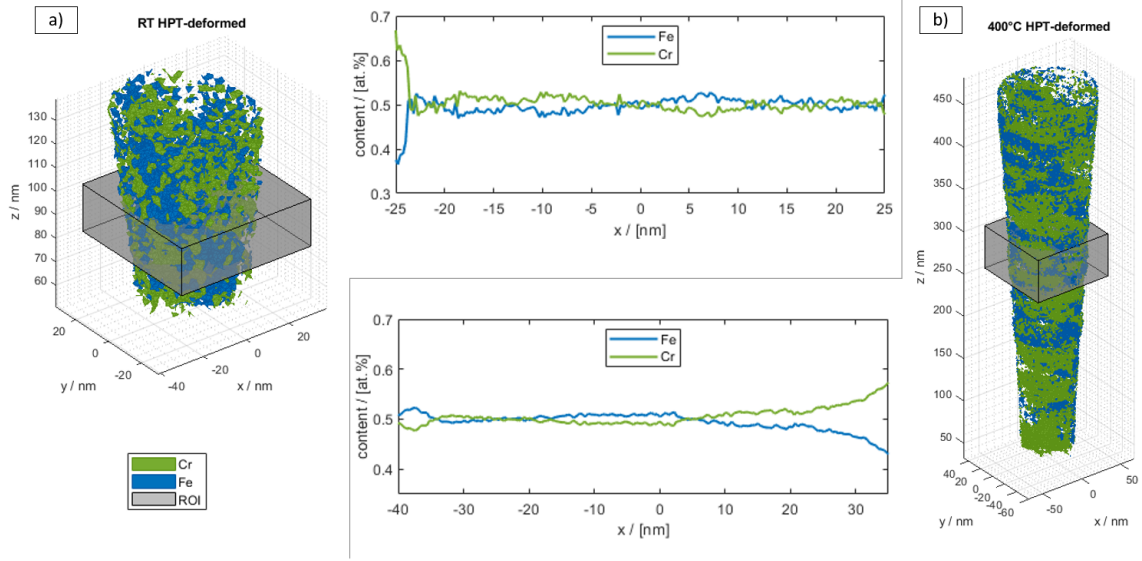
Figure 3.4.: APT measurements for $Fe_{50}Cr_{50}$ samples HPT-processed at **a)** RT and at **b)** 400°C. The chemical composition within the grey box (ROI) is displayed as a function of the displacement into the x-coordinate.

Magnetic measurements using a superconducting quantum interference device (SQUID) were performed at the same two materials. Figure 3.5a) shows the hysteresis loops of the RT and 400°C-deformed sample displayed by full and open symbols, respectively. The saturation magnetization of the measurement at 5 K (blue curves) was higher than for the 300 K hysteresis loop (red curves). This is because of the influence of thermal energy disturbing the alignment of the magnetic spins. This effect was slightly stronger pronounced for the RT-deformed sample, which could have indicated a higher fraction of unbound surface spins, e.g., on the grain surface or atoms within a grain boundary. However, the magnetic moment of the measured $Fe_{50}Cr_{50}$ samples remained below the theoretical value for bulk Fe, which is 222 emu·g^{-1} [57], 111 emu·g^{-1} for $Fe_{50}Cr_{50}$, respectively. The coercivity was in the range of a semi-hard material, behaved as expected and was decreased for higher measurement temperatures, as visible in the inset of Figure 3.5a). A field cooling procedure was applied to the measurement depicted by the blue curves. First, the samples were heated up to 350 K, which is well above T_N of bulk Cr ($T_{N,Cr}$=311 K [58]), to transform a possible anti-ferromagnetic ordering into a paramagnetic state. Then, an external magnetic field of 7 T was applied while the material was cooled through $T_{N,Cr}$ to 5 K, at which the hysteresis loop was recorded directly after. As expected by the preceding experiments, no shift in the hysteresis indicating an exchange bias coupling was found.

24
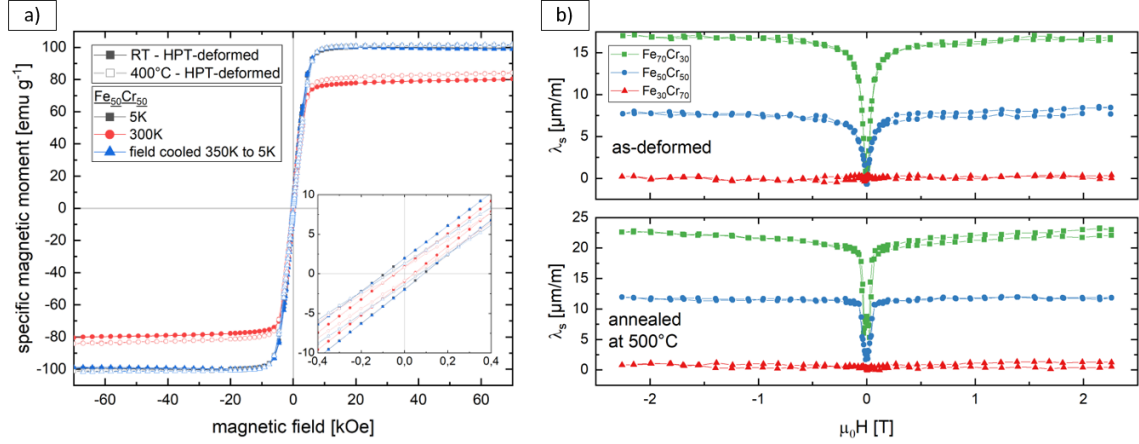
Figure 3.5.: **a)** Hysteresis measurements on RT and 400°C-deformed $Fe_{50}Cr_{50}$ samples. No exchange bias shifting the hysteresis loops is found. **b)** Magnetostrictive measurements on as-deformed (upper graph) and 500°C annealed (lower graph) samples. The high values for λ_s confirm a FeCr solid solution.

This is because the material exhibits a supersaturated solid solution, which is a solely ferromagnetic phase without any anti-ferromagnetic contribution [59].

The previous experiments explained how to properly manufacture a supersaturated solid solution of a FeCr alloy with equal chemical distribution. In the following, we extended the chemical compositions of the materials, sampling the binary phase diagram to study a broader variety of compositions. Starting with an AM-ingot, these samples were HPT-deformed at RT applying 7.5 GPa and 25 revolutions. The obtained samples were denoted to 'as-deformed' in the following and were cut into different pieces for further processing. The as-deformed materials ($Fe_{70}Cr_{30}$, $Fe_{50}Cr_{50}$ and $Fe_{30}Cr_{70}$) exhibited a nanocrystalline microstructure and were the base material for annealing treatments. For annealing temperatures above 400°C and annealing treatments longer than 10 h, the samples were encapsulated under Ar-atmosphere to prevent the formation of any oxide or Cr-N phases.

First, the influence of different annealing temperatures applied for 1 h on the as-deformed materials was studied. BSE-images of all three alloys revealed a nanocrystalline microstructure in the as-deformed state. With increasing temperature grain coarsening took place, which was stronger pronounced for a higher Fe content and higher annealing temperatures (c.f. Publication B Figure B.1). On small length scales, APT revealed the formation of a solid solution after HPT. For larger volumes and to examine whereas the material was a composite or solid solution magnetostrictive

3. Results and Discussion

measurements were applied. The magnetostrictive measurements were performed on the as-deformed and 500°C annealed samples perpendicular and parallel to the applied magnetic field direction. The effective saturation magnetostriction λ_s for polycrystalline materials was calculated by

$$\lambda_s = \frac{2}{3}(\lambda_\parallel - \lambda_\perp) \tag{3.1}$$

and plotted against the applied magnetic field $\mu_0 H$ in Figure 3.5b). The maximum signal was reached for the Fe-rich $Fe_{70}Cr_{30}$ sample for the as-deformed state as well as for the 500°C annealed state obtaining a λ_s of 17 ppm and 23 ppm, respectively. For comparison, the magnetostriction of bulk Cr $\lambda_{s,Cr}$ is below 1 ppm [60] and bulk Fe reaches a negative value $\lambda_{s,Fe} = $ -9.3 ppm due to a crystallographic anisotropic behavior. A λ_s value as high as measured is only possible if a solid solution is present. This solid solution also remained for all chemical compositions upon annealing up to 500°C.
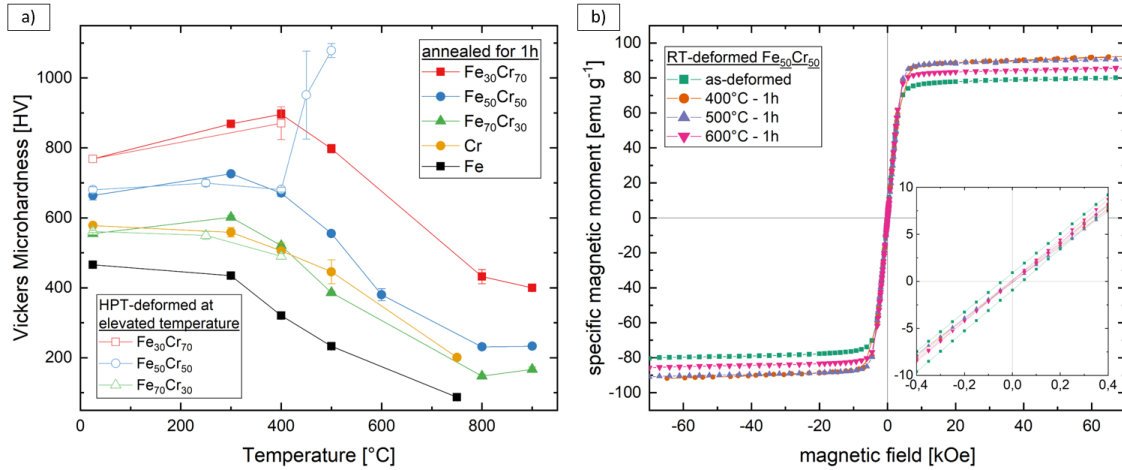
Figure 3.6.: **a)** Hardness measurements on different HPT-deformed Fe_xCr_{1-x} samples. The full symbols represent annealed states, while the open symbols show the hardness of samples HPT-deformed at elevated temperatures. Please note the formation of the σ-phase for the medium composition upon deformation. **b)** Hysteresis measurements on $Fe_{50}Cr_{50}$ annealed at different temperatures.

The higher λ_s values for the annealed state were explained by the reduced number of microstructural defects within the material [61]. This was further confirmed by hardness measurements shown in Figure 3.6a).

A hardening of the material upon annealing at higher temperatures was found

for the FeCr alloys but not for the elemental materials. This effect is known for nanocrystalline materials and usually denoted as 'hardening by annealing' peak. The higher the Cr-content, the higher was the temperature where the peak in hardness appears. Generally, the alloyed materials exhibited a higher hardness compared to the elemental - and also severely deformed - samples. To further elaborate the survey on HPT-processing of FeCr, the hardness of samples deformed at elevated temperatures is also plotted (open symbols). They follow the trend of a subsequent annealing except for the $Fe_{50}Cr_{50}$ composition, where an abrupt increase in hardness for HPT-deformation temperatures above 400°C was reported. The 450°C-deformed sample showed a composite structure of an FeCr-alloy and the σ-phase, therefore the pronounced error bar. When deforming at 500°C a bulk sample of almost pure σ-phase was formed.

Magnetic hysteresis measurements shown in Figure 3.6b) were performed on $Fe_{50}Cr_{50}$ samples annealed at different temperatures. In the as-deformed state a high microstructural defect density enhanced H_C [62]. Upon annealing the defects density was reduced and a small H_C was measured, which was below the resolution limit of the SQUID magnetometer. Further, the M_S was influenced and changed with respect to the defect density and grain size [63–65].
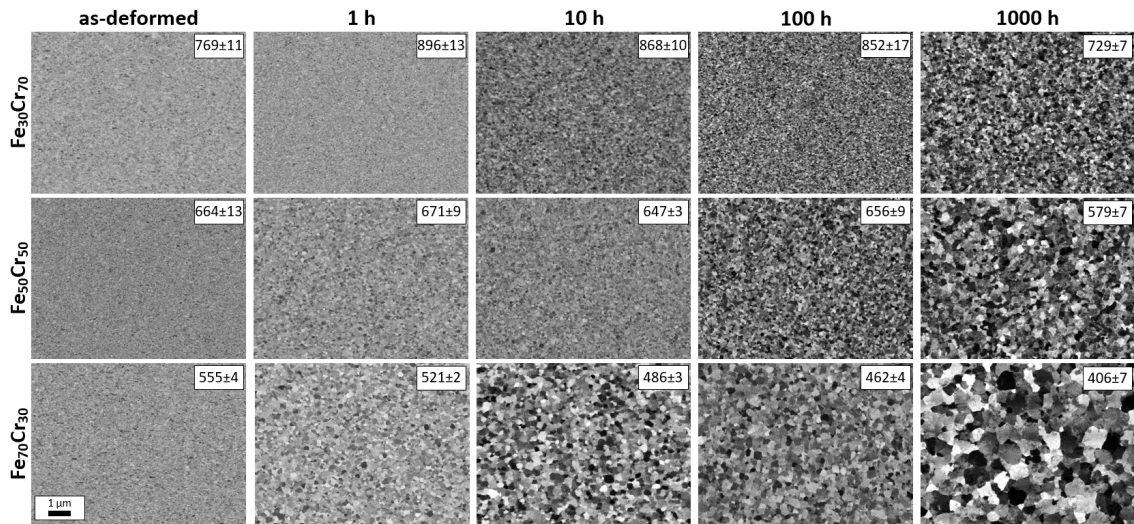
Figure 3.7.: BSE-images of different FeCr-alloys annealed for different times at 400°C. The inset shows values of corresponding hardness measurements.

To produce Fe- and Cr-rich phases, the HPT-deformed FeCr samples were annealed for different durations at a constant temperature of 400°C, which was within the

3. Results and Discussion

miscibility gap of the thermodynamic equilibrium phase diagram (Figure 2.8) but below the temperature of sigma phase formation. A decomposition and in particular a spinodal decomposition was expected. BSE-images of all samples and applied annealing times (ranging from 1 h to 1000 h) were shown in Figure 3.7. A grain coarsening for longer annealing times and for higher Fe-content was found.
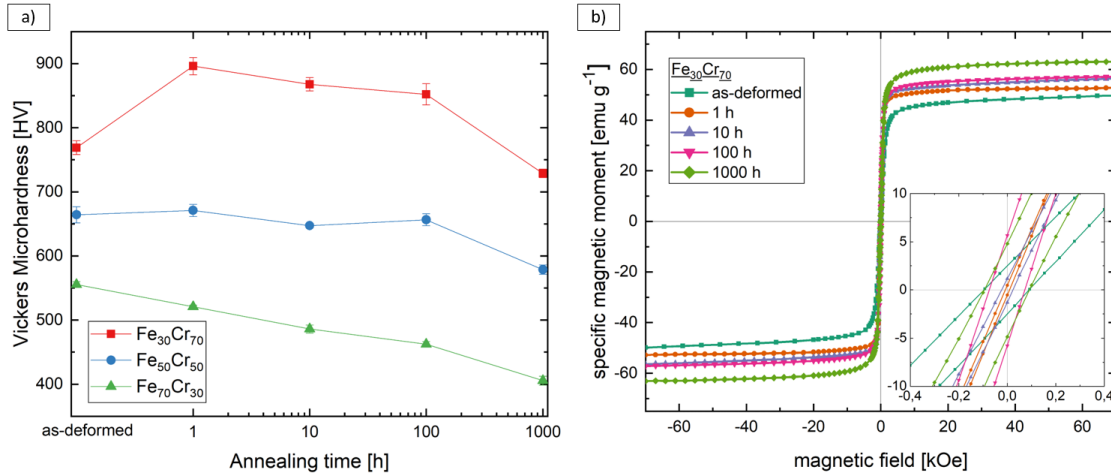
Figure 3.8.: **a)** Hardness measurements of different FeCr-alloys annealed for different times at 400°C. **b)** Magnetic hysteresis of HPT-deformed $Fe_{30}Cr_{70}$ measured at 40 K after a magnetic field cooling from 350 K and an applied field of 7 T.

Corresponding hardness measurements are depicted in Figure 3.8a). The hardness of the Fe-rich sample (green curve) decreases approximately in a logarithmic way with the annealing time. This behaviour is not present for the medium composition (blue curve) as the hardness stays relatively constant up to 100 h. The Cr-rich sample shows an increased hardness after 1 h of annealing, which decreases in the following annealing steps and reaches a similar hardness as it started with, after 1000 h of annealing.

Motivated by the work of Xiong et al. [59] the Cr-rich sample was chosen for further magnetic experiments. This was because of the interpretation of the magnetic Fe-Cr phase diagram, which shows broad chemical regions of ferromagnetic (Fe-rich) and anti-ferromagnetic (Cr-rich) phases. They are only separated by a small paramagnetic region at similar Cr-content. Thus, an (insufficient) decomposition likely forms a ferromagnetic and anti-ferromagnetic phase, which would not be the case for Fe-rich samples. In Figure 3.8b) magnetic hysteresis loops after a magnetic field cooling from 350 K down to 40 K at an applied field of 7 T are shown. The measurement was

performed at 40 K to avoid a possible region of magnetic disordering (spin glass region) at even lower temperatures. However, there was no significant shift of the hysteresis visible, which would have indicated the presence of an exchange bias.
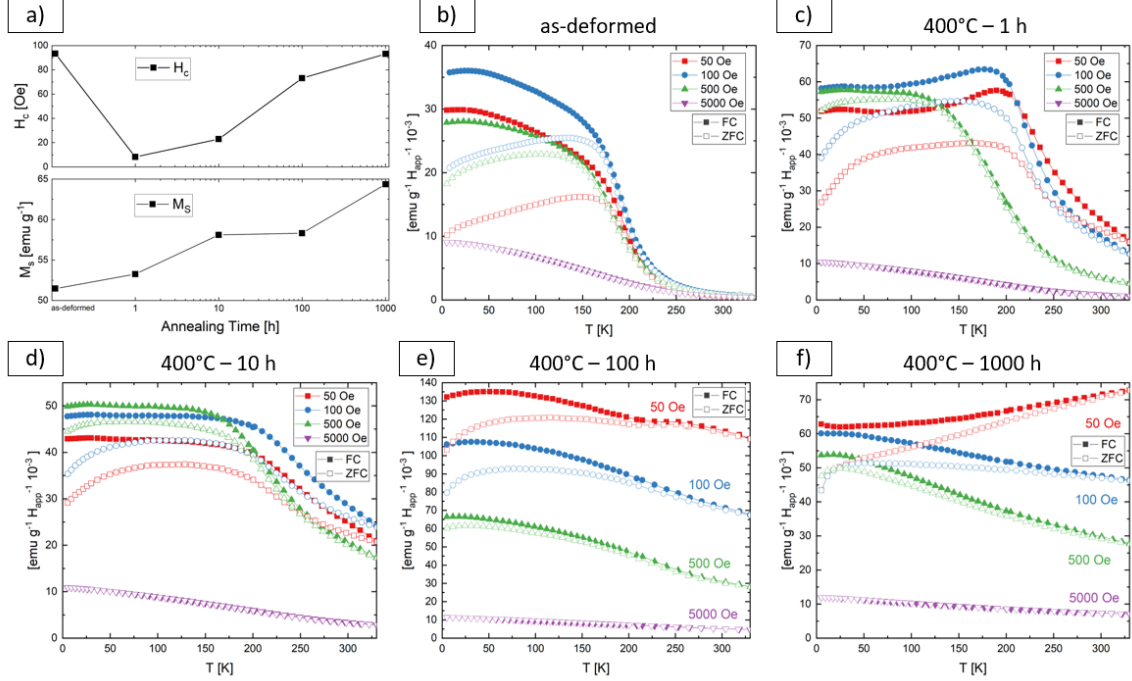
Figure 3.9.: **a)** Magnetic properties of HPT-deformed $Fe_{30}Cr_{70}$ as a function of annealing time. **b)-f)** Normalized ZFC-FC measurements of HPT-deformed and annealed $Fe_{30}Cr_{70}$. Please note the different scaling of the ordinate.

In Figure 3.9a) important magnetic parameters are plotted as a function of annealing time. A relatively high amount of residual stresses led to a high H_C of the as-deformed material. After annealing for 1 h the defects could have annihilated and reduced stresses inside the Fe-rich grains resulting in a small H_C. H_C increased again with increasing annealing times. As we assumed a spinodal decomposition, the Fe-rich ferromagnetic particles would have precipitated at very small volumes and could have grown by time but due to the low temperature and slow decomposition, still a small grain size (or Fe-rich particle size) would remain. According to the left side of the Herzer diagram (c.f. Figure 2.6) H_C is increasing by increasing grain size, describing this H_C development. M_S increased up to ~65 emu/g. Using the theoretical M_S value for bulk Fe [57] and applying a linear approximation the measured M_S fits well to the intended Fe concentration of 30 at.%.

Figure 3.9b-f) shows zero field cooling (ZFC) and field cooling (FC) measurements

of the $Fe_{30}Cr_{70}$ samples. For every annealing step, a series of ZFC-FC measurements was recorded to study the development of the nanostructured system. The applied bias fields was increased after every measurement (50, 100, 500, 5000 Oe using red, blue, green purple curves, respectively). ZFC-FC measurements are usually used to determine for nano-particle systems whether a correlation between thermal energy, magnetic anisotropy and ferromagnetic percolation exists. Thus, the presence of ferromagnetic clusters within a non-magnetic material, as well as their interaction among themselves can be studied [66]. Important aspects of measured ZFC-FC curves are enumerated in the following. First, as expected for metallic materials, the ZFC curve is lower than the FC curve. Second, the blocking peak should be discussed in detail. When fitting the curves, not only one peak is necessary, but two distributions contribute. These distributions could originate from two differently sized ferromagnetic clusters (spinodal decomposition of Fe-rich and Cr-rich phases) and/or from two clusters having a different anisotropy constant. Additional experiments (APT, TEM, SQUID) will be necessary to clarify if cluster sizes, the magnetocrystalline anisotropy of phases facing different chemical compositions, shape- or strain-anisotropies are the reason for this appearance. Third, these two distributions seem to evolve differently for different annealing treatments. In general, the blocking peak temperature increases as the volume of the investigated nanocrystals (or herein, the volume of segregated phases) increases. Focussing on the lowest bias field measurements (50 Oe, red curves) of Figure 3.9b) and c) the peak at lower temperature grows somewhat stronger in height than the higher temperature peak. However, this higher temperature peak seems to broaden in the following graphs d) and e) and also to shift towards higher temperatures, exceeding the limit of measurement in Figure 3.9f). Thus, the volumetric size of the segregated phases is growing. And fourth, for higher applied bias fields, the observed two peaks are less pronounced. Thus, a higher external applied magnetic field is less sensitive to distinguish between the two distributions and the profile of the distributions are influencing the resulting field dependent ZFC-FC curves.

Although no exchange bias was measured, SQUID magnetometry could have indicated a beginning (spinodal-) decomposition. The temperature dependent magnetic measurements are highly interesting but difficult to interpret. For further investigations, an influence of interacting ferromagnetic clusters thus, Ruderman-Kittel-Kasuya-Yosida (RKKY)-interaction, but also the possibility of a Dzyaloshinskii–Moriya interaction (DMI) should be considered. On the other hand, the magnetic behavior of FeCr alloys drastically change upon chemical composition and temperature [59].

In combination with a strained and probably textured microstructure an expanded magnetic phase diagram could be elaborated. In addition, it should be mentioned, that the commonly accepted value for $T_{N,Cr}$ is 311.5 K [58] but an older literature by Shull et al. [67] reported a much higher $T_{N,Cr}$ value of ∼475 K. Therefore, one should probably consider effects (strain, precipitates, chemical composition of a supersaturated solid solution, etc.) influencing the $T_{N,Cr}$ and adapt the field cooling prior hysteresis measurements accordingly.
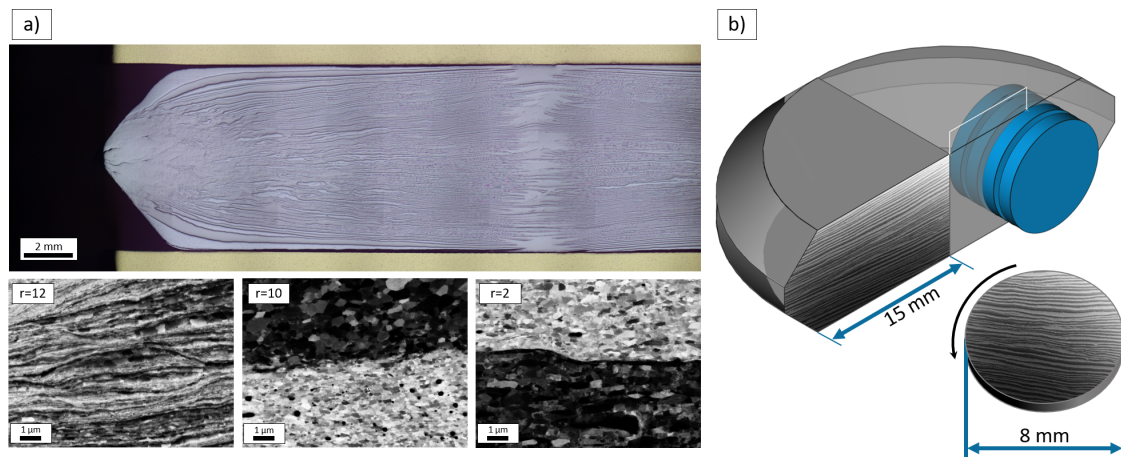
Figure 3.10.: **a)** Optical micrograph image of a multi-sector HPT disc after 20 revolutions using 14 pieces of alternating Fe and Cr. About 260 layers are counted. The lower images are recorded by BSE and show the Fe (bright contrast) and Cr (dark contrast) interface at different radii. **b)** Schematic of the 2-stage HPT-process. The blue disc are cut at a certain radius suitable for another HPT-device allowing a further deformation of the material while rotating the shear plane perpendicular.

Nevertheless, aiming an exchange bias, a proper decomposition of the material by heat treatments was not successful. In another attempt, the transition between a two-phase composite and the formation of a supersaturated solid solution was studied. Therefore, a two-stage HPT-procedure was applied. Motivated by the multi-sector disc approach [68] the first HPT-step uses 7 pieces of pure Fe and Cr each as starting material. The pieces were shaped like slices of a pie, with 15 mm length and ≈ 25° opening angle and were arranged prior deformation, forming a disc with alternating sections of Fe and Cr. Prior HPT-deformation the anvils were heated to ≈ 100°C and during deformation the inner friction was utilized to maintain slightly elevated deformation temperatures for 20 revolutions. This allowed to refine the material, reduce phase distances and simultaneously preserve the two-phase structure. In the

3. Results and Discussion

upper image of Figure 3.10a) an optical microscope image of the halved sample is shown. A layered structure of more than 260 Fe and Cr layers was observed. BSE images on the bottom of Figure 3.10a) were recorded at different radii showing the interfaces between Fe (bright contrast) and Cr (dark contrast). Even at higher radii the phases remained separated and did not mix. This sample, processed in the first HPT-step was used as starting material for the second step. Figure 3.10b) schematically shows the further processing, where several discs (marked in blue) were cut, fitting in a smaller HPT-device. The shear plane of HPT-deformation of the second step was rotated about 90°, thus again a kind of multi-sector disc approach was obtained.
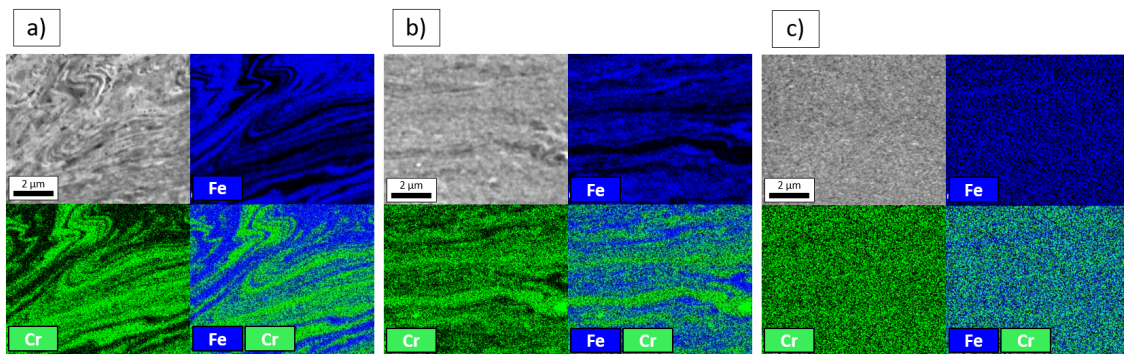
Figure 3.11.: SEM images and corresponding EDS maps of a 2-stage HPT sample, deformed for 20 rotations at ≈ 100°C in first and additional 40 rotations at 400°C in the second step. A separated distribution of Fe (blue) and Cr (green) phases is visible for $r \approx 0$ mm **a)** and $r = 1$ mm **b)**. At $r = 3$ mm **c)** the size of refined phases is below the resolution limit of EDS.

Exemplarily, the analysis of one sample with certain HPT-parameters is herein presented in detail. Within the second stage, the sample was deformed for additional 40 rotations at 400°C. As presented in Figure 3.11, SEM as well as EDS-map measurements were conducted to the polished surface of the halved HPT disc in tangential direction. At about $r \approx 0$ mm the separated Fe and Cr phases are clearly visible in Figure 3.11a). For $r = 1$ mm the phase distances are reduced until no differences can be obtained by EDS for $r \geq 3$ mm as shown in Figure 3.11b) and c), respectively.

The sample was further analysed by radially resolved EDS-spot measurements. In Figure 3.12a) the Cr content is plotted as a function of the radius for every spot measurement. The horizontal line represents the calculated mean value of all measurements of one certain radius. For $r \approx 0$ mm and $r = 1$ mm the chemical composition is broadly distributed. A small acceleration voltage (3 keV) was used to

32
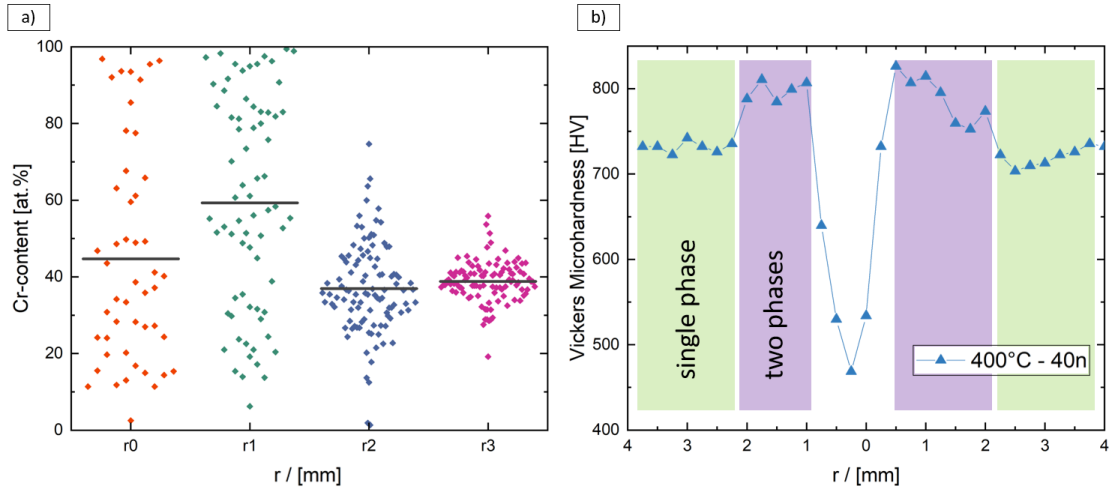
Figure 3.12.: Radially resolved EDS **a)** and hardness **b)**measurements of a 2-stage HPT sample, deformed for 20 rotations at ≈100°C in first and additional 40 rotations at 400°C in the second step.

minimize the interaction volume of the electron beam. However, it was occasionally interacting with separated phases and partly with a mixture of both phases. This changed for higher radii, where the distribution of chemical composition narrows. The material tended to form a solid solution for higher deformation grades or more specifically, EDS was not capable to resolve the strongly reduced phase distances. For hardness measurements presented in Figure 3.12b), two distinct regions are recognized. Starting from the center of the HPT disc, the hardness values increase with increasing radius, thus increasing applied strain. It reaches a maximum between $r \approx 1$ mm and $r \approx 2$ mm. For higher deformation grades, the hardness value is again reduced and stagnates. The results are in agreement with the previous observations, as the region of higher hardness can be explained by a strongly refined but separated phases, which stabilise themselves mutually. For a single phase thus, if a solid solution is formed, the hardness values are lower and tend to saturate (c.f. hardness values of Figures 3.6a) and 3.7).

This specific sample showed a radially changing microstructure starting from a two phase structure at $r = 0$ mm and resulting solid solution at $r = 3$ mm. To check if any exchange bias was present in any microstructural state in between, SQUID magnetometry was applied to specimens for different radii. The hysteresis presented in Figure 3.13 were measured after a 7 T field cooling from 350 K to 40 K at the final
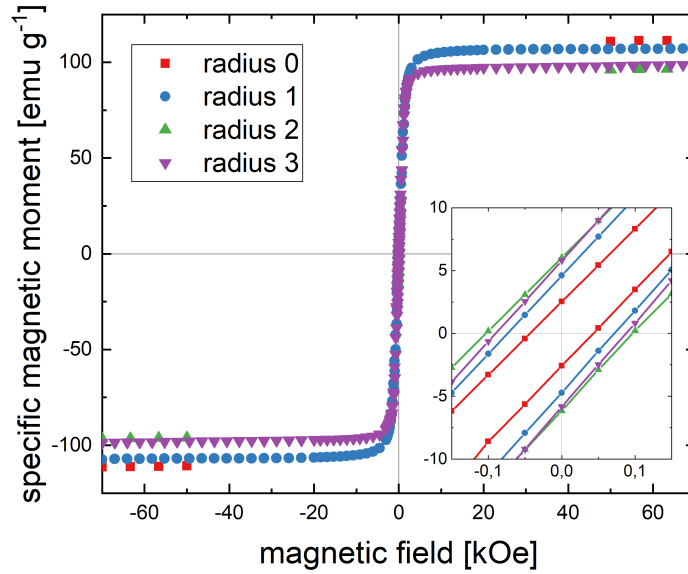
Figure 3.13.: Radially resolved SQUID hysteresis measurements of a 2-stage HPT sample, deformed for 20 rotations at ≈100°C in first and additional 40 rotations at 400°C in the second step.

temperature. The inset shows the region around H_C but no shift of the hysteresis along field cooling direction was found for any specimen.

As already mentioned above, plastic deformation allows to reduce microstructural feature sizes, which e.g. increases the interface area of two phases. However, it also induces a variety on microstructural defects, which influence magnetic properties. As exchange bias is an interface effect, it is expected to be very sensitive to microstructural imperfections. Therefore, a further advanced processing route was elaborated. The formation of a solid solution should be avoided, yet a lower strain was needed. To reduce microstructural defects and to sharpen the Fe-Cr interfaces annealing was applied after HPT-deformation. However, to reach a sufficient small phase refinement, this procedure was repeated several times. Herein, a sample was deformed for 20 rotations at ≈ 100°C in the first stage and annealed in Ar-atmosphere for 24 h at 400°C directly after. Within the second stage, the sample was subsequently deformed for 5, 3 and 1 rotation, whereas the same annealing treatment was performed in between every HPT-deformation.

In Figure 3.14 the analysis of this sample is presented. The EDS measurements in Figure 3.14a) show the intended two phase structure. Measured hardness values in Figure 3.14b) are increasing with increasing radius but stay below the maximum of

Figure 3.14.: EDS **a)**, hardness **b)** and SQUID **c)** measurements of a 2-stage HPT sample. The sample is deformed for 20 rotations at $\approx$ 100°C in the first stage and additionally for 5, 3 and 1 rotation at 400°C during the second stage. Between every deformation step, the sample is annealed for 24 h at 400°C.

our previous results shown in Figure 3.12b). Therefore, a two-phase structure could be assumed. Though, a SQUID hysteresis curve (Figure 3.14c), red curve) measured at 40 K with the field cooling procedure (already described above), does again not show any exchange bias. Even if the sample was annealed again for 24 h at 400°C, no shift of hysteresis was observed.

3.2. High-Pressure Torsion Induced Exchange Coupling

Large H_C could be expected for refined hard-magnetic phases (Type II magnet of Figure 2.7). As grain refinement is a fundamental feature of HPT, we applied HPT-deformation to $SmCo_5$ powder. Yet, the deformation of brittle materials usually portrays a challenging task. With respect to metals, this is mainly due to the lack of slip planes that act as enabler of plastic deformation. Applying the already presented powder HPT route, at first a consolidation has to take place and afterwards the actual deformation including phase refinement occurs. A localization, thus regions of strain concentration, often recognized as shear bands, would lead to an inhomogeneously deformed sample.

In Figure 3.15a), b) and c) examples for samples HPT-deformed for 1, 10 and 20 revolutions are shown, respectively. The deformation was possible because of the chosen HPT-set up, the so called 'quasi-constrained HPT' [20]. It includes a small cavity in the anvils as depicted in Figure 2.1 and allows a maximal confinement of
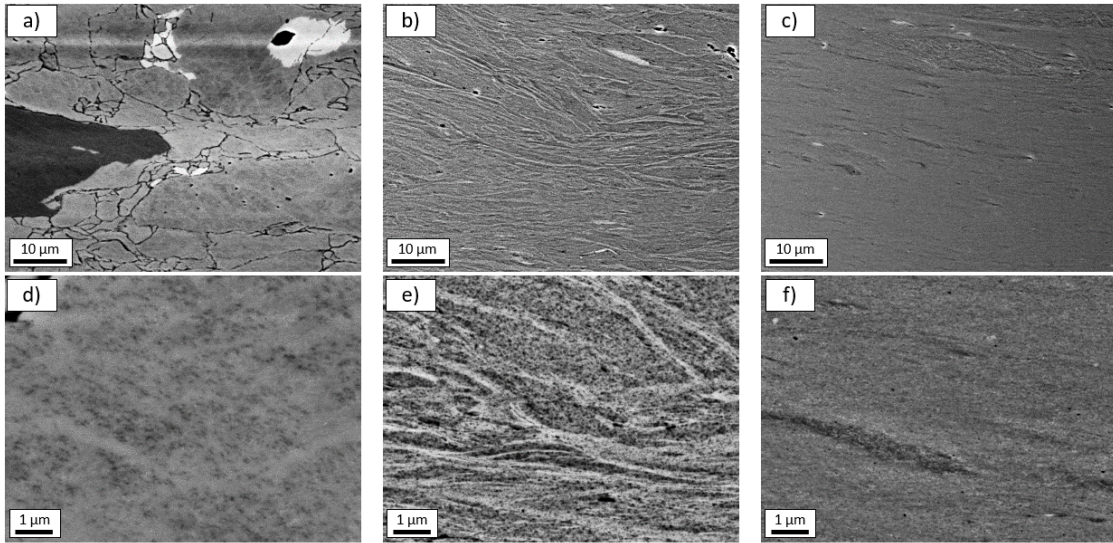
Figure 3.15.: BSE-images of HPT-deformed SmCo$_5$ powder samples at r≈3 mm recorded in tangential viewing direction and deformed for 1, 10 and 20 revolutions **a)**,**b)** and **c)**, respectiveley. The microstructure at higher magnification is shown in **d)**, **e)** and **f)**.

the consolidated powder-pellet. The material tending to flow out the edge of the anvils is hindered by a high friction evolving at the HPT-disc edge. This leads to a backpressure inducing a hydrostatic pressure within the anvils processing zone, thus inside the sample material. Because of this high hydrostatic pressure, the formation of cracks is hindered and the material is forced to be deformed and refined. While the sample in Figure 3.15a) show a pronounced separation between large inital powder particles, an already strong refinement is found for Figure 3.15b) and c). BSE images of the same samples at higher magnifications presented in Figure 3.15c), d) and f) show a clear difference between the microstructure within one grain, a composition of elongated and refined grains and an ultra-fine grained microstructure, respectively.

The HPT-deformed material was further studied by synchrotron high energy X-ray diffraction (HEXRD) presented in Figure 3.16a). Samples subjected to a different amount of applied HPT revolutions thus applied strain, were measured at a radius of 3 mm. The vertical lines represent the positions of peaks corresponding to the SmCo$_5$ phase and were taken from the literature (Crystallography Open Database; COD 1524132) [69]. The expected significant peak broadening as well as a reduced intensity of X-ray diffraction (XRD) signal is visible for samples subjected to higher deformation grades. This can be explained by the already observed grain refinement in Figure 3.15 as well as by a possible formation of an amorphous phase [70]. Magnetic

measurements showed an interesting behavior. For the compacted sample, the lowest H_C as well as lowest M_S was found. A slight improvement was found by increasing the applied strain (1 revolution) but it stagnated for the 10 revolution sample. For even higher deformation grades (20 revolutions) the H_C was further increased.
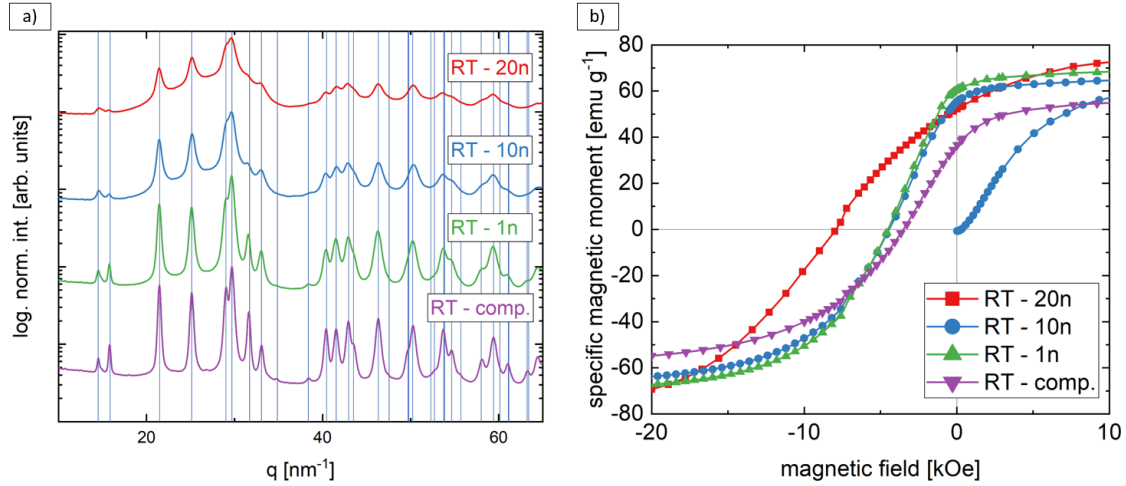
Figure 3.16.: **a)** Synchrotron XRD measurements of differently HPT-deformed $SmCo_5$ samples at r≈3 mm. **b)** Corresponding magnetic measurements showing the demagnetizing branch of a hysteresis.

In a further study, the influence of HPT-deformation temperatures was investigated. In Figure 3.17a) the HEXRD pattern of $SmCo_5$ samples deformed for 10 (solid lines) and 20 (dotted lines) revolutions are shown. The deformation temperature was varied between RT (green), 250°C (blue) and 400°C (red). For the RT and 250°C deformed sample a higher degree of deformation is monitored by peak broadening. For the 400°C deformed sample, no significant differences between 10 or 20 revolutions are visible. Probably, recovering mechanism were already activated at this temperature and a steady state was reached [21, 24]. It should be emphasized, that the formation of additional peaks, thus other phases was not recognized in any pattern.

Magnetic measurements were performed for the 10 revolution samples. The H_C was highest for the 250°C deformed sample. This further included a high squareness of the hysteresis loop in the 2nd quadrant, implying a slightly textured material. The RT as well as the higher temperature deformation sample exhibited a reduced H_C. Elevated temperatures often allow to extend the limits of deformation, however, for the $SmCo_5$ samples and a maximized H_C a deformation temperature below 400°C should be envisaged.

3. Results and Discussion
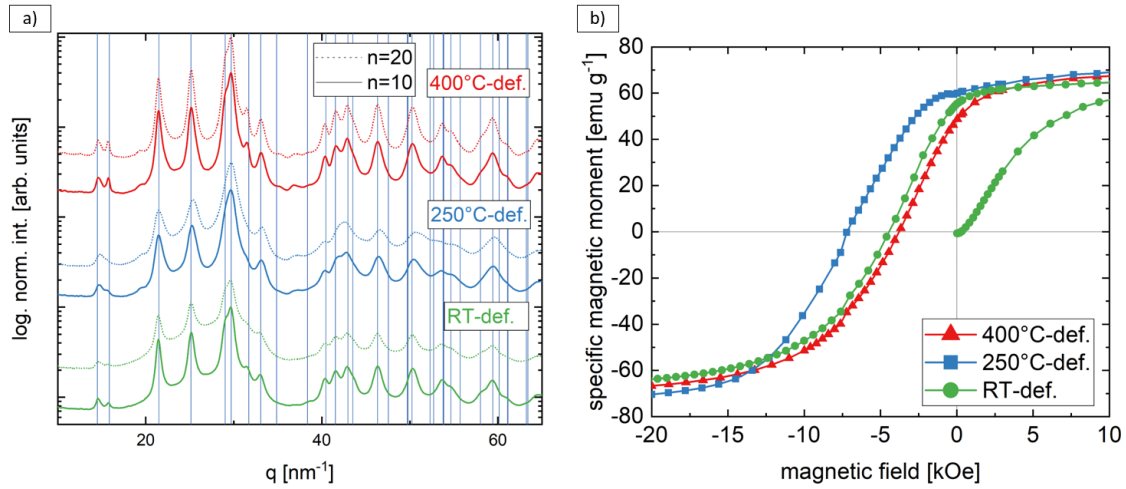
Figure 3.17.: **a)** Synchrotron XRD measurements of HPT-deformed SmCo$_5$ samples at r≈3 mm deformed at different temperatures. The dotted and continuous lines represent samples with 20 and 10 revolutions, respectively. **b)** Magnetic measurements corresponding to samples deformed for 10 revolutions showing the demagnetizing branch of a hysteresis.
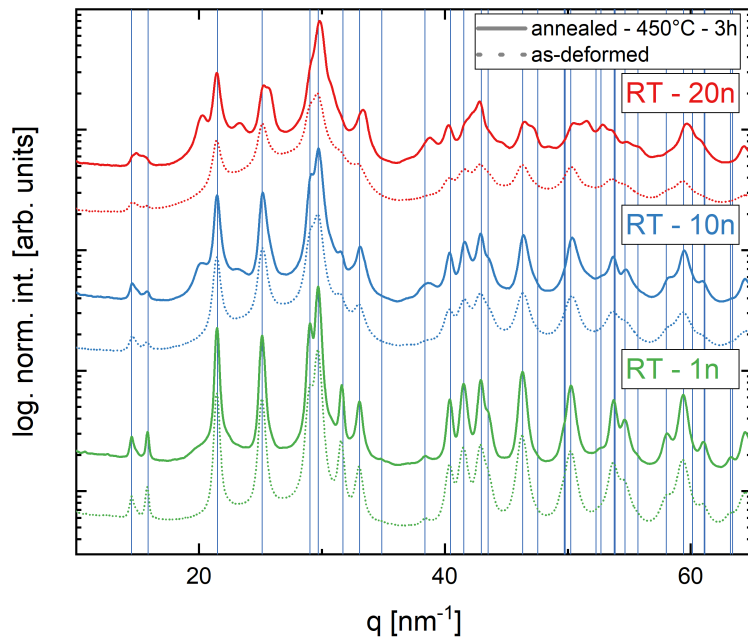
Figure 3.18.: Synchrotron XRD measurements of as-deformed (dotted lines) and HPT-deformed and subsequently annealed (continuous lines) SmCo$_5$ samples at r≈3 mm.

Samples deformed at RT were subsequently exposed to an annealing treatment. The samples were encapsulated in glass tubes containing an Ar-atmosphere to prevent oxidation and exposed to 450°C for 3 h. HEXRD measurements are shown in Figure

3.18. The interpretation allows to elucidate on an important characteristic. The annealing procedure only very slightly affects the sample deformed for 1 revolutions (green), e.g., the onset of a newly forming peak is found for $q \approx 20$ nm^{-1}. This specific peak indicates the formation of an additional phase and grows faster for higher deformation grades. Phase formations at low temperatures are often referred to a reduced annealing temperature induced by HPT-deformation and are always related to the higher defect density in these SPD materials [13, 71].
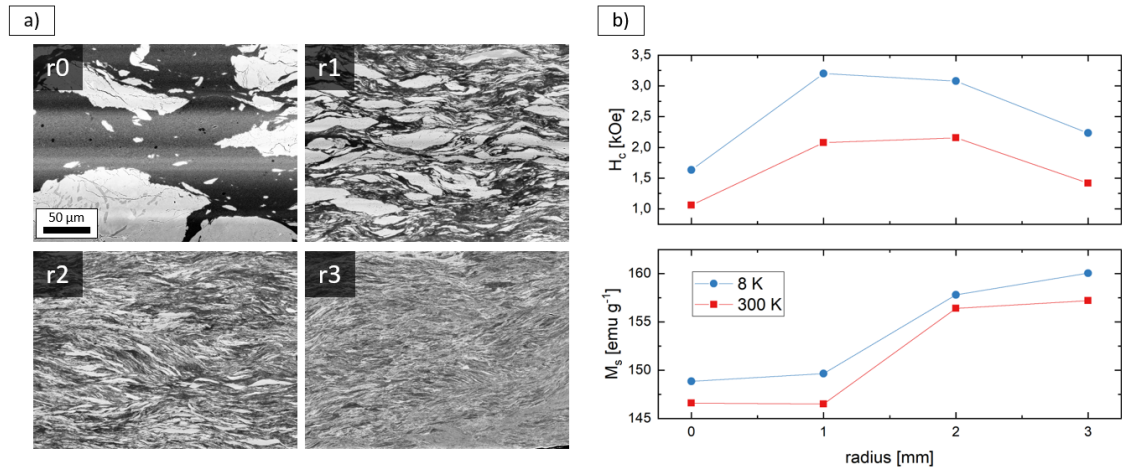
Figure 3.19.: **a)** BSE-images of an HPT-deformed Fe-SmCo$_5$ composite consisting of 47 wt.% Fe at different radii. At higher radii, a stronger phase refinement of the Fe (dark) and SmCo$_5$ (bright) phases are visible. **b)** Summarized magnetic properties obtained by radially resolved SQUID magnetometry.

In the following, another SmCo$_5$ based PM was processed by HPT. Here, soft-magnetic Fe was added to form a composite and to induce an exchange coupling as described by Type III in Figure 2.7. BSE-images of such a composite consisting of 47 wt.% Fe and 53 wt.% SmCo$_5$ are shown in Figure 3.19a). The images were recorded at different radii and directly demonstrate the influence of applied shear strain on the microstructure. For the center of the HPT-disc at r0 (radius = 0 mm) the initial Fe (dark contrast) and SmCo$_5$ (bright contrast) particles are clearly visible. As the applied strain increases, the SmCo$_5$ particles are reduced in size and start to elongate into the radial HPT-disc direction. For r3, the phase distances are reduced to about 1 µm. The sample was cut into smaller pieces to radially resolve the corresponding magnetic properties. The results of SQUID hysteresis measurements are depicted in Figure 3.19b). On the upper graph the H$_C$ and on the bottom graph the M$_S$ is shown

3. Results and Discussion

as a function of the radius. The properties were slightly improved for measurements at lower temperatures (8 K) because of the smaller contribution of thermal fluctuations. Interestingly, H_C is not strictly increasing with applied strain, rather a maximum at radii of about 1-2 mm is found. Furthermore, at about the same strain level the value for M_S starts to increase. This is expected to originate in the formation of a FeCo-alloy providing a higher magnetisation compared to an α-Fe phase.
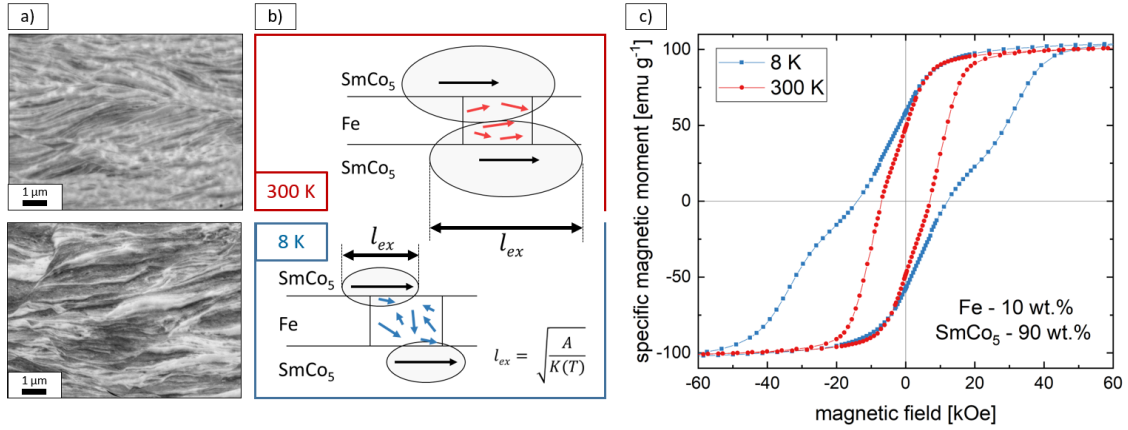
Figure 3.20.: **a)** BSE-images of HPT-deformed Fe-SmCo$_5$ composites consisting of 24 wt.% Fe (upper image) and 47 wt.% Fe (lower image) at r = 3 mm. **b)** The lamellar microstructure is modelled to explain the influence of the temperature dependency of the exchange length on the coupling mechanism between the Fe and SmCo$_5$ phase. **c)** Hysteresis loops measured at 8 K (blue curve) and 300 K (red curve) of an HPT-deformed Fe-SmCo$_5$ composites consisting of 10 wt.% Fe.

As already stated, the overall chemical composition can easily be varied for the HPT-process. Figure 3.20a) shows BSE images at high magnification of a composites consisting of 24 wt.% Fe (upper image) and 47 wt.% Fe (lower image) at a radius of 3 mm. The lamellar morphology already recognized in Figure 3.19a), is generated on an even smaller length scale for the lower Fe content. An alternating structure of Fe and SmCo$_5$ phases is visible. Exemplarily, a magnetic hysteresis measurement of a Fe-SmCo$_5$ composite consisting of 10 wt.% Fe is presented in Figure 3.20c). A strong difference between measuring at 8 K (blue curve) and 300 K (red curve) was recognized. The formation of the pronounced 'knee' for the low temperature measurement indicates a superposition of a soft and a hard magnetic phase, as the demagnetization of the Fe and SmCo$_5$ phase takes place at different applied fields. This is not apparent for exchange coupled spring magnets, where the resulting hysteresis features a convex shape. [51]. Exactly this exchange coupling behavior was measured

at 300 K for the same sample. To explain this manner, we consider the sample's lamellar morphology and take a temperature dependency of the magnetocrystalline anisotropy constant $K(T)$ into account [72]. As schematically described in Figure 3.20b) the exchange length l_{ex} of the hard magnetic $SmCo_5$ phase scales inversely proportional to K. Therefore, the volume of coupled Fe phase is dependent on the temperature and thus, to the over all magnetic performance of the composite.
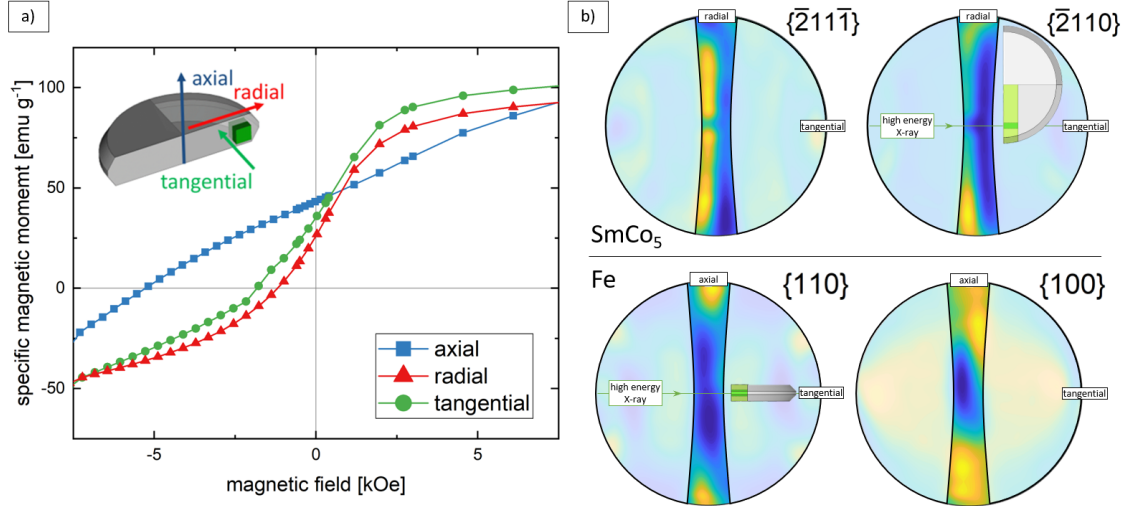
Figure 3.21.: **a)** Demagnetizing curves starting from +70 kOe for an HPT-deformed Fe-$SmCo_5$ composites consisting of 26 wt.% Fe. The sample is measured with the external field applied in three different directions with respect to the HPT-disc (inset). **b)** Pole figure representations of the same sample based on HEXRD measurements for two $SmCo_5$ planes (upper graphs) and two Fe planes (lower graphs).

The applied shear deformation by HPT, allowed to induce a texture in both phases of the Fe-$SmCo_5$ composite. This effect is of great relevance for the engineering of novel PMs and results in an anisotropic magnetic behavior leading to improved magnetic performance. In Figure 3.21a) three demagnetizing curves of the same sample are presented. The direction of applied field between the measurements was changed with respect to the HPT-disc. Rather similar curves were recorded for the radial and tangential direction (red and green curve, respectively). The axial direction however, showed a strongly increased H_C. For a PM having an uniaxial magnetocrystalline anisotropy (c.f. Figure 2.3) and a polycrystalline but textured microstructure, there should be differences in magnetic behavior for the easy axis and the hard axis [73]. In case of the HPT-deformed Fe-$SmCo_5$ composite, the basal plane of the $SmCo_5$ corresponds to the hard axis and the c-axis of the crystal is parallel to the easy axis,

thus responsible for a large H_C. This observation was further supported by extensive HEXRD analysis. In Figure 3.21b) pole figure representations of the HPT-deformed Fe-SmCo$_5$ composite are shown. The upper figures correspond to SmCo$_5$ planes and the yellowish color within the plots to a higher number of corresponding surface normals pointing in similar directions. For example, the $\{\bar{2}110\}$ plane is parallel to the c-axis of the hexagonal crystal. The high intensity in the pole figure representation into the radial direction indicates an aligned orientation of the SmCo$_5$ crystals with the c-axis parallel to the axial HPT-disc direction. Likewise the Fe phase is analyzed and a slight texture of the $\{110\}$ planes are found to orient parallel to the tangential HPT-disc direction.

3.3. Hard-Magnetic Rare-Earth-Free MnBi

Another topic realized in the framework of this thesis (see Publication F), was the successful manufacturing of the hard-magnetic rare-earth-free α-MnBi by utilizing HPT. As starting material powder blends consisting of Mn and Bi in an equiatomic ratio were used. A direct formation of the α-MnBi phase by basic HPT-deformation could not be documented by the presented samples but with the addition of an subsequent thermal treatment, the α-MnBi phase formed. In the following, some major findings of an extensive and complex experimental exploration are presented.

As a thermal treatment was found to be indispensably for the α-MnBi phase formation, the Mn-Bi composite was tuned regarding the microstructure and morphology. Therefore, the powder blend was subjected to BM prior a compaction process by HPT and an additional deformation. This resulted in a homogeneous dispersion of Mn particles with sizes of less than a few μm within a Bi matrix. Therefore, the interface area among both phases was strongly increased and diffusion between Mn and Bi should be possible. In Figure 3.22a) BSE images of an HPT-compacted MnBi composite, subjected to increasing annealing times are shown. Already after 4 h at 230°C, the α-MnBi phase is identified (arrows). After 24 h, cigar shaped silhouettes are found denoted to the newly forming phase. However, if the annealing time was further increased, this phase was vanishing. The visible amount of α-MnBi phase inversely scaled with an forming oxide layer on the HPT-disc surface (120 h image), which was affirmed by EDS measurements. As a consequence, an exposure to oxygen was avoided during all further annealing experiments.
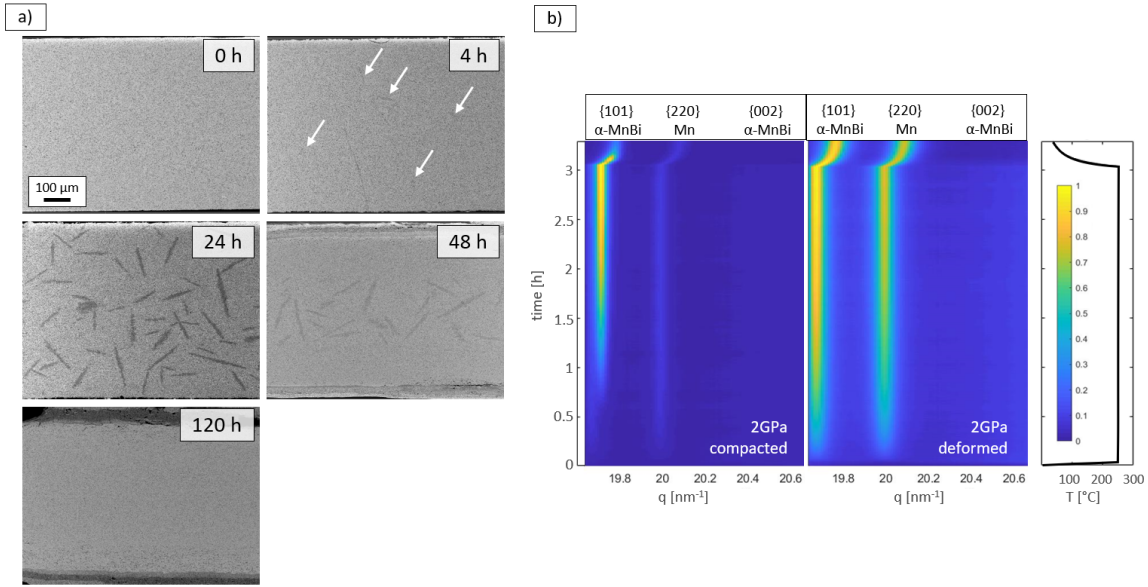
Figure 3.22.: **a)** BSE-images of HPT-compacted MnBi BM-powder blends. The material is annealed for different times at 230°C. After 4 h the emerging α-MnBi phase can be identified (arrows) and a maximum is found at 24 h. For longer annealing times the α-MnBi phase starts to dissapear and an oxide layer is formed on the HPT-disc surface. **b)** Intensity plots of in-situ HEXRD annealing experiments including an intensity scale bar and temperature profile of the experiment. The α-MnBi phase formation starts much faster for the HPT-deformed sample.

Because the initial phase formation was of great relevance for a bulk material containing a high volume fraction of α-MnBi phase, this process was examined in detail by in-situ HEXRD annealing experiments. In Figure 3.22b) integrated intensity plots for an HPT-compacted (left) and an HPT-deformed (right) sample is presented. The samples were annealed at 240°C for 3 h within an Ar-atmosphere. The α-MnBi phase formation started at about 2000 s for the compacted sample, but was strongly enhanced for the deformed sample, as the corresponding α-MnBi peak was already visible after roughly 200 s.

To further enhance the α-MnBi phase formation, the annealing procedure was adapted. Although a complete understanding of the effects of an external applied magnetic field during annealing is lacking, a beneficial effect on phase formations, in particular for the Mn-Bi system is reported [74–76]. Therefore, a vacuum chamber fitting between the poles of an electromagnet was constructed. The scheme of an additional sample holder is shown in Figure 3.23a). The halved HPT-discs (highlighted in green) are mounted in an especially designed sample holder and heated by two

heating cartridges through the direct heat transfer of the copper stock. Additionally, the often reported texture induced by HPT has to be considered, if an external applied field penetrates the sample. Therefore, the samples were attached in a special way defining the field direction during annealing. This allows to extract three pieces out of one HPT-disc, where the external magnetic field is applied in three different directions with respect to the HPT-disc orientation (radial, tangential, axial) as drawn in Figure 3.23b).
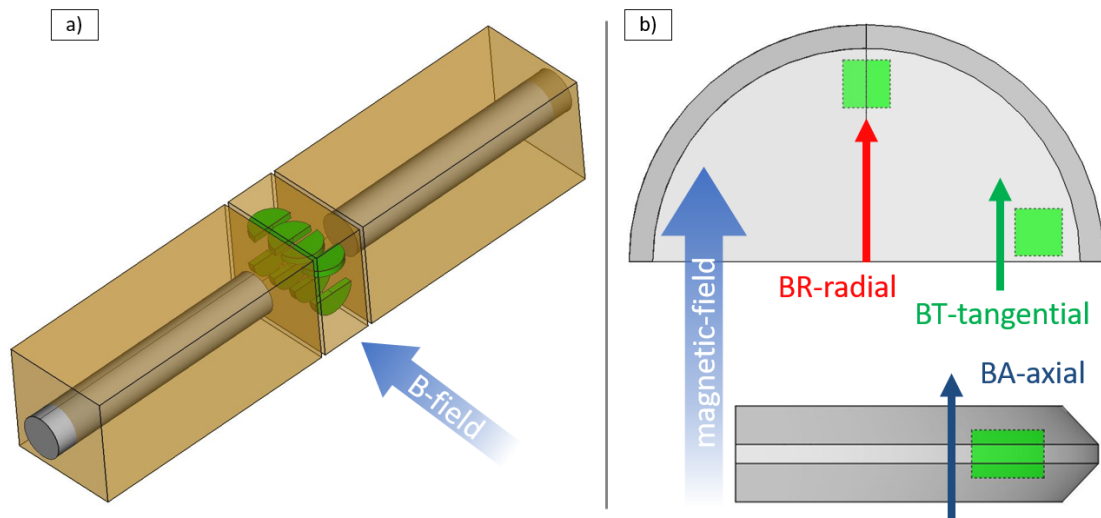
Figure 3.23.: **a)** Schematic representation of the custom build vacuum annealing construction used for all MVA experiments. Two heating cartridges (grey cylinders) are mounted in Cu-blocs, which clasps another Cu-bloc containing the samples. **b)** The halved HPT-disc samples penetrated by the external applied magnetic field (indicated by a blue arrow) in different configurations. Depending on the cut-out position of samples for further processing, they are magnetic field annealed in radial, tangential or axial direction with respect to the HPT-disc orientation.

When using MnBi powder blends without prior BM, the homogeneity of the resulting microstructure was much more related to the amount of applied deformation. In Figure 3.24a) the microstructure of an HPT-compacted and an HPT-deformed (10 revolution) sample after an subsequent magnetic field assisted vacuum annealing (MVA) is shown. Several important findings were recognized. Larger Mn particles (dark contrast) were found for the compacted sample when compared to the deformed one. This further resulted in a stronger localization of the forming α-MnBi phase (medium dark contrast), as the phase was only found on the direct Mn-Bi interface. Moreover, for the deformed sample, a much higher fraction of α-MnBi phase was visible. Magnetic

SQUID measurements in Figure 3.24b) support the described optical appearance, when comparing the saturation magnetization for the compacted (M_S = 9.89 emu/g) and deformed (M_S = 33.92 emu/g) sample. Because the contribution of elemental Mn (paramagnetic) and Bi (diamagnetic) to the total M_S value is neglectable, the volume fraction of the α-MnBi phase can be calculated by a direct interpolation using the theoretical M_S = 79 emu/g [77]. Thus, the compacted sample contains about 12% and the deformed sample exceeds 50%. When the same sample (HPT-deformed) was measured at lower temperatures (8K), the H_C was strongly decreased. This is an unusual but well known property of the α-MnBi phase, as the magnetocrystalline anisotropy increases with increasing temperature [78, 79].
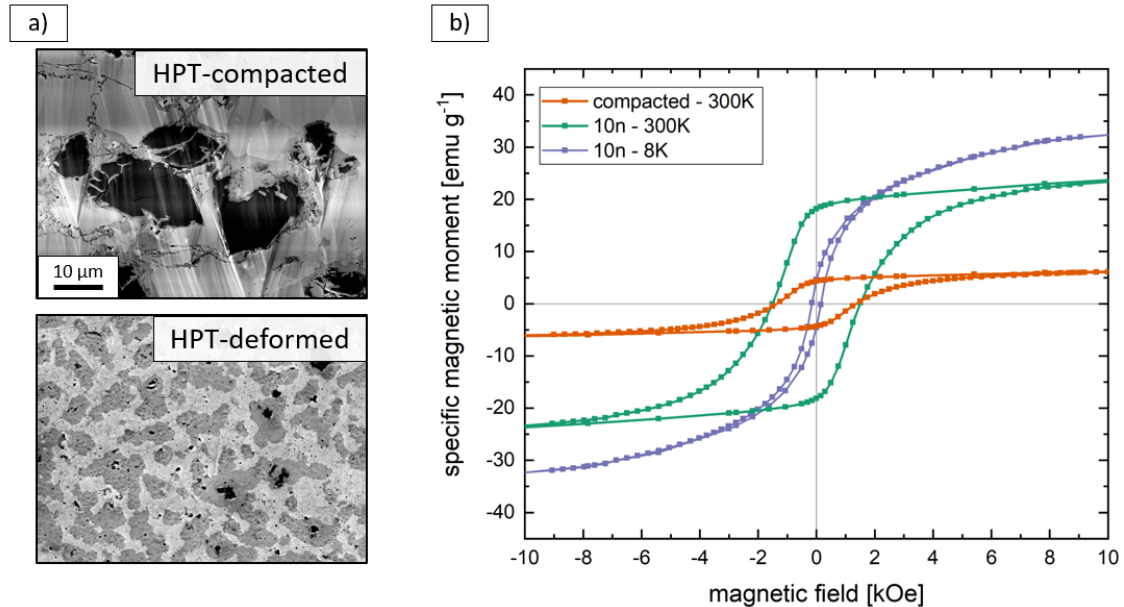
Figure 3.24.: **a)** BSE-images of HPT-compacted and HPT-deformed (10 revolutions) MnBi powder blends after MVA for 4 h at 2 T applied field. Smaller Mn particles (dark contrast) and a higher volume fraction of the α-MnBi phase is visible after deformation. **b)** Corresponding magnetic hysteresis measurements for the MVA-compacted (brown curve) and MVA-deformed (green curve) sample, as well as an measurement at lower temperature(8 K, purple curve).

As depicted in Figure 3.23b), three differently annealed samples could be extracted out of one HPT-disc. In Figure 3.25a-c) these samples (B_{ax}, B_{rad}, B_{tan}) are measured by SQUID magnetometry. For each sample, three hysteresis were recorded, while the measuring field was again applied in three respective directions (M_{ax}, M_{rad}, M_{tan}). For the B_{ax} sample, a magnetic isotropic behavior is found. An increasing magnetic anisotropy is reported for the B_{rad} and B_{tan} samples. This is explained by the formation

3. Results and Discussion

of a textured α-MnBi phase. The phase formation, driven by diffusion processes seems to be facilitated in the shear-plane of the HPT-disc allowing the highest magnetic anisotropy for the B_{tan} sample. When the MVA-field was applied normal to the shear-plane, the growth of the α-MnBi phase seems to be hindered, thus the isotropic behavior is seen in Figure 3.25a).
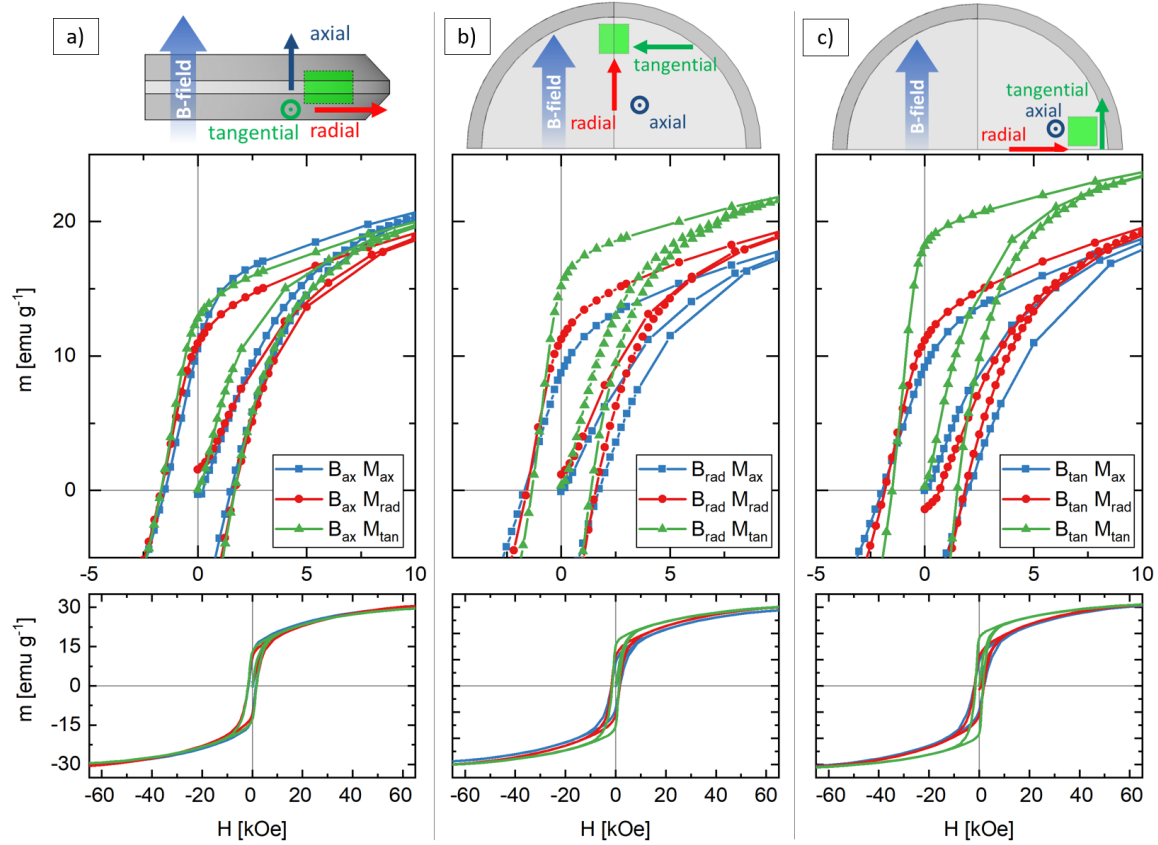
Figure 3.25.: Magnetic hysteresis measurements at 300 K of an HPT-deformed (10 revolutions) sample. Accordingly to Figure 3.23b) the sample is MVA in **a)** axial, **b)** radial and **c)** tangential HPT-disc direction. The schematic drawings on top additionally show the direction of the applied measurement field.

The main driving field for the α-MnBi phase formation during MVA is the enhanced defect density within the material. Therefore, a 'multi-step' process was developed where the HPT-deformation and subsequent MVA was repeated. Within the first step the Mn-Bi composite undergoes a phase refinement and a multitude of microstructural defects are implemented. After the subsequent MVA, thus the second step, the α-MnBi phase formation was introduced. Similar to the comparison of compacted and deformed samples, the phase refinement and formation is stronger pronounced

for higher deformation grades as described above. The following additional HPT-deformation is herein defined as third step, where the composite material (Bi, Mn and α-MnBi phase) again undergoes a phase refinement and the defect density is increased. This is extremely beneficial for the 4th step, where diffusion processes during the MVA are enhanced and a further volumetric increase of the α-MnBi phase was found.
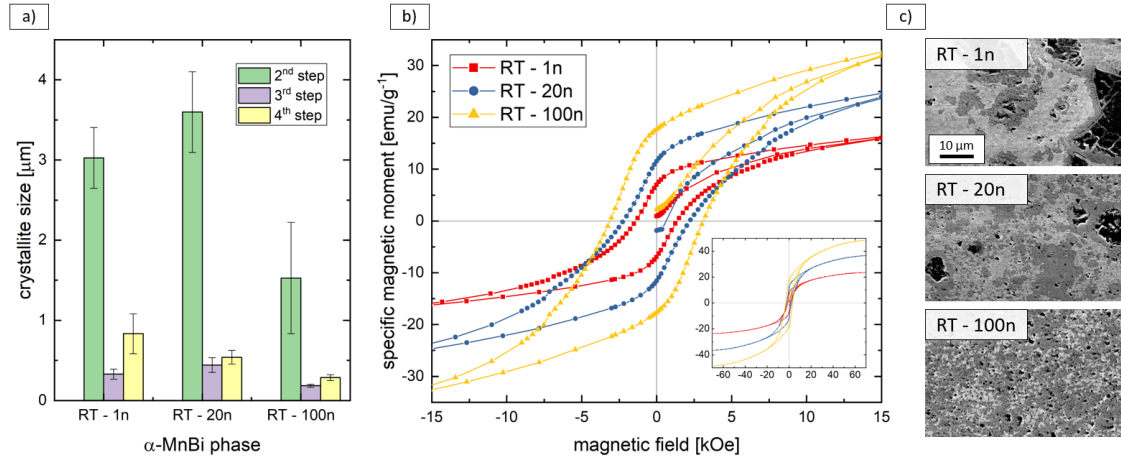
Figure 3.26.: **a)** Crystallite sizes of the α-MnBi phase after different processing steps. **b)** Magnetic hysteresis measurements at 300 K of differently deformed MnBi composites after the 4th processing step. **c)** Corresponding BSE-images of showing the HPT-defomation related distribution of Mn particles and amount of visible α-MnBi phase.

Figure 3.26 summarizes the main findings of this 'multi-step' process, which could in principle be repeated for several times as well as longer annealing times. The microstructure evolution during the process steps were monitored by XRD measurements. In Figure 3.26a) the crystallite sizes of the forming α-MnBi phase obtained by Rietveld analysis is presented. A strong refinement of the hard magnetic phase after the third step is found which stays small for the final MVA. Because the α-MnBi phase is diffusion related, it preferably forms at the Mn-Bi interface. This is why the amount of primarily applied revolutions (first step) strongly matters as it influences the microstructure, in particular the distribution and size of Mn particles. This is imposingly shown in Figure 3.26b), where magnetic hysteresis loops after the 4th step are depicted. The M_S value of the 100 rotation sample reaches 55 emu/g, which equals to about 70% α-MnBi phase. The influence of applied shear strain was further recognized by BSE images recorded after the 4th step shown in Figure 3.26c).

4

Outlook

Within the framework of this thesis, multiple processing routes have been studied and several principal ideas have been tested. Although, an extensive experimental work has been performed, several aspects could not be pursued as it is beyond the scope of the thesis, even though each one of them is scientifically interesting. Some of these considerations, which could be important for future studies, are expressed in the following.

In general, the main drawback of HPT is the limited sample size when set in comparison with industrially used PMs. Although it is possible to process nanostructured or ultra fine grained microstructures with bulk dimensions, it is not suitable for large industrial applications. However, the effects studied by HPT can be transferred to other, more continuous techniques, i.a., rolling, accumulative roll bonding or rotary swaging.

This is especially interesting for the formation of the α-MnBi phase. From the scientific point of view, and relating to the present work, the variation of annealing treatments are of high interest. The amount of α-MnBi nucleation sites could be increased by HPT but to which extent phase nucleation and growth rely on external applied fields and/or texture is a still open question. In fact, the phase nucleation itself deserves a closer inspection as preliminary magnetic results on as-deformed HPT samples, but compared to the presented samples, with a very large number of revolutions applied, show a remarkably high H_C (about 1.5 T). Comparable results could be expected when reducing the (high purity) Mn particle sizes prior plastic deformation. This, as well as studying the impact of oxides, would lead to reduced diffusion pathways and enhanced α-MnBi phase formation. Especially the combi-

4. Outlook

nation with another soft-magnetic phase, probably present within the composite prior annealing, could form an exchange coupled spring magnet which definitely is of fundamental scientific and industrial interest. Moreover, any repetitive combination of plastic deformation and thus improved diffusion by annealing would be of technological relevance, not only for the Mn-Bi system but also for any thermally activated phase formations (e.g. FeNi, CoZr, MnAl). The alloying of MnBi with Mg, Sb or Sn is already suggested in the literature [74, 80–82], as it stabilizes the α-MnBi phase. Such alloying elements could further reduce the size of forming FM particles and thus, increase the H_C. Thermocaloric measurements could be helpful to understand the phase transformations, in particular the contribution of defect density and its temperature dependent annihilation.

Within the Fe-Cr material system, an unusual high volume fraction of the σ-phase is obtained. Although it exhibits a complex crystal structure, high brittleness and hardness, the opportunity to form large volumetric quantities of this phase has not been reported before. By adjusting the annealing and HPT-deformation parameters, one could either tune the formation and/or distribution of this phase to form a soft-tough composite. The relevance of this phase to the 475°C embrittlement as well as the influence of plastic deformation and temperature on the phase formation, could be of fundamental interest for the fracture community [83]. Furthermore, the σ-FeCr phase is known for its weak magnetism and its potential candidate as itinerant ferromagnet [84]. Correlations between lattice vibrations and magnetism could be studied, as well as possible applications of the unusually high value of the specific heat featured by the σ-FeCr phase.

However, the relevance of Fe-Cr composites for a large exchange bias is expected to be low. Both elements are abundant and cheap but Cr exhibits a weak AFM coupling compared to e.g., CoO or NiO. Changing the AFM material as well as texturing the particles, which are reduced in size as much as possible (minimizing uncoupled surface spins and maximizing coupling interface area), could be successful. Exchange bias usually is found in 2-D materials though, large volumetric 3-D exchange bias materials could be investigated by means of neutron diffraction experiments.

The magnetic properties for the SmCo based experiments could be enhanced, utilizing two effects. First, the refinement partly leads to an amorphization [85] usually reducing hard-magnetic performance. Second, the high defect density within the composite material for exchange coupled spring magnets reduces the coupling

50

performance. Both could be evaded by appropriate annealing treatments, either by long annealing times at lower temperature or by an intermediate annealing step prior to an additional HPT-deformation. Crystallization of amorphous volumes and a higher phase refinement could be achieved. In addition, the textured microstructure could be improved by applying a magnetic field during powder compaction prior HPT-deformation. Conducting a magnetic field during HPT-deformation, combined with annealing would broaden the possibilities to extensively study phase transformations, again applicable for several material systems.

Summary

Permanent magnets (PMs) are an important part of our daily life. The worldwide demand for PMs is increasing and thus the need for raw materials. Political instabilities in countries of origin and an inequitable geological distribution of suitable deposits for the production of raw materials give rise to the volatility of the market and risks of instabilities in global supply chains. This is of great relevance for governmental institutions as it affects the economic and social development. This study is dedicated to the search for alternatives, thereby either rendering special microstructures capable for magnetic coupling effects or utilize material systems at best without or reduced critical materials.

For the first time, SPD by HPT was utilized to realize microstructures aiming for hard magnetic properties. The advantage of a strong grain and phase refinement by HPT was combined with the choice of different magnetic materials to design and tune the microstructure. This allowed for producing bulk sized sample, while reaching for small microstructural length scales, where magnetic coupling interactions take place.

An extensive study to fabricate Fe-Cr nano-composites was presented. A good deformation behavior was expected yet, limitations of HPT-processability required a survey on different processing routes. A strongly enhanced σ-FeCr phase formation was reported which finally was circumvented by using AM ingots as starting material for HPT-deformation. The formation of a supersaturated solid solution was found by a combination of extensive microstructural (APT, HEXRD, SEM, TEM,TKD) and magnetic (SQUID, ZFC-FC, magnetostriction) analysis. Astonishingly, the processed nanocrystalline and metastable FeCr alloys showed a remarkable temperature stability. Although substantial effort was put into the decomposition into elemental Fe and Cr

phases using a variety of different processing routes and heat treatments, no exchange bias was found for this material system.

On the other hand, HPT on the brittle intermetallic $SmCo_5$ phase was possible and led to a significant phase refinement resulting in an increased H_C. Increasing the deformation temperature to 250°C leads to enhanced magnetic properties. However, the phase stability upon annealing was reduced with increased amount of applied strain.

HPT induced exchange coupling between Fe and $SmCo_5$ phases was reported. The magnetic performance was best for certain deformation grades and higher $SmCo_5$ phase contents. The exchange coupling mechanism could be switched on and off by varying the temperature utilizing a temperature dependency of the magnetocrystalline anisotropy of the $SmCo_5$ phase. The phase refinement was further accompanied by the evolution of a texture in both phases, as shown by extensive HEXRD analysis and SQUID-magnetometry.

A highlight of this thesis is the successful production of the hard-magnetic REE-free α-MnBi phase. The phase formation in large volumes is a challenging task but was realized by utilizing the high material defect density introduced by HPT. This allowed strongly enhanced diffusion processes during a subsequent annealing treatment, thus enhanced α-MnBi phase formation. The processing has been even more improved by using annealing treatments with an external applied magnetic field. A fundamental understanding of the initial phase formation was obtained by in-situ HEXRD annealing experiments. The influence of the shear deformation on the α-MnBi phase formation induced by field annealing procedure was studied by extensive SQUID-magnetometry. Applying an alternating processing routine of HPT-deformation and field annealing led to α-MnBi phase content of about 70%.

Within this thesis, HPT was utilized as a method of choice as extremely high deformation grades and therefore, refined microstructures and high material defect densities were achieved. This allowed to process composite materials as well as supersaturated solid solutions exhibiting bulk dimensions. By subsequent annealing treatments, the high defect density yielded to enhance diffusion processes, thus acted as a model system for material processing techniques. Hence, the magnetic properties could be tuned by the strong grain and phase refinement of the microstructure. In return, magnetic measurements were further used to complement traditional microstructural characterization methods.

6

Bibliography

[1] J M D Coey. Permanent magnet applications, *Journal of Magnetism and Magnetic Materials* (2002).

[2] Kôtarô Honda and Shôzô Saitô. On K. S. Magnet Steel, *Physical Review* **16**, no. 6 (1920), pp. 495–500.
DOI: 10.1103/PhysRev.16.495.

[3] Laura H. Lewis and Félix Jiménez-Villacorta. Perspectives on Permanent Magnetic Materials for Energy Conversion and Power Generation, *Metallurgical and Materials Transactions A* **44**, no. S1 (2013), pp. 2–20.
DOI: 10.1007/s11661-012-1278-2.

[4] Oliver Gutfleisch et al. Magnetic Materials and Devices for the 21st Century: Stronger, Lighter, and More Energy Efficient, *Advanced Materials* **23**, no. 7 (2011), pp. 821–842.
DOI: 10.1002/adma.201002180.

[5] European Commission. Joint Research Centre. *The role of rare earth elements in wind energy and electric mobility: an analysis of future supply/demand balances.* LU: Publications Office, 2020.

[6] J. M. D. Coey. Hard Magnetic Materials: A Perspective, *IEEE Transactions on Magnetics* **47**, no. 12 (2011), pp. 4671–4681.
DOI: 10.1109/TMAG.2011.2166975.

[7] Katherine Bourzac. The rare-earth crisis, *Technology Review Inc.* **114**, no. 3 (2011), pp. 58–63.

[8] D. Bauer et al. U.S. Department of Energy Critical Materials Strategy, (2010).
DOI: 10.2172/1000846.

[9] *COMMUNICATION FROM THE COMMISSION TO THE EUROPEAN PARLIAMENT, THE COUNCIL, THE EUROPEAN ECONOMIC AND SOCIAL COMMITTEE AND THE COMMITTEE OF THE REGIONS Critical Raw Materials Resilience: Charting a Path towards greater Security and Sustainability.* 2020.

6. Bibliography

[10] European Commission. Joint Research Centre. *Supply chain analysis and material demand forecast in strategic technologies and sectors in the EU: a foresight study.* LU: Publications Office, 2023.

[11] *Proposal for a REGULATION OF THE EUROPEAN PARLIAMENT AND OF THE COUNCIL establishing a framework for ensuring a secure and sustainable supply of critical raw materials and amending Regulations (EU) 168/2013, (EU) 2018/858, 2018/1724 and (EU) 2019/1020.* 2023.

[12] J.M.D. Coey. Permanent magnets: Plugging the gap, *Scripta Materialia* **67**, no. 6 (2012), pp. 524–529.
DOI: 10.1016/j.scriptamat.2012.04.036.

[13] Kaveh Edalati et al. Nanomaterials by severe plastic deformation: review of historical developments and recent advances, *Materials Research Letters* **10**, no. 4 (2022), pp. 163–256.
DOI: 10.1080/21663831.2022.2029779.

[14] Robert O. Ritchie. The conflicts between strength and toughness, *Nature Materials* **10**, no. 11 (2011), pp. 817–822.
DOI: 10.1038/nmat3115.

[15] Reinhard Pippan et al. Nanokristalline Metalle. Neue Werkstoffe aus plastischer Hochverformung, *Physik in unserer Zeit* **41**, no. 1 (2010), pp. 23–29.
DOI: 10.1002/piuz.201001215.

[16] Terry C. Lowe and Ruslan Z. Valiev. The use of severe plastic deformation techniques in grain refinement, *JOM* **56**, no. 10 (2004), pp. 64–68.
DOI: 10.1007/s11837-004-0295-z.

[17] Y. Estrin and A. Vinogradov. Extreme grain refinement by severe plastic deformation: A wealth of challenging science, *Acta Materialia* **61**, no. 3 (2013), pp. 782–817.
DOI: 10.1016/j.actamat.2012.10.038.

[18] Ghader Faraji and Hesam Torabzadeh. An Overview on the Continuous Severe Plastic Deformation Methods, *MATERIALS TRANSACTIONS* **60**, no. 7 (2019), pp. 1316–1330.
DOI: 10.2320/matertrans.MF201905.

[19] R.Z Valiev, R.K Islamgaliev, and I.V Alexandrov. Bulk nanostructured materials from severe plastic deformation, *Progress in Materials Science* **45**, no. 2 (2000), pp. 103–189.
DOI: 10.1016/S0079-6425(99)00007-9.

[20] Anton Hohenwarter et al. Technical parameters affecting grain refinement by high pressure torsion, *International Journal of Materials Research* **100**, no. 12 (2009), pp. 1653–1661.
DOI: 10.3139/146.110224.

[21] R. Pippan et al. Saturation of Fragmentation During Severe Plastic Deformation, *Annual Review of Materials Research* **40**, no. 1 (2010), pp. 319–343.
DOI: 10.1146/annurev-matsci-070909-104445.

[22] I.-W Chen, E.J Winn, and M Menon. Application of deformation instability to microstructural control in multilayer ceramic composites, *Materials Science and Engineering: A* **317**, no. 1-2 (2001), pp. 226–235.
DOI: 10.1016/S0921-5093(01)01161-3.

[23] R. Pippan et al. The Limits of Refinement by Severe Plastic Deformation, *Advanced Engineering Materials* **8**, no. 11 (2006), pp. 1046–1056.
DOI: 10.1002/adem.200600133.

[24] Karoline Sophie Kormout, Reinhard Pippan, and Andrea Bachmaier. Deformation-Induced Supersaturation in Immiscible Material Systems during High-Pressure Torsion: Deformation-Induced Supersaturation, *Advanced Engineering Materials* **19**, no. 4 (2017), p. 1600675.
DOI: 10.1002/adem.201600675.

[25] Monika Antoni et al. Can Severe Plastic Deformation Tune Nanocrystallization in Fe-Based Metallic Glasses?, *Materials* **16**, no. 3 (2023), p. 1260.
DOI: 10.3390/ma16031260.

[26] I.S. Tereshina et al. Magnetic hysteresis properties of nanocrystalline (Nd,Ho)-(Fe,Co)-B alloy after melt spinning, severe plastic deformation and subsequent heat treatment, *Journal of Alloys and Compounds* **681** (2016), pp. 555–560.
DOI: 10.1016/j.jallcom.2016.04.228.

[27] Petr Straumal et al. Aging of WE43 magnesium alloy after mechanical crushing and subsequent high pressure torsion, *Letters on Materials* **9**, no. 3 (2019), pp. 370–374.
DOI: 10.22226/2410-3535-2019-3-370-374.

[28] M Wurmshuber et al. Ultrafine-grained Tungsten by High-Pressure Torsion – Bulk precursor versus powder processing route, *IOP Conference Series: Materials Science and Engineering* **580**, no. 1 (2019), p. 012051.
DOI: 10.1088/1757-899X/580/1/012051.

[29] Kurt Heinz Jürgen Buschow, Frank R Boer, et al. *Physics of magnetism and magnetic materials*. Vol. 7. Springer, 2003.

[30] Jeotikanta Mohapatra and Jia Ping Liu. "Rare-Earth-Free Permanent Magnets: The Past and Future", *Handbook of Magnetic Materials*. Vol. 27. Elsevier, 2018, pp. 1–57.
DOI: 10.1016/bs.hmm.2018.08.001.

[31] Ralph Skomski. *Simple models of magnetism*. OCLC: ocn138342362. Oxford ; New York: Oxford University Press, 2008.

[32] Felix Jimenez-Villacorta and Laura H Lewis. "Nanomagnetism", *Advanced Permanent Magnetic Materials*. 2014, pp. 160–189.

[33] R. Skomski and D. J. Sellmyer. "Intrinsic and Extrinsic Properties of Advanced Magnetic Materials", *Handbook of Advanced Magnetic Materials*. Ed. by Yi Liu, David J. Sellmyer, and Daisuke Shindo. Boston, MA: Springer US, 2006, pp. 1–57.
DOI: 10.1007/1-4020-7984-2_1.

6. Bibliography

[34] Fernando Maccari. "Investigations on ThMn12-type and Mn-Al compounds as permanent magnet candidates". Dissertation. Darmstadt: Technische Universität, 2022.
DOI: 10.26083/tuprints-00021140.

[35] Stephen Blundell. *Magnetism in condensed matter*. Oxford master series in condensed matter physics. Oxford ; New York: Oxford University Press, 2001.

[36] Alex Huber and Rudolf Schäfer. *Magnetic Domains - The Analysis of Magnetic Microstructures*. Berlin, Heidelberg: Springer, 1998.
DOI: 10.1007/978-3-540-85054-0.

[37] Lukas Weissitsch et al. Magnetic Materials via High-Pressure Torsion Deformation of Powders, *MATERIALS TRANSACTIONS* (2023), MT–MF2022026.
DOI: 10.2320/matertrans.MT-MF2022026.

[38] J. M. D. Coey. *Magnetism and Magnetic Materials*. Cambridge University Press, 2010.

[39] H. Kronmüller. Theory of Nucleation Fields in Inhomogeneous Ferromagnets, *physica status solidi (b)* **144**, no. 1 (1987), pp. 385–396.
DOI: 10.1002/pssb.2221440134.

[40] Rainer Hilzinger and Werner Rodewald. *Magnetic Materials: Fundamentals, Products, Properties, Applications*. 2013.

[41] Jagannath Jena et al. Elliptical Bloch skyrmion chiral twins in an antiskyrmion system, *Nature Communications* **11**, no. 1 (2020). Number: 1 Publisher: Nature Publishing Group, p. 1115.
DOI: 10.1038/s41467-020-14925-6.

[42] Karin Everschor-Sitte and Matthias Sitte. *English: The vector field of two, two-dimensional magnetic skyrmions: a) a hedgehog skyrmion and b) a spiral skyrmion*. 2015.

[43] Atsushi Ono and Sumio Ishihara. Double-Exchange Interaction in Optically Induced Nonequilibrium State: A Conversion from Ferromagnetic to Antiferromagnetic Structure, *Physical Review Letters* **119**, no. 20 (2017). Publisher: American Physical Society, p. 207202.
DOI: 10.1103/PhysRevLett.119.207202.

[44] I. V. Soldatov and R. Schäfer. Selective sensitivity in Kerr microscopy, *Review of Scientific Instruments* **88**, no. 7 (2017), p. 073701.
DOI: 10.1063/1.4991820.

[45] information@eso.org. *ESO Supernova*.

[46] https://newatlas.com/author/adam-williams. *Extraordinary Museum of the Future turns heads in Dubai*. Section: Architecture. 2022.

[47] *High-strength low-alloy (HSLA) automotive steels — from Docol*.

[48] SVG by Indolences Recoloring and ironing out some glitches done by Rainer Klute. *Stylised atom. Blue dots are electrons, red dots are protons and black dots are neutrons*. 2007.

[49] *MICRESS - The MICRostructure Evolution Simulation Software*.

[50] Giselher Herzer. Soft magnetic nanocrystalline materials, *Scripta Metallurgica et Materialia* **33**, no. 10-11 (1995), pp. 1741–1756.
DOI: 10.1016/0956-716X(95)00397-E.

[51] E.F. Kneller and R. Hawig. The exchange-spring magnet: a new material principle for permanent magnets, *IEEE Transactions on Magnetics* **27**, no. 4 (1991). Conference Name: IEEE Transactions on Magnetics, pp. 3588–3560.
DOI: 10.1109/20.102931.

[52] W. H. Meiklejohn and C. P. Bean. New Magnetic Anisotropy, *Physical Review* **102**, no. 5 (1956), pp. 1413–1414.
DOI: 10.1103/PhysRev.102.1413.

[53] Aurélie Jacob, Erwin Povoden-Karadeniz, and Ernst Kozeschnik. Revised thermodynamic description of the Fe-Cr system based on an improved sublattice model of the sigma-phase, *Calphad* **60** (2018), pp. 16–28.
DOI: 10.1016/j.calphad.2017.10.002.

[54] H. Okamoto. Supplemental Literature Review of Binary Phase Diagrams: Ag-Co, Ag-Er, Ag-Pd, B-Ce, Bi-La, Bi-Mn, Cu-Ge, Cu-Tm, Er-Y, Gd-Tl, H-La, and Hg-Te, *Journal of Phase Equilibria and Diffusion* **36**, no. 1 (2015), pp. 10–21.
DOI: 10.1007/s11669-014-0341-7.

[55] Stanisław M. Dubiel and Jakub Cieślak. Sigma-Phase in Fe-Cr and Fe-V Alloy Systems and its Physical Properties, *Critical Reviews in Solid State and Materials Sciences* **36**, no. 4 (2011), pp. 191–208.
DOI: 10.1080/10408436.2011.589232.

[56] Chih-Chun Hsieh and Weite Wu. Overview of Intermetallic Sigma Phase Precipitation in Stainless Steels, *ISRN Metallurgy* **2012** (2012), pp. 1–16.
DOI: 10.5402/2012/732471.

[57] B. D. Cullity and C. D. Graham. *Introduction to magnetic materials.* 2nd ed. Hoboken, N.J: IEEE/Wiley, 2009.

[58] A T Dinsdale. SGTE data for pure elements, *CALPHAD: Comput. Coupling Phase Diagrams Thermochem.* **15** (1991), pp. 317–425.
DOI: 10.1016/0364-5916(91)90030-N.

[59] Wei Xiong et al. Phase Equilibria and Thermodynamic Properties in the Fe-Cr System, *Critical Reviews in Solid State and Materials Sciences* **35**, no. 2 (2010), pp. 125–152.
DOI: 10.1080/10408431003788472.

[60] E. W. Lee and M. A. Asgar. Magnetostriction and Anomalous Thermal Expansion of Chromium, *Physical Review Letters* **22**, no. 26 (1969), pp. 1436–1439.
DOI: 10.1103/PhysRevLett.22.1436.

6. Bibliography

[61] Haijun Tang et al. Effect of microstructure and defects on the magnetostriction of oriented TDT-110 alloys, *Journal of University of Science and Technology Beijing, Mineral, Metallurgy, Material* **15**, no. 1 (2008), pp. 53–57.
DOI: 10.1016/S1005-8850(08)60011-0.

[62] T. D. Shen, R. B. Schwarz, and J. D. Thompson. Soft magnetism in mechanically alloyed nanocrystalline materials, *Physical Review B* **72**, no. 1 (2005), p. 014431.
DOI: 10.1103/PhysRevB.72.014431.

[63] William Fuller Brown. The Effect of Dislocations on Magnetization Near Saturation, *Physical Review* **60**, no. 2 (1941), pp. 139–147.
DOI: 10.1103/PhysRev.60.139.

[64] S. Colis et al. Structural defects in Sr2FeMoO6 double perovskite: Experimental versus theoretical approach, *Journal of Applied Physics* **98**, no. 3 (2005), p. 033905.
DOI: 10.1063/1.1997286.

[65] E. M. Plotnikova et al. Influence of the structure defects on the magnetic properties of the FePt/Fe bilayer, *Journal of Applied Physics* **115**, no. 13 (2014), p. 134318.
DOI: 10.1063/1.4870866.

[66] Surender Kumar Sharma, ed. *Complex Magnetic Nanostructures*. Cham: Springer International Publishing, 2017.
DOI: 10.1007/978-3-319-52087-2.

[67] C. G. Shull and M. K. Wilkinson. Neutron Diffraction Studies of Various Transition Elements, *Reviews of Modern Physics* **25**, no. 1 (1953), pp. 100–107.
DOI: 10.1103/RevModPhys.25.100.

[68] A. Hohenwarter. Microstructure, strength and fracture toughness of CuNb nanocomposites processed with high pressure torsion using multi-sector disks, *Scripta Materialia* **189** (2020), pp. 48–52.
DOI: 10.1016/j.scriptamat.2020.07.061.

[69] Saulius Gražulis et al. Crystallography Open Database (COD): an open-access collection of crystal structures and platform for world-wide collaboration, *Nucleic Acids Research* **40**, no. D1 (2012), pp. D420–D427.
DOI: 10.1093/nar/gkr900.

[70] Hosni Idrissi, Philippe Carrez, and Patrick Cordier. On amorphization as a deformation mechanism under high stresses, *Current Opinion in Solid State and Materials Science* **26**, no. 1 (2022), p. 100976.
DOI: 10.1016/j.cossms.2021.100976.

[71] B. Straumal, A. Korneva, and P. Zięba. Phase transitions in metallic alloys driven by the high pressure torsion, *Archives of Civil and Mechanical Engineering* **14**, no. 2 (2014), pp. 242–249.
DOI: 10.1016/j.acme.2013.07.002.

[72] SG Sankar et al. Magnetocrystalline anisotropy of Sm Co 5 and its interpretation on a crystal-field model, *Physical Review B* **11**, no. 1 (1975), p. 435.
DOI: 10.1103/PhysRevB.11.435.

[73] S. G. Sankar et al. Magnetocrystalline anisotropy of Sm Co 5 and its interpretation on a crystal-field model, *Physical Review B* **11**, no. 1 (1975), pp. 435–439.
DOI: 10.1103/PhysRevB.11.435.

[74] Wenyong Zhang et al. High energy product of MnBi by field annealing and Sn alloying, *APL Materials* **7**, no. 12 (2019), p. 121111.
DOI: 10.1063/1.5128659.

[75] Daiki Miyazaki et al. Enhancement of the Phase Formation Rate during In-Field Solid-Phase Reactive Sintering of Mn-Bi, *MATERIALS TRANSACTIONS* **58**, no. 5 (2017), pp. 720–723.
DOI: 10.2320/matertrans.MBW201609.

[76] A.M. Gabay, G.C. Hadjipanayis, and J. Cui. New anisotropic MnBi permanent magnets by field-annealing of compacted melt-spun alloys modified with Mg and Sb, *Journal of Magnetism and Magnetic Materials* **495** (2020), p. 165860.
DOI: 10.1016/j.jmmm.2019.165860.

[77] Jihoon Park et al. Electronic Structure and Maximum Energy Product of MnBi, *Metals* **4**, no. 3 (2014), pp. 455–464.
DOI: 10.3390/met4030455.

[78] Tu Chen and W. Stutius. The phase transformation and physical properties of the MnBi and Mn1.08Bi compounds, *IEEE Transactions on Magnetics* **10**, no. 3 (1974). Conference Name: IEEE Transactions on Magnetics, pp. 581–586.
DOI: 10.1109/TMAG.1974.1058367.

[79] Jun Cui et al. Current progress and future challenges in rare-earth-free permanent magnets, *Acta Materialia* **158** (2018), pp. 118–137.
DOI: 10.1016/j.actamat.2018.07.049.

[80] Shunda Lu et al. Effect of Mg content on the microstructure and magnetic properties of rare-earth-free MnBi alloys, *Journal of Magnetism and Magnetic Materials* **570** (2023), p. 170499.
DOI: 10.1016/j.jmmm.2023.170499.

[81] Peter Kainzbauer et al. The Ternary Bi-Mn-Sb Phase Diagram and the Crystal Structure of the Ternary T Phase Bi0.8MnSb0.2, *Journal of Phase Equilibria and Diffusion* **40**, no. 4 (2019), pp. 462–481.
DOI: 10.1007/s11669-019-00719-x.

[82] Angshuman Sarkar and Amitava Basu Mallick. Synthesizing the Hard Magnetic Low-Temperature Phase of MnBi Alloy: Challenges and Prospects, *JOM* **72**, no. 8 (2020), pp. 2812–2825.
DOI: 10.1007/s11837-020-04134-3.

6. Bibliography

[83]   P. J. Grobner. The 885° F (475° C) embrittlement of ferritic stainless steels, *Metallurgical Transactions* **4**, no. 1 (1973), pp. 251–260.
DOI: 10.1007/BF02649625.

[84]   S. M. Dubiel, J. Cieslak, and M. Reissner. Effect of magnetism on the lattice dynamics in the sigma-phase FeCr alloys, *Europhysics Letters* **101**, no. 1 (2013). Publisher: EDP Sciences, IOP Publishing and Società Italiana di Fisica, p. 16008.
DOI: 10.1209/0295-5075/101/16008.

[85]   Franziska Staab et al. Hard magnetic SmCo5-Cu nanocomposites produced by severe plastic deformation, *Acta Materialia* **246** (2023), p. 118709.
DOI: 10.1016/j.actamat.2023.118709.

7
List of appended Publications and Proceedings

In the framework of the present doctoral thesis, the following conference-proceedings paper (Publication A) and peer-reviewed manuscripts (Publication B-F) were prepared.

- Publication A

  Processing of Nanostructured Bulk Fe-Cr Alloys by Severe Plastic Deformation

  L. Weissitsch, M. Stückler, S. Wurster, R. Pippan, and A. Bachmaier
  Materials Science Forum **1016** (2020).
  doi: 10.4028/www.scientific.net/MSF.1016.1603

- Publication B:

  Nanocrystalline FeCr alloys synthesised by severe plastic deformation – A potential material for exchange bias and enhanced magnetostriction

  L. Weissitsch, S. Wurster, A. Paulischin, M. Stückler, R. Pippan, and A. Bachmaier
  Journal of Magnetism and Magnetic Materials **534** 168017 (2021).
  doi: 10.1016/j.jmmm.2021.168017

- Publication C:

  Strain Induced Anisotropic Magnetic Behaviour and Exchange Coupling Effect in Fe-SmCo₅ Permanent Magnets Generated by High Pressure Torsion

  L. Weissitsch, M. Stückler, S. Wurster, P. Knoll, H. Krenn, R. Pippan, and A. Bachmaier
  Crystals **10** 1026 (2020).
  doi: 10.3390/cryst10111026

- Publication D:

  Manufacturing of Textured Bulk Fe-SmCo₅ Magnets by Severe Plastic Deformation

  L. Weissitsch, M. Stückler, S. Wurster, J. Todt, P. Knoll, H. Krenn, R. Pippan, and A. Bachmaier
  Nanomaterials **12** 963 (2022).
  doi: 10.3390/nano12060963

- Publication E:

  Magnetic Materials via High-Pressure Torsion of Powders
  L. Weissitsch, F. Staab, K. Durst, A. Bachmaier
  Materials Transactions **(64)**7 1537-1550 (2023).
  doi: 10.2320/matertrans.MT-MF2022026

- Publication F:

  Synthesis of hard magnetic α-MnBi phase by high pressure torsion and field assisted annealing
  L. Weissitsch, S. Wurster, M. Stückler, T. Müller, H. Krenn, R. Pippan, and A. Bachmaier
  Journal of Magnetism and Magnetic Materials **584** 171082 (2023).
  doi: 10.1016/j.jmmm.2023.171082

The manuscripts listed above are presented in detail on the following appendix pages.

Remark

For all appended publications, the doctoral candidate, Lukas Weissitsch, performed all experiments, data analysis and interpretation as well as writing of the manuscripts, with some exceptions given below.

- Stefan Wurster assisted by TKD, EBSD and EDS measurements as well as interpretation, in particular in publication A, B, C and D. He further contributed to the development of the experimental magnetic-field annealing set-up of publication F.

- Alexander Paulischin performed the experimental part of the magnetostrictive results in publication B.

- Timo Müller provided help at the experimental part of the HEXRD results at the beamline in publication B and F.

- Juraj Todt was in charge of the experimental part of the HEXRD results at the beamline and supported by the data interpretation in publication D.

- Mirjam Spuller assisted with sample preparation in publication C and D.

- Georg Holub assisted with sample preparation in publication C.

- Franziska Staab contributed equally in writing, conceptualization and editing to the publication E.

List of co-authored Publications

- M. Stückler, H. Krenn, R. Pippan, <u>L. Weissitsch</u>, S. Wurster and A. Bachmaier, *Magnetic binary supersaturated solid solutions processed by severe plastic deformation*, Nanomaterials **9** (2018). doi: 10.3390/nano9010006

- M. Stückler, <u>L. Weissitsch</u>,S.Wurster, P. Felfer, H. Krenn, R. Pippan, and A. Bachmaier, *Magnetic dilution by severe plastic deformation*, AIP Advances **10** 015210 (2020). doi: 10.1063/1.5128058

- M. Stückler, H. Krenn, P. Kürnsteiner, B. Gault, F. De Geuser, <u>L. Weissitsch</u>, S. Wurster, R. Pippan, and A. Bachmaier, *Intermixing of Fe and Cu on the atomic scale by high-pressure torsion as revealed by DC- and AC-SQUID susceptometry and atom probe tomography*, Acta Materialia **196** 210-219 (2020). doi: 10.1016/j.actamat.2020.06.035

- M. Stückler, C. Teichert, A. Matković, H. Krenn, <u>L. Weissitsch</u>, S. Wurster, R. Pippan and A. Bachmaier, *On the magnetic nanostructure of a Co-Cu alloy processed by high-pressure torsion*, Journal of Science: Advanced Materials and Devices **6(1)** 33-41 (2020). doi: 10.1016/j.jsamd.2020.09.013

- M. Stückler, <u>L. Weissitsch</u>, S. Wurster, H. Krenn, R. Pippan and A. Bachmaier, *Sampling the Cu-Fe-Co phase diagram by severe plastic deformation for enhanced soft magnetic properties*, Journal of materials research and technology, **12**, 1235-1242 (2021). doi: 10.1016/j.jmrt.2021.03.073

- M. Stückler, J. Zálešák, T. Müller, S. Wurster,<u>L. Weissitsch</u>, P. Felfer, C. Gammer, R. Pippan and A. Bachmaier, *Oxide-stabilized microstructure of severe plastically deformed CuCo alloys*, Journal of Alloys and Compounds **901** 163616 (2022). doi: 10.1016/j.jallcom.2022.163616

- S. Wurster, <u>L. Weissitsch</u>, M. Stückler, P. Knoll, H. Krenn, R. Pippan, and A. Bachmaier, *Tuneable magneto-resistance by severe plastic deformation*, Metals **9(11)** 1188 (2019). doi: 10.3390/met9111188

- S. Wurster, M. Stückler, <u>L. Weissitsch</u>, T. Müller and A. Bachmaier, *Microstructural changes influencing the magnetoresistive behavior of bulk nanocrystalline materials*, Applied Sciences **10(15)** 5094 (2020). doi: 10.3390/app10155094

- S. Wurster, M. Stückler, <u>L. Weissitsch</u>, H. Krenn, A. Hohenwarter, R. Pippan and A. Bachmaier, *Soft magnetic properties of ultra-strong and nanocrystalline*

pearlitic wires, Nanomaterials **12(1)** 23 (2021). doi: 10.3390/nano12010023

- M. Zawodzki, <u>L. Weissitsch</u>, H. Krenn, S. Wurster and A. Bachmaier, *Exchange Bias Demonstrated in Bulk Nanocomposites Processed by High-Pressure Torsion*, Nanomaterials **13(2)** 344 (2023). doi: 10.3390/nano13020344

- M. Kasalo, S. Wurster, M. Stückler, M. Zawodzki, <u>L. Weissitsch</u>, R. Pippan and A. Bachmaier, *Magnetoresistive behaviour of ternary Cu-based materials processed by high-pressure torsion*, IOP Conference Series: Materials Science and Engineering **1249(1)** 012047 (2022). doi: 10.1088/1757-899X/1249/1/012047

List of Conference Contributions

- Care Innovation 2023, Vienna/Austria, talk. *Novel Rare Earth Free Permanent Magnets*

- nanoSPD 2023, Bengaluru/India, talk. *Bulk Rare Earth Free Permanent Magnets by Severe Plastic Deformation and Advanced Annealing Procedures*

- MMM 2022, Minneapolis/United States, talk. *Bulk Rare Earth Free MnBi-based Permanent Magnets by Severe Plastic Deformation*

- ÖPG Tagung 2022, Leoben/Austria, talk. *Exchange Coupled Bulk Rare Earth Free Permanent Magnets*

- NANO 2022, Sevilla/Spain, talk. *Bulk Rare Earth Free Permanent Magnets by Severe Plastic Deformation*

- 1st Materials Science Colloquium, Lech am Arlberg/Austria, talk. *Generating Bulk Rare Earth Free Permanent Magnets by Severe Plastic Deformation*

- ISNR 2021, Leoben/Austria, poster. *Severe Plastic Deformation as an Innovative Method to Enhance Magnetic Properties in Bulk Materials*

- REPM 2021, online/United States, talk. *Novel bulk non-rare earth Mn-Bi permanent magnets processed by severe plastic deformation*

- THERMEC 2021, online/Austria, talk. *Processing of Nanostructured Bulk FeCr Alloys by Severe Plastic Deformation*

- JEMS 2020, online/Portugal, talk. *Magnetic properties of exchange biased nanocrystalline bulk Fe Cr alloys produced by severe plastic deformation*

- ESM 2019, Brno/Czech Republic, poster. *Tuneable magnetic properties of nanocrystalline Fe-Cr alloys*

- BNM 2019, Ufa/Russion Federation, talk. *Synthesis of nanocomposites by HPT deformation of magnetic powders*

- JEMS 2019, Uppsala/Sweden, poster. *Tuneable magnetic properties of nanocrystalline Fe-Cr alloys produced by severe plastic deformation*

- ESI-Seminar 2019, Admont/Austria, talk. *Hard-magnetic nanostructured materials*

- TMS 2019 - 148th annual meeting, San Antonio/United States, talk. *Structural Evolution in Fe-Cr alloys - The Effect of Processing*

Processing of nanostructured bulk Fe-Cr alloys by severe plastic deformation

Lukas Weissitsch, Martin Stückler, Stefan Wurster, Reinhard Pippan and Andrea Bachmaier

Erich Schmid Institute of Materials Science, Austrian Academy of Sciences, Jahnstraße 12, 8700 Leoben, Austria

Abstract

The processing of binary alloys consisting of ferromagnetic Fe and antiferromagnetic Cr by severe plastic deformation (SPD) with different chemical compositions has been investigated. Although the phase diagram exhibits a large gap in the thermodynamical equilibrium at lower temperatures, it is shown that techniques based on SPD help to overcome common processing limits. Different processing routes including initial ball milling (BM) and arc melting (AM) and a concatenation with annealing treatments prior to high-pressure torsion (HPT) deformation are compared in this work. Investigation of the deformed microstructures by electron microscopy and synchrotron X-ray diffraction reveal homogeneous, nanocrystalline microstructures for HPT deformed AM alloys. HPT deformation of powder blends and BM powders leads to an exorbitant increase in hardness or an unusual fast formation of a σ-phase and therefore impede successful processing.

Keywords: severe plastic deformation; high-pressure torsion; ball mill; arc melting; nanostructured Fe-Cr alloy

A. Processing of nanostructured bulk Fe-Cr alloys by severe plastic deformation

A.1. Introduction

Despite the fact that binary Fe-Cr alloys are intensively studied in the past, several characteristics of this system are still not fully understood. Good mechanical properties in combination with great corrosion resistance [1] are known, but also the prominent 475°C embrittlement [2] and the σ-phase formation in a narrow compositional region [3, 4] in a more negative manner. Whilst details of the phase diagram are currently discussed and adapted [5, 6], a description of spin glass formation [7] and a strong swelling resistance under irradiative environments can be found in literature [8, 9], increasing the versatility of this system.

At lower temperatures, the elemental Fe and Cr exhibit the same bcc crystal structure, but their magnetic properties differ significantly: Fe is ferromagnetic, Cr conversely is antiferromagnetic. Since the fabrication possibilities reached microstructural sizes in the nanometer regime, a break-trough in processing thin films of Fe-Cr was made. These materials are well known due to a discovery named the giant magnetoresistance [10, 11]. Especially when coupling effects at ferro- and antiferromagnetic interfaces occur, phenomena as exchange bias are found, first discovered by Meiklejohn and Bean more than 60 years ago [12–14].

However, limitations are given by the resulting sample sizes. While magnetic effects can comfortably be studied and tuned by varying the thickness of films or size of spherical particles, it is getting more complex when sample sizes reach bulk dimensions. Hence, the processing of bulk materials with an internal nanostructure that still can be used for mass production is appreciated due to generally interesting coupling effects in nanocomposites consisting of two different magnetic materials [15]. To give an example, applying effects like the exchange bias in bulk samples will drastically improve the energy product, making this composites suitable for permanent magnet applications. Covering the future demand for renewable energy requires an increasing amount of magnetic materials, where in the best case the use of rare earth elements should be avoided [16].

The investigation of nanostructured bulk materials can offer a huge amount of possibilities, but in particular the processing of these materials in bulk form is a challenging task. SPD by HPT is an opportunity to evade some processing limits. It allows the production of bulk alloys with non-equilibrium compositions below the melting point [17]. In this study the challenges of processing Fe-Cr alloys as a rare-earth-free alternative for permanent magnets are described. Different processing routes

70

combining initial ball milling (BM) or arc melting (AM) prior to HPT deformation are investigated and an optimized processing route to obtain bulk, homogeneous nanocrystalline Fe-Cr alloys is found.

A.2. Materials and Experimental

Three different compositions consisting of nominal 30, 50 and 70 at.% Fe ($\pm$ 0.5 at.%) were processed. For HPT and BM, conventional powders were used as starting materials, for AM experiments conventional flakes. All materials are stored and handled in Ar, BM was carried out in Ar-atmosphere. For BM, a planetary ball mill (Retsch PM400) was used, with an 1:20 powder to ball ratio. Powders were milled at 400 rpm for a total milling time of 20 h. A Buehler AM device under a Ti-gettered high purity Ar atmosphere was used to prepare homogeneously mixed ingots. The ingots were cut in discs with 8 mm diameter and 1 mm thickness, which are subsequently deformed by HPT.

The powders were hydrostatically compacted under Ar-atmosphere at a nominal pressure of 5 GPa and afterwards severely deformed at 7.5 GPa with 0.6 turns per minute, applying a high shear strain at room temperature (RT), 250°C or 400°C. The resulting bulk samples were 8 mm in diameter and had a thickness between 0.35 mm and 0.6 mm. The used setup is described in more detail elsewhere [18]. For certain samples intermediate annealing between compaction and HPT deformation for 2 h at 1000°C under vacuum was also performed. Annealing of HPT deformed samples was performed for 1 h in air at different temperatures of 300°C, 400°C, 500°C, 600°C and 800°C.

Scanning electron microscopy (SEM) using back scattered electron diffraction (BSE), electron backscatter diffraction (**EBSD!** (**EBSD!**)) using transmission Kikuchi diffraction (TKD) and energy dispersive X-ray spectroscopy (EDS) were used for detailed microstructural characterization. If not specified otherwise, all microstructural investigations were performed at a radius r $\geq$ 2 mm to assure a homogeneously deformed microstructure [19]. Vickers microhardness was measured along the diameter in steps of Δr = 0.25 mm. Synchrotron as well as X-ray diffraction measurements (XRD) were carried out in axial direction of the HPT disc using the facilities at Deutsches Elektronen-Synchrotron (DESY) and a Bruker Phaser D2 XRD equipment with Co-K$_\alpha$ radiation, respectively.
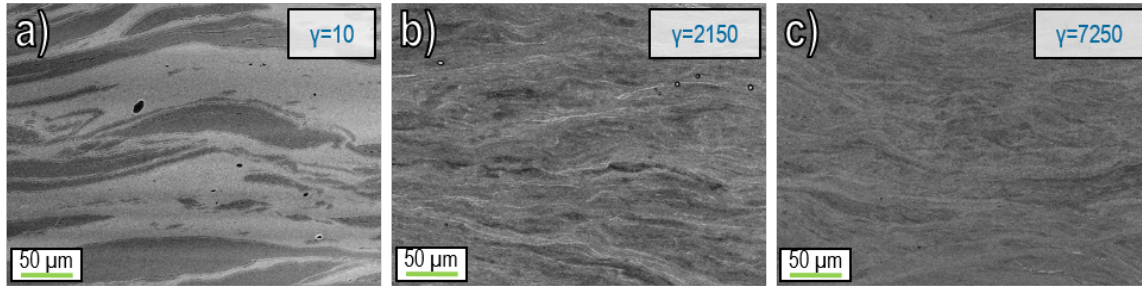
Figure A.1.: BSE images of $Fe_{50}Cr_{50}$ in tangential direction, deformed to different strains and temperatures: a) $\gamma= 10$ and RT, b) $\gamma= 2150$ and 400°C, c) $\gamma= 7250$ and 250°C.

A.3. Comparison of different processing routes

Processing of Fe-Cr powder blends by HPT deformation. The phase diagram of Fe and Cr exhibits an immiscibility gap at low temperatures [6]. If compacting and subsequently deforming elemental powder blends with such a characteristic by HPT, the evolving microstructure can consist of a single phase supersaturated alloy or lead to a nanocomposite with partial supersaturation [15, 17]. Powder blends of each Fe-Cr composition are HPT deformed and show similar characteristics. As an example, BSE images of the microstructures obtained after HPT deformation of the $Fe_{50}Cr_{50}$ powder blend are shown in Fig.A.1. In Fig.A.1a, an inhomogeneous microstructure with separated phases of Fe (bright) and Cr (dark) are visible at low strains after HPT deformation at RT. The limits of HPT processing are already reached due to an increase of hardness, leading to massive crack formation during HPT deformation. Elevated deformation temperatures usually lead to a final microstructure with larger grains, but allow the application of an higher amount of strain due to the reduced hardness of the processed material. Fig.A.1b and c show the final microstructures of $Fe_{50}Cr_{50}$, deformed at 400°C and 250°C, respectively. Through the increased HPT deformation temperature, it was possible to apply a higher shear strain in both samples. Furthermore, co-deformation of Fe and Cr is visible and a significantly refined structure at higher shear strains is noticed. Final microhardness values at the outer edge of the HPT samples exceed 800 HV, which approaches the strength of the HPT anvils.

Successful HPT processing further depends on the composition of the Fe-Cr samples: samples with higher Cr content ($Fe_{30}Cr_{70}$) are observed to more likely fail during the deformation process due to shear band formation, a rapid increase in hardness or crack formation during processing. Even samples with lower Cr content ($Fe_{70}Cr_{30}$) exhibit crack formation during HPT deformation. To conclude, although co-deformation is

observed, further refinement of the microstructure, which would be necessary to reach supersaturated states is impeded by the high hardness and crack formation of the Fe-Cr samples.
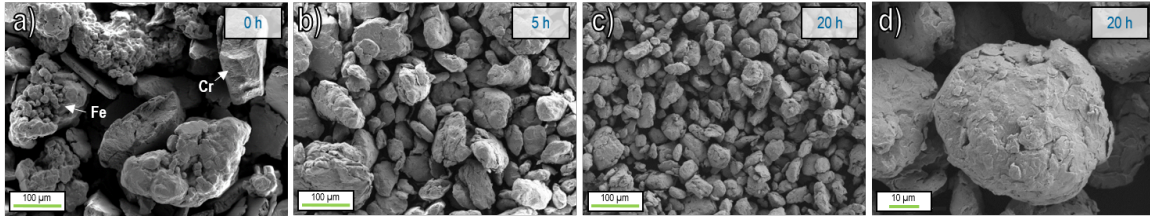
Figure A.2.: SEM images of BM $Fe_{50}Cr_{50}$-powders: a) 0 h, initial powders can be identified, b) after 5 h milling, c) after 20 h milling and d) magnified image after 20 h milling.

The effect of initial BM prior to HPT deformation. To circumvent the phase refinement step, BM is carried out to mechanically alloy the powders prior to HPT compaction and deformation. The milling process was interrupted several times to extract powders, which have been further investigated by XRD, SEM and EDS. In Fig.A.2, SEM images of $Fe_{50}Cr_{50}$ powders after different milling times are shown. Without milling, separated Fe and Cr particles can be identified (Fig.A.2a). With increasing milling time, the powder particles decrease in size and form a more globular shape. The particle size after 20 h of milling ranges between a few tens of μm to less than 100 μm. EDS measurements show that the chemical composition converged to the original weight composition already after 15 h of milling time, indicating a homogeneous dispersion of Fe and Cr in the powder blends. The same results are obtained for increased Fe or Cr contents ($Fe_{70}Cr_{30}$ or $Fe_{30}Cr_{70}$), indicating that alloying by BM was successful.

XRD measurements of the BM $Fe_{50}Cr_{50}$ powder blends are shown in Fig.A.3. Theoretical diffraction maxima of pure Fe (green, higher angle) and Cr (blue, lower angle) are calculated using the lattice constants taken from [20], which are indicated by straight lines and labeled by the miller indices. The resulting peak maxima after 20 h milling time stay between the calculated maxima of the pure elements. To prove the homogeneous distribution of Fe and Cr in the powders, the peak with highest intensity is analysed by Voigt functions. If the peak is fitted best by two functions, it can be assumed that Fe and Cr exists as two coexisting separated phases. However, the difference between experimental and fitted peak reaches a minimum, when plotting with just one single Voigt function. Therefore, it is assumed that a single phase Fe-Cr alloy powder is produced. Further, the fitted peak positions are evaluated with respect

to Vegard's law, revealing the same chemical composition as EDS measurements do. Indicating the consistency, the results are identical to the weight of the powders before starting the BM process.

The BM powder blends are then compacted under Ar-atmosphere and deformed by HPT. In Fig.A.4a, the microstructure of a compacted $Fe_{50}Cr_{50}$ sample after applying only a small amount of shear strain is depicted. The original particle surfaces can still be identified. Although the sample was HPT deformed to a maximum shear strain of $\gamma = 40$ at RT, it was not enough to merge the particles on a microscale. By increasing the deformation temperature, it is possible to apply higher shear strains. Hence, former individual powder particles cannot be identified in Fig.A.4b and A.4c. A bulk material with homogeneous microstructure is reached for both deformation temperatures.

Processing FeCr alloys by BM and subsequent HPT is also successfull for lower Cr contents ($Fe_{70}Cr_{30}$). Crack formation due to high hardness values can, however, not be prevented for samples containing 50 at.% Cr and more.

Because BM powder blends already experience a high amount of deformation, an-
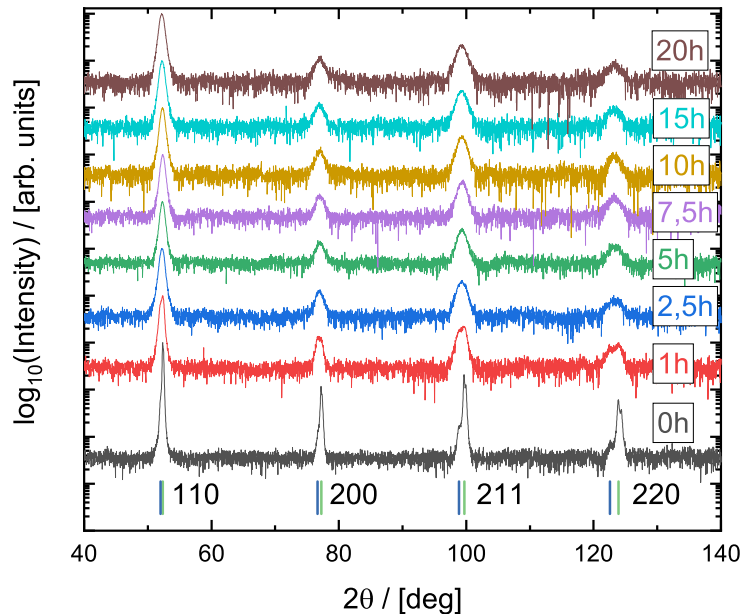
Figure A.3.: XRD measurements of BM $Fe_{50}Cr_{50}$ powders with increasing milling times. Straight lines indicate the positions of theoretical diffraction maxima of Fe (green) and Cr (blue).
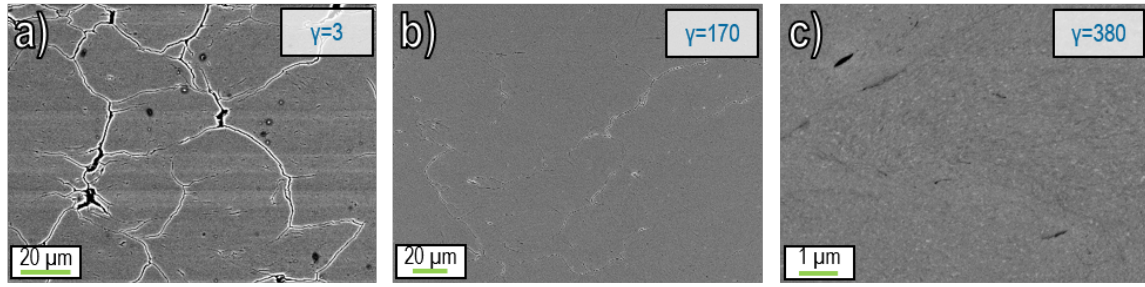
Figure A.4.: BSE images of compacted and HPT deformed $Fe_{50}Cr_{50}$ BM powder blends: a) $\gamma= 3$ at RT, b) $\gamma= 170$ at 250°C, c) $\gamma= 380$ at 400°C.

nealing prior to HPT deformation is done to soften the powder particles. Homogeneous microstructures can be achieved for samples with a low Cr content ($Fe_{70}Cr_{30}$) after HPT deformation of these intermediate annealed samples. The microhardness after HPT deformation is less than 600 HV (Fig.A.7a). For higher Cr contents, a steadily increasing microhardness as a function of the radius with maximum values of 900 HV and 1000 HV can be found (Fig.A.7a), leading to massive crack formation during HPT deformation.
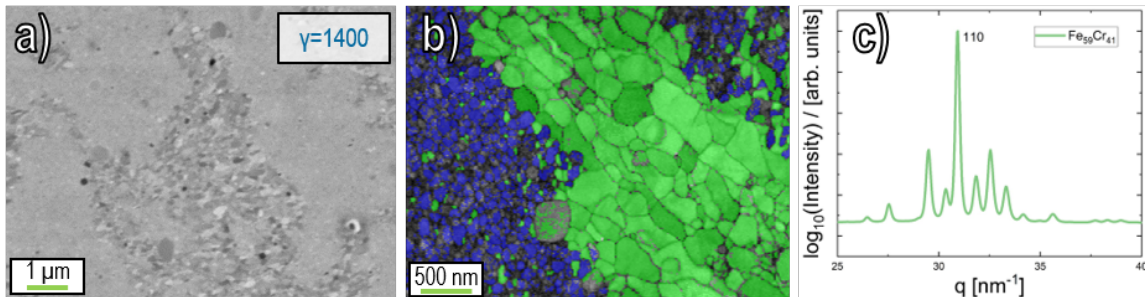
Figure A.5.: a) BSE image of HPT deformed $Fe_{59}Cr_{41}$ produced from BM powder blends with intermediate annealing prior to HPT deformation. b) TKD phase map with pattern quality overlay (blue: σ-phase, green: bcc-{Fe,Cr}), c) Synchrotron XRD measurements indicate σ-phase formation.

According to the phase diagram, a magnetic, but mechanically unwanted σ-phase, can be found in a narrow region around 50 at.% [6]. The formation of this phase by annealing should require an enormous time [3]. Fig.A.5a shows a BSE image of an HPT deformed $Fe_{59}Cr_{41}$ alloy with intermediate annealing prior to HPT deformation. A very fine structure as well as a coarse-grained phase can be seen. TKD measurements confirm the formation of σ-phase after HPT deformation. A phase map of a $Fe_{59}Cr_{41}$ alloy after HPT deformation is shown in Fig.A.5b. The phase map is overlapped with the pattern quality image to illustrate grain boundaries. The grain size of the Fe

phase is significantly larger compared to the σ-phase. Fig.A.5c shows the results from synchrotron XRD measurements. Beside the main bcc 110 reflection, several peaks are observed. They can be associated to the formation of the σ-phase. In literature, it is shown that plastic deformation favours the formation of the σ-phase [3], which might be the reason for the quick σ-phase formation during HPT deformation.

HPT deformation of AM alloys. The Fe-Cr alloys produced by AM were HPT deformed at RT. It was possible to produce samples with a homogeneous microstructure for all chemical compositions. BSE images of the final microstructures are shown in Fig.A.6. The corresponding microhardness along the radius is displayed in Fig.A.7a with filled symbols for the HPT deformed AM alloys. When comparing to the intermediate annealed BM powder samples, major differences are found. For the HPT deformed BM powder samples one can see a hardness increase with the radius, indicating that a steady state microstructure in the alloys (e.g. completely finished intermixing, steady state grain size in phases) is not reached. Further, the σ-phase formation leads to a massive hardness increase for the $Fe_{50}Cr_{50}$ sample. On the contrary, the HPT deformed AM alloys display a constant microhardness over the sample radius, hence a homogeneous microstructure in the steady state is reached.
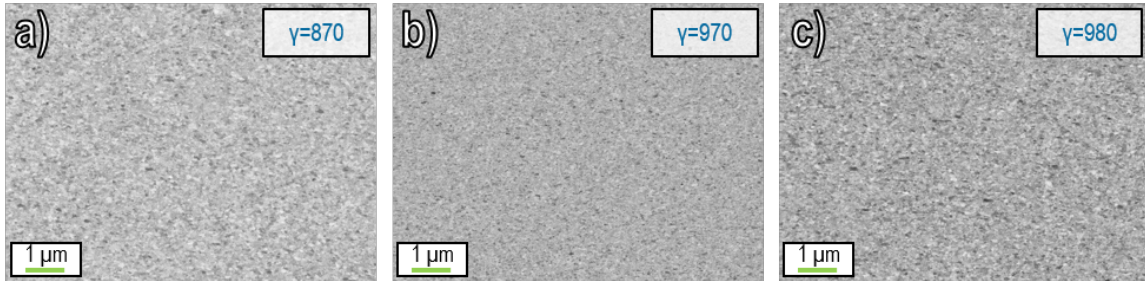
Figure A.6.: BSE images of HPT deformed AM FeCr alloys. a) $Fe_{30}Cr_{70}$, b) $Fe_{50}Cr_{50}$, c) $Fe_{70}Cr_{30}$.

To produce a hard magnetic material with a high energy product induced by exchange coupling, a structure with nanometer-sized Fe and Cr must be achieved. Therefore, after successful processing, annealing experiments are performed to decompose the microstructure and form a nanocomposite. BSE images after annealing (not shown), display coarsening of the structure, corresponding hardness measurements are shown in Fig.A.7b. For all three compositions, an increase in hardness is found for low annealing temperatures, which might be related to decomposition and/or an effect named hardening by annealing [21]. When the annealing temperatures are further increased, the microhardness decreases. The microhardness as well as the hardening

effect is further shifted to higher annealing temperatures with increasing Cr content. Detailed characterization of the annealed microstructures and resulting magnetic properties will be carried out in a further study.
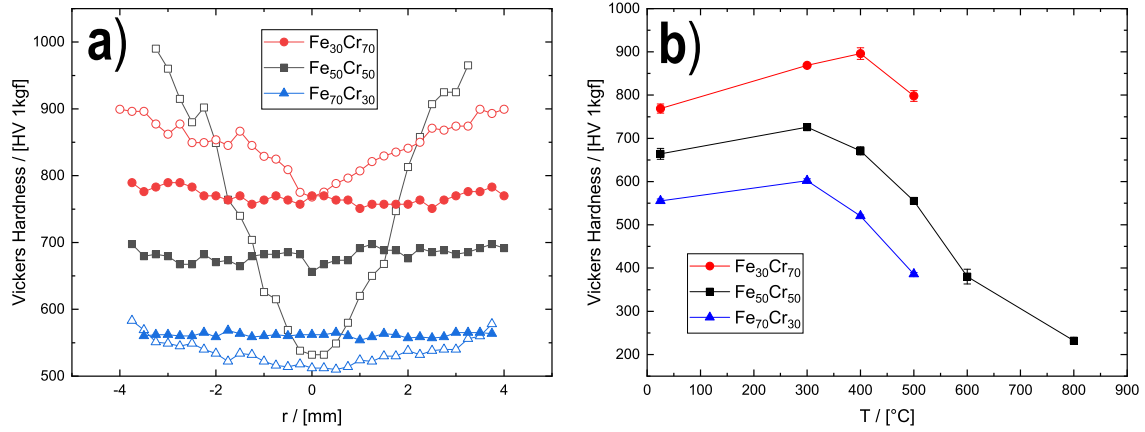
Figure A.7.: a) Microhardness of HPT deformed FeCr alloys: open symbols correspond to samples processed from BM powders and intermediate annealing before HPT deformation, filled symbols show HPT deformed AM samples. b) Microhardness of HPT deformed AM samples in as-deformed and annealed states.

A.4. Conclusion

The challenges of processing FeCr alloys by HPT are presented using different processing routes. It is shown that HPT processing of conventional powder blends leads to a microstructure of very fine but separated Fe and Cr phases. Crack formation is a limiting problem. Using BM, Fe-Cr alloys for three different compositions are successfully manufactured. Subsequent HPT deformation is performed after an intermediate annealing step. However, an unwanted and unusual fast growing σ-phase is identified after HPT deformation, which limits the formation of an homogeneous microstructure by an immense increase in hardness. Finally, $Fe_{30}Cr_{70}$, $Fe_{50}Cr_{50}$ and $Fe_{70}Cr_{30}$ samples with an homogeneous nanocrystalline microstructure are obtained using AM prior to HPT deformation. Furthermore, annealing of as-deformed samples, leads to a hardening of the microstructure which is found for all chemical compositions.

Acknowledgements

A.5. References

[1] D. Mortimer and W. B. A. Sharp. Oxidation of Fe—Cr Binary Alloys, *British Corrosion Journal* **3**, no. 2 (1968), pp. 61–67.
     DOI: 10.1179/000705968798326424.

[2] P. J. Grobner. The 885° F (475° C) embrittlement of ferritic stainless steels, *Metallurgical Transactions* **4**, no. 1 (1973), pp. 251–260.
     DOI: 10.1007/BF02649625.

[3] Stanisław M. Dubiel and Jakub Cieślak. Sigma-Phase in Fe-Cr and Fe-V Alloy Systems and its Physical Properties, *Critical Reviews in Solid State and Materials Sciences* **36**, no. 4 (2011), pp. 191–208.
     DOI: 10.1080/10408436.2011.589232.

[4] J.-M. Joubert. Crystal chemistry and Calphad modeling of the sigma-phase, *Progress in Materials Science* **53**, no. 3 (2008), pp. 528–583.
     DOI: 10.1016/j.pmatsci.2007.04.001.

[5] Aurélie Jacob, Erwin Povoden-Karadeniz, and Ernst Kozeschnik. Revised thermodynamic description of the Fe-Cr system based on an improved sublattice model of the sigma-phase, *Calphad* **60** (2018), pp. 16–28.
     DOI: 10.1016/j.calphad.2017.10.002.

[6] Wei Xiong et al. Phase Equilibria and Thermodynamic Properties in the Fe-Cr System, *Critical Reviews in Solid State and Materials Sciences* **35**, no. 2 (2010), pp. 125–152.
     DOI: 10.1080/10408431003788472.

[7] S K Burke et al. The evolution of magnetic order in CrFe alloys. II. Onset of ferromagnetism, *Journal of Physics F: Metal Physics* **13**, no. 2 (1983), pp. 451–470.
     DOI: 10.1088/0305-4608/13/2/020.

[8] D.S. Gelles. Void swelling in binary FeCr alloys at 200 dpa, *Journal of Nuclear Materials* **225** (1995), pp. 163–174.
     DOI: 10.1016/0022-3115(95)00053-4.

[9] NP Filippova, VA Shabashov, and AL Nikolaev. Mossbauer study of irradiation-accelerated short-range ordering in binary Fe-Cr alloys, *Physics of Metals and Metallography c/c Fizika Metallov i Metallovedenie* **90**, no. 2 (2000), pp. 145–152.

[10]   M. N. Baibich et al. Giant Magnetoresistance of (001)Fe/(001)Cr Magnetic Superlattices, *Physical Review Letters* **61**, no. 21 (1988), pp. 2472–2475.
DOI: 10.1103/PhysRevLett.61.2472.

[11]   G. Binasch et al. Enhanced magnetoresistance in layered magnetic structures with antiferromagnetic interlayer exchange, *Physical Review B* **39**, no. 7 (1989), pp. 4828–4830.
DOI: 10.1103/PhysRevB.39.4828.

[12]   W. H. Meiklejohn and C. P. Bean. New Magnetic Anisotropy, *Physical Review* **102**, no. 5 (1956), pp. 1413–1414.
DOI: 10.1103/PhysRev.102.1413.

[13]   J Nogués and Ivan K Schuller. Exchange bias, *Journal of Magnetism and Magnetic Materials* **192**, no. 2 (1999), pp. 203–232.
DOI: 10.1016/S0304-8853(98)00266-2.

[14]   R. E. Camley et al. Magnetization dynamics: A study of the ferromagnet/antiferromagnet interface and exchange biasing, *Journal of Vacuum Science & Technology A: Vacuum, Surfaces, and Films* **17**, no. 4 (1999), pp. 1335–1339.
DOI: 10.1116/1.581817.

[15]   A. Bachmaier et al. Tailoring the magnetic properties of nanocrystalline Cu-Co alloys prepared by high-pressure torsion and isothermal annealing, *Journal of Alloys and Compounds* **725** (2017), pp. 744–749.
DOI: 10.1016/j.jallcom.2017.07.200.

[16]   Oliver Gutfleisch et al. Magnetic Materials and Devices for the 21st Century: Stronger, Lighter, and More Energy Efficient, *Advanced Materials* **23**, no. 7 (2011), pp. 821–842.
DOI: 10.1002/adma.201002180.

[17]   Karoline Sophie Kormout, Reinhard Pippan, and Andrea Bachmaier. Deformation-Induced Supersaturation in Immiscible Material Systems during High-Pressure Torsion: Deformation-Induced Supersaturation, *Advanced Engineering Materials* **19**, no. 4 (2017), p. 1600675.
DOI: 10.1002/adem.201600675.

[18]   Anton Hohenwarter et al. Technical parameters affecting grain refinement by high pressure torsion, *International Journal of Materials Research* **100**, no. 12 (2009), pp. 1653–1661.
DOI: 10.3139/146.110224.

[19]   Martin Stückler et al. Magnetic Binary Supersaturated Solid Solutions Processed by Severe Plastic Deformation, *Nanomaterials* **9**, no. 1 (2018), p. 6.
DOI: 10.3390/nano9010006.

[20]   G. Chiarotti. "1.6 Crystal structures and bulk lattice parameters of materials quoted in the volume", *Interaction of Charged Particles and Atoms with Surfaces*. Ed. by G. Chiarotti. Vol. 24c. Series Title: Landolt-Börnstein - Group III Condensed Matter. Berlin/Heidelberg: Springer-Verlag, 1995, pp. 21–26.
DOI: 10.1007/10086066_6.

[21]   O. Renk et al. Increasing the strength of nanocrystalline steels by annealing: Is segregation necessary?, *Scripta Materialia* **95** (2015), pp. 27–30.
DOI: 10.1016/j.scriptamat.2014.09.023.

B

Nanocrystalline FeCr alloys synthesised by severe plastic deformation - a potential material for exchange bias and enhanced magnetostriction

Lukas Weissitsch, Stefan Wurster, Martin Stückler, Alexander Paulischin, Reinhard Pippan and Andrea Bachmaier

Erich Schmid Institute of Materials Science, Austrian Academy of Sciences, Jahnstraße 12, 8700 Leoben, Austria

Abstract

This work gives insights into processing and characterisation of bulk nanocrystalline FeCr materials. The investigated FeCr alloys, consisting of 30, 50 and 70 at.% ferromagnetic Fe and remaining anti-ferromagnetic Cr, are processed by arc melting and subsequent severe plastic deformation by high pressure torsion. The physical similarities between elemental Fe and Cr in combination with the nanocrystalline structure of the as-deformed alloys, necessitates advanced characterisation techniques for the as-deformed state: In-situ annealing synchrotron X-ray diffraction measurements as well as electron microscopy experiments are linked to magnetostrictive measurements and reveal a single phase microstructure. Surprisingly, the nanocrystalline FeCr alloys remain supersaturated solid solutions upon annealing above 500 °C, meaning a decomposition in a FeCr nanocomposite is suppressed. For the chosen annealing conditions grain growth is faster than decomposition and enhanced magnetostrictive values are found compared to materials in the as-deformed state.

B. Nanocrystalline FeCr alloys synthesised by severe plastic deformation

B.1. Introduction

Tuning material properties by forming single phase alloys and varying chemical composition is often impeded by the existence of large miscibility gaps at the thermodynamic equilibrium of binary phase diagrams. Notwithstanding the difficulties in fabrication, there is a strong interest in such metastable phases created materials as they offer the opportunity to tune and enhance physical properties. For quite some time, it is known to overcome these processing limits by techniques such as vapour deposition [1], mechanical alloying (MA) [2] or severe plastic deformation (SPD) generating metastable phases [3–5]. The formation of supersaturated solid solutions by MA or SPD is accompanied by a high defect density and decreased microstructural sizes. This evinces characterisation challenges for the binary nanocrystalline FeCr system: Due to the same crystal structure and similar lattice parameters of elemental Fe and Cr, it is difficult to distinguish whether finely dispersed elemental nanocrystalline grains or a (supersaturated) solid solution is present [2]. Possible characterisation methods are magnetic measurements. Apart from the tuneability of the saturation magnetostriction of heterostructures [6, 7] Bormio-Nunes et. al [8] reported an increasing saturation magnetostriction value for FeCr solid solutions. The aforementioned heterostructure of coexisting ferromagnetic Fe and anti-ferromagnetic Cr phases could give rise to an effect referred to as exchange bias.

The exchange bias features a shifted hysteresis loop, which originates from an unidirectional anisotropy created at the interface of the two types of magnetic materials. This occurs, when the ferro-antiferromagnetic phase boundary is cooled through the Néel temperature (T_N) while a magnetic field is applied [9]. Since magnetic exchange interactions appear on the nanometre-scale and the exchange bias effect is related to the phase boundaries, this effect is typically observed in microstructures obtained by well controllable synthetization techniques. Thin films or core-shell nanostructures [10] are well controllable during processing and therefore, such material systems allow a proper investigation of fundamental physical properties [11]. On the other hand, it is difficult to investigate the same effects in bulk materials [12], exhibiting dimensions of several millimetres or larger. The bottleneck nowadays is the synthesis

of a nanostructured bulk material exhibiting a high homogeneity therefore, enabling an up-scaling of materials with improved magnetic properties. Notwithstanding the above, the amount of interfaces is thought to directly influence the intensity of the magnetic effect, which makes magnetic nanostructured bulk materials necessary [9, 13].

Severe plastic deformation by high-pressure torsion (HPT) is a promising approach to overcome processing limitations, for above mentioned miscibility gaps of binary material systems [5] and furthermore a method of choice to tailor magnetic properties [14, 15]. One big advantage of materials processed by HPT is the sample size, as they exhibit bulk dimensions up to several centimetres [16, 17]. The principal goal of this work is the production of a bulk material consisting of alternating interfaces of elemental ferromagnetic Fe and anti-ferromagnetic Cr. Therefore, the synthesis of a nanocrystalline supersaturated solid solution of FeCr by HPT is aimed for a subsequent annealing treatment. The increased total grain boundary area of nanocrystalline materials is expected to favour a decomposition [18] of the FeCr solid solution in separated phases and therefore, into a nanostructured composite. A following magnetic field cooling is meant to induce an exchange bias, as already reported for HPT-compacted Co-NiO heterostructures [19]. However, processing and the characterization of nanocrystalline HPT deformed FeCr-alloys prior to field cooling is challenging. Evading processing limitations due to a pronounced miscibility gap in the binary phase diagram [20], we already reported an enormous increase in hardness during HPT-deformation but also on the successful processing and formation of a homogeneous nanocrystalline microstructure for a wide range of chemical compositions [3]. In this work we clarify, if these materials exhibit a supersaturated solid solution or if they are already in a nanocrystalline two phase state. We report on in-situ high-energy X-ray diffraction (HEXRD) experiments where a solid solution without any decomposition upon annealing is presumed and verify these results by magnetostrictive measurements.

B.2. Experimental

Binary alloys consisting of nominal 30, 50 and 70 at.% Fe and 70, 50, and 30 at.% Cr, respectively, were processed by arc melting and subsequent HPT-deformation. As starting materials, conventional flakes (Fe: 99.99+% < 10 mm, Cr: 99.995% 1-25 mm,

B. Nanocrystalline FeCr alloys synthesised by severe plastic deformation

both from HMW Hauner GmbH & Co. KG) were used. All materials were stored and handled in an Ar-filled glovebox to protect the high purity materials against contamination.

For arc-melting (AM/0.5 device, Edmund Buehler GmbH), a Ti-gettered high purity Ar atmosphere was used. To ensure chemical homogeneity the ingots were turned around and remelted at least five times. From arc melted ingots, cylinders with 8 mm diameter were prepared by electrical discharge machining and cut in discs with 1 mm thickness, which were subsequently deformed by HPT. A detailed description of the used HPT setup can be found in Ref. [21]. A nominal pressure of 7.5 GPa with a rotational frequency of 0.6 min^{-1} was used for the deformation process and 21 to 25 revolutions are applied (corresponding to a shear strain γ of $\sim$450 at radius $r = 3$ mm [22]). To avoid an increase of the processing temperature during deformation, high pressure air cooling was conducted.

After deformation, the sample is cut for further investigations and all measurements were performed at a radius $r \geqslant 2$ mm. Respective orientations are explained in detail in Reference [15]. Scanning electron microscopy (SEM; LEO 1525, Carl Zeiss Microscopy GmbH) images were made in tangential HPT-disc orientation in backscattered electron (BSE) detection mode. The chemical composition was determined by energy dispersive X-ray spectroscopy (EDX; XFlash 6|60 device, Bruker), using the Bruker software package Esprit 2.2. The grain size of selected samples was quantitatively evaluated by Transmission Kikuchi Diffraction (TKD) and electron backscatter diffraction (EBSD) measurements using a Bruker e$^-$-Flash^{FS} detector. Hardness measurements (Micromet 5104, Buehler) were performed in tangential direction on the polished sample along the diameter in steps of $\Delta r = 0.25$ mm and were averaged for a radius 2 mm $\leqslant r \leqslant 3.5$ mm. For annealing experiments, quarters or half discs of as-deformed samples were exposed to 300 °C, 400 °C and 500 °C for 1 h in a conventional furnace. The samples were wrapped in a protective foil before heat treatment and were quenched with ethanol after the annealing process.

For magnetostrictive measurements, an electromagnet (Type B-E 30, Bruker) with conical poles (diameter 176 mm), providing a constant air gap (50 mm) and a maximal field of 2.25 T, was used. Within the air gap, the sample was placed into an encapsulating sample chamber, protecting from rapid temperature changes. The magnetostriction was measured using strain gauges (HBM, 1-LY11-0.6/120) applied with glue Z70 from HBM. As a reference a piece of W, a very low magnetostrictive

material is measured at the same time with a strain gauge of the same batch. According to [23], the magnetostriction of W can be expected to be below 0.005 ppm in a magnetic field of 2 T. The strain gauge on the sample and the reference were placed parallel and on top of each other within the sample chamber and conducted to a half-Wheatstone bridge. The signal of the strain gauges was processed with an amplifier (HBM-Quantum^x MX410). Additionally, the constancy of the temperature was confirmed by a temperature measurement within the sample holder and the applied magnetic field was recorded, using a Hall-probe (Model 475 DSP, Lakeshore).

Synchrotron high-energy X-ray diffraction (HEXRD) experiments were carried out at the beamline P21.2 at PETRA III (DESY, Hamburg, Germany). The specimens were measured in transmission mode, while the spot size was set to 200 x 200 µm^2 and a photon energy of 60 keV was used. In-situ annealing HEXRD experiments were performed using the following sequence: Heating to 520 °C, holding the temperature for 1 h and cooling. A Varex XRD 4343 flat panel detector captured diffraction patterns every 5 seconds. The experimental setup was realised by a heating microscope stage (THMS600 Linkam, Tadworth, United Kingdom), which was adapted to place the samples inside an Ar-flushed chamber to suppress the formation of oxides. The custom made chamber is designed to minimize the interaction of the beam with the furnace and allowed the diffracted beam to exit the probe chamber while the temperature was measured via a thermocouple. The temperature was calibrated by measuring a Cu sample with the same settings and comparing the changing lattice parameter during thermal expansion. For data processing, the pyFAI package [24] and further analysing the Matlab voigt package [25] was used.

B.3. Results

B.3.1. Characterisation of the microstructure

The microstructures of room temperature (RT) HPT-deformed samples at r = 3 mm with different chemical compositions are shown in Figure B.1. The Fe-content increases from the top to bottom row. In the first column, BSE images of as-deformed FeCr alloys are depicted. Nanocrystalline and homogeneously deformed microstructures are visible. To quantify the grain sizes of the alloys in the as-deformed state, TKD is conducted exemplarily for one composition ($Fe_{50}Cr_{50}$). In Figure B.2 a) a crystal orientation map

B. Nanocrystalline FeCr alloys synthesised by severe plastic deformation
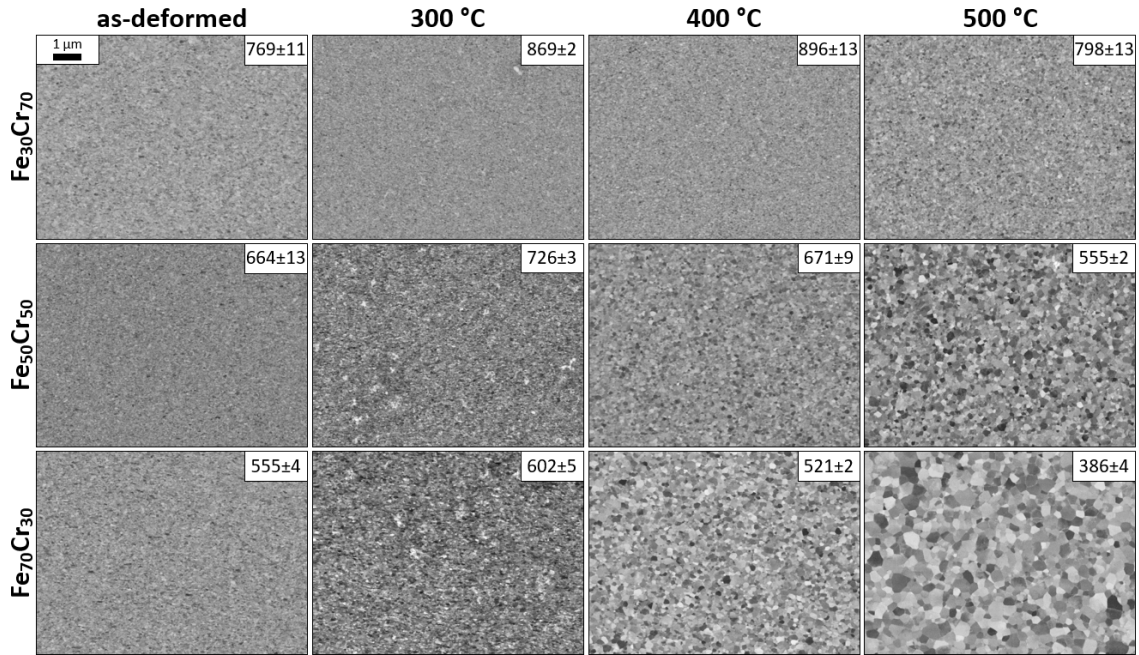
Figure B.1.: BSE images of the microstructure of HPT-deformed FeCr alloys. The Fe content increases from the top to the bottom row. The first column shows the microstructure of as-deformed samples. The next columns depict microstructural changes with increasing annealing temperatures (300 °C, 400 °C and 500 °C, respectively). Averaged Vickers-hardness values are depicted in the corresponding images as insets. The magnification is the same in all images.

revealed by TKD is shown. Recording several images and interpolating the data of 1256 grains with a log-normal distribution reveal a median grain size of 101 nm (standard deviation = 86 nm; $\sigma = 0.579$, $\mu = -2.288$). Please note the different scale bar in Figure B.2 b), where an EBSD scan of the same alloy after annealing for 1h at 500 °C is shown. The obtained median grain size is 307 nm (1456 grains, standard deviation = 160 nm; $\sigma = 0.449$, $\mu = -1.180$). Results from Vickers-hardness testing are indicated as insets within each SEM micrograph (Figure B.1). The hardness measurements along the radius, display a constant hardness, which indicates a homogeneously deformed state (denoted as 'as-deformed' in the following). To induce decomposition, the as-deformed samples are annealed for one hour at different temperatures (Figure B.1). The change in the microstructure strongly depends on the chemical composition. Nearly no change in the SEM images for the Cr-rich sample ($Fe_{30}Cr_{70}$), depicted in the first row of Figure B.1, is visible, when annealing up to 400 °C. However, the hardness increases, which is a common feature for nanocrystalline materials [26–28], is covered. A slightly increased grain size, accompanied by a hardness decrease, is
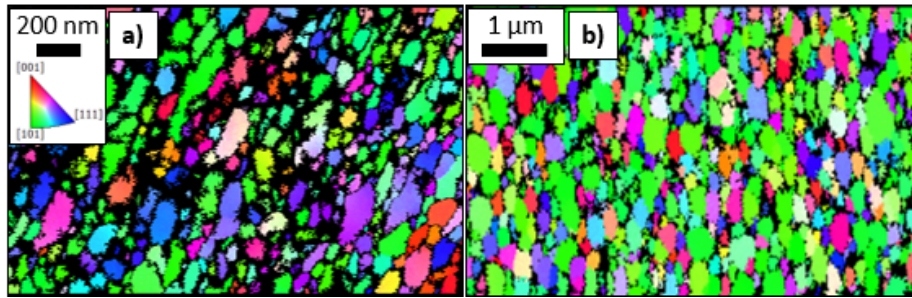
Figure B.2.: Crystal orientation maps of **a)** an as-deformed $Fe_{50}Cr_{50}$ alloy recorded in axial HPT disc direction by TKD. **b)** EBSD scan of an $Fe_{50}Cr_{50}$ alloy after annealing at 500 °C (1 h) measured in tangential direction but showing the crystal orientation in axial direction. Note the different scale bars.

seen for the 500 °C annealed sample. The medium composition sample ($Fe_{50}Cr_{50}$) shows a slight contrast difference in SEM images between the as-deformed and 300 °C annealed state. The microstructure remains almost constant even when annealing at 400 °C (shown in the 3rd column) until a significant grain growth is found for 500 °C annealing. The hardness increases upon annealing at 300 °C but decreases for higher annealing temperatures. Differences for every state are visible for the Fe rich sample ($Fe_{70}Cr_{30}$). At 300 °C, a slight grain growth is observed together with an increased hardness. Samples annealed at 400 °C and 500 °C exhibit a significant increase in grain size as well as a decrease of microhardness below the as-deformed state. Summarized, at intermediate temperatures the hardness increases for all chemical compositions, whereby the hardness peaks at higher temperatures for higher Cr content. Further, microstructural changes and grain growth are stronger pronounced for FeCr alloys containing a higher amount of Fe.

Laboratory XRD measurements of the as-deformed and annealed states (not shown) revealed broad peaks. They can either result from the formation of a supersaturated state or be due to the nanocrystalline state of individual Fe and Cr phases present in the as-deformed condition. Additionally, a co-existence of both configurations is conceivable. Thus, to clarify this point and to further investigate the decomposition of FeCr alloys, which are possibly in a non-equilibrium state, in-situ annealing experiments using synchrotron XRD are performed. Due to the high brilliance of the beamline [29], it was expected to resolve individual peaks for Fe or Cr phases, if existent, and to precisely determine the phases of the as-deformed and annealed states. Representatively, the most intense peak [110] of selected patterns of the in-situ experiment is shown in Figure B.3 for all three FeCr compositions. The vertical lines indicate reference values
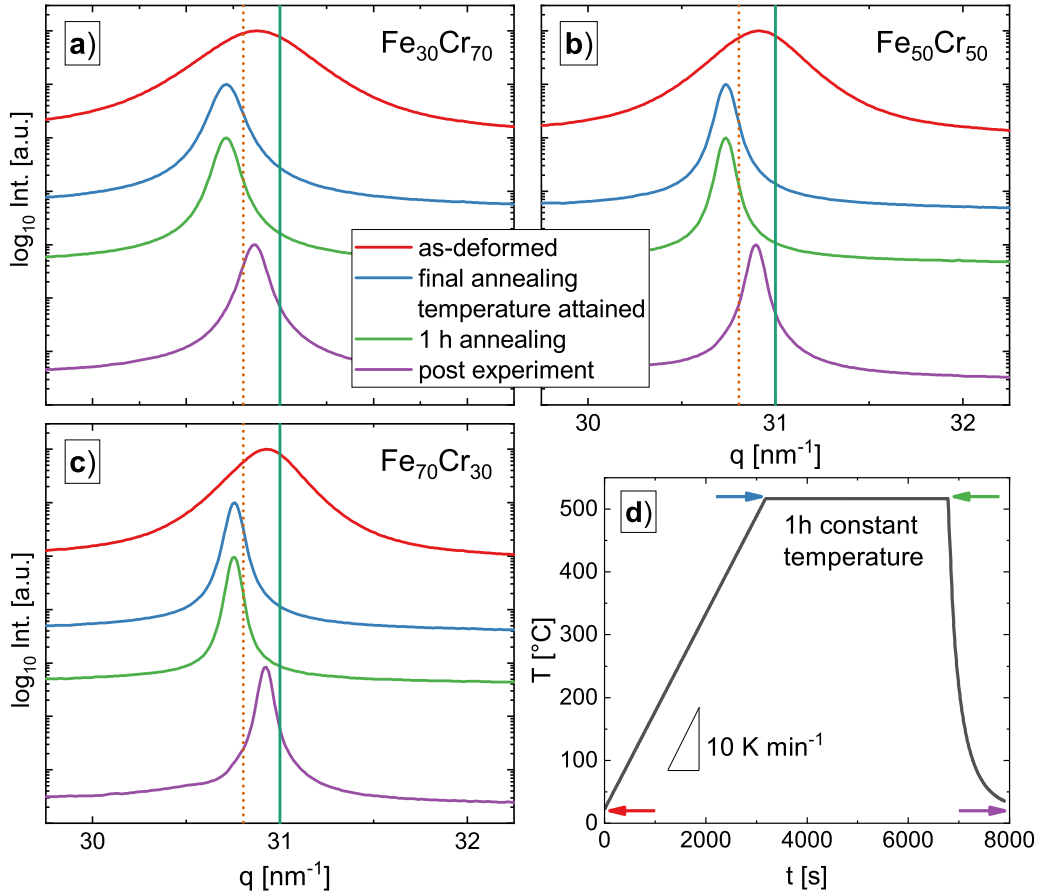
Figure B.3.: HEXRD synchrotron data of the [110] peak for HPT-deformed FeCr samples consisting of **a)** $Fe_{30}Cr_{70}$, **b)** $Fe_{50}Cr_{50}$ and **c)** $Fe_{70}Cr_{30}$. Vertical lines denote theoretical reference lines for Fe (solid, turquoise) and Cr (dashed, brown). The selected patterns belong to in-situ annealing experiments and are extracted at different times and temperatures, visualized **d)** by arrows in an exemplarily temperature profile.

for elemental Fe (solid, turquoise) and Cr (dashed, brown) calculated with lattice constants from [30]. The depicted peaks correspond to different temperatures during the in-situ experiment. The top peaks (red) belong to the beginning of the experiment, representing the as-deformed state. A significant peak broadening is again found for all three chemical compositions. According to Vegard's law [31] the peak positions follow the trend of the chemical composition determined by EDX measurements of the FeCr alloys. The Fe contents obtained with EDX for the alloys depicted in Figure B.3 a), b) and c) are 27.8±3.3 at.%, 48.7±0.8 at.% and 69.1±1.1 at.%, respectively. The blue peaks are recorded at the end of the heating process, when a constant temperature of 520 °C is reached. Because of the thermal expansion of the lattice, a shift towards a lower reciprocal lattice vector is visible. This is accompanied with a
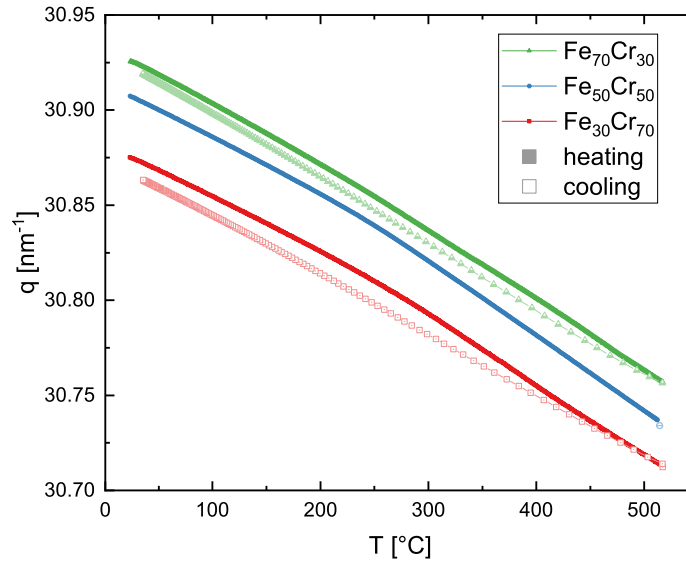
Figure B.4.: [110] peak position for every pattern during heating (full symbols) and cooling (empty symbols) for HPT-deformed FeCr alloys determined by fitting the HEXRD in-situ data by a single Voigt profile. The cooling is not covered experimentally for the $Fe_{50}Cr_{50}$ alloy.

significantly sharpened shape of the peak, indicating larger crystallite sizes and/or diminishing crystallographic defects. The green peak is recorded after 1 hour of isothermal annealing at 520 °C and shows almost no deviations with respect to the blue pattern. The purple peaks at the bottom correspond to an ex-situ measurement after the sample cooled down to room temperature and can be directly compared with the red line.

The recorded patterns are fitted with Voigt-profiles. It should be mentioned, that for every peak one single Voigt-profile is used. Although fitting by one peak implies a solid solution, an overlapping of two peaks corresponding to separated Fe and Cr is also possible. Unfortunately, the similar crystal structures (both body centred cubic) and the similar lattice parameters with less than 0.02 Å difference (see Reference [30]) lead to very similar peaks for Fe and Cr, with almost no differences. Despite the high brilliance of the synchrotron, a pattern fitting with two separated Voigt-peaks is ambiguous. The shape, as well as intensity and position, strongly depend on the fitting starting parameters which allows no clear statement. Nevertheless, using a single Voigt peak profile, a high accordance is reached for the calculated pattern with respect to the measured HEXRD data. The peak positions as a function of the temperature process while heating (filled symbols) and cooling (empty symbols) is shown in Figure B.4. A difference between these processes is recognised: While the

peak position changes as expected linearly during cooling, the heating curve is bended. Although, no peak separation is found (see Figure B.3) the varying slope indicates a superposition of processes, quite likely dedicated to a change in the microstructure.

Therefore, the Voigt-profiles are analysed in more detail, as it is a convolution of a Gauss and Cauchy (Lorentz) distribution. The full width half maximum (FWHM) of a single Voigt profile can be parsed into the breadths of its Cauchy and Gaussian components. Keijser et al. [32] linked the individual peak widths to size (Cauchy) and strain (Gauss) broadening, respectively. The evolution of peak widths for each composition is shown in the supplementary data file. It is found that the Cauchy peak width decreases with increasing annealing temperature. In contrast, the Gaussian FWHM barely changes until 250 °C before it decays rapidly with increasing temperature, indicating a reduction in internal stresses. The contribution of internal stresses to the overall peak width observed in Figure B.3 is strongly reduced, when the heating process is finished. The remaining narrowing of the peaks, upon further isothermal annealing, originates from size effects and therefore grain growth, which is in accordance with SEM investigations of the annealed FeCr alloys (see Figure B.1). After annealing for one hour at 520 °C, no peak separation or broadening of the peak due to a superposition of its elemental Fe and Cr peaks is found. We therefore conclude, that all FeCr alloys exhibit a nanocrystalline, supersaturated solid solution state before and after the annealing treatment. To decompose these alloys, higher annealing temperatures are necessary.

B.3.2. Magnetostrictive measurements

In principle, 3d-elements like Fe exhibit a low magnetostrictive response [33] but when alloyed with Al, Si, Ge or Ga an increased value was found [34]. This is explained by the substitution of an Fe atom by a non-magnetic metal. The magnetostriction of arc melted FeCr alloys without subsequent plastic deformation was measured by Bormio-Nunes et al. [8]. They processed FeCr solid solutions, with a Cr content between 5.3 and 30.7 at.% and found an increased saturation magnetostriction compared to the magnetostriction of the pure elements. Besides the interesting question, if a higher Cr content further increases the magnetostriction, an enhanced value confirms our results from Section B.3.1, as the increased magnetostriction is only present in the FeCr solid solution. Therefore, we conducted magnetostrictive measurements on all FeCr alloys in the as-deformed state as well as in one annealed state.

Figure B.5.: Effective magnetostriction as a function of applied magnetic field for three FeCr alloy after HPT-deformation at RT.

Assuming a perfectly isotropic material, the magnetostriction measured parallel and perpendicular to the applied magnetic field [35], follows $\lambda_\parallel = -2\ \lambda_\perp$. The anisotropy of magnetostrictive behaviour is further influenced by the crystal structure and crystallographic directions. Therefore, the effective saturation magnetostriction λ_s for polycrystalline materials is usually described by

$$\lambda_s = \frac{2}{3}(\lambda_\parallel - \lambda_\perp) \tag{B.1}$$

According to equation B.1 the magnetostrictive behaviour of as-deformed FeCr alloys as a function of the applied magnetic field is shown in Figure B.5. The saturation value increases with increasing Fe content. At a maximal applied field $\mu_0 H = 2.25$ T the signal is close to 0 ppm for the as-deformed $Fe_{30}Cr_{70}$ sample, whereas the samples consisting of $Fe_{50}Cr_{50}$ and $Fe_{70}Cr_{30}$ reach 8 ppm and 17 ppm, respectively. To give a comparison, the magnetostriction of elemental Cr is very small ($\lambda_s^{nm} < 1$ ppm) [36] and elemental Fe exhibits a crystallographic anisotropic magnetostriction, which results in a negative value $\lambda_s^m = -9.3$ ppm according to equation B.1 [35, 37]. Preliminary SQUID magnetometry measurements conducted on the $Fe_{30}Cr_{70}$ sample, exclude a paramagnetic state at room temperature but indicate the presence of superparamagnetic particles, possible existing within the high amount of grain boundaries of the nanocrystalline material [38]. Applying these values and using the $\frac{Fe}{Cr}$

B. Nanocrystalline FeCr alloys synthesised by severe plastic deformation

volume fraction f, the volumetrically weighted balance between a magnetostrictive λ_s^m and a non-magnetostrictive λ_s^{nm} component for the effective saturation magnetisation λ_s^{eff}

$$\lambda_s^{eff} = f\lambda_s^m + (1-f)\lambda_s^{nm} \tag{B.2}$$

gives deeper insights into the Fe based nanocrystalline alloys [39]. Obviously, this approximation does not hold for our presented alloys as equation B.2 yields an even smaller quantity in λ_s. We can either conclude on an existing solid solution or must assume other mechanisms giving a large positive contribution to the measured magnetostriction. If we assume separated phases, equation B.2 does not consider contributions of surface spins and grain boundaries. Nevertheless it is known, that both, surface- and bulk- magnetoelastic coupling contribute to the magnetoelastic tensor [6], which is further important for nanocrystalline materials [40]. To describe the magnetostrictive behaviour of nanocrystalline materials, Slawska-Waniewska et al. [41] expanded equation B.2 to

$$\lambda_s^{eff} = f\lambda_s^m + (1-f)\lambda_s^{nm}(f) + f\lambda_s^s \frac{S}{V} \tag{B.3}$$

where λ_s^s describes the interface contribution such as surface spins to the effective saturation magnetostriction. $\frac{S}{V}$ is the surface to volume fraction, which can be rewritten in $\frac{3}{R}$ for spherical grains with an effective grain radius R. For the FeCr system only the third term contribute with a positive value to λ_s^{eff} keeping in mind, that the measured λ_s values for $Fe_{50}Cr_{50}$ and $Fe_{70}Cr_{30}$ presented in Figure B.5 are positive. If the second term is neglected and the measured values for λ_s^{eff} as well as a grain size radius of 50 nm (median grain diameter obtained by TKD measurements - see Figure B.2) are used, we can estimate a value for λ_s^s. For the $Fe_{70}Cr_{30}$ composition a $\lambda_s^s \approx 400 \cdot 10^{-6}$ nm is necessary to fit our measurements. Comparing λ_s^s values for FeCr alloys to other Fe based nanocrystalline materials, they differ by one ($Fe_{30}Cr_{70}$) or two ($Fe_{50}Cr_{50}$ and $Fe_{70}Cr_{30}$) orders of magnitude [40, 41]. Therefore, surface spin contributions to the effective saturation magnetostriction are not excluded but cannot be the main contribution of the increased λ_s^{eff} and consequently, Fe and Cr have to be present in the form of a solid solution.

Hall et al. [42] used etched single crystals of FeCr and found an increasing magnetostriction ($\lambda_{[100]} = 51.7$ ppm) when alloying Fe with Cr up to 21.1 at.% for the crystallographic [100] direction. But they also describe a concurrently decreased value for the [111] direction ($\lambda_{[111]} = $ -2.7 ppm), if compared to elemental Fe [43]. According

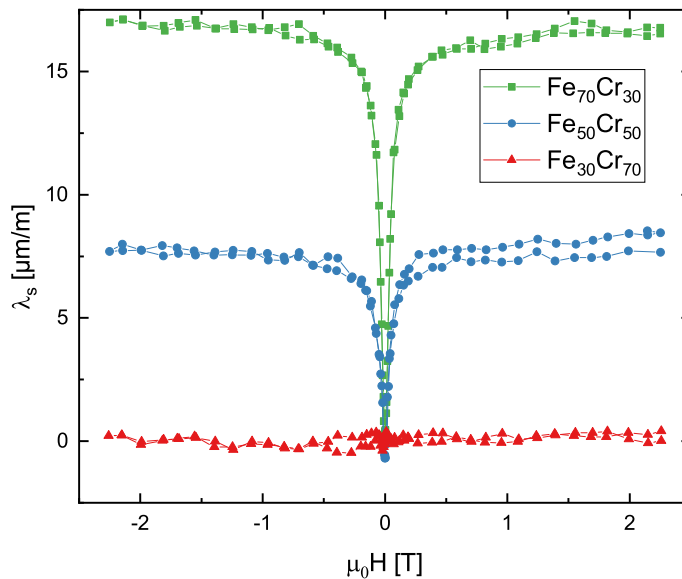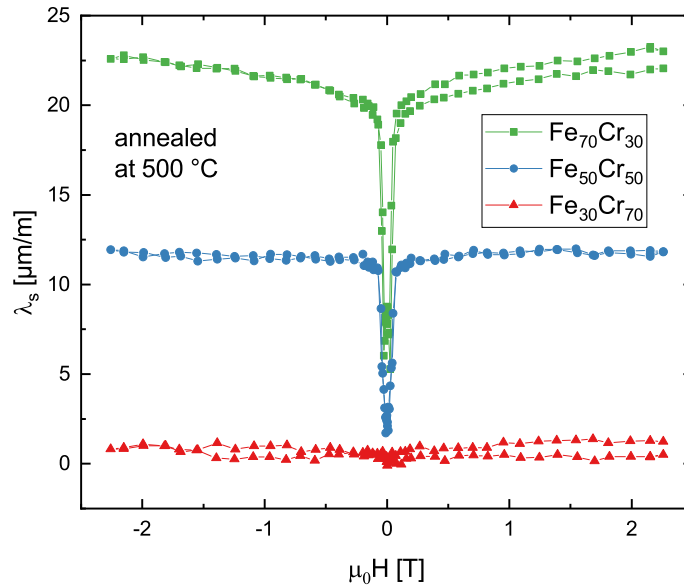Figure B.6.: Effective magnetostriction as a function of applied magnetic field for three FeCr alloys, HPT deformed at RT and subsequently annealed at 500 °C for 1 h.

to the relation

$$\lambda_s^{eff} = \frac{1}{5}(2\lambda_{100} + 3\lambda_{111}) \tag{B.4}$$

λ_s^{eff} results in 19 ppm, which is in excellent agreement with results on $Fe_{70}Cr_{30}$, keeping in mind that it is an HPT-deformed sample exhibiting a nanocrystalline microstructure. Furthermore, comparable results are found in the work of Bormio-Nunes et al. [8]. For the identical chemical composition of $Fe_{70}Cr_{30}$, they reported λ_s values between 23 ppm and 47 ppm depending on the measured side of their cubic samples. The results of magnetostrictive measurements of annealed samples (500 °C for 1h) are shown in Figure B.6. For all samples, the saturation magnetostriction increases compared to as-deformed samples. The signal for the $Fe_{30}Cr_{70}$ sample is slightly positive, the $Fe_{50}Cr_{50}$ and $Fe_{70}Cr_{30}$ samples reach 12 ppm and 23 ppm, respectively. The increased magnetostriction with respect to the as-deformed state is thought to originate from a decreased number of crystal defects and a possible reduction of residual stresses [44] and further, analysis of EBSD scans (see Figure B.2) revealed a slightly stronger texture for the annealed sample, which could also enhance magnetostriction values [7, 45, 46]. Due to the large, positive values, a solid solution is still present for all FeCr compositions but no further improvement of λ_s^{eff} by an increasing Cr content is found as motivated by Bormio-Nunes et al. [8].

During this work, we successfully produced nanocrystalline FeCr supersaturated

solid solutions over a broad chemical composition and clarified that the alloys do not exhibit a two-phase structure in the nanocrystalline regime and confirmed the existence of a solid solution. Astonishingly a demixing into separated Fe and Cr phases was suppressed by a remarkable temperature stability of the solid solution up to 520 °C. As the principle aim was to decompose the microstructure into a nanocrystalline two-phase material, enabling the formation of an exchange biased material, a more complex annealing treatment and HPT-processing route has to be found, which is part of ongoing studies. Beforehand, adding substitutional elements could stabilise the microstructure even further and hinder grain growth. This could preserve the nanocrystalline structure during annealing, while a decomposition takes place.

B.4. Conclusion

Nanocrystalline FeCr alloys consisting of $Fe_{30}Cr_{70}$, $Fe_{50}Cr_{50}$ and $Fe_{70}Cr_{30}$ are processed by HPT-deformation at RT. Upon annealing, the microstructure starts to coarsen between 300 °C and 500 °C, which is stronger pronounced for higher Fe contents. All materials investigated exhibit a hardening effect upon annealing with a peak between 300 °C and 400 °C followed by a softening at elevated annealing temperatures. In-situ HEXRD annealing experiments point towards a supersaturated solid solution of FeCr. However, concurrent finely dispersed Fe and Cr phases cannot be completely ruled out by microstructural investigations. Up to temperatures of 520 °C, no peak separation or broadening due to phase decomposition is found in HEXRD experiments. To clarify the ambiguous results from HEXRD experiments in regard of the prevailing phases, magnetostrictive measurements were conducted for HPT-deformed as well as subsequently annealed materials. Results show a clear deviation with respect to elemental Fe or Cr. The saturation magnetostriction $\lambda_s(\mu_0 H = 2.25\ T)$ is 0 ppm (1 ppm), 8 ppm (12 ppm) and 17 ppm (23 ppm) for the as-deformed (500 °C annealed) alloys consisting of $Fe_{30}Cr_{70}$, $Fe_{50}Cr_{50}$ and $Fe_{70}Cr_{30}$, respectively. After excluding a magnetostrictive contribution from interfaces, these values are explained by the formation of a supersaturated solid solution by HPT-deformation, which persists during annealing and validates findings from the synchrotron HEXRD measurements. To decompose these FeCr solid solutions and to enable exchange bias effects, more complex processing routes are necessary.

Declaration of Competing Interest: The authors declare, that they have no

known competing financial interests or personal relationships, that could have appeared to influence the work reported in this paper.

Acknowledgements

B.5. References

[1]   E Ma. Alloys created between immiscible elements, *Progress in materials science* **50**, no. 4 (2005), pp. 413–509.
DOI: 10.1016/j.pmatsci.2004.07.001.

[2]   T Koyano et al. Mechanical alloying process of Fe-Cr powders studied by magnetic measurements, *Journal of applied physics* **73**, no. 1 (1993), pp. 429–433.
DOI: 10.1063/1.353867.

[3]   Lukas Weissitsch et al. "Processing of Nanostructured Bulk Fe-Cr Alloys by Severe Plastic Deformation", *THERMEC 2021*. Vol. 1016. Materials Science Forum. Trans Tech Publications Ltd, 2021, pp. 1603–1610.

[4]   A Bachmaier et al. The formation of supersaturated solid solutions in Fe–Cu alloys deformed by high-pressure torsion, *Acta materialia* **60**, no. 3 (2012), pp. 860–871.
DOI: 10.1016/j.actamat.2011.10.044.

[5]   Karoline Sophie Kormout, Reinhard Pippan, and Andrea Bachmaier. Deformation-Induced Supersaturation in Immiscible Material Systems during High-Pressure Torsion, *Advanced Engineering Materials* **19**, no. 4 (2017), p. 1600675.

[6]   H Szymczak, R Żuberek, and J Gonzalez. Mechanisms responsible for magnetostriction in heterogeneous magnetic systems, *Journal of magnetism and magnetic materials* **191**, no. 1-2 (1999), pp. 199–202.
DOI: 10.1016/S0304-8853(98)00335-7.

[7]   Yongjun Han et al. Tailoring the heterogeneous magnetostriction in Fe-Co alloys, *Journal of Alloys and Compounds* **699** (2017), pp. 200–209.
DOI: 10.1016/j.jallcom.2016.12.223.

[8]   Cristina Bormio-Nunes et al. Magnetostriction of Fe–Cr and Fe–Cr–B Alloys, *IEEE Transactions on Magnetics* **52**, no. 5 (2016), pp. 1–4.
DOI: 10.1109/TMAG.2015.2512271.

[9]   Josep Nogués and Ivan K Schuller. Exchange bias, *Journal of Magnetism and Magnetic Materials* **192**, no. 2 (1999), pp. 203–232.
DOI: 10.1016/S0304-8853(98)00266-2.

[10]   Chris Binns et al. Exchange bias in FeCr core–shell nanoparticles, *Nano letters* **13**, no. 7 (2013), pp. 3334–3339.
DOI: 10.1021/nl40.1587t.

[11]   S Giri, M Patra, and S Majumdar. Exchange bias effect in alloys and compounds, *Journal of Physics: Condensed Matter* **23**, no. 7 (2011), p. 073201.
DOI: 10.1088/0953-8984/23/7/073201.

[12]   IJ McDonald et al. Exchange Bias in Bulk α-Fe/γ-Fe70Mn30 Nanocomposites for Permanent Magnet Applications, *ACS Applied Nano Materials* **2**, no. 4 (2019), pp. 1940–1950.
DOI: 10.1021/acsanm.8b02319.

[13]   SH Chung, A Hoffmann, and M Grimsditch. Interplay between exchange bias and uniaxial anisotropy in a ferromagnetic/antiferromagnetic exchange-coupled system, *Physical Review B* **71**, no. 21 (2005), p. 214430.
DOI: 10.1103/PhysRevB.71.214430.

[14]   A Bachmaier et al. Tailoring the magnetic properties of nanocrystalline Cu-Co alloys prepared by high-pressure torsion and isothermal annealing, *Journal of Alloys and Compounds* **725** (2017), pp. 744–749.

[15]   Lukas Weissitsch et al. "Strain Induced Anisotropic Magnetic Behaviour and Exchange Coupling Effect in Fe-SmCo$_5$ Permanent Magnets Generated by High Pressure Torsion", vol. 10. 11. Multidisciplinary Digital Publishing Institute, 2020, p. 1026.
DOI: 10.3390/cryst10111026.

[16]   A Hohenwarter and R Pippan. Sample Size and Strain-Rate-Sensitivity Effects on the Homogeneity of High-Pressure Torsion Deformed Disks, *Metallurgical and Materials Transactions A* **50**, no. 2 (2019), pp. 601–608.
DOI: 10.1007/s11661-018-4989-1.

[17]   Zenji Horita et al. Severe Plastic Deformation under High Pressure: Upsizing Sample Dimensions, *MATERIALS TRANSACTIONS* (2020), MT–M2020074.
DOI: 10.2320/matertrans.MT-M2020074.

[18] B. Schuh et al. Mechanical properties, microstructure and thermal stability of a nanocrystalline CoCrFeMnNi high-entropy alloy after severe plastic deformation, *Acta Materialia* **96** (2015), pp. 258–268.
DOI: https://doi.org/10.1016/j.actamat.2015.06.025.

[19] E Menéndez et al. Cold compaction of metal–ceramic (ferromagnetic–antiferromagnetic) composites using high pressure torsion, *Journal of alloys and compounds* **434** (2007), pp. 505–508.
DOI: 10.1016/j.jallcom.2006.08.142.

[20] Wei Xiong et al. Phase equilibria and thermodynamic properties in the Fe-Cr system, *Critical Reviews in Solid State and Materials Sciences* **35**, no. 2 (2010), pp. 125–152.

[21] Anton Hohenwarter et al. Technical parameters affecting grain refinement by high pressure torsion, *International Journal of Materials Research* **100**, no. 12 (2009), pp. 1653–1661.
DOI: 10.3139/146.110224.

[22] RZ Valiev and IV Alexandrov. Nanostructured materials from severe plastic deformation, *Nanostructured materials* **12**, no. 1-4 (1999), pp. 35–40.
DOI: 10.1016/S0965-9773(99)00061-6.

[23] Piotr Leonidovich Kapitza. The study of the magnetic properties of matter in strong magnetic fields. Part V.—Experiments on magnetostriction in dia-and para-magnetic substances, *Proceedings of the Royal Society of London. Series A, Containing Papers of a Mathematical and Physical Character* **135**, no. 828 (1932), pp. 568–600.

[24] Giannis Ashiotis et al. The fast azimuthal integration Python library: pyFAI, *Journal of applied crystallography* **48**, no. 2 (2015), pp. 510–519.
DOI: 10.1107/S1600576715004306.

[25] Mahmut Ruzi. *voigt line shape fit.* website. MATLAB Central File Exchange, 57603-voigt-line-shape-fit. 2020.

[26] O Renk et al. Increasing the strength of nanocrystalline steels by annealing: Is segregation necessary?, *Scripta materialia* **95** (2015), pp. 27–30.
DOI: 10.1016/j.scriptamat.2014.09.023.

[27] Xiaoxu Huang, Niels Hansen, and Nobuhiro Tsuji. Hardening by annealing and softening by deformation in nanostructured metals, *Science* **312**, no. 5771 (2006), pp. 249–251.
DOI: 10.1126/science.1124268.

[28] RZ Valiev et al. On the origin of the extremely high strength of ultrafine-grained Al alloys produced by severe plastic deformation, *Scripta Materialia* **63**, no. 9 (2010), pp. 949–952.
DOI: 10.1016/j.scriptamat.2010.07.014.

[29] Z Hegedüs et al. "Imaging modalities at the Swedish Materials Science beamline at PETRA III", *IOP Conference Series: Materials Science and Engineering.* Vol. 580. 1. IOP Publishing. 2019, p. 012032.
DOI: 10.1088/1757-899X/580/1/012032.

[30]   G. Chiarotti. *1.6 Crystal structures and bulk lattice parameters of materials quoted in the volume: Datasheet from Landolt-Börnstein - Group III Condensed Matter*. Ed. by G. Chiarotti. Interaction of Charged Particles and Atoms with Surfaces - in SpringerMaterials. DOI: 10.1007/10086066{_}6.

[31]   Lars Vegard. Die Konstitution der Mischkristalle und die Raumfüllung der Atome, *Zeitschrift für Physik* **5**, no. 1 (1921), pp. 17–26. DOI: 10.1007/BF01349680.

[32]   Th H De Keijser et al. Use of the Voigt function in a single-line method for the analysis of X-ray diffraction line broadening, *Journal of Applied Crystallography* **15**, no. 3 (1982), pp. 308–314.

[33]   Peter James et al. Calculated trends of the magnetostriction coefficient of 3d alloys from first principles, *Applied Physics Letters* **76**, no. 7 (2000), pp. 915–917. DOI: 10.1063/1.125628.

[34]   R Grössinger, R Sato Turtelli, and N Mehmood. Materials with high magnetostriction, *IOP Conference Series: Materials Science and Engineering* **60** (2014), p. 012002. DOI: 10.1088/1757-899x/60/1/012002.

[35]   Marcelo J Dapino et al. On magnetostrictive materials and their use in adaptive structures, *Structural Engineering and Mechanics* **17**, no. 3-4 (2004), pp. 303–330.

[36]   EW Lee and MA Asgar. Magnetostriction and Anomalous Thermal Expansion of Chromium, *Physical Review Letters* **22**, no. 26 (1969), p. 1436. DOI: 10.1103/PhysRevLett.22.1436.

[37]   A.E. Clark. "Chapter 7 Magnetostrictive rare earth-Fe2 compounds", vol. 1. Handbook of Ferromagnetic Materials. Elsevier, 1980, pp. 531–589. DOI: 10.1016/S1574-9304(05)80122-1.

[38]   AA Mazilkin et al. Competition for impurity atoms between defects and solid solution during high pressure torsion, *Scripta Materialia* **173** (2019), pp. 46–50. DOI: 10.1016/j.scriptamat.2019.08.001.

[39]   Giselher Herzer. Nanocrystalline soft magnetic materials, *Physica Scripta* **1993**, no. T49A (1993), p. 307. DOI: 10.1088/0031-8949/1993/T49A/054.

[40]   P Garcia Tello, JM Blanco, and J Gonzalez. Effective anisotropy and saturation magnetostriction of soft magnetic FeZrB (Cu) amorphous and nanocrystalline alloys, *Nanotechnology* **14**, no. 2 (2003), p. 304. DOI: 10.1088/0957-4484/14/2/339.

[41]   A Ślawska-Waniewska, R Żuberek, and P Nowicki. Saturation magnetostriction of FeZrB (Cu) nanocrystalline alloys, *Journal of magnetism and magnetic materials* **157** (1996), pp. 147–148. DOI: 10.1016/0304-8853(95)01190-0.

[42] RC Hall. Single-Crystal Magnetic Anisotropy and Magnetostriction Studies in Iron-Base Alloys, *Journal of Applied Physics* **31**, no. 6 (1960), pp. 1037–1038.
DOI: 10.1063/1.1735741.

[43] Kurt Heinz Jürgen Buschow, Frank R Boer, et al. *Physics of magnetism and magnetic materials.* Vol. 7. Springer, 2003.
DOI: 10.1007/b100503.

[44] JM Makar and DL Atherton. Effects of stress on the magnetostriction of 2% Mn pipeline steel, *IEEE transactions on magnetics* **30**, no. 4 (1994), pp. 1388–1394.
DOI: 10.1109/20.305537.

[45] Jiheng Li et al. Texture evolution and magnetostriction in rolled (Fe81Ga19) 99Nb1 alloy, *Journal of alloys and compounds* **476**, no. 1-2 (2009), pp. 529–533.
DOI: 10.1016/j.jallcom.2008.09.087.

[46] Yangkun He et al. Determination of bulk domain structure and magnetization processes in bcc ferromagnetic alloys: Analysis of magnetostriction in F e 83 G a 17, *Physical Review Materials* **2**, no. 1 (2018), p. 014412.
DOI: 10.1103/PhysRevMaterials.2.014412.

B.6. Appendix of Paper B

Supplementary
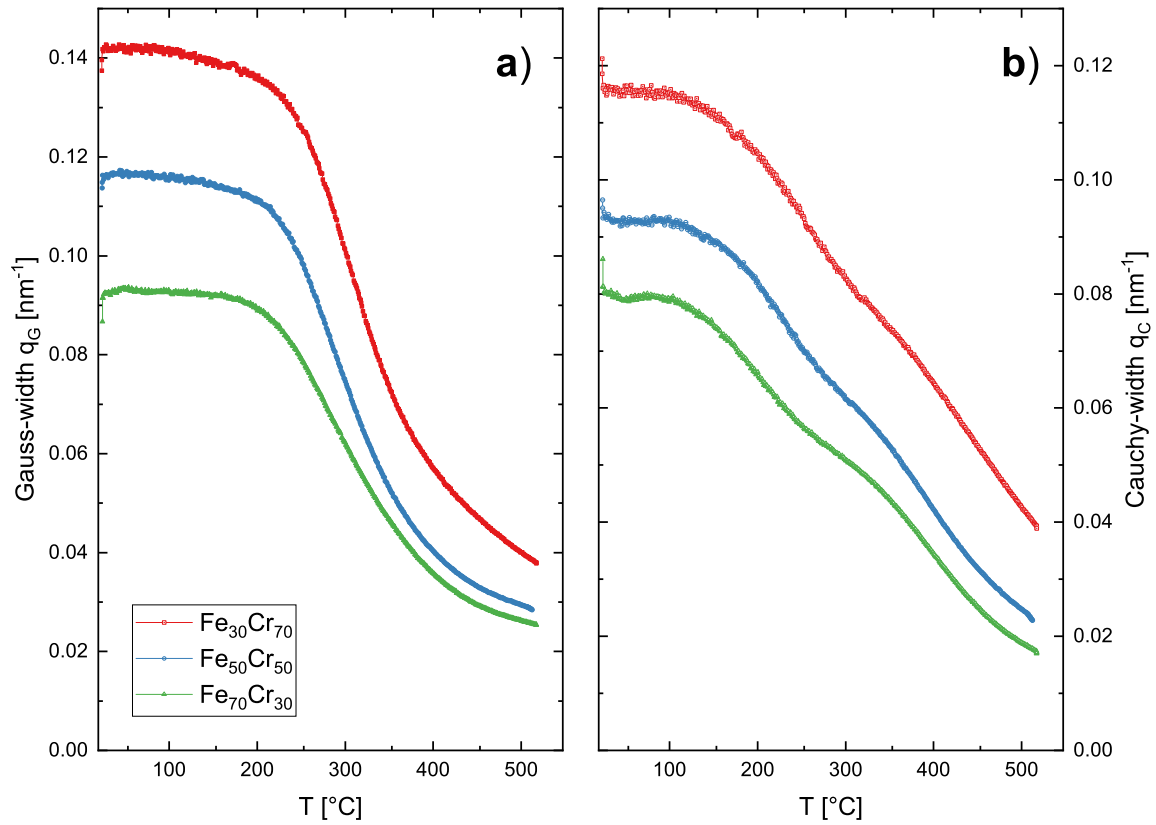
Supplementary B.1.: The [110] peak of the in-situ synchrotron annealing experiment is fitted by a single Voigt-peak. The FWHM is separated into a Gaussian **a)** and Cauchy **b)** contribution and plotted against the increasing temperature during heating.

Strain Induced Anisotropic Magnetic Behaviour and Exchange Coupling Effect in Fe-SmCo$_5$ Permanent Magnets Generated by High Pressure Torsion

Lukas Weissitsch[a], Martin Stückler[a], Stefan Wurster[a], Peter Knoll[b], Heinz Krenn[b], Reinhard Pippan[a] and Andrea Bachmaier[a]

[a] _Erich Schmid Institute of Materials Science, Austrian Academy of Sciences, Jahnstraße 12, 8700 Leoben, Austria_

[b] _Institute of Physics, University of Graz, Universitätsplatz 5, 8010 Graz, Austria_

Abstract

High-pressure torsion (HPT), a technique of severe plastic deformation (SPD), is shown as a promising processing method for exchange-spring magnetic materials in bulk form. Powder mixtures of Fe and SmCo$_5$ are consolidated and deformed by HPT exhibiting sample dimensions of several millimetres, being essential for bulky magnetic applications. The structural evolution during HPT deformation of Fe-SmCo$_5$ compounds at room- and elevated- temperatures of chemical compositions consisting of 87, 47, 24 and 10 wt.% Fe is studied and microstructurally analysed. Electron microscopy and synchrotron X-ray diffraction reveal a dual-phase nanostructured composite for the as-deformed samples with grain refinement after HPT deformation. SQUID magnetometry measurements show hysteresis curves of an exchange coupled nanocomposite at room temperature, while for low temperatures a decoupling of Fe and SmCo$_5$ is observed. Furthermore, exchange interactions between the hard- and

soft-magnetic phase can explain a shift of the hysteresis curve. Strong emphasis is devoted to the correlation between the magnetic properties and the evolving nano-structure during HPT deformation, which is conducted for a 1:1 composition ratio of Fe to $SmCo_5$. SQUID magnetometry measurements show an increasing saturation magnetisation for increasing strain γ and a maximum of the coercive field strength at a shear strain of $\gamma = 75$.

Keywords: nanostructured composite; Fe-$SmCo_5$ heterostructure; exchange coupled; spring magnet; high-pressure torsion; nucleation field; bulk dimensions
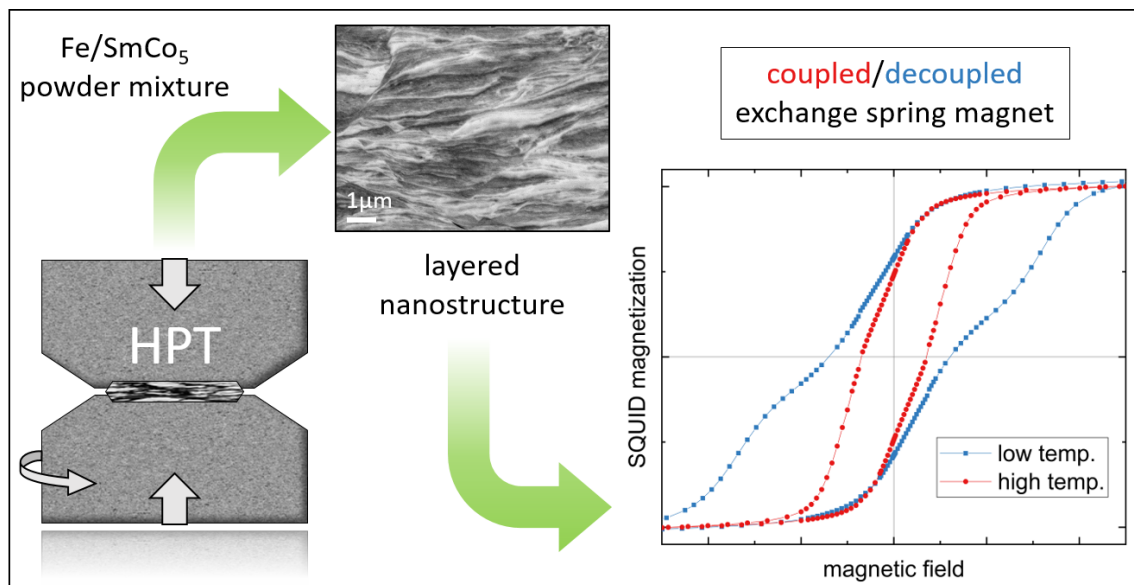
Figure C.0.: Graphical Abstract

C.1. Introduction

Permanent magnets are designed for a high saturation magnetisation, a high Curie temperature and a high anisotropy resulting in a strong coercivity and yielding a high energy product. The maximal achievable energy product of a magnet is a widely used and crucial parameter to compare different magnetic materials or processing routes. Compared to Nd-Fe-B based magnets, the intermetallic Sm-Co compounds offer a relatively low saturation magnetisation. Sm-Co based magnets instead provide the highest Curie temperatures (up to 1190 K), which is essential for applications

at elevated temperatures [1]. State-of-the-art magnetic materials, which provide a maximum magnetic field, require supplementary cooling, reducing the overall efficiency [2]. Moreover, the demand for permanent magnetic materials is strongly increasing, no matter if implemented in electric motors for vehicles or in windmills producing renewable energy. The achievable magnetic properties of common magnetic materials are already close to theoretical predictions [3]. Furthermore, mining and production processes of rare-earth elements are often correlated to political instabilities in the countries of origin and to monopolistic situations, which influences the price of elements on the world market [4].

The promising approach of exchange coupled spring magnets as permanent magnetic materials is an interesting field for research. The concept, first introduced nearly 30 years ago by Kneller and Hawig [5], combines the high remanence and saturation magnetisation of a soft-magnet and the huge coercive field strength of a hard magnet. Therefore the energy product of a magnet is increased, when the required magnetic anisotropy, provided by the hard magnetic phase, stabilises the coupled soft magnetic phase against demagnetisation. Soon after, the influence of the morphology, such as feature size and geometry between hard and soft magnetic phases, on the resulting hysteresis loop was studied. According to theoretical considerations, energy products higher than 120 MGOe, which is considerably higher than present high performance hard magnets (about 50–60 MGOe), should be achieved [4, 6, 7]. The concept further predicts, that the dimension of the soft-magnetic phase has to be smaller than the exchange length of the hard-magnetic phase, which necessitates nanostructuring. First experiments were conducted on well tuneable thin films and another techniques have been used, such as core-shell structured nanoparticles, rapidly quenched ribbons or mechanically milled powders [8]. Despite important contributions on fundamental knowledge, up-scaling and processing of bulk samples with an internal nanostructure is nowadays a challenging task.

Nanostructured materials are commonly produced by bottom-up methodologies, which compulsorily requires a consolidation step of powder precursors as bulk solid magnets are desired for practical applications. Depending on the technological process, the magnets suffer from a weak particle bonding, which favours mechanical instabilities as well as corrosion vulnerability. A residual porosity diminishes the bulk magnetic properties and thermal treatment during a sintering process lead to grain growth, which is another limiting factor. Severe plastic deformation (SPD) by high-pressure torsion (HPT) is a top-down approach to obtain nanostructured materials, i.e., grain

refinement is induced in a bulk material upon processing. Thus, common processing limits can be avoided and bulk samples in millimetre sized dimensions are obtained, which have been recently increased to the 100 mm regime [9–12]. In this study, we demonstrate the feasibility of HPT-deformation to process exchange coupled spring magnets. In the materials investigated, Fe is used as soft magnetic phase and $SmCo_5$ as hard magnetic phase. The successful fabrication and microstructural characterization of a dual-phase nanostructured composite is described in detail and resulting magnetic properties are measured. Additionally, the dependency of magnetic properties on the applied strain during HPT-deformation is investigated.

C.2. Materials and Methods

The HPT-deformation procedure is best described as a severe shearing process by torsion. In an idealised process the applied shear γ is defined by

$$\gamma = \frac{2\pi r}{t}n \tag{C.1}$$

as a function of the radius r within a disc subjected to n revolutions. The sample thickness t is considered to be constant. The used HPT setup is described in detail in ref. [10].

As starting materials conventional powders (Fe: MaTeck $99.9\% - 100 + 200$ mesh; $SmCo_5$: Alfa Aesar, intermetallic fine powder), which are stored and handled in an Ar filled glove box, are used to obtain the desired chemical composition. The investigated compounds consist of 10, 24, 47 and 87 wt.% soft magnetic Fe and 90, 76, 53 and 13 wt.% hard magnetic $SmCo_5$, respectively. Weighing the starting powders is very precise about an error below ± 0.15 wt.%. Additional EDX measurements along the cross-section on final samples, reveal an over-all-error of less than ± 1.5 wt.%. This does not hold for smaller specimen extracted at high applied strains exhibiting a separation into two phases: Here the local chemical composition varies to a far greater extent and does not exactly average to an exact global sample composition. The mixed powders are hydrostatically compacted under Ar-atmosphere using the HPT device at a nominal pressure of 5 GPa and a quarter revolution. Shortly thereafter, the samples are severely deformed at 7.5 GPa with a rotational frequency of 0.6 min^{-1} to avoid a significant increase of the processing temperature, which is further suppressed by high pressure air cooling. These samples are denoted as room-temperature (RT)

deformed samples in the following. No prediction of the deformation behaviour of composites can be made on simple basis of the corresponding material properties [13, 14]. During HPT-deformation at RT crack formation, a higher sample hardness and a limited amount of revolutions is not avoidable for certain compositions. To apply a higher amount of strain while avoiding crack formation, the influence of deformation temperature on the deformation behaviour and phase evolution, is investigated. Hence, HPT-deformation at elevated temperatures (250 °C and 400 °C) is carried out for selected samples.

After deformation the samples are cut into pieces for specific investigations. A schematic drawing of an as-deformed sample is depicted in Figure C.1. The excised SQUID samples are displayed as well positions and directions, where measurements are carried out. Scanning electron microscopy (SEM; LEO 1525, Carl Zeiss Microscopy GmbH, Oberkochen, Germany) images are made in tangential direction as well as the backscattered electron detection mode (BSE). Chemical evaluations are obtained with energy dispersive X-ray spectroscopy (EDX; XFlash 6–60, Bruker, Berlin, Germany) while using the software package Esprit 2.2 from Bruker. For line-scans, an acceleration voltage of 3–5 keV is used, resulting in a calculated maximal excitation volume radius of 70 nm and the obtained data are averaged over 7 pixels for smoothing. Vickers hardness measurements (Micromet 5104, Buehler, Lake Bluff, IL, USA) are carried out in tangential direction on the polished sample along the diameter in steps of $\Delta r = 0.25$ mm. A mean value is calculated if the measured microhardness saturates in a plateau (usually valid for: $2.0 < r < 3.5$ mm). Synchrotron X-ray diffraction (XRD) measurements are carried out in axial orientation and transmission mode (Petra III: P07 synchrotron facility at Deutsches Elektronen-Synchrotron DESY, Hamburg, Germany; Beam Energy: 100 keV; Beam Size: 0.2×0.2 mm^2). The signals are calibrated with a CeO_2 reference and integrated with pyFAI. The processing software Fityk is subsequently used for peak analysis. As theoretical reference peaks the Crystallography Open Database (COD) is used ($SmCo_5$: COD 1524132, Fe: COD 9006587).

A SQUID-Magnetometer (Quantum Design MPMS-XL-7,Quantum Design, Inc., San Diego, CA, USA) operated with the manufacturer's software MPMSMultiVu Application (version 1.54) is used for magnetic measurements. The hysteresis is measured at different temperatures in magnetic fields up to 70 kOe. Magnetic measurements are exclusively performed at RT deformed samples. The magnetic field is applied in axial HPT-disc orientation, if not other stated. For strain dependent

measurements several SQUID samples are cut out of one HPT-disc (see Figure C.1), whereas different radii can be linked to a specific amount of strain according to Equation (C.1). Due to finite sample sizes, rather a range of radii is observed instead of one specific radius. The investigated samples still represent bulk dimensional material, meaning the applied strain is averaged within radii of ± 0.5 mm.

In Table C.1, the processing parameters of all used samples in this study are summarised. Their chemical composition, deformation temperature *def.-temp*, number of HPT-revolutions n and resulting strain γ at r = 3 mm, according to Equation (C.1), is given.
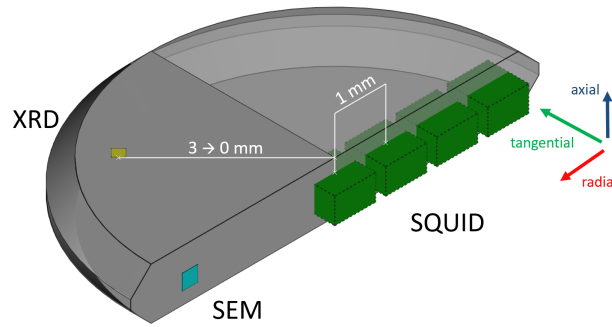
Figure C.1.: Schematic illustration of a halved HPT-deformed disc. The positions of SQUID-samples at varying radii are outlined (green boxes) with respect to the used cutting directions. Exemplarily axial XRD (yellow) and tangential SEM (turquoise) measurements are indicated.

Table C.1.: Summarised processing parameters of used samples in this study. n depicts the number of torsions and γ(r3) the shear strain at radius = 3 mm.

Nr	Fe/wt.%	SmCo$_5$/wt.%	Def.-Temp	n	γ(r3)
1	10	90	RT	25	396
2	24	76	RT	25	445
3	47	53	RT	7	111
4	87	13	RT	14	206
5	47	53	250 °C	8	118
6	47	53	400 °C	18	265

C.3. Results

C.3.1. Influence of Processing Parameters on Structural Evolution

In Figure C.2, the microstructure of the 47 wt.% Fe–53 wt.% $SmCo_5$ sample HPT-deformed at 7 revolutions at RT is shown for different positions along the HPT-disc. For all applied strains, a heterostructure is observed. In the center of the HPT-disc, at radius about 0, the lowest amount of shear strain ($\gamma \sim 0$) is applied and the material is mainly deformed by compression. BSE images show an inhomogeneous structure with separated phases of Fe (dark contrast) and $SmCo_5$ (bright contrast). According to Equation (C.1), the applied strain increases with increasing radius: $\gamma \sim$ 37, $\sim$75 and $\sim$111 for r1, r2, r3, respectively. Plastic deformation is mainly observed in the Fe phase, limited plastic deformation, a splitting and localized shearing of the $SmCo_5$ phases is found. Nonetheless, a refinement of the structure is noticed with increasing strain. This behaviour during HPT-deformation is also observed for all other investigated chemical compositions (see Appendix C.7). The magnified image at r3 shows that the microstructural features become very small and finely dispersed, but strong contrast changes in the BSE image reveal still separated Fe and $SmCo_5$ phases. The phases are elongated in radial direction, but offer a thickness well below 1 μm in axial direction. At the applied pressure it was not possible to fabricate samples with a higher strain due to slipping between sample and anvils. The sample hardness saturates at 648 ± 15 HV.

By varying the Fe content in the initial powder mixtures, a larger amount of strain can be applied. Figure C.3 shows the microstructure at r3 of three different compositions at two different magnifications. The sample consisting of 10 wt.% Fe–90 wt.% $SmCo_5$ is depicted in Figure C.3a) after 25 HPT revolutions. Strong contrast differences reveal the bright $SmCo_5$ matrix with small Fe rich areas at a strain of $\gamma \sim$ 396. The radial elongation of the Fe phase is in the range of a few μm, while the axial dimension is significantly below 1 μm. Figure C.3b) shows the microstructure of the sample consisting of 24 wt.% Fe–76 wt.% $SmCo_5$, HPT-deformed for 25 revolutions corresponding to a strain of $\gamma \sim$ 445. At lower magnifications the absence of contrast differences would indicate a homogeneous microstructure, which is not confirmed when looking at higher magnifications. A lamellar morphology, well below 1 μm is still visible. A similarity to the microstructure of the sample consisting of 47 wt.% Fe–53 wt.% $SmCo_5$ (Figure C.2) is noticed. A sample with further increased Fe

content (87 wt.% Fe–13 wt.% SmCo$_5$) is shown in Figure C.3c). 14 HPT rotations are applied which corresponds to a strain of $\gamma \sim 206$. The microstructure shows a Fe matrix with finely elongated SmCo$_5$ phases. A further deformation is limited by an immense hardness increase leading to crack formation at the used HPT conditions. The microhardness of the samples in Figure C.3a–c) reaches 616 ± 15, 657 ± 5 and 833 ± 11 HV, respectively.
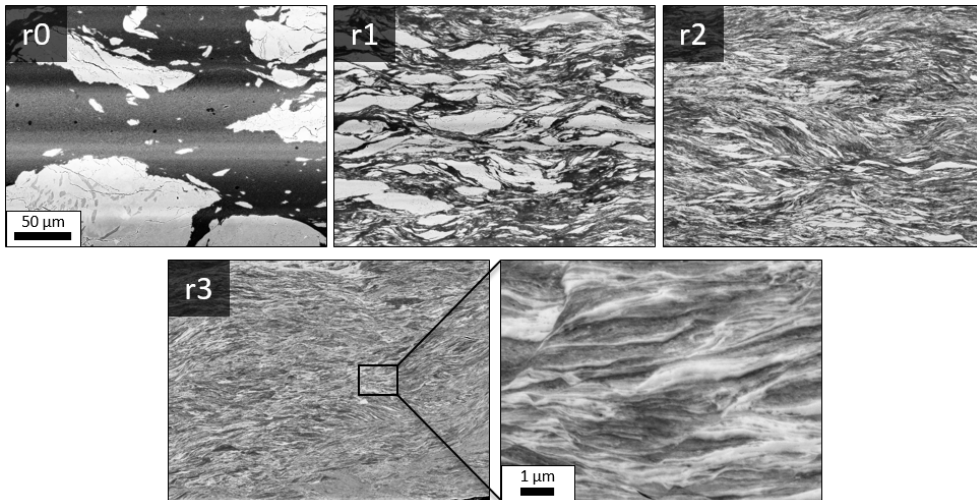
Figure C.2.: BSE images at the same magnification of a HPT-deformed sample at RT consisting of 47 wt.% Fe–53 wt.% SmCo$_5$ at different radii. The higher magnified image is taken at r = 3 mm.
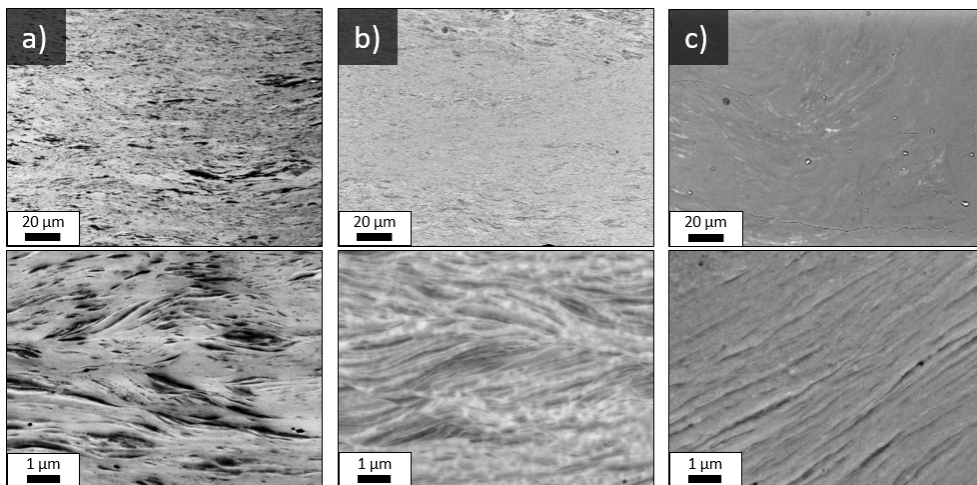
Figure C.3.: BSE images with two magnifications of HPT-deformed (RT) Fe-SmCo$_5$ samples at r = 3 mm consisting of (**a**) 10, (**b**) 24 and (**c**) 87 wt.% Fe.

To investigate the lamellar microstructure in more detail, an EDX line-scan is

carried out for one composition (47 wt.% Fe–53 wt.% SmCo$_5$). The scan direction is performed in axial HPT-disc direction, crossing the phases perpendicular as can be seen in the image of the microstructure in Figure C.4a) (top row). Strong changes of the Fe content can be explained by sharp interfaces between the Fe and SmCo$_5$ phase (Figure C.4). Because the excitation volume of the electron beam exceeds the dimension size of the phases, a smoothening occurs. Thus, the interaction volume of the electron beam always interacts with both phases suppressing 100%-Fe peaks. The ratio between Co and Sm content is calculated and analysed by a log-normal distribution which exhibits a peak at 4.84 ± 0.36. This closely corresponds to the stoichiometric distribution of the starting material of SmCo$_5$ and indicates that the phases remain unchanged during deformation and refinement. Similar line-scans are performed on the sample deformed at 400 °C . Here an increased maximum of the distribution is found pointing towards a higher Co to Sm ratio (e.g., Sm$_2$Co$_{17}$).
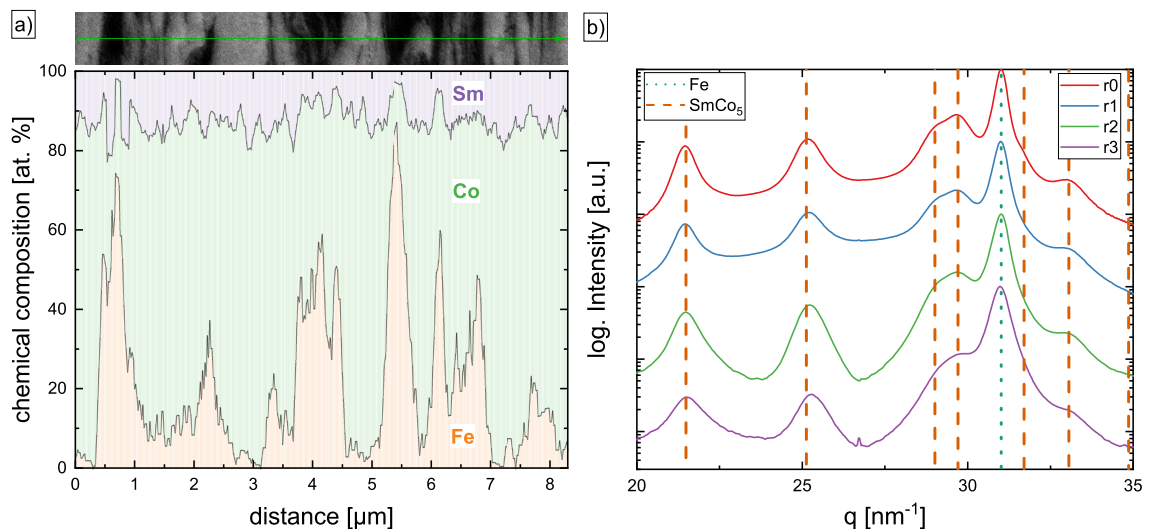
Figure C.4.: (**a**) EDX line-Scan at r3 in axial direction for the 47 wt.% Fe–53 wt.% SmCo$_5$ sample shown in Figure C.2. The alternating Fe content represents the two-phase microstructure. (**b**) Synchrotron XRD measurements of the RT-deformed 47 wt.% Fe–53 wt.% SmCo$_5$ sample for different radii.

Another proof for the stability of the phases during the deformation process are synchrotron XRD measurements. In Figure C.4b) measurements of the 47 wt.% Fe–53 wt.% SmCo$_5$ sample along the radius corresponding to the positions of the BSE images in Figure C.2 are presented. The theoretical reference peaks are in close accordance with the measured ones. With increasing radius, a peak broadening due to a grain size decrease is visible. The formation of additional phases cannot be observed.

C. Strain Induced Anisotropic Magnetic Behaviour and Exchange Coupling by HPT

Elevated deformation temperatures often helps to overcome processing limits, but usually lead to a final microstructure with larger grain sizes of the as-deformed state in the respective phases [15]. Figure C.5a) shows synchrotron XRD-pattern for three Fe-$SmCo_5$ samples consisting of 47 wt.% Fe–53 wt.% $SmCo_5$, which were HPT-deformed at RT, 250 °C and 400 °C . With increasing temperature, the peaks are getting sharper indicating coarser grains, but the Fe and $SmCo_5$ phases remain stable up to a deformation temperature of 250 °C . A strong difference is found at a deformation temperature of 400 °C . Several peaks are formed which cannot be related to the $SmCo_5$ phase. The formation of Sm_2Co_7 and Sm_2Co_{17} phases is observed and examples of corresponding peaks are highlighted by black (Sm_2Co_7) and blue (Sm_2Co_{17}) arrows. To investigate the influence of the amount of strain for phase formations under elevated deformation temperatures, the XRD-patterns of one 400 °C-deformed sample are shown in Figure C.5b) as a function of radius. At r0 the peaks correspond to the theoretical references of Fe and $SmCo_5$. The formation of additional phases is observed at higher radii, thus, the results show that the decomposition of $SmCo_5$ into Sm_2Co_7 and Sm_2Co_{17} is not taking place at higher deformation temperature alone. The structural transition starts at a strain of $\gamma \sim 90$ (r1 - blue arrow in Figure C.5 b) and is more pronounced at even higher amounts of strain.
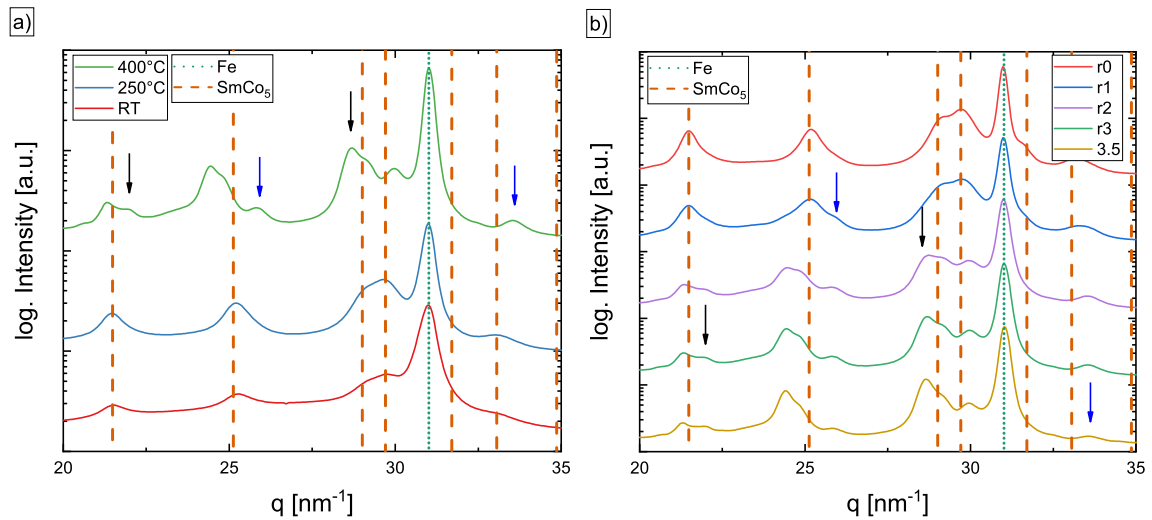
Figure C.5.: Synchrotron XRD measurements of several Fe-47 wt.% samples deformed at different temperatures at r3 (**a**) and for the sample deformed at 400 °C as a function of the radius (**b**). Examples of peak positions of the Sm_2Co_7 (black) and Sm_2Co_{17} (blue) are indicated by arrows.

C.3.2. Magnetic Properties

The magnetic properties of RT-deformed Fe-SmCo$_5$ compounds consisting of 87, 47, 24 and 10 wt.% Fe are measured using a SQUID with the field applied in axial HPT-disc direction (see Figure C.1). HPT-deformation induces a structure with lamellar morphology, where a polycrystalline microstructure is still present in both phases. Therefore, the applied magnetic field is perpendicular to this visible lamellar phase morphology. For every hysteresis measurement, a magnetic field up to ± 70 kOe is applied. In Figure C.6, the measured magnetic moment is normalized to the mass of the sample and plotted versus the applied magnetic field. Hysteresis measurements at 8 K reveal decoupled hysteresis loops: The recoil curve (when the field is increased after demagnetisation) shows the behaviour of a superposition of a soft and a hard magnetic phase, i.e., the behaviour of an exchange-spring magnet without coupling. This is because of the formation of a 'knee' due to two separated independent phases [5]. Therefore, the soft magnetic α-Fe phase is recognised by a high saturation magnetisation and a demagnetisation at low fields. The hard magnetic SmCo$_5$ phase is demagnetised at higher applied fields forming the 'knee'. This effect can be seen in the hysteresis curve of all chemical compositions, but is stronger pronounced at higher SmCo$_5$ contents. At higher measurement temperatures, a coupling between soft and hard magnetic phases is clearly present, showing less constriction of the (more smooth) hysteresis curves. Hysteresis measurements at 300 K (red curves) cannot be explained by a simple superposition of a separate Fe and SmCo$_5$ hysteresis. Here an exchange coupling is turned on, displaying an overall concave hysteresis profile with a concomitant decrease of coercivity. The mass saturation magnetisation is decreasing with decreasing Fe content. In contrast, the value of the 8 K hysteresis lies slightly higher for all measurements. Although the maximal applied magnetic field of the hysteresis is 70 kOe, a complete saturation for the samples consisting of 47, 24 and 10 wt.% Fe cannot be ensured, see Figure C.6b–d).

HPT-Induced Anisotropy

The influence of the HPT induced microstructure on the magnetic behaviour is investigated by applying a magnetic field in different directions to the HPT disc for Fe-SmCo$_5$ samples with a Fe content of 24 and 47 wt.% deformed at RT. The field is applied either in axial direction of the HPT-disc (as described above) or in tangential sample direction. The axial and tangential direction of the SQUID sample with respect
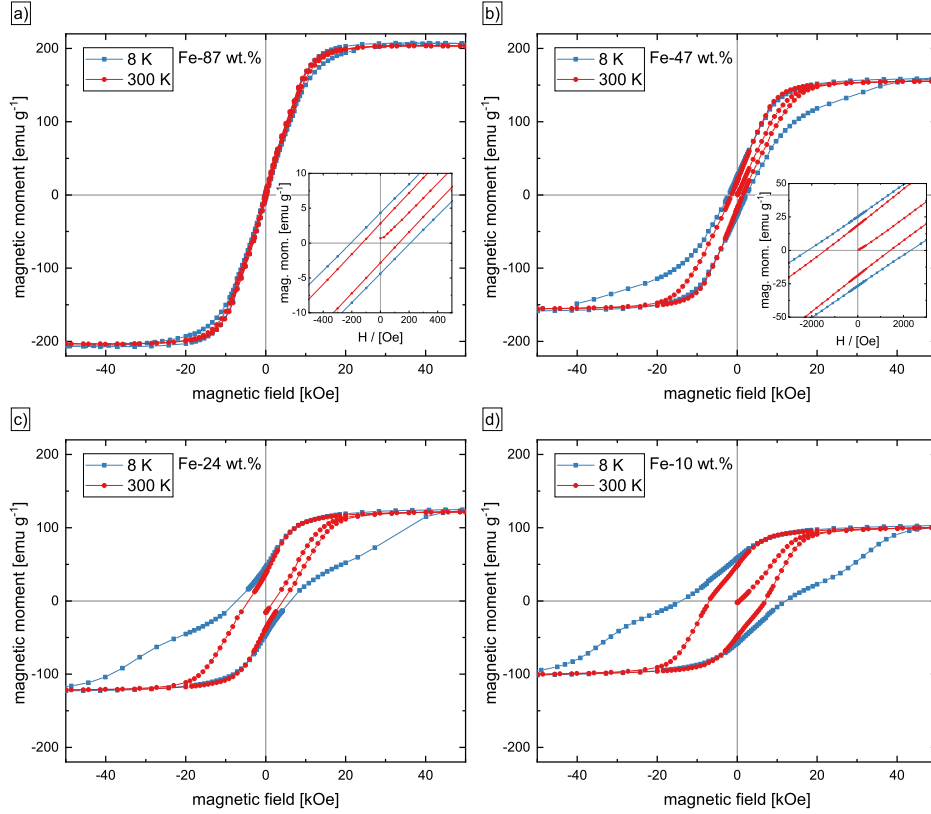
Figure C.6.: Hysteresis loops of HPT processed Fe-SmCo samples measured at 300 K (red, dots) and 8 K (blue, cubes) consisting of (**a**) 87, (**b**) 47, (**c**) 24 and (**d**) 10 wt.% Fe. All diagrams are identically scaled, therefore insets in (**a**,**b**) help to directly compare the coercivities at different temperatures.

to the HPT disc is visualized in Figure C.1 as well as in the inset of Figure C.7. The respective directions are denoted as axial and tangential in the following. The axial and tangential hysteresis of the selected samples consisting of 47 and 24 wt.% Fe are shown in Figure C.7a) and b). A higher susceptibility as well as a lower coercivity can be observed in the tangential direction, compared to the axial direction. A considerable shift of the tangential hysteresis to negative magnetic fields for the Fe-47 wt.% sample and to positive fields for the Fe-24 wt.% sample is visible. The difference between the positive and negative coercivities is ∼420 Oe and ∼710 Oe for the Fe-24 wt.% and Fe-47 wt.% sample, respectively. While the axial hysteresis is measured first and finished at a maximum applied field of 70 kOe, the fully magnetised samples are mounted in tangential direction on the SQUID sample holder. Therefore, the direction of the shift is explained whether the sample is rotated up- or downwards. Furthermore, the remanence is changed in both directions due to the shift. Looking at Figure C.7b), specific attention has to be given on the different saturation magnetisation values for

the tangential hysteresis between positive and negative fields. As mentioned before, a completely magnetised hysteresis for the low Fe-content samples in axial direction cannot be assured. Due to the positive horizontal shift, the saturation magnetisation is not reached at positive fields whereas for decreasing fields, the shift assists a full magnetisation process. Hence, the measured values for the saturation magnetisation between applied negative and positive field of this hysteresis is different.
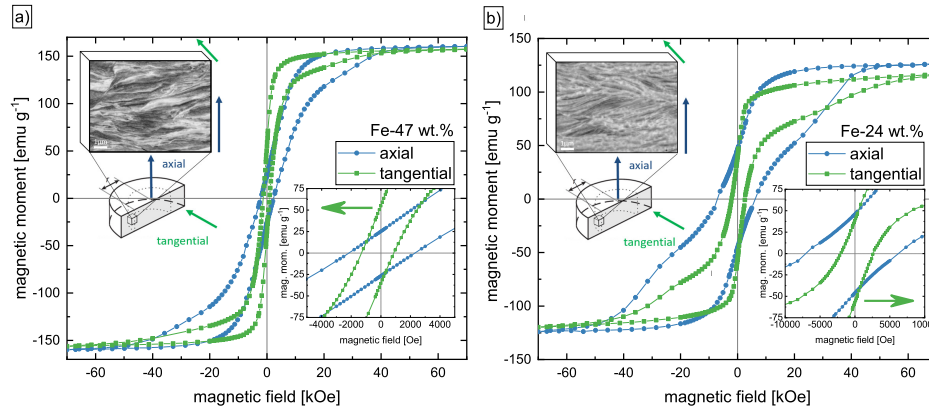
Figure C.7.: Hysteresis loops measured at 8 K in axial and tangential direction for Fe-SmCo$_5$ samples with (**a**) 24 and (**b**) 47 wt.% Fe content. The inset shows the direction of the applied magnetic field compared to the HPT-disc.

C.3.3. Strain-Dependent Magnetic Properties

The influence of the applied strain on the magnetic properties is investigated for the Fe-SmCo$_5$ sample containing 47 wt.% Fe–53 wt.% SmCo$_5$. The strain is calculated according to Equation C.1 for integer radii and the measured hysteresis correspond to different applied strains (Figure C.8). All samples have dimensions of several hundred μm in all spatial directions as shown in Figure C.1. As a result, the sample preserves not a specific amount of applied strain, it rather varies as a linear relation of their radial position. In the following the radius is used as sample indication and the reader is referred to Figure C.2, where the microstructure of the samples is shown. At r0, the spacing of the phases is larger than 50 μm as can be seen in Figure C.8, which changes drastically when looking at r1. Here, the deformation process leads to a two-phase microstructure where the SmCo$_5$ phase is fragmented and elongated, the spacing of the phases is significantly below 50 μm in the axial direction. At r2 and r3, the morphology is further refined, where the axial dimension for the SmCo$_5$ phase is below 10 μm at r2 and well below 1 μm at r3. An exchange coupled hysteresis is found

at 300 K for all samples. Therefore, it must be noticed again, that a relatively low applied strain for the sample at r0 corresponds to a radius between $0 < r \leq 0.5$ mm ($0 < \gamma < 20$) and already results in an exchange coupled magnet. At r2 ($\gamma = 75$) a maximum of the coercivity is found ($\sim$2000 Oe at 300 K and $\sim$3500 Oe at 8 K). Decoupled hysteresis are found at 8K, whereas the 'knee' is most pronounced for strains of $\gamma = 37$ to 75. At a maximum strain of $\gamma = 111$, the appearance of the 'knee' as well as the coercivity decreases again.
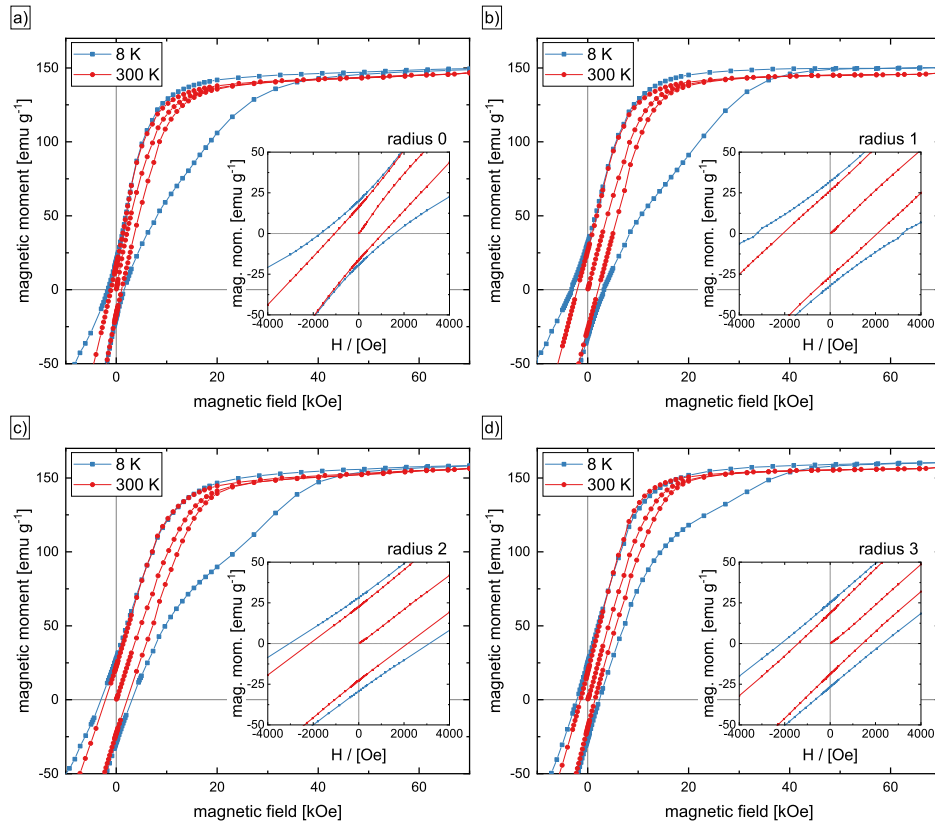
Figure C.8.: Hysteresis loops of HPT processed Fe-SmCo samples measured at 300 K (red, dots) and 8 K (blue, cubes) of a 47 wt.% Fe–53 wt.% SmCo$_5$ sample at a) r0, b) r1, c) r2 and d) r3.

C.4. Discussion

In this work, Fe-SmCo$_5$ composites with different amounts of Fe are processed by HPT-deformation. SmCo$_5$ exhibits a hexagonal crystal structure, whereas α-Fe is body centered cubic. During HPT-deformation, no ideal co-deformation of both phases takes place, Fe covers more strain than SmCo$_5$ particles. Nevertheless, both phases

are refined resulting in an alternating finely dispersed phase morphology with a phase spacing in the 100 nm regime. Compared to a cubic crystal, hexagonal structures provide less sliding planes and are more prone to localized shear and brittle behaviour. The deformation of hexagonal crystal structures is usually limited by pronounced crack formation or accompanied by phase transformations [11, 13, 16–18]. Especially at low strains, the $SmCo_5$ phase shows a lack of phase deformation and the formation of cracks in this phase is visible. Nonetheless, fragmentation and phase refinement is observed. However, most of the plastic deformation is localized in the Fe phase, where grain refinement as in single phase HPT deformed Fe is expected. When the composites are exposed to a higher amount of strain, the $SmCo_5$ phase is plastically deformed to a higher extend. For the Fe phase, a grain refinement with increasing strain is observed instead. It is assumed, that fracturing and localized shear of the brittle and mechanically harder $SmCo_5$ phase dominates the deformation behaviour until the hardness of the Fe and $SmCo_5$ phase converges due to the grain refinement of the Fe phase. Then, the $SmCo_5$ phase provides a higher plasticity [19]. However, local mutual hardness differences might lead to a partial co-deformation or an alternating deformation of the two phases. The rheologically harder phase tends to local necking and breaks into smaller fragments leading to the even more refined structure at the highest strains [20]. However, the possibility to deform hexagonal $SmCo_5$ is noticeable.

For exchange coupled magnets two magnetic phases are necessary. Thereby the hard magnetic material is the main phase, providing a high anisotropy and coercivity. The addition of a soft magnetic phase reduces the anisotropy and coercivity, but enhances the magnetisation and remanence [21]. Depending on morphology (e.g., spheres, layers, cylinders) of the dispersion and used hard and soft magnetic materials, a maximised theoretical energy product can be achieved. The energy product usually peaks around 30 wt.% soft magnetic material, which emphasizes the importance of a hard magnetic material matrix, which encloses the soft magnetic phase. Another crucial parameter is the exchange length for the soft magnetic material. Because of the small magnetic anisotropy constant of the soft phase, the spin orientation of the hard phase induces an exchange coupling into the soft phase. At the interface the spins of the soft phase align with the hard phase. This usually holds if the dimensions of the soft phase do not exceed a range of twice the exchange length

$$l_{ex}^{soft} = \sqrt{\frac{A^{soft}}{K_1^{soft}}} \tag{C.2}$$

C. Strain Induced Anisotropic Magnetic Behaviour and Exchange Coupling by HPT

where A denotes the exchange constant and K the anisotropy constant (for α-Fe: A $= 2.5 \times 10^{-11}$ Jm^{-1}, K$_1 = 4.6 \times 10^4$ Jm^{-3}, l$_{ex} = 23$ nm) [5, 22]. SEM investigations (Figures C.2, C.3 and C.4a) show a fine phase morphology in the 100 nm regime, sustained by a peak broadening in XRD experiments (Figure C.4b). The dimensions of the phases being small enough, are confirmed by the measured magnetic properties. As depicted in Figure C.6, completely exchange coupled hysteresis with a concave shape are found. The results are comparable to magnetic measurements received of ball milled Fe-SmCo powders [2].

By analysing the virgin curves presented in Figure C.6, a material classification between nucleation controlled and pinning controlled magnets can be given [23]. While existing domains are easily expanded in nucleation controlled magnets, microstructural obstacles (e.g., dislocations or vacancies, such as they occur after HPT deformation) impede the movement of domain walls, which act as pinning centers. Therefore, the initial susceptibility is lower and the saturation magnetisation is reached at higher fields indicating a pinning controlled magnetic material after HPT-deformation.

The hysteresis shapes at 8 K strongly differ from the 300 K curves, where exchange coupling is found. Hysteresis curves showing such a 'knee' at low temperatures are suggested as a decoupled compound, when hard and soft magnetic phases do not interact and are measured as magnetically independent phases [5]. The effect, that decoupling at decreasing temperatures occurs, can be explained by a temperature dependence of the magnetocrystalline anisotropy of the hard SmCo$_5$ phase [24]. As the anisotropy increases with decreasing temperature, according to Equation (C.2) the exchange length decreases [25]. Therefore, the ratio between total volume and exchange coupled volume diminishes at lower temperatures [26].

The shapes of tangential and axial hysteresis in Figure C.7b) are completely different. In axial direction a sheared and decoupled hysteresis is visible. The tangential curve offers a higher susceptibility with nearly no decoupling characteristics. This behaviour is similar for the hysteresis in Figure C.7a) besides a stronger pronounced decoupling due to the higher SmCo$_5$ content. Both tangential hysteresis are horizontally shifted which can be explained by the microstructure and the magnetic nucleation field. In the literature, a texture formation of hexagonal crystal structures is often observed during HPT-deformation. Therefore, the c-axis orientates into the shearing or tangential direction [17, 27, 28]. Furthermore, the c-axis also represents the magnetically easy axis, which means that all SmCo$_5$ crystals are easily demagnetised. In the case of

116

the used SmCo$_5$ material, this also explains the higher susceptibility compared to the axial hysteresis. Hence, we assume that the microstructure of HPT-deformed Fe-SmCo$_5$ composites consists of a lamellar-like structure with the easy axis of the hard magnetic phase oriented in tangential direction. The soft magnetic spins align in the same direction. When the field is reversed areas with opposite spins have to be formed. This requires a so called nucleation field H$_n$ and is described by

$$H_n \cong \frac{K^{hard}}{\mu_0 M_s^{soft}}$$

(C.3)

where K is the anisotropy constant and M_s the saturation magnetisation [5, 29]. If the hysteresis cannot be demagnetised completely, a pinning between hard and soft magnetic spins remains. The nucleation field is changed due to a varying magnetisation and the material is demagnetised at different fields.

In the literature, ball milling experiments, as a processing technique using plastic deformation, are mainly used to fabricate Fe-SmCo$_5$ magnets. Although the production technique differs a lot, comparisons of the results can be made. Rong et al. [2] reported a decrease in coercivity when milling the powder up to 10 h. They describe the formation of an amorphous structure, due to a reduced hard-phase stability. Further, they found an increasing saturation magnetisation because of the formation of a FeCo-alloy providing a higher magnetisation compared to α-Fe. During HPT also a strong decrease in coercivity and a slight increase in the magnetisation is found when the applied strain of the HPT-deformed sample exceeds $\gamma = 75$. Besides a slight peak broadening, no amorphization is found in our corresponding synchrotron XRD measurements (Figure C.4b), which could explain the coercivity deterioration. Detailed TEM studies at the interfaces between the Fe-SmCo$_5$ interfaces could reveal the formation of a small non-magnetic layer in between, if a slight decomposition of the SmCo$_5$ structure is present. However, this is beyond the scope of this work, which aims to show that HPT-deformation is an alternative process to manufacture exchange coupled nanocomposites.

Therefore, future investigations will cover the influence of applied amount of strain on the magnetic behaviour for different chemical compositions and other phases. For example, the magnetic properties will be enhanced when Fe is substituted by FeCo alloys and SmCo$_5$ by other SmCo based intermetallic phases such as Sm$_2$Co$_7$ or Sm$_2$Co$_{17}$. The HPT-parameters, such as a different deformation temperature, will be adjusted and could lead to a better deformation performance, while the

phases remain stable. In the present study it could be shown that Fe and $SmCo_5$ phases remain stable until 250 °C (see Figure C.5a). Moreover, the stability of the finely dispersed heterostructure of the magnets will be tested by annealing at higher temperatures to show the utilization for technical applications. Finally, subsequent annealing treatments at low temperatures after deformation are expected to reduce crystal defects, introduced by the shearing process, which again is expected to improve magnetic performance.

C.5. Conclusions

For the first time, the possibility of producing nanostructured Fe-SmCo exchange spring magnets by HPT-deformation over a broad chemical composition range is demonstrated. HPT-deformation at elevated temperatures (T > 250 °C) leads to a strain induced phase transformation of the SmCo-phase, whereas room temperature deformation allows the production of a defined heterogeneous nanostructured morphology preserving the soft-magnetic Fe phase and hard magnetic $SmCo_5$-phase. In contrast to other techniques, it is possible to fabricate nanostructured bulk samples already exhibiting dimensions of several centimetres without any thermal compaction or sintering process. Spring magnetic behaviour at 300 K and a decoupling effect at lower temperatures (8 K) are found for all chemical compositions. HPT-deformation leads to an anisotropic microstructure, which is magnetically investigated for two different chemical compositions in axial and tangential HPT-disc directions. The influence of the applied strain on the magnetic properties is investigated on the Fe-$SmCo_5$ sample with medium composition, revealing an optimum amount of strain of $\gamma = 75$, for the used initial powder size, showing the highest coercivity.

Acknowledgements

Abbreviations

The following abbreviations are used in this manuscript:

BSE	Backscattered Electrons
COD	Crystallography Open Database
EDX	Energy Dispersive X-ray Spectroscopy
HPT	High-Pressure Torsion
RT	Room Temperature
SEM	Scanning Electron Microscopy
SPD	Severe Plastic Deformation
SQUID	Superconducting Quantum Interference Device
TEM	Transmission Electron Microscopy

C.6. References

[1] A Ray and K Strnat. Magnetic properties of rare earth-cobalt phases $R_5 Co_{19}$, *IEEE Transactions on Magnetics* **11**, no. 5 (1975), pp. 1429–1430.

[2] Chuanbing Rong et al. Self-nanoscaling of the soft magnetic phase in bulk SmCo/Fe nanocomposite magnets, *Journal of materials science* **46**, no. 18 (2011), pp. 6065–6074.
DOI: 10.1007/s10853-011-5568-7.

[3] Oliver Gutfleisch. Controlling the properties of high energy density permanent magnetic materials by different processing routes, *Journal of Physics D: Applied Physics* **33**, no. 17 (2000), R157.

[4] Oliver Gutfleisch et al. Magnetic materials and devices for the 21st century: stronger, lighter, and more energy efficient, *Advanced materials* **23**, no. 7 (2011), pp. 821–842.
DOI: 10.1002/adma.201002180.

[5] Eckart F Kneller and Reinhard Hawig. The exchange-spring magnet: a new material principle for permanent magnets, *IEEE Transactions on Magnetics* **27**, no. 4 (1991), pp. 3588–3560.
DOI: 10.1109/20.102931.

[6] Ralph Skomski and JMD Coey. Giant energy product in nanostructured two-phase magnets, *Physical Review B* **48**, no. 21 (1993), p. 15812.
DOI: 10.1103/PhysRevB.48.15812.

[7] PK Sahota et al. Ultrahard magnetic nanostructures, *Journal of Applied Physics* **111**, no. 7 (2012), 07E345.
DOI: 10.1063/1.3679453.

[8] Eric E Fullerton, JS Jiang, and SD Bader. Hard/soft magnetic heterostructures: model exchange-spring magnets, *Journal of Magnetism and Magnetic Materials* **200**, no. 1-3 (1999), pp. 392–404.
DOI: 10.1016/S0304-8853(99)00376-5.

[9] Ruslan Zafarovich Valiev, Rinat K Islamgaliev, and Igor V Alexandrov. Bulk nanostructured materials from severe plastic deformation, *Progress in materials science* **45**, no. 2 (2000), pp. 103–189.
DOI: 10.1016/S0079-6425(99)00007-9.

[10] Anton Hohenwarter et al. Technical parameters affecting grain refinement by high pressure torsion, *International Journal of Materials Research* **100**, no. 12 (2009), pp. 1653–1661.
DOI: 10.3139/146.110224.

[11] Kaveh Edalati and Zenji Horita. A review on high-pressure torsion (HPT) from 1935 to 1988, *Materials Science and Engineering: A* **652** (2016), pp. 325–352.
DOI: 10.1016/j.msea.2015.11.074.

[12] A Hohenwarter and R Pippan. Sample Size and Strain-Rate-Sensitivity Effects on the Homogeneity of High-Pressure Torsion Deformed Disks, *Metallurgical and Materials Transactions A* **50**, no. 2 (2019), pp. 601–608.

[13] Karoline Sophie Kormout, Reinhard Pippan, and Andrea Bachmaier. Deformation-Induced Supersaturation in Immiscible Material Systems during High-Pressure Torsion, *Advanced Engineering Materials* **19**, no. 4 (2017), p. 1600675.
DOI: 10.1002/adem.201600675.

[14] Reinhard Pippan et al. Saturation of fragmentation during severe plastic deformation, *Annual Review of Materials Research* **40** (2010), pp. 319–343.
DOI: 10.1146/annurev-matsci-070909-104445.

[15] O Renk and R Pippan. Saturation of grain refinement during severe plastic deformation of single phase materials: reconsiderations, current status and open questions, *Materials transactions* **60**, no. 7 (2019), pp. 1270–1282.
DOI: 10.2320/matertrans.MF201918.

[16] A Bachmaier et al. Tailoring the magnetic properties of nanocrystalline Cu-Co alloys prepared by high-pressure torsion and isothermal annealing, *Journal of Alloys and Compounds* **725** (2017), pp. 744–749.
DOI: 10.1016/j.jallcom.2017.07.200.

[17] H Wang et al. Transformation pathway from alpha to omega and texture evolution in Zr via high-pressure torsion, *Applied Physics Letters* **114**, no. 6 (2019), p. 061903.
DOI: 10.1063/1.5087721.

[18] Martin Stückler et al. Magnetic Binary Supersaturated Solid Solutions Processed by Severe Plastic Deformation, *Nanomaterials* **9**, no. 1 (2019), p. 6.
DOI: 10.3390/nano9010006.

[19] SS Kiparisov, IA Kiyanskii, and VE Perel'man. Theoretical and experimental investigation of the process of plastic deformation of sintered composite materials IV. Technological basis for controlling the state of the elements of the "hard" phase during deformation, *Soviet Powder Metallurgy and Metal Ceramics* **26**, no. 11 (1987), pp. 899–902.
DOI: 10.1007/BF00794107.

[20] I-W Chen, EJ Winn, and M Menon. Application of deformation instability to microstructural control in multilayer ceramic composites, *Materials Science and Engineering: A* **317**, no. 1-2 (2001), pp. 226–235.
DOI: 10.1016/S0921-5093(01)01161-3.

[21] Ralph Skomski et al. Predicting the future of permanent-magnet materials, *IEEE Transactions on Magnetics* **49**, no. 7 (2013), pp. 3215–3220.
DOI: 10.1109/TMAG.2013.2248139.

[22] H Kronmüller et al. Micromagnetism and microstructure of hard magnetic materials, *Journal of Physics D: Applied Physics* **29**, no. 9 (1996), p. 2274.
DOI: 10.1088/0022-3727/29/9/008.

[23] Karl J Strnat and Reinhold MW Strnat. Rare earth-cobalt permanent magnets, *Journal of Magnetism and Magnetic Materials* **100**, no. 1-3 (1991), pp. 38–56.
DOI: 10.1016/0304-8853(91)90811-N.

[24] SG Sankar et al. Magnetocrystalline anisotropy of Sm Co 5 and its interpretation on a crystal-field model, *Physical Review B* **11**, no. 1 (1975), p. 435. DOI: 10.1103/PhysRevB.11.435.

[25] J Ping Liu et al. Temperature dependence of magnetic hysteresis of RCo x: Co nanocomposites (R= Pr and Sm), *Journal of Applied Physics* **87**, no. 9 (2000), pp. 6740–6742. DOI: 10.1063/1.372826.

[26] LP Muñoz Ortega et al. Temperature effect on dipolar and exchange interactions for SmCo5+ Fe65Co35 nanocomposite powders, *Journal of Applied Physics* **111**, no. 7 (2012), 07B505. DOI: 10.1063/1.3672070.

[27] BJ Bonarski et al. Texture evolution of Mg during high-pressure torsion, *Journal of materials science* **43**, no. 23-24 (2008), pp. 7513–7518.

[28] Yi Huang et al. Microstructure and texture evolution in a magnesium alloy during processing by high-pressure torsion, *Materials Research* **16**, no. 3 (2013), pp. 577–585.

[29] ZJ Guo et al. Exchange-coupled Sm–Co/Nd–Co nanomagnets: correlation between soft phase anisotropy and exchange field, *Applied physics letters* **81**, no. 11 (2002), pp. 2029–2031. DOI: 10.1063/1.1504869.

122

C.7. Appendix of Paper C

Radial Microstructure

In this section, supplementary information on the processed samples is given. The change of the microstructure as a function of applied strain is described in detail for sample Nr. 3 in Section C.3.1. Similarities are found for sample Nr. 1, 2 and 4, depicted in Figures C.9, C.10 and C.11, respectively. The radial microstructure for samples deformed at elevated temperatures is found in Figures C.12 (250 °C) and C.13 (400 °C).
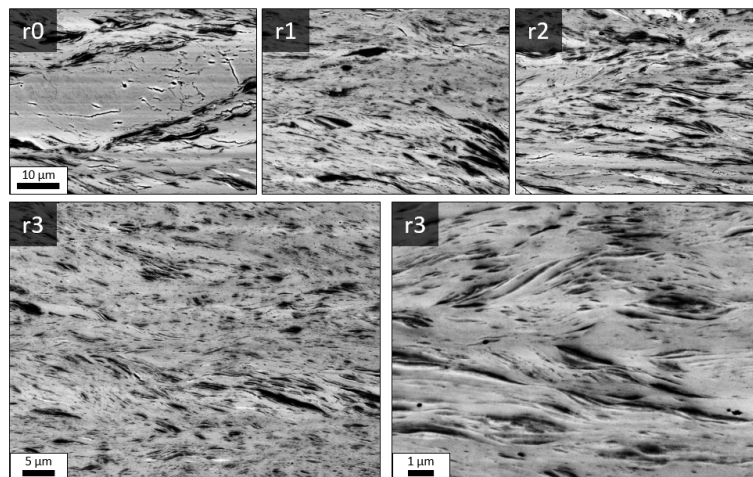
Figure C.9.: BSE images of a HPT-deformed sample (Nr. 1) at RT consisting of 10 wt.% Fe–90 wt.% $SmCo_5$ at different radii. The scale bar in r0 also applies to r1 and r2. Images of two magnifications are presented for r3.
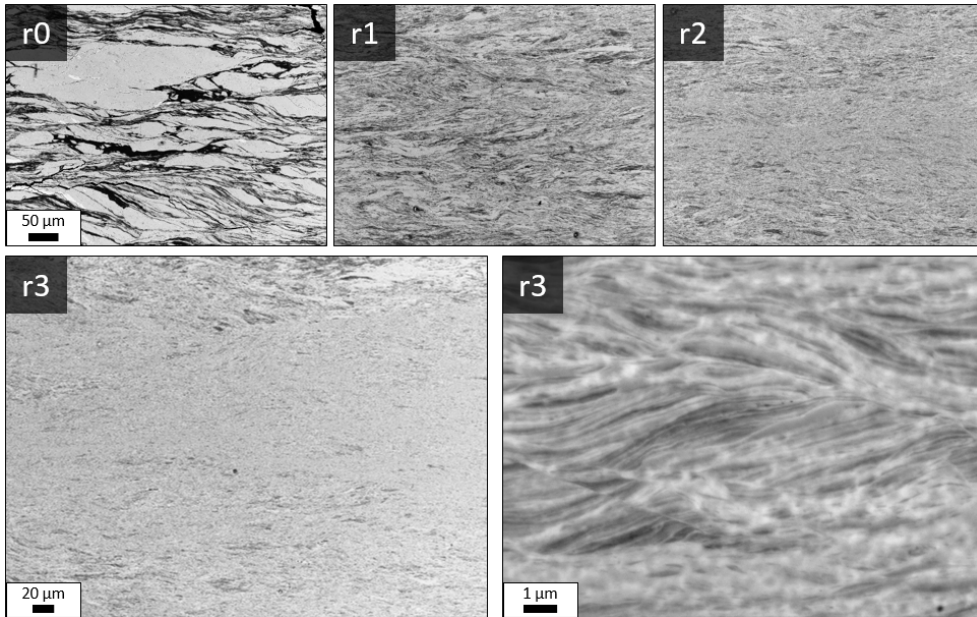
Figure C.10.: BSE images of a HPT-deformed sample (Nr. 2) at RT consisting of 24 wt.% Fe–76 wt.% $SmCo_5$ at different radii. The scale bar in r0 also applies to r1 and r2. Images of two magnifications are presented for r3.
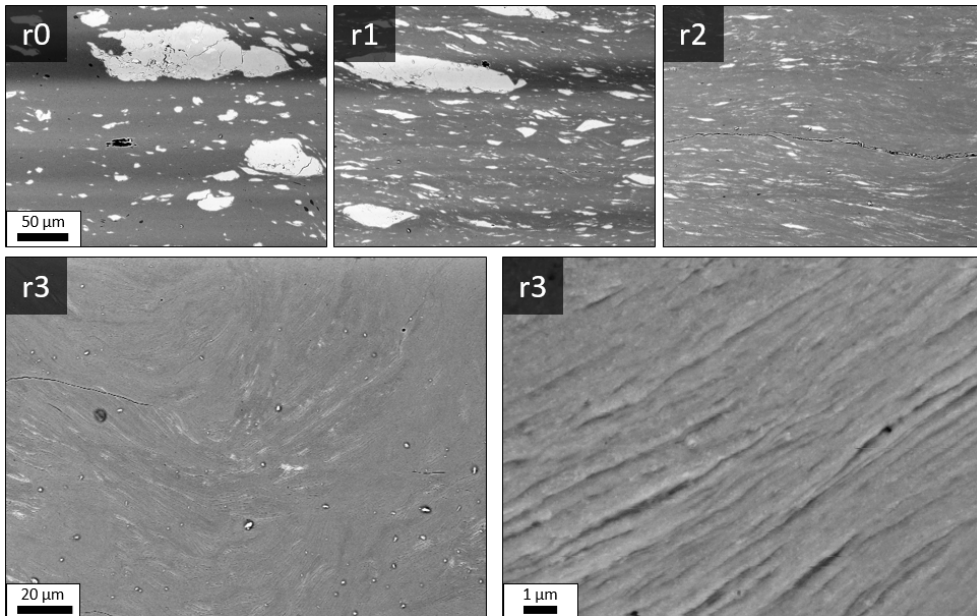
Figure C.11.: BSE images of a HPT-deformed sample (Nr. 4) at RT consisting of 87 wt.% Fe–13 wt.% $SmCo_5$ at different radii. The scale bar in r0 also applies to r1 and r2. Images of two magnifications are presented for r3.
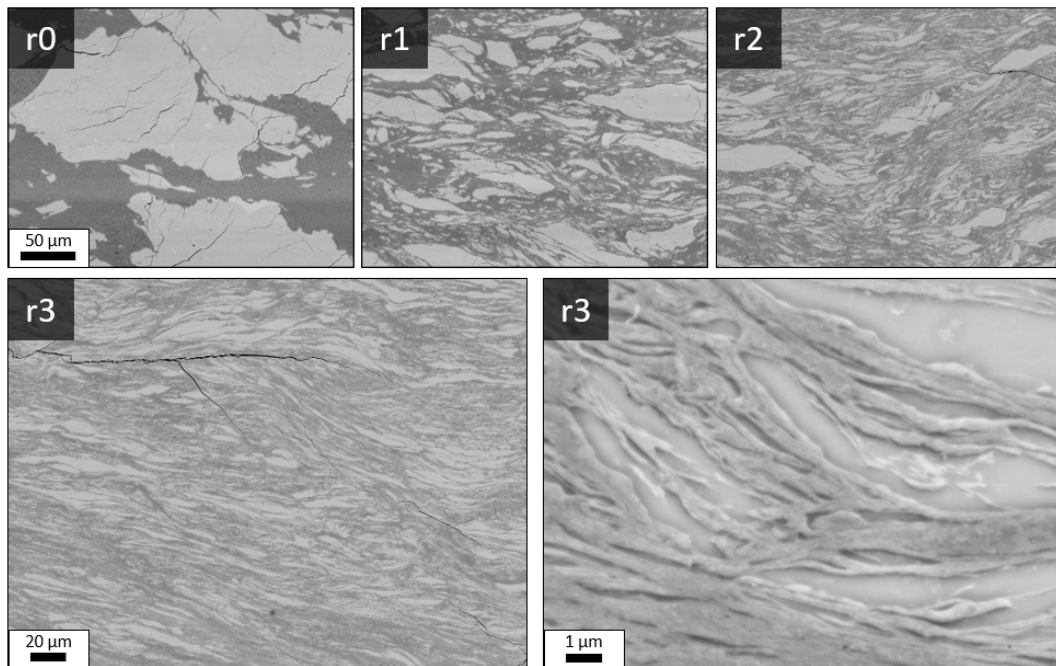
Figure C.12.: BSE images of a HPT-deformed sample (Nr. 5) at 250 °C consisting of 47 wt.% Fe–53 wt.% SmCo$_5$ at different radii. The scale bar in r0 also applies to r1 and r2. Images of two magnifications are presented for r3.
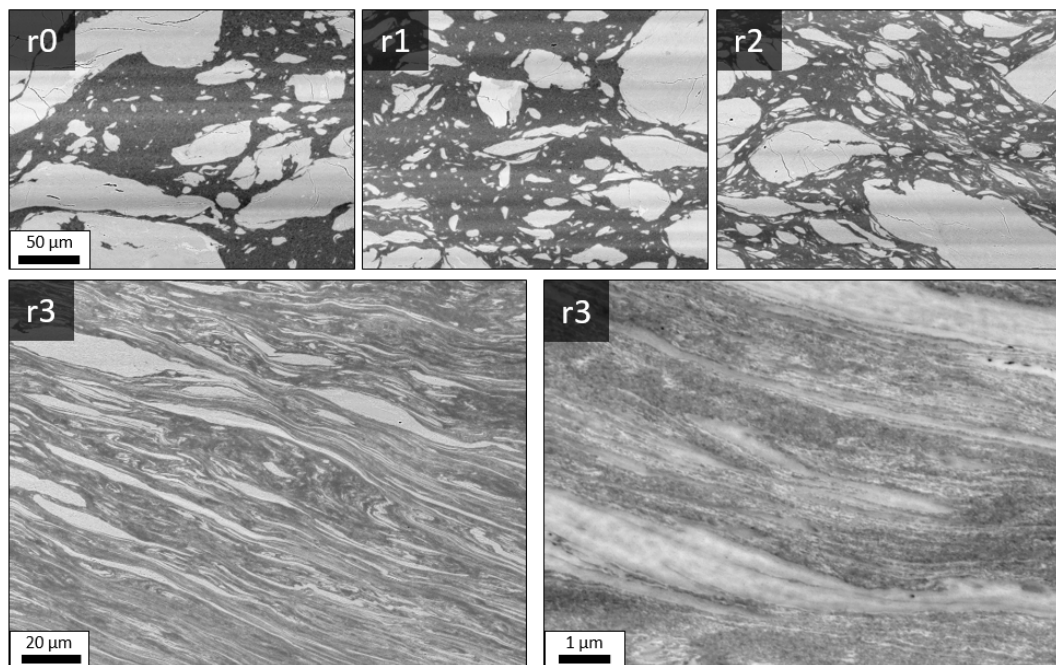
Figure C.13.: BSE images of a HPT-deformed sample (Nr. 6) at 400 °C consisting of 47 wt.% Fe–53 wt.% SmCo$_5$ at different radii. The scale bar in r0 also applies to r1 and r2. Images of two magnifications are presented for r3.

$\mathcal{D}$

Manufacturing of Textured Bulk Fe-SmCo$_5$ Magnets by Severe Plastic Deformation

Lukas Weissitsch[a], Martin Stückler[a], Stefan Wurster[a], Juraj Todt[b], Peter Knoll[c], Heinz Krenn[c], Reinhard Pippan[a] and Andrea Bachmaier[a]

[a] _Erich Schmid Institute of Materials Science, Austrian Academy of Sciences, Jahnstraße 12, 8700 Leoben, Austria_
[b] _Department of Material Physics, Montanuniversität Leoben, 8700 Leoben, Austria;_
[c] _Institute of Physics, University of Graz, Universitätsplatz 5, 8010 Graz, Austria_

Abstract

Exchange-coupling between soft- and hard-magnetic phases plays an important role in the engineering of novel magnetic materials. To achieve exchange coupling, a two-phase microstructure is necessary. This interface effect is further enhanced if both phase dimensions are reduced to the nanometer scale. At the same time, it is challenging to obtain large sample dimensions. In this study, powder blends and ball-milled powder blends of Fe-SmCo$_5$ are consolidated and are deformed by high-pressure torsion (HPT), as this technique allows us to produce bulk magnetic materials of reasonable sizes. Additionally, the effect of severe deformation by ball-milling and severe plastic deformation by HPT on exchange coupling in Fe-SmCo$_5$ composites is investigated. Due to the applied shear deformation, it is possible to obtain a texture in both phases, resulting in an anisotropic magnetic behavior and an improved magnetic performance.

Keywords: high-pressure torsion; ball milling; nanostructured materials; exchange coupling; magnetic anisotropy
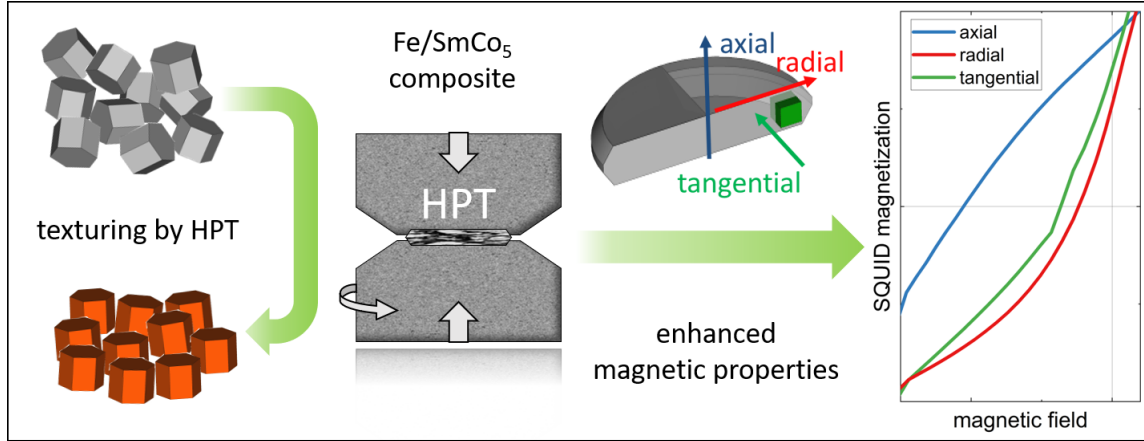
Figure D.0.: Graphical Abstract

D.1. Introduction

One parameter, which limits the performance of permanent magnets, is a sub-optimal remanent magnetization (M_r). This usually leads to a reduced energy product - BH_{max} - albeit only if a very high coercivity (H_c) is reached. An enhancement can generally be realized by three pathways. First, manufacturing a textured magnetic material, where the magnetically easy axis of many crystallites is aligned in one direction. Such textured magnets show a pronounced rectangular hysteresis loop when the measuring field is applied parallel to the easy axis and are referred to as anisotropic magnets [1]. Second, by combining a hard-magnetic with a soft-magnetic phase forming an exchange-spring magnetic material. If the soft-magnetic phase is finely dispersed within the hard phase, the high magnetization of the soft-magnetic material is stabilized by the large anisotropy field of the hard-magnetic material, as initially described by Kneller and Hawig [2]. Therefore, the magnetic polarization of the soft phase remains oriented with the enclosing hard phase resisting demagnetization, while it increases the magnetic moment of the entire material. Third, a refinement of the microstructure could lead to an increase in M_r. In addition, a unimodal grain size distribution increases the coercivity [3, 4].

Combining all three pathways and simultaneously manufacturing bulk-like magnets, which are indispensable for large-scale applications, is challenging [5]. Nanocrystalline

microstructures can be achieved, e.g., by ball-milling and the ball-milled powders can be aligned in external magnetic fields to obtain a texture [6, 7]. However, subsequent powder consolidation usually involves thermal treatments, which leads to grain growth and a coarsening of the microstructure [8].

In a previous study, we already demonstrated the feasibility of severe plastic deformation (SPD) using HPT-deformation of Fe and $SmCo_5$ powders to produce Fe-$SmCo_5$ exchange-coupled spring magnets with a broad range of chemical compositions [9]. Therein, special emphasis was devoted to the evolution of the microstructure during deformation and its correlation to magnetic properties. It was possible to reduce grain sizes and phase dimensions by HPT-deformation, while simultaneously being able to obtain bulk-sized magnets. A nanocrystalline, lamellar, dual phase structure with phase thicknesses below 1µm was presented for deformation at room temperature. Additionally, an increasing saturation magnetization (M_s) and H_c with an increasing deformation strain was observed. However, the maximum H_c already peaked at a relatively low amount of applied strain. A beneficial effect of plastic deformation on the magnetic performance is also reported for different material systems, which could peak at a certain amount of applied strain [10, 11].

Herein, we demonstrate the combination of all three approaches - texture, exchange-coupling, phase and grain refinement - to improve the performance of permanent magnets by SPD using HPT. The study is performed in direct comparison with ball-milled and consolidated Fe and $SmCo_5$ powders. Thus, the effect of HPT-deformation on the magnetic properties can be isolated. The ball-milled powders are then subsequently HPT-deformed, which allows a study of the effect of preceding ball-milling on the HPT-deformation and the resulting magnetic properties. Besides, the potential of HPT-deformation to induce texture is proven.

D.2. Materials and Methods

Powder blends with three chemical compositions (66, 43 and 26 wt.% Fe: MaTeck 99.9% -100 + 200 mesh and remaining $SmCo_5$: Alfa Aesar, intermetallic fine powder; in the following denoted with the suffix 1-3, respectively) are used for the experiments. Parts of the powder blends are milled in an air-cooled planetary ball mill (Retsch PM400) with an 1:15 powder-to-ball ratio of 400 rpm between 1-3 h. To prevent heat development inside the jar, an alternating 5 minutes' interval of mill-time and cooling-

time was programmed. Powder handling, ball-milling and the consolidation process are carried out in an Ar-atmosphere. All powder blends (un-milled and ball-milled) are hydrostatically consolidated using an HPT device. Parts of the consolidated pellets are subsequently HPT-deformed by applying 7.5 GPa at room temperature. Thus, three different types of samples are obtained: ball-milled powder samples (denoted as 'BM' in the following), ball-milled and HPT deformed powder samples ('BM + HPT') and un-milled but HPT-deformed powder samples ('HPT'). Based on our previous work [9], we limited HPT-deformation for this study to a maximum number of 3 rotations, which corresponds to a shear strain $\gamma = 56$ at a radius of 3 mm. HPT disc sizes are 8 mm in diameter and about 0.6 mm in thickness, whereas samples for magnetic measurements were cut out with a wire saw. In Figure D.1, the positions of measurements and measurement directions in relation to HPT-deformation directions are given.

Demagnetizing curves (1$^{\text{st}}$ half of complete hysteresis curve) between ± 70 kOe at 300 K, starting from $H_{\text{max}} = +70$ kOe, are recorded with a SQUID-Magnetometer (Quantum Design MPMSXL-7, Quantum Design, Inc., San Diego, CA, USA) using the manufacturer's software MPMSMultiVu Application (version 1.54). The magnetic field was applied in different HPT-disc directions as depicted in Figure D.1.

To investigate the microstructure after HPT-deformation, scanning electron microscopy (SEM; LEO 1525, Carl Zeiss Microscopy GmbH, Oberkochen, Germany) in backscattered electron detection mode (BSE) is performed on the HPT-deformed samples. For texture analysis, electron backscatter diffraction (EBSD) measurements are performed with a Bruker e-Flash$^{\text{FS}}$ detector on an HPT-deformed Fe sample.

Commercially available and ball-milled powder blends were characterized using conventional X-ray diffraction (XRD, D2 Phaser Bruker Corporation, Billerica, MA, USA) with Co-K$_\alpha$ radiation after different milling times. The theoretical reference peaks were found in the Crystallography Open Database (SmCo₅: COD 1524132, Fe: COD 9006587) [12].

Synchrotron X-ray diffraction (HEXRD) measurements in transmission mode (Petra III: P07B, DESY, Hamburg, Germany) were carried out to analyze the texture selected nanocomposite samples (with highest SmCo₅ content) as a function of the radius. The beam energy used was 87.1 keV and the shutter size 0.1×0.1 mm^2, while using a Perkin Elmer XRD 1621 detector. The obtained data were calibrated with a diffraction pattern of LaB₆ powder (LaB₆: COD 1000057) and further processed
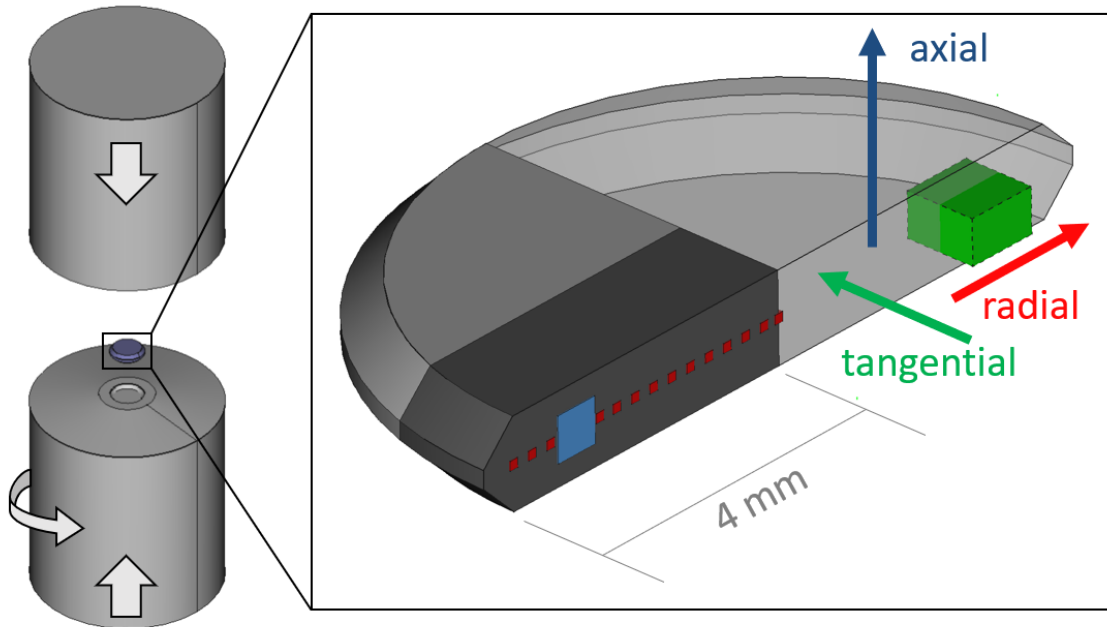
Figure D.1.: Schematic representation of the HPT-setup consisting of two anvils and the sample whereat a halved HPT-disc is shown in more detail. The position and size of a SQUID specimen is highlighted in green. Respective HPT-deformation directions are shown as coloured arrows. SEM measurements are conducted in a tangential direction at a radius ≈ 3 mm as highlighted in blue. Radially resolved HEXRD texture analysis is performed on a specimen (dark grey) in a tangential direction (red areas) in transmission mode.

with DigitalMicrograph using the PASAD package (PASAD-tools.v0.1) [13] and an in-house-developed Matlab$^{\text{TM}}$ code. The codes' output gives an integrated intensity as a function of the angle corresponding to the Debye diffraction cone for every chosen diffraction peak. For pole figure analysis and orientation density function (ODF) estimations, the Matlab$^{\text{TM}}$ toolbox MTEX (version 5.7.0) was used [14]. Therein, the selected and processed Debye ring was used to extrapolate an ODF estimation, allowing us to recalculate a pole figure. Due to the high crystal symmetry of the investigated phases, a full ODF by spherical tomography is not necessary to claim on a certain present texture [15]. However, large areas on the pole figure representations are extrapolated and likely contain errors. This is why a transparent mask is used to overlay the pole figure representations in this work, indicating a focus on the information obtained from uncovered areas.

D.3. Results and Discussion

D.3.1. Sample Processing and Magnetic Properties

XRD measurements of commercially available and ball-milled powder blends, containing 34, 57 and 74 wt.% $SmCo_5$ and remaining Fe, are presented in Figure D.2a-c, respectively. In the initial state (bottom pattern), Fe and $SmCo_5$ peaks are visible for all compositions. To monitor the ball-milling process, parts of the powder blends are removed in steps of 30 min and are measured by XRD. With the increasing milling time, a significant peak broadening is observed for both phases. The broadening of the $SmCo_5$ peaks takes place already at an earlier stage of ball-milling and therefore the peaks tend to vanish for longer milling times and for powder blends with lower $SmCo_5$ contents. Hence, a partly amorphous phase cannot be excluded. The powder blend with the highest $SmCo_5$ content (Figure D.2c) tends to agglomerate and due to the similarity of the 30 min and 60 min XRD pattern, no further energy input into the powder blend by prolonged ball milling is expected.

In the literature, an intermixing of elements, especially the formation of α-Fe(Co) and interstitial SmCo(Fe) phases, are reported [16–19]. Although the formation of other phases seems to originate in the severe deformation process, an additionally temperature process is present in all reports. In this study, a temperature treatment of the powders as well as during the HPT-processing is completely evaded. However, we do not exclude the formation or diffusion of Fe or Co on an atomic scale, but in all recorded XRD patterns, no additional peaks are found. Thus, neither decomposition of $SmCo_5$ nor a significant formation of an FeCo phase during milling is observed.

In Figure D.3, the demagnetizing curves of the samples with the highest $SmCo_5$ content are exemplarily shown for the un-milled powder blend and all processing routes. The processing history has a strong influence on the demagnetization curve. Ball-milling barely increases H_c, but leads to an increased M_s. HPT-deformation of the BM powder decreases the susceptibility, while M_r remains constant but M_s and H_c increases. Besides a slightly smaller M_s, this behavior is even more strongly pronounced for the 'HPT' sample.

The magnetic properties of all processed samples are summarized in Table 1. H_c is determined by a linear fit of data points close to zero crossing. An increase of M_r and H_c with increasing $SmCo_5$-content is found for all samples. For all compositions,
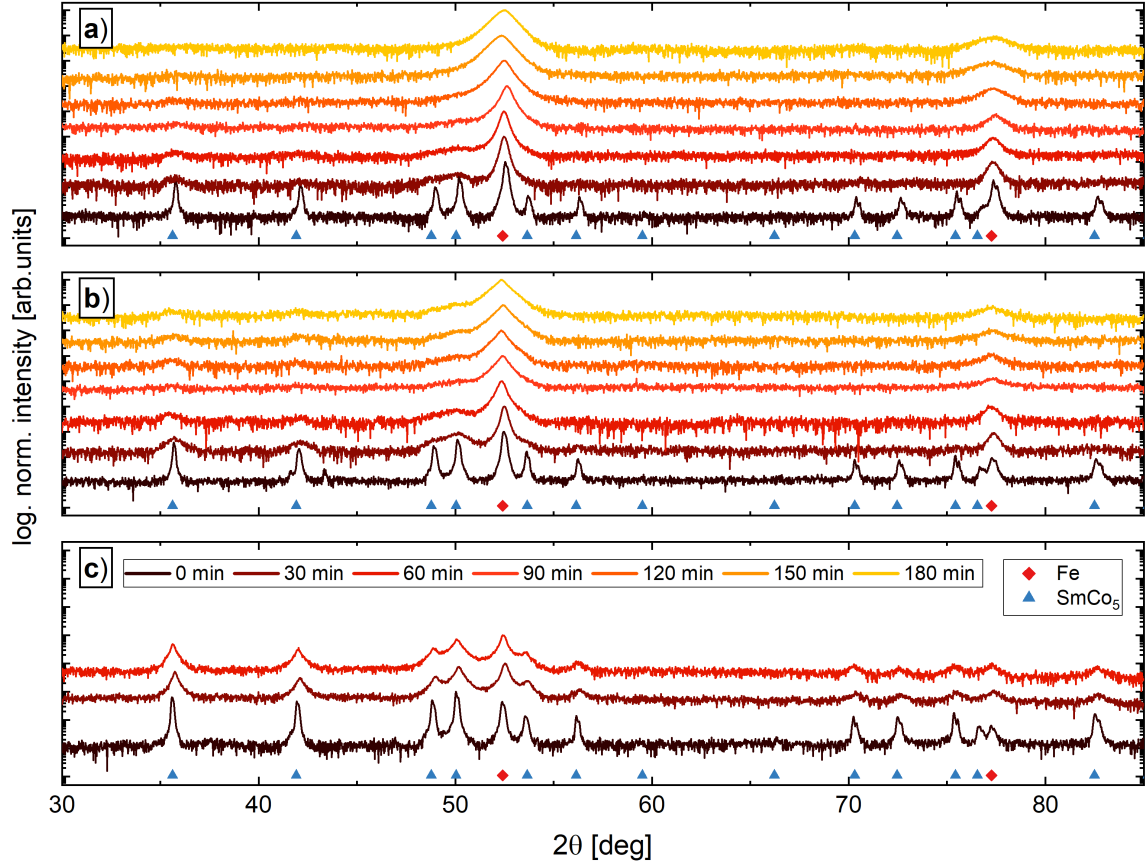
Figure D.2.: XRD measurements as a function of milling time for powders consisting of 66 wt.% Fe-34 wt.% SmCo$_5$ (a), 43 wt.% Fe-57 wt.% SmCo$_5$ (b) and 26 wt.% Fe-74 wt.% SmCo$_5$ (c). The theoretical reference peaks are found in the Crystallography Open Database (SmCo$_5$: COD 1524132, Fe: COD 9006587).

both magnetic parameters are highest for HPT-deformed samples without previous ball-milling.

The approach to the presented M$_s$ value is obtained by a linear fit for 1/H at fields above 35 kOe, determining the intersection with the ordinate. Samples containing a higher amount of Fe show a higher M$_s$. Expected M$_s$ values for single phase SmCo$_5$ are 112 emug^{-1} [20] and 218 emug^{-1} for bulk Fe [21]. Applying a superposition based on the samples' chemical composition depicted in Table 1, a calculated M$_s$ reveals 180, 158 and 138 emug^{-1} for composition 1, 2 and 3, respectively. M$_s$ values for HPT-deformed samples lay constantly beneath these theoretical values.

Due to the domain-wall pinning mechanisms and/or a present texture, one could argue that even 70 kOe are not sufficient enough to completely saturate the material [22, 23]. For the ball-milled and HPT-deformed samples, on the other hand, the M$_s$
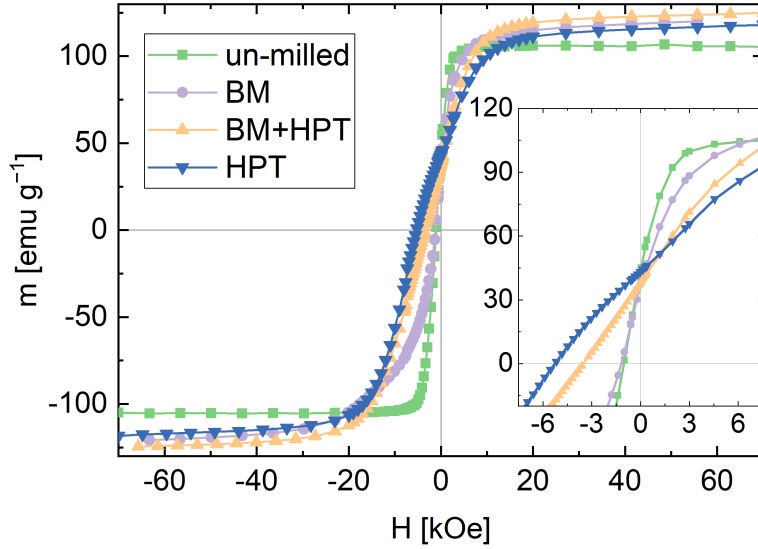
Figure D.3.: Demagnetizing curves starting from +70 kOe for the un-milled powder blend, ball-milled powder sample (BM), ball-milled and HPT-deformed powder sample (BM + HPT) and un-milled and HPT-deformed powder sample (HPT), exemplified for samples with the highest SmCo₅-content. The inset shows the demagnetizing branches in more detail.

values are partly above the theoretical value. This is most likely due to processing steps itself, i.e., ball-milling, where abrasions of the hardened steel jar and balls, but also powder-handling could enrich the Fe content of the powders. However, the powder blends containing the highest amount of SmCo₅ could only be milled for 1 h and the increase in M_s is more strongly pronounced for powders with a lower SmCo₅ content which have been milled for a longer time (3 h). Thus, the assumption of Fe enrichment within the ball-milling and powder-handling process is further supported.

To enable exchange coupling, the magnetic materials should exhibit a two-phase microstructure with alternating hard- and soft-magnetic phases. A simple consideration, valid for a perfect model system, implemented by a length within a complete exchange coupling, is expected. This critical length for the soft magnetic phase is approximately defined by twice the Bloch-wall width $\delta_w = \pi \sqrt{\frac{A^{\mathrm{hard}}}{K^{\mathrm{hard}}}}$ of the hard phase, as its magnetic stray field only reaches a certain distance and hinders the soft phase to change its orientation upon an opposed magnetic field. Here, A^{hard} and K^{hard} are the exchange and anisotropy constant of the hard-magnetic phase [24, 25]. With A^{hard} = $1.2 \cdot 10^{-11}$ Jm^{-1} and K^{hard} = $17.2 \cdot 10^6$ Jm^{-3} [26, 27] for SmCo₅, an optimum soft phase thickness of ≈ 5.3 nm is obtained. Another approximation for the soft phase thickness is based on the idea of how easy the spins of that material align with the hard phase. The exchange length $l_{\mathrm{ex}}^{\mathrm{soft}} = \sqrt{\frac{A^{\mathrm{soft}}}{K^{\mathrm{soft}}}}$ depends on A^{soft} and K^{soft},

Table D.1.: Magnetic properties measured by SQUID magnetometry. Ball-milled and powder samples are denoted as 'BM', ball-milled and HPT deformed powder samples as 'BM + HPT' and un-milled and HPT deformed powder samples as 'HPT'. The prefix 'rad' and 'tang' denotes measurements with the magnetic field applied parallel to the radial or tangential HPT-disc direction, respectively. For all other listed HPT-deformed samples without any prefix, the field is applied parallel to the axial HPT-disc direction. The suffix 1–3 corresponds to the chemical composition. H_c depicts the coercivity measured in Oe, M_s is the saturation magnetization determined as described in the text and M_r denotes the remanence, both given in the specific mass moment emu g^{-1}.

Sample	Fe/(wt.%)	$SmCo_5$/(wt.%)	H_c/(Oe)	M_s/(emu g^{-1})	M_r/(emu g^{-1})
un-milled3	26	74	-1033	106	43,2
BM3	26	74	-1184	125	36,4
BM+HPT1	66	34	-274	196	5,4
BM+HPT2	43	57	-686	172	10,2
BM+HPT3	26	74	-3526	128	38,0
rad BM+HPT3	26	74	-1472	128	28,9
tang BM+HPT3	26	74	-1434	129	36,5
HPT1	66	34	-887	172	14,1
HPT2	43	57	-2366	150	30,8
HPT3	26	74	-5264	122	43,2
rad HPT3	26	74	-1192	120	26,3
tang HPT3	26	74	-1903	120	35,3

expressing the same constants but for the soft-magnetic phase. For α-Fe: $A^{soft} = 2.5 \times 10^{-11}$ Jm^{-1} and $K^{soft} = 4.6 \times 10^4$ Jm^{-3}, $l_{ex} \approx 23$ nm is obtained [2, 24]. Although this soft phase thickness differs by a factor of ≈ 4, both values give an idea for the optimum dimensions of the Fe phase.

To investigate the microstructure after HPT-deformation, scanning electron microscopy in backscattered electron detection mode (BSE) is performed on the HPT-deformed samples (Figure D.4). Using a BSE contrast, Fe or Fe-rich areas exhibit a dark contrast and $SmCo_5$ or $SmCo_5$-rich areas a bright contrast, respectively. Although the same chemical composition is present, the microstructure of the samples with the lowest $SmCo_5$ content after HPT-deformation differs significantly. Ball-milling has a clear influence on the dispersion of the phases, as contrast differences in Figure D.4a are hardly visible, while a more heterogeneous microstructure is depicted in Figure D.4d for the HPT sample. For both samples, however, a lamellar microstructure, well suited for exchange coupling, is missing. With the increasing $SmCo_5$ content, a similar morphology is obtained for the BM + HPT2 sample (Figure D.4b). Although,

the larger $SmCo_5$ phases are visible as well. In the case of the 'HPT'-sample, a lamellar morphology is obtained (Figure D.4e). A similar lamellar microstructure is found for the samples with the highest $SmCo_5$ content (Figure D.4c,f). For these samples, different thicknesses of the phases are present, and all are well below 1μm. For exchange coupling, theoretical considerations prefer the soft-magnetic phase embedded in a hard-magnetic matrix [24, 28]. Based on XRD and SEM investigations, the HPT-samples (Figure D.4e,f) containing 57 and 74 wt.% $SmCo_5$ and the BM + HPT-samples with 74 wt% $SmCo_5$ (Figure D.4c) are most promising for a high exchange coupling effect, which is confirmed by the magnetic measurements (cf. Table 1). However, a completely exchanged coupled material is not expected due to the large number of different sized lamellae.

In general, no beneficial influence of initial ball-milling on the microstructural evolution (e.g., homogeneity of deformation to achieve lamellar microstructure for all compositions, prevention of shear band formation, further phase refinement) during HPT-deformation is observed, with consequences for resulting magnetic properties. In fact, a partly amorphous $SmCo_5$ phase resulting from initial ball-milling, which would reduce H_c, cannot be excluded.
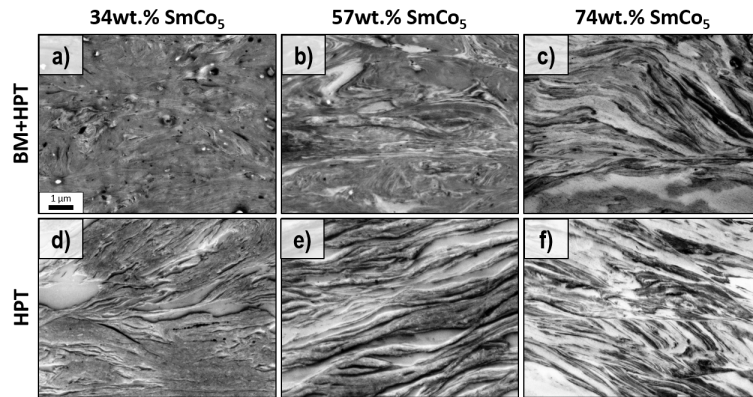
Figure D.4.: BSE images of ball-milled and HPT-deformed powder samples (**a-c**) and unmilled and HPT deformed powder samples (**d-f**) in tangential direction with 34 (**a,d**), 57 (**b,e**) and 74 wt.% $SmCo_5$ (**c,f**). The scale bar in (**a**) also applies to all other images.

HPT-deformed samples with the highest amount of $SmCo_5$ show the best hard magnetic properties. Thus, magnetic properties of these HPT-deformed samples are measured in other HPT-disc directions as well. In Figure D.5, the demagnetization curves in axial (blue), radial (red) and tangential (green) HPT-disc directions are shown for the BM + HPT3 (Figure D.5a) and the HPT3 sample (Figure D.5). By applying the magnetic measurement field parallel to the radial and tangential

directions drastically reduces H_c for both samples. M_r, however, is nearly unchanged. Additionally, the shape of the demagnetizing curves for the radial and tangential HPT-disc directions is different compared to the axial direction and the curves also exhibit an increased susceptibility. Although the characteristics of the radial and tangential curves are relatively similar, the tangential curve saturates faster and resists against demagnetization a little bit longer. Furthermore, the BM + HPT3 sample shows a linear m(H) behavior in the second quadrant, while the HPT sample reveals a convex bent shape. The magnetic properties obtained from these measurements are again summarized in Table 1.
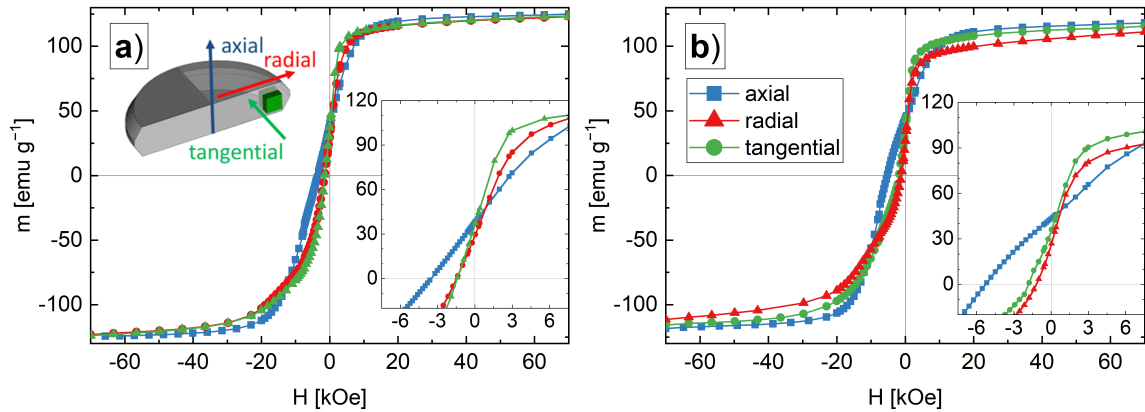
Figure D.5.: Demagnetizing curves starting from +70 kOe for the ball-milled and HPT-deformed powder (BM + HPT3) samples (**a**) and un-milled and HPT-deformed powder (HPT3) samples (**b**). The schematic illustration in (**a**) visualizes the measurement directions in respect of the different HPT-disc directions (axial: blue; radial: red; tangential: green). The insets show the demagnetizing branches in more detail.

For textured hard magnets, the coercivity strongly changes, if the measurement field is applied parallel or perpendicular to the easy axis of the crystals due to its large magnetocrystalline anisotropy [1, 29–31]. The higher susceptibility is caused by the uncoupled volume of the Fe phase, as the magnetic moment originating from $SmCo_5$ in the magnetically hard direction (basal plane) would saturate much slower. The magnetocrystalline anisotropy of Fe is much lower compared with $SmCo_5$, but again, the difference between tangential and radial demagnetization curve can be explained with a textured microstructure. The crystallographic (100) direction is the Fe easy axis, which should be aligned in the tangential HPT-disc direction, whereas the radial direction should correspond to the crystallographic (110) semi-hard direction [29].

D.3.2. X-ray Texture Analysis

Synchrotron X-ray diffraction (HEXRD) measurements are carried out to analyze the texture of the as-deformed BM + HPT3 and HPT3 samples (with highest SmCo$_5$ content) as a function of the radius. The recorded diffraction rings clearly show a variation of intensities, which indicates the existence of a preferred microstructural crystallite orientation [15]. For an appropriate comparison and based on the diffraction rings, pole figure representations are created. To verify our results obtained by synchrotron measurements, EBSD measurements are conducted on an HPT-deformed single-phase Fe sample. In Figure D.6a, the EBSD-recorded {110} and {100} pole figures for pure Fe are shown. In Figure D.6b–d, the HEXRD Fe {110} and {100} and SmCo$_5$ {$\bar{2}11\bar{1}$} and {$\bar{2}110$} pole figures are presented. The Fe pole figures show the typical simple shear texture for both the EBSD and the synchrotron data-sets, which allows us to extend the pole figure analysis to the SmCo$_5$ phase.
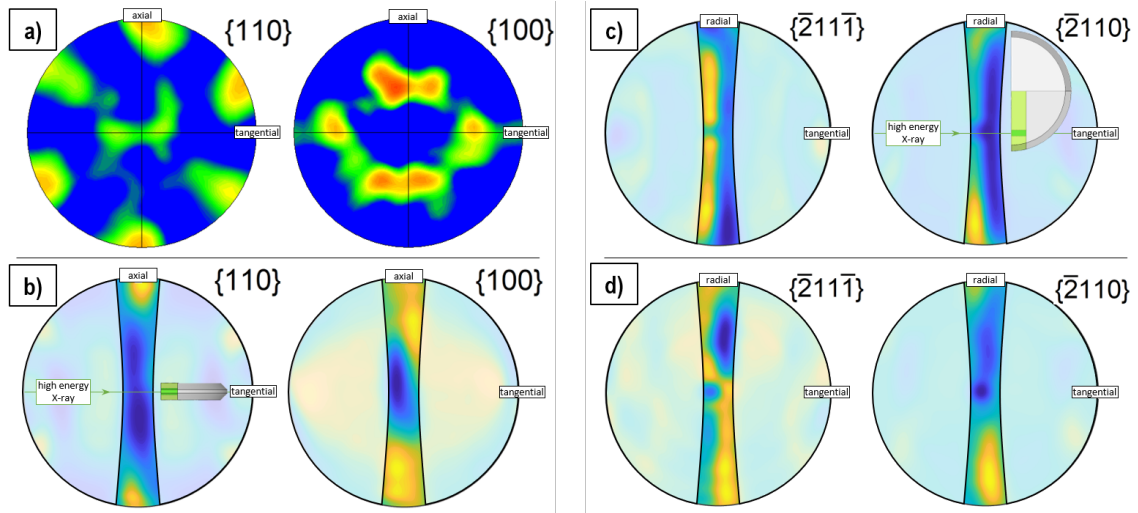
Figure D.6.: EBSD pole figure of Fe based on EBSD measurements (**a**). Pole figure representations of Fe reconstructed based on a HEXRD measurement of the HPT-deformed composite HPT3 (**b**) and a representation of the same sample and diffraction pattern for two SmCo$_5$ planes (**c**). Pole figure representation for the BM + HPT3 sample and the same SmCo$_5$ planes (**d**). An inset in the image (**b**) for the Fe phase and in (**c**) for the SmCo$_5$ phase visualizes the relative position of the HPT disc with respect to the incident X-ray beam and shown pole figures. The position of the HEXRD measurement within the sample is highlighted. The pole figure representations are partly covered with a transparent mask to lay the focus on the information obtained from less extrapolated areas.

The {$\bar{2}110$} planes are oriented parallel to the c-axis with their surface normal in the basal plane of the SmCo$_5$ crystal. The corresponding pole figure shows a minimum

in axial HPT-disc direction but a pronounced intensity is visible in radial direction, meaning that the crystal-plane normal preferably pointing in this direction. The $\{\bar{2}11\bar{1}\}$ and $\{\bar{2}110\}$ planes comprise an angle of 39°. For the $\{\bar{2}11\bar{1}\}$ pole figures, this results in an intensity maxima pointing to angles closer to the axial HPT-disc direction. Thus, the hexagonal crystals of the $SmCo_5$ phase tend to align their c-axis parallel to the axial HPT-disc direction with the basal plane parallel to the shear plane, spanned by radial and tangential directions. This behavior is similar for the BM + HPT3 and HPT3 samples, but is strongly pronounced for the latter one and generally for larger applied shear strain (larger radius of HPT-disc). For the hard magnetic $SmCo_5$ phase, a clear correlation of texture with resulting magnetic properties is found. Regarding the soft magnetic Fe phase, the magnetically easy axis directions {100} partly orient in a tangential HPT-disc direction, leading to a stiffer hysteresis loop (cf. Figure D.5).

D.4. Conclusions

In summary, HPT deformation offers an easy way to produce exchange-coupled bulk Fe-$SmCo_5$ magnets from commercially available powder blends without any thermal treatments or complicated processing steps. Although ball-milling enhances H_c, no beneficial effect for subsequent HPT-deformation is observed compared to un-milled powders. After deformation, the formation of a heterogeneous microstructure with a lamellar morphology and enhanced coercivity is observed. The magnetic anisotropic characteristic of the Fe-$SmCo_5$ magnets is correlated to a crystallographic texture in both the Fe and the $SmCo_5$ phase. The $SmCo_5$ crystals tend to orient their c-axes parallel to the axial HPT-disc direction with their basal plane in the shear plane. The Fe phase aligns its magnetic easy axis in the tangential HPT-disc direction.

(Grant No. 757333).

Acknowledgments

D.5. References

[1] D Hu et al. Structure and magnetic properties of bulk anisotropic SmCo5/α-Fe nanocomposite permanent magnets prepared via a bottom up approach, *Journal of alloys and compounds* **538** (2012), pp. 173–176.
DOI: 10.1016/j.jallcom.2012.05.079.

[2] Eckart F Kneller and Reinhard Hawig. The exchange-spring magnet: a new material principle for permanent magnets, *IEEE Transactions on Magnetics* **27**, no. 4 (1991), pp. 3588–3560.
DOI: 10.1109/20.102931.

[3] R Fischer et al. Grain-size dependence of remanence and coercive field of isotropic nanocrystalline composite permanent magnets, *Journal of magnetism and magnetic materials* **153**, no. 1-2 (1996), pp. 35–49.
DOI: 10.1016/0304-8853(95)00494-7.

[4] He Shu-Li et al. Effects of grain size distribution on remanence and coercivity of Pr2Fe14B nanocrystalline magnet, *Chinese Physics* **14**, no. 5 (2005), p. 1055.
DOI: 10.1088/1009-1963/14/5/036.

[5] Ming Yue, Xiangyi Zhang, and J Ping Liu. Fabrication of bulk nanostructured permanent magnets with high energy density: challenges and approaches, *Nanoscale* **9**, no. 11 (2017), pp. 3674–3697.

[6] Chuan-bing Rong, Van Vuong Nguyen, and J Ping Liu. Anisotropic nanostructured magnets by magnetic-field-assisted processing, *Journal of Applied Physics* **107**, no. 9 (2010).

[7]   BZ Cui et al. Anisotropic SmCo5 nanoflakes by surfactant-assisted high energy ball milling, *Journal of Applied Physics* **107**, no. 9 (2010).

[8]   Chuanbing Rong et al. Fabrication of bulk nanocomposite magnets via severe plastic deformation and warm compaction, *Applied Physics Letters* **96**, no. 10 (2010).

[9]   Lukas Weissitsch et al. Strain Induced Anisotropic Magnetic Behaviour and Exchange Coupling Effect in Fe-SmCo$_5$ Permanent Magnets Generated by High Pressure Torsion, *Crystals* **10**, no. 11 (2020), p. 1026.
        DOI: 10.3390/cryst10111026.

[10]   Hailing Li et al. Tuning the microstructure and magnetic properties of bulk nanocomposite magnets with large strain deformation, *Journal of Magnetism and Magnetic Materials* **425** (2017), pp. 84–89.

[11]   IV Shchetinin et al. Structure and magnetic properties of Sm2Fe17Nx alloys after severe plastic deformation by high pressure torsion, *Materials Letters* **274** (2020), p. 127993.

[12]   Saulius Gražulis et al. Crystallography Open Database (COD): an open-access collection of crystal structures and platform for world-wide collaboration, *Nucleic Acids Research* **40**, no. D1 (2012), pp. D420–D427.
        DOI: 10.1093/nar/gkr900.

[13]   C Gammer et al. Quantitative local profile analysis of nanomaterials by electron diffraction, *Scripta materialia* **63**, no. 3 (2010), pp. 312–315.
        DOI: 10.1016/j.scriptamat.2010.04.019.

[14]   F. Bachmann, R. Hielscher, and H. Schaeben. Texture Analysis with MTEX–Free and Open Source Software Toolbox, *Solid State Phenomena* **160** (2010), pp. 63–68.
        DOI: 10.4028/www.scientific.net/SSP.160.63.

[15]   H-R Wenk and S Grigull. Synchrotron texture analysis with area detectors, *Journal of applied crystallography* **36**, no. 4 (2003), pp. 1040–1049.
        DOI: 10.1107/S0021889803010136.

[16]   JM Le Breton et al. A structural investigation of SmCo5/Fe nanostructured alloys obtained by high-energy ball milling and subsequent annealing, *Journal of Physics D: Applied Physics* **43**, no. 8 (2010), p. 085001.

[17]   Viorel Pop et al. Structural and magnetic behaviour of SmCo5/α-Fe nanocomposites obtained by mechanical milling and subsequent annealing, *Rom. J. Phys* **55**, no. 1-2 (2010), pp. 127–136.

[18]   Y Shen et al. Effect of milling time on magnetic properties and structures of bulk Sm-Co/α-(Fe, Co) nanocomposite magnets, *Journal of Applied Physics* **111**, no. 7 (2012).

[19]   Xiang-Yuan Xiong et al. Atom probe study on the bulk nanocomposite SmCo/Fe permanent magnet produced by ball-milling and warm compaction, *Journal of magnetism and magnetic materials* **323**, no. 22 (2011), pp. 2855–2858.

[20]   S Foner et al. Magnetic Properties of Cobalt-Samarium with a 24-MG Oe Energy Product, *Applied Physics Letters* **20**, no. 11 (1972), pp. 447–449.

[21] Masane Kin et al. Improvement of saturation magnetization of Fe nanoparticles by post-annealing in a hydrogen gas atmosphere, *Journal of Applied Physics* **117**, no. 17 (2015), 17E714.
DOI: 10.1063/1.4919050.

[22] R Chau, MB Maple, and WJ Nellis. Shock compaction of SmCo5 particles, *Journal of applied physics* **79**, no. 12 (1996), pp. 9236–9244.

[23] Jian Zhang et al. Structure, magnetic properties, and coercivity mechanism of nanocomposite SmCo 5/α-Fe magnets prepared by mechanical milling, *Journal of Applied Physics* **89**, no. 10 (2001), pp. 5601–5605.

[24] Ralph Skomski et al. Predicting the future of permanent-magnet materials, *IEEE Transactions on Magnetics* **49**, no. 7 (2013), pp. 3215–3220.
DOI: 10.1109/TMAG.2013.2248139.

[25] Stephen Blundell. *Magnetism in condensed matter*. Oxford master series in condensed matter physics. Oxford ; New York: Oxford University Press, 2001.

[26] J. M. D. Coey. *Magnetism and Magnetic Materials*. Cambridge University Press, 2010.

[27] A Ermolenko. Magnetocrystalline anisotropy of rare earth intermetallics, *IEEE Transactions on Magnetics* **12**, no. 6 (1976), pp. 992–996.

[28] JS Jiang and SD Bader. Rational design of the exchange-spring permanent magnet, *Journal of Physics: Condensed Matter* **26**, no. 6 (2014), p. 064214.

[29] Raymond Kwesi Nutor et al. Research Progress of Stress-Induced Magnetic Anisotropy in Fe-Based Amorphous and Nanocrystalline Alloys, *Journal of Electromagnetic Analysis and Applications* **09**, no. 04 (2017), pp. 53–72.
DOI: 10.4236/jemaa.2017.94006.

[30] Jingming Liang et al. Anisotropic SmCo 5 nanocrystalline magnet prepared by hot deformation with bulk amorphous precursors, *IEEE Transactions on Magnetics* **54**, no. 11 (2018), pp. 1–4.

[31] Ana M Schönhöbel et al. Nanocrystalline Sm-based 1: 12 magnets, *Acta Materialia* **200** (2020), pp. 652–658.

Magnetic Materials via High-Pressure Torsion of Powders

Lukas Weissitsch[a], Franziska Staab[b], Karsten Durst[b] and Andrea Bachmaier[a]

[a] _Erich Schmid Institute of Materials Science, Austrian Academy of Sciences, Jahnstraße 12, 8700 Leoben, Austria_

[b] _Physical Metallurgy (PhM), Materials Science Department, Technical University of Darmstadt, Alarich-Weiss-Str. 2, 64287 Darmstadt, Germany_

Abstract

Magnets are key materials for the electrification of mobility and also for the generation and transformation of electric energy. Research and development in recent decades lead to high performance magnets, which require a finely tuned microstructure to serve applications with ever increasing requirements. Besides optimizing already known materials and the search on novel material combinations, an increasing interest in unconventional processing techniques and the utilization of magnetic concepts is apparent. Severe plastic deformation (SPD), in particular by high-pressure torsion (HPT) is a versatile and suitable method to manufacture microstructures not attained so far, but entitling different magnetic coupling mechanisms fostering magnetic properties. In this work, we review recent achievements obtained by HPT on soft and hard magnetic materials, focusing on powder as starting materials. Furthermore, we give specific attention to the formation of magnetic composites and highlight the opportunities of powder starting materials for HPT to exploit magnetic interaction mechanisms.

Keywords: severe plastic deformation; high-pressure torsion; powder; magnetic materials; nanocomposite; magnetic and microstructure tuning; exchange mechanism
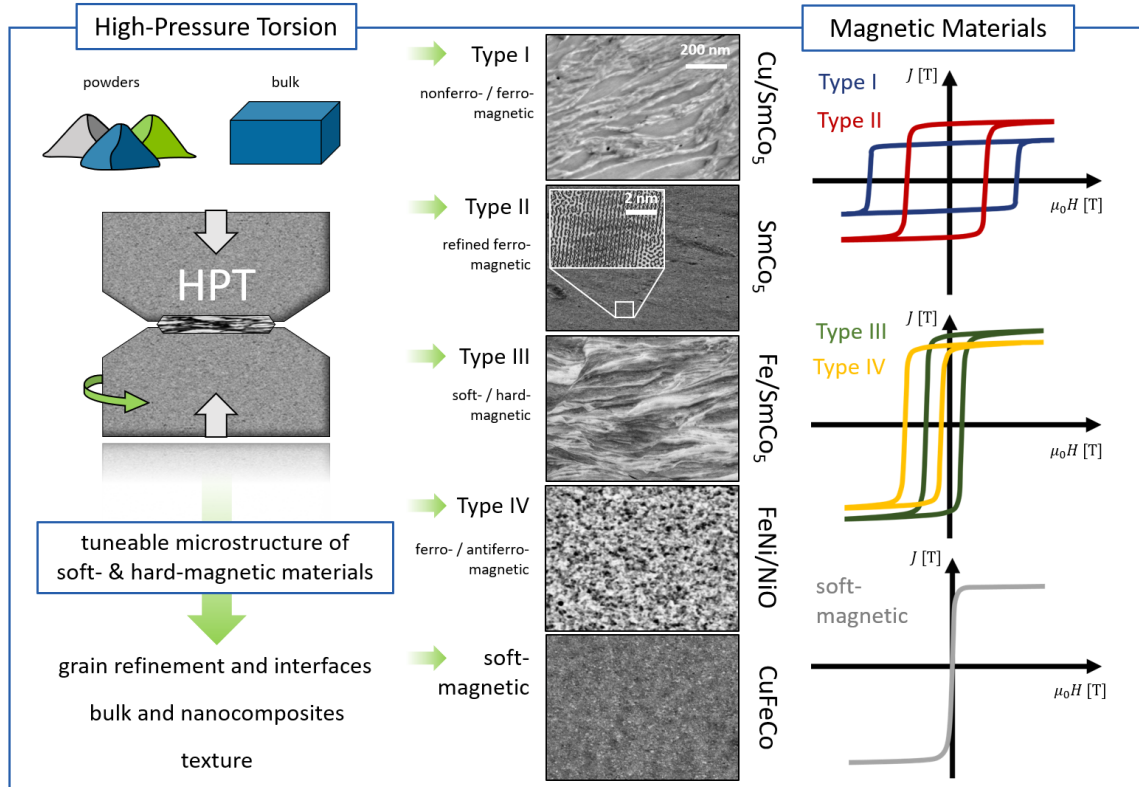
Figure E.0.: Graphical Abstract

E.1. Introduction

Severe plastic deformation (SPD) is a well-known and effective method to produce ultrafine grained or nanocrystalline (nc) materials. One classic SPD method is high-pressure torsion (HPT), a novel process for the production and treatment of magnetic materials promising particularly noticeable magnetic properties. The grain refinement during HPT processing is accompanied with the formation of various kinds of lattice defects and unique microstructural features, but also to the formation of a shear texture [1, 2]. HPT-deformation is widely used in processing many kinds of single-phase materials and also a variety of (nano-)composite structures can be obtained [3, 4]. Furthermore, the possibility for phase transformations [5–8] has been shown as well as the evolution of thermodynamically metastable phases such as supersaturated

solid solutions [3, 9] or amorphous structures, similar to rapid solidification processes [10]. This variety of HPT-induced microstructural evolutions is accompanied by a noteworthy manufacturing advantage. As initial materials for HPT processing, coarse-grained multi-phase alloys, powder blends of different elements or any other combination of solid starting materials can be used. The HPT process applied to powder blends represents a tool for possible mixing, consolidation and subsequent alloying obtaining a solid solution or nanocomposite material by the high amount of applied shear strain. Thus, additional processing steps (e.g., sintering) to achieve a bulk material are not necessary. The torsional shear straining under high hydrostatic pressures by HPT can prevent the formation and propagation of cracks, so that also brittle materials, such as most of the hard magnetic phases, can be plastically deformed up to large strains. This is specifically of importance for the consolidation, refinement and plastic deformation of powder mixtures, where large hydrostatic stresses are required to form bulk samples from powders [11]. The application of powders enables a free selection of the elements or rather phases, resulting in no limitations by phase diagrams regarding metallurgical processing routes, due to the limitation of phase formations from a melt. The process hence represents a tool for mechanical alloying, phase transformations and supersaturation, often accompanied with pronounced grain refinement, while still resulting in bulk materials. The free selection of the starting powders is especially interesting, since thermodynamically metastable chemical compositions but also composite structures are achievable.

Further benefits of the obtained bulk samples from HPT are their complete density and large sample sizes. Typical HPT discs exhibit diameters of 10–50 millimeters, with the possibility of an upscaling, while simultaneously microstructural length scales are strongly reduced [12]. For example, the manufacturing of conventional permanent magnets on an industrial scale is based on powder metallurgical processing, requiring elaborate powder fabrication followed by sintering and further heat treatments. An excellent summary on processing routes for the most important permanent magnet systems can be found in Ref. [13]. A corresponding review [14] is addressed to the industrial importance of magnetic composites, so called bonded magnets, as well as to novel manufacturing techniques. The HPT process applied to powder blends resulting in bulk materials can go beyond the limitations of conventional processing routes, since the hard magnetic phase and the grain boundary phase can be chosen freely.

HPT-deformation is traditionally used to tune and study advanced mechanical properties. In recent years, a growing interest in functional characteristics of HPT

materials is also apparent, since the microstructure strongly controls the magnetic properties of magnetic materials and can be further used to tune them. The performance of magnetic materials correlates with main advantages of HPT, i.e., grain refinement of single-phase materials, the possibility to form nanostructured composites or supersaturated solid solutions, while simultaneously texture formation through the deformation process is feasible [15, 16]. Thus, an increasing interest of material scientists in the field of magnetism is recognized together with new possibilities for the development of magnetic materials. For instance, deformation induced metastable phases with large defect densities can be used as precursors for further processing, i.e., annealing treatments with enhanced dynamics or phase formations.

This article focuses on magnetic materials processed by HPT. It is organized as follows: Section 2 gives a short overview on intrinsic and extrinsic magnetic properties of hard and soft magnetic materials, considering the influence of microstructure and exchange interactions on the magnetic properties. Section 3 gives a short overview on bulk magnetic materials prepared by HPT. Section 4 is dedicated to HPT processing of magnetic powder blends and includes our own recent research on different magnetic materials. The last section contains an outlook on further research and summarizes the open questions in this field.

For further information and a more detailed discussion on dynamic interplay between microstructure evolution and magnetic properties, the interested reader is referred to some excellent review articles [11, 13, 14, 17–21].

E.2. Magnetic Mechanisms and Microstructural Tuning

The theoretical upper limit for achievable magnetic properties is governed by a combination of the intrinsic magnetic properties: magnetocrystalline anisotropy, exchange interactions, saturation magnetization (M_s) and Curie-Temperature (T_C). The exchange interactions are parameterized by the exchange stiffness (A), whereas the magnetocrystalline anisotropy is parameterized by the anisotropy constant (K_1). As schematically shown in Fig. E.1, the intrinsic curve is determined by the saturation magnetization M_s and the anisotropy field H_a giving the reversal field for a defect free single-domain Stoner-Wohlfarth particle by coherent rotation [22, 23]. Using

$$H_\mathrm{a} = \frac{2K_1}{\mu_0 M_\mathrm{s}} \tag{E.1}$$

the anisotropy field (H_a) can be calculated [22]. If particles or grain sizes exceed the single domain particle size, domains are formed to minimize energy, in particular to reduce the stray field energy. However, the formation of a domain wall requires energy since the magnetic moments inside the domain wall do not align along their easy magnetization direction given by the magnetocrystalline anisotropy. Important characteristic length scales are the (Bloch) domain wall width $\delta_0 = \pi\sqrt{\frac{A}{K_1}}$ as well as the exchange length $L_{ex} = \sqrt{\frac{A}{K_1}}$ which are in the range of 2 to 5 nm for most ferromagnetic materials such as Fe, Ni, Co, $SmCo_5$, $Nd_2Fe_{14}B$ [22]. Real materials do not obey the intrinsic hysteresis curve for a defect free single-domain Stoner-Wohlfarth particle, because the magnetization reversal processes are controlled by the microstructure. For instance, grain sizes, grain boundaries, and any structural defects can act as nucleation sites for reversed domains but also hinder domain wall movement. Therefore, the measured hysteresis curve, called extrinsic curve, does not reach the upper limit, as depicted in Fig. E.1. Coercivity (H_c), M_s, remanent magnetization (M_r or B_r) and rectangularity of the second quadrant (often characterized by the maximum energy product $(BH)_{max}$), which are technically important parameters of permanent magnetic materials, are hence strongly affected by the microstructure.

The discrepancy between the anisotropy field H_a and the coercivity H_c, originating from defects and imperfections, is called Brown's Paradox and is given by $H_c \leq H_a$ [22]. The discrepancy and thus the real structural details of a magnet is usually described by the "Kronmüller factor" α_K, where H_c equals $\alpha_K H_a$ [24]. In fact, it is difficult to obtain a α_K larger than 0.3 [25]. Therefore, besides good intrinsic properties, given by the comprised phases, a proper modification of the microstructure is required to tune the shape of the measured hysteresis loops and hence the magnetic properties. Microstructural features include the degree of texture (alignment of crystallites or grains), as well as the size distribution of the phase and precipitates. Also other defects, like porosity or dislocations can influence the magnetization behavior [8].

Depending on the microstructure two different coercivity mechanisms are distinguished. In nearly defect free permanent magnets nucleation of reversed domains controls the coercivity (nucleation-type magnets), whereas pinning of domain wall movement controls the coercivity in magnets with high defect densities (pinning-type magnets) [27]. Pinning of domain walls can occur at various defects, which are often regions with a low anisotropy (small K_1) due to chemical disorder, such as precipitates, dislocations and grain boundaries. It is one major reason for the increase of H_c, often called as magnetic hardening, and most effective if the size of the pinning centers is
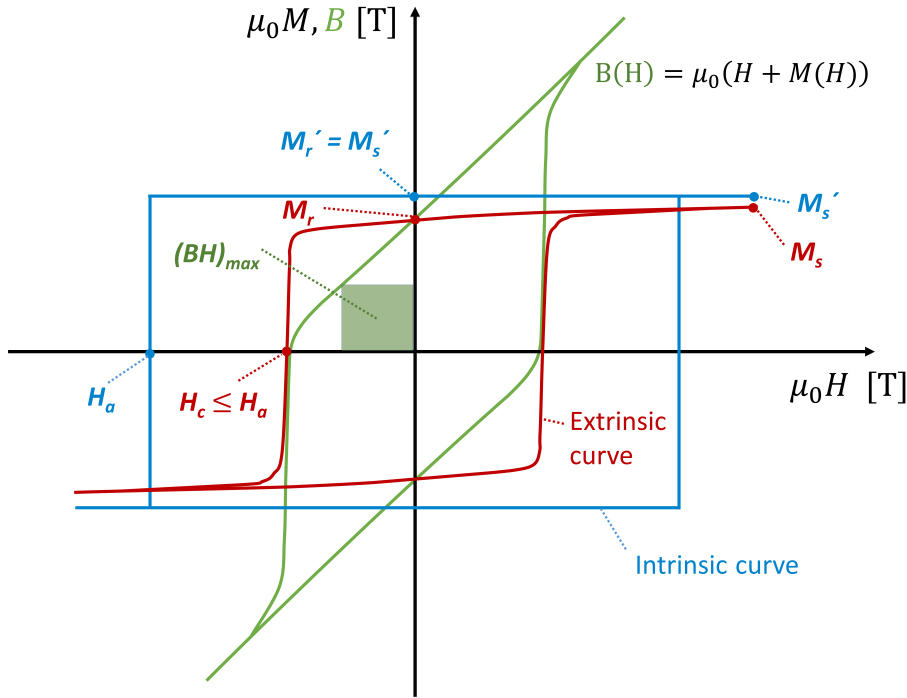
Figure E.1.: Schematic drawing of magnetic hysteresis: Magnetization $\mu_0 M$ or magnetic flux density B as a function of applied field $\mu_0 H$. The intrinsic properties of a material outline the theoretical upper limitation for magnetic materials (blue curve). Microstructural features decrease the upper limit of magnetic parameters (red curve) known as the Brown's Paradox. Experimentally measured signals are frequently obtained in cgs-units, requiring thus additional measurements of the sample (e.g. density), to transform the units into SI-units. An extensive summary to transform magnetic units is published by the NIST [26].

comparable to the domain wall width δ_0 [27]. Pinning of domain walls at dislocations is especially interesting for soft magnetic materials, due to their broad domain walls and the resulting increase of pinning strength [28, 29]. Thereby, $H_c \sim \sqrt{\rho_{VS}}$, with ρ_{VS} representing the density of dislocations [30]. The reason for impeding domain wall motion is based on magnetoelastic interactions between the elastic stress field of dislocations and magnetic domain walls, as well as on stress-induced anisotropy contributions [30–32]. Besides the coercivity, also the initial susceptibility and the magnetization behavior are affected by dislocations in soft magnetic materials. Hard magnetic materials exhibit narrow domain walls leading to small pinning strength [28, 29]. However, for the hard magnetic $SmCo_5$, Fidler et al.[33] reported a strong interaction between prismatic dislocation loops and domain walls.

Another microstructural feature which has a very crucial impact on the magnetic properties, especially the H_c, is the grain size. A more detailed description on the influence can be given when distinguishing soft and hard magnetic materials (Fig. E.2(a)). This categorization is typically done by coercivity and the values for the two classes are given in Fig. E.2(b) [21, 34].
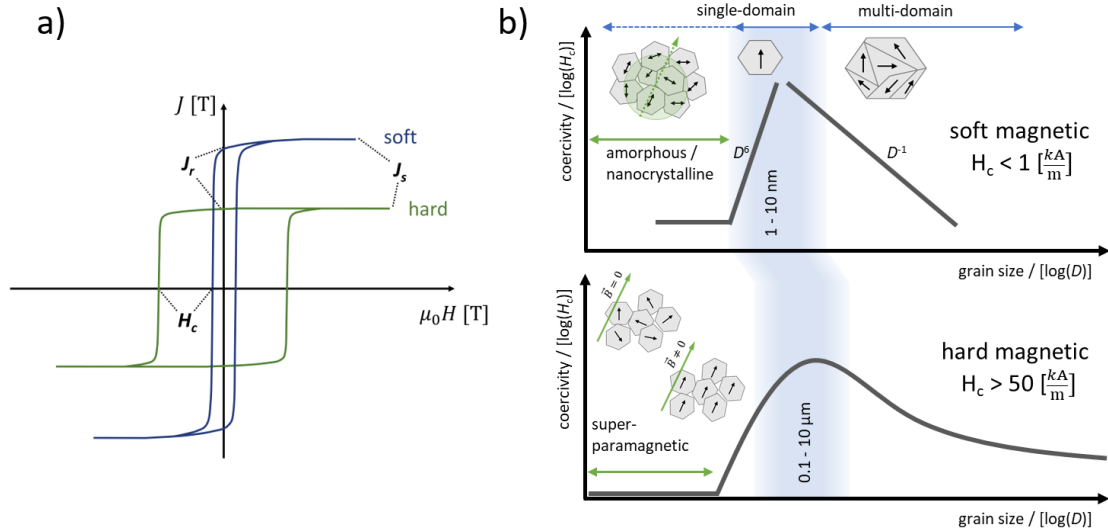
Figure E.2.: (a) Magnetic hysteresis curve of soft and hard magnetic materials with marked characteristic values. (b) Schematic representation of coercivity (H_c) as a function of the particle diameter (D) for soft (upper graph) and hard magnetic (lower graph) materials. Please consider the different scaling for H_c for soft and hard magnetic materials and the logarithmic application. Adapted from Refs. [21, 34–38]

The most prominent impact of grain sizes on coercivity is demonstrated by Herzer for soft magnetic materials (upper graph in Fig. E.2(b)). Therein, the H_c scales inversely with the grain size until it approaches a maximum in the range of the single domain sizes [35]. The single domain size is reached when the energy required for the formation of a domain wall within the grain, exceeds the particle's stray field energy, this region is herein roughly indicated by the shading in Fig. E.2(b). For even smaller grain sizes the coercivity strongly decreases by D^6. Essentially, when crystallites are further decreased in size and reach an amorphous state, soft magnetic properties are not necessarily enhanced and H_c is not vanishing. Instead the so-called random anisotropy model explains a remaining coercivity which is based on the exchange length L_{ex}, depicted as a green circle within Fig. E.2(b). If $L_{ex} \gg d$ is fulfilled, within this length scale, a statistical averaging of the anisotropic moments leads to the

formation of a non-vanishing H_c. Some commercial soft magnetic materials are also nanocomposites, in which a crystalline phase is embedded in an amorphous matrix and the model of Herzer has been successfully applied to describe their coercivity behavior. Most importantly, if there is a long-range order of the amorphous structure and at the same time a uniaxial anisotropy is present, the dependency on coercivity is changed from D^6 to D^3 [39].

For hard magnetic materials, the drawn characteristics in the lower part of Fig. E.2(b) shows a tendency of a maximum in coercivity close to the single domain size, without a defined power law dependency on the grain size. Most significantly, due to their higher magnetocrystalline anisotropy, the single domain size is increased. The coercivity dependence on grain size does not allow a strict proportionality as depicted in the upper part of Fig. E.2(b) since all possible microstructural features, but also the interplay of intrinsic and extrinsic properties or chemical variations contribute separately and in a different extent. A widely known model is the one by Ramesh et al. which expresses H_c as a function of $\ln(D)$ for grain sizes larger than 3 µm. The model suggests a higher nucleation probability of reversing domains for larger grain sizes [40, 41]. A conclusive model is still lacking, thus several explanations are present [42, 43]. Nevertheless, several observations, i.e., experimental data from Lee et al. [44] suggest a grain size dependency on H_c. A further decrease in grain size well below the single domain size, at which a maximal H_c is present, is again usually accompanied by a decreasing H_c, likely reaching a superparamagnetic state. Therein, magnetic moments directly align with the applied field, as they are completely separated and do not show any exchange interactions. As a result, the obtained hysteresis loop shows a vanishing H_c and consequently no B_r, but can reach a magnetic saturation at sufficiently high fields. Counterintuitively, for soft magnetic materials the random anisotropy model increases H_c compared to hard magnetic materials, in which the superparamagnetic state is present. However, the superparamagnetic state can also be reached in soft magnetic materials decreasing the coercivity e.g. when applying temperature.

For permanent magnets the maximum stored energy $(BH)_{\text{max}}$, which is defined as the maximum product of B and H in the second quadrant of the $B - H$-curve, is of critical interest and should be as high as possible. Therefore, a high H_c and a high degree of texture is necessary in order to reach maximum values for B_r and to increase $(BH)_{\text{max}}$. Depending on the microstructure two different coercivity mechanisms are distinguished as described above. For nucleation-type magnets, the coercivity reaches its maximum value at grain sizes at which only a single domain state is present. If

a particle consists of several domains and an external magnetic field is applied, a domain having a favorable orientation of magnetization will grow at the expense of a poorly aligned domain. If only one domain is present in a particle, the alignment along the external field will occur via rotation of the magnetization direction, which usually costs more energy compared to growing of favorable aligned domains due to the magnetocrystalline anisotropy. This is the reason for the maximum coercivity at single domain grain sizes.
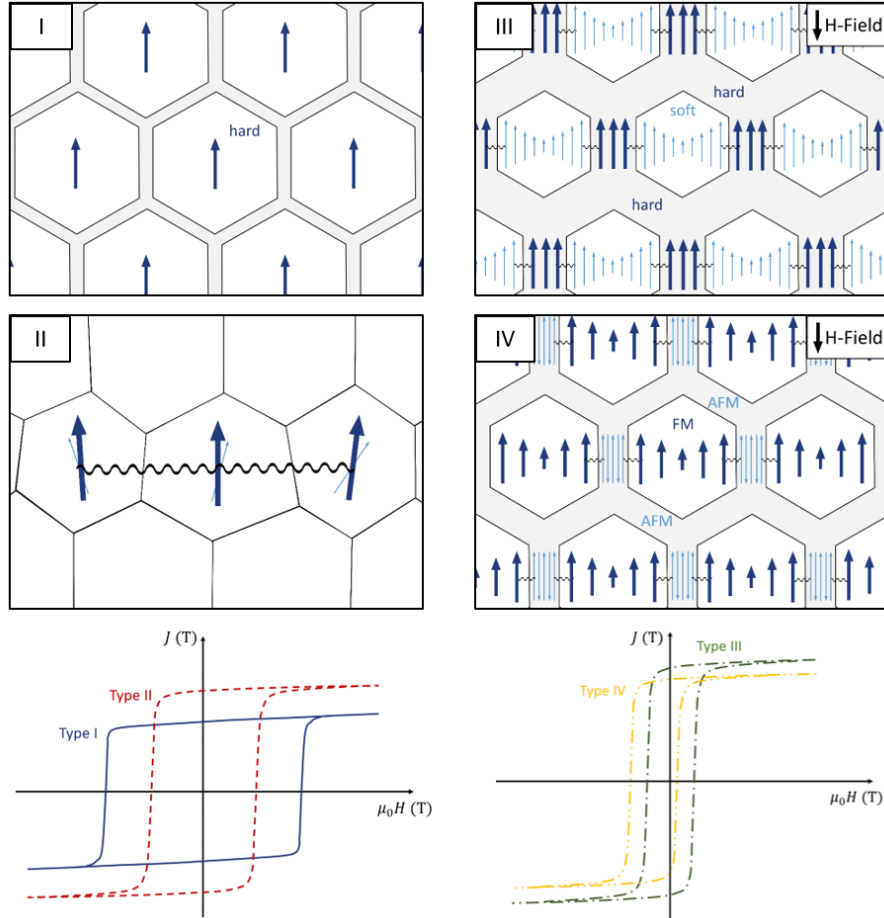
Figure E.3.: Basic schematic representations of microstructures of nucleation-type permanent magnets with the corresponding characteristic magnetic hysteresis curves. Type I: decoupled isolated single domain particles, Type II: exchange interaction of particles, Type III: exchange coupled soft and hard magnetic phases, Type IV: exchange bias due to coupling of ferro- and antiferromagnetic interfaces. Adapted from Refs. [34, 40].

There are different basic schematic types of microstructures for nucleation-type magnets leading to different magnetic properties as depicted in Fig. E.3 together with the shape of their corresponding idealized hysteresis loops [34]. The type I

microstructure leads to the highest coercivity and consists of aligned single domain ferromagnetic particles, separated by a thin non-magnetic layer. This layer magnetically decouples the individual ferromagnetic particles, which hence behave as single permanent magnets. In order to magnetically decouple the individual ferromagnetic particles, the non-magnetic grain boundary phase needs to be thicker than the exchange length to suppress exchange interactions between the magnetic moments of neighboring particles.

If there is no second phase and the microstructure only consists of small ferromagnetic particles, type II is obtained. The ferromagnetic particles are exchange coupled within the surrounding grains, leading to a vectorial alignment of the magnetic moments close to the grain boundaries and thereby to an increasing remanence. If, in addition to the hard magnetic phase a second soft magnetic phase is added, a type III microstructure is achieved. Exchange coupling between the different phases, allows a further increase of the remanence due to the high saturation magnetization of the soft magnetic material. Because the hard magnetic phase stabilizes the soft magnetic one against magnetization reversal, this type of microstructure is referred to exchange coupled spring magnet [41].

Using a composite consisting of a ferromagnetic and an antiferromagnetic phase and cooling the material in the presence of a static magnetic field from a temperature above the Néel-temperature to one below it (while the temperature treatment remains below the Curie-temperature of the ferromagnetic phase) leads to an exchange bias, as shown for the microstructure type IV. The exchange interactions at the interfaces between the antiferromagnetic and the ferromagnetic phase inhibit the magnetic spins of the ferromagnetic phase to rotate, leading to a shift of the hysteresis curve along the field axis of field cooling [42].

Conventional microstructures often exhibit more than two phases or a more complex grain structure with changing chemical compositions ("core-shell" structures) could be present, resulting in different mixed types. The complexity of microstructures and hence, magnetic interactions is expected to further increase in future. However, Fig. E.3 represents the basic simplified schematic interactions, which can be adapted accordingly.

Besides the different phases and the grain size, also the texture is very crucial, especially for hard magnetic materials. To obtain high values for $(BH)_{\max}$, anisotropic magnets are required, where all grains should be aligned along their easy magnetization

direction and the volume fraction of the hard magnetic material should be as high as possible [43]. The conventional production route for rare earth-transition metal-based permanent magnets such as NdFeB and SmCo is based on the powder-metallurgical sintering route [13]. Due to the particularity of the $Nd_2Fe_{14}B$ phase, having an anisotropic grain growth perpendicular to the c-axis, di-upsetting leads to highly anisotropic Nd–Fe–B magnets. However, this feature is not present in other compounds with excellent intrinsic magnetic properties. For these, bonding of nanocrystalline powders by a polymer, which are usually aligned in an external field, is another method of producing bulk permanent magnets [14]. However, by using polymers the amount of magnetic material and consequently B_r and $(BH)_{\max}$ are reduced.

Therefore, to generate permanent magnets, there is a challenge to find new processing techniques in order to achieve a microstructure with highly textured, well-aligned single domain particles of different compounds exhibiting excellent intrinsic magnetic properties. HPT-deformation can be used for the production and tuning of magnetic materials by controlling various microstructural features. It is a promising process which can go beyond the conventional processing techniques.

E.3. High-Pressure Torsion of Bulk Magnetic Materials

Decreasing the grain size to the nc regime can drastically improve soft magnetic properties (drastic reduction in coercivity and lower losses) due to exchange coupling [35, 44]. Although HPT on magnetic materials such as Fe, Co, and Ni were already reported in 1935 by Bridgman, the first works considering the magnetic properties of these HPT processed materials were published in the 1990s [45, 46]. However, in HPT-deformed bulk single-phase materials (e.g., Co, Ni, Fe, Fe-Si alloys), soft magnetic properties could not be fully achieved and often an increase in coercivity is reported [45–53]. One of the reasons is a too large saturation grain size in single-phase materials, which means that the power law dependence of the coercivity on the grain size, as shown in Fig. E.2, was never fulfilled. Another important point that hinders the achievement of truly soft magnetic properties is the high density of defects, which are introduced during HPT-deformation.

HPT processing decreases microstructural feature sizes, which makes it possible to additionally increase coercivity in hard magnetic materials (type II hard magnetic material, c.f. Fig. E.2(b)). Several groups report a coercivity enhancement in different

hard magnetic materials due to grain refinement after HPT processing, compared to the initial state [54–58]. In addition to grain refinement in some HPT-deformed hard magnetic materials, a (partial) amorphization has been observed [54, 59–62]. In Ref. [60], for example, an amorphous structure was induced in Nd(Pr)-Fe-B alloys after HPT to large strains. Subsequent annealing resulted in recrystallization, the formation of stable magnetic and non-magnetic phases. In consequence, significant improvements in hard magnetic properties were reported. Another approach is to deform already amorphous magnetic materials by HPT [63–68]. In Ref. [63], for example, the effect of HPT-deformation and subsequent annealing on structure and magnetic properties of an overquenched melt-spun $Nd_9Fe_{85}B_6$ alloy was investigated. During HPT-deformation, α-Fe nanograins are formed which act as nucleation sites for $Nd_2Fe_{14}B$. Thus, uniform and nc α-Fe and $Nd_2Fe_{14}B$ grains formed during subsequent annealing improving coercivity and remanence (type III hard magnetic material, c.f. Fig. E.2(b)). A similar influence on microstructural development and improved magnetic properties were observed [64, 65, 67–73]. HPT-deformation can further lead to phase decomposition during deformation in hard magnetic alloys [74]. For a $Sm_2Fe_{17}N_x$ alloy [74], phase decomposition in α-Fe and SmN was observed, which lead to an exchange coupled type III hard magnetic material with increased coercivity, remanence, and saturation magnetization. Recently, the microstructural changes of the $Sm_2Fe_{17}N_3$ compound upon HPT-deformation were further studied by Hosokawa et al. [75] HPT-deformation can also enhance the kinetics of phase formation and/or transformations. For example, the synthetization of $L1_0$-FeNi tetrataenite during HPT-deformation and subsequent annealing has been studied in Refs. [76–82]. Up to now, the only successful $L1_0$-FeNi phase formation using HPT-deformation has been reported in Refs. [80–82]. Additionally, the various defects introduced by HPT can act as pinning sites in hard magnetic materials, hindering domain wall movement and changing the magnetization reversal process from nucleation to a pinning dominated one. For example, this effect has been observed in MnAl based materials, which is prone to twin formation during HPT-deformation [57, 58, 63, 83–87]. However, the influence of extensive twinning on coercivity is discussed controversially in literature [86].

E.4. HPT-Deformation of Magnetic Powders

HPT-deformation of powders is as old as the HPT process itself, as already Bridgman applied it to powders in 1935 [88]. Even though he used the term "self-welding" he reported consolidation in materials such as Y, Er [88] and borox glass [89]. Nowadays, besides the consolidation of metallic powders [90–92] also composites [93, 94] have been generated by HPT applied to powder blends. As starting powders commercially available powders of single elements or alloys can be used as well as powders produced by ball milling or finely crushed ribbons.

As already discussed in the introduction, the free selection of the starting powders is especially interesting, during the HPT process using powders as starting materials, since thermodynamically metastable chemical compositions often interesting for soft magnetic materials, but also composite structures are achievable. This is of great benefit, in particular for hard magnetic materials, where the hard magnetic phase and the grain boundary phase can be chosen freely. The microstructures shown schematically in Fig. E.3 can be generated by the choice of the initial powders, the consolidation and deformation process (see Fig. E.4).
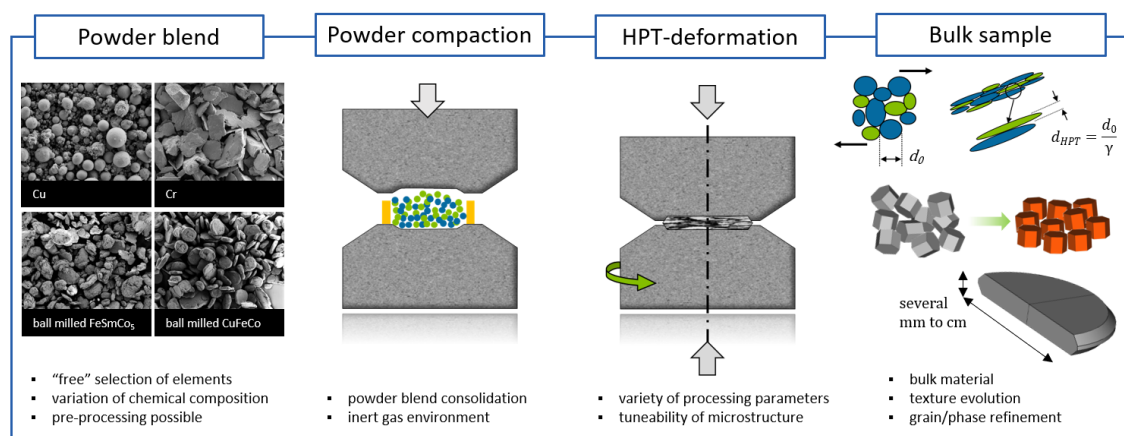
Figure E.4.: Schematic representation of powder-based HPT processes. Usually any kind of powders or powder mixtures are consolidated by a compaction step. The obtained pellet is deformed by HPT resulting in bulk materials with enhanced microstructural features.

A general HPT processing route of powders is schematically shown in Fig. E.4. In a first step the powder or powder blend is chosen, which can be pretreated in any kind. The powder gets poured into the lower anvil by the aid of a Cu-ring, which is stuck to the lower anvil as depicted in Fig. 4. The mixture is pre-compressed, already often accompanied by a slight rotation and/or oscillation by a few degrees. This leads

to cold compaction and the formation of a stable pellet. Depending on the materials but also on their reactivity due to an increased surface to volume ratio, oxidation sensitivity has to be considered. This can be impeded by using inert gas atmospheres for storage, handling and also compaction, if special equipment is used [95]. The actual HPT-deformation is commonly done in a second step. By variation of different process parameters such as pressure, strain, strain rate and temperature, different microstructures and hence different magnetic properties can be adjusted. Compared to the deformation of bulk materials the HPT-deformation of powders usually leads to finer microstructures and a higher hardness. This behavior can be beneficial for mechanical or magnetic properties and is related to the higher amount of precipitates and oxide particles of powder materials [3, 92, 96, 97].

The variety of possible chemical compositions, desired microstructures and material phase distributions is accompanied with challenges within the HPT-processing. Intrinsic material parameters, their compatibility of plasticity as well as the phase composition often lead to an inhomogeneous morphology or a general brittle sample behavior [3, 98]. Localization of the deformation is sometimes difficult to avoid and a microstructural saturation through the whole cross section of the HPT-sample could be unattainable due to the radial strain dependency and an enormous hardness increase at the HPT-disc edge [12] Although, the high hydrostatic pressures during HPT, which is further increased by the cavity of the anvils - the so called constrained HPT setup - helps to circumvent these processing limitations. Therefore, a comparability of the applied shear strain between different samples is a challenging task to obtain. The additional variety of possible processing parameters include a change of the strain rate or the deformation at low or elevated temperatures, thus further investigations and improvements of processes and its parameters are needed.

E.4.1. HPT-deformation of powders to obtain soft magnetic materials

It is well known that materials with supersaturated phases, synthesized by HPT from alloy compositions immiscible at the thermodynamic equilibrium, yield smaller grain sizes compared to single phase materials [2]. This is also true for powder mixtures consisting of ferromagnetic and diamagnetic elements (e.g. CoCu, FeCu, FeAg) [99, 100]. In these HPT-deformed samples, an initial multiphase structure vanishes as a saturated state (steady state microstructure) is reached. This usually is obtained for

shear strains above 1000, which equals to about 50 to 150 HPT rotations for a steady state regime, depending on the sample dimensions and the considered radius [12]. Subsequent annealing induces demixing and grain growth. Thus, annealing treatments can also be used as a further tool to tune magnetic properties [101].

For example, fcc single phase nanocrystalline microstructures were achieved in CoCu alloys (similar to type I microstructure of permanent magnets), where the grain sizes decreased from 100 nm to 77 nm with increasing Co contents [99]. APT and TEM investigations clearly show that a homogeneous Cu and Co concentration is obtained even in nm regions [101, 102]. Paramagnetic features for Co contents less than 50 wt.% (Fig. E.5(a)) and a decrease of the magnetic moment per Co-atom with Cu-content, which might originate from Ruderman-Kittel-Kasuya-Yosida-interaction, were observed with superconducting quantum interference device (SQUID) hysteresis measurements [103]. The microstructure remained single phase up to annealing temperatures of 400°C, but higher annealing temperatures induced phase separation into pure Cu and Co. The measured coercivity increased with increasing Cu-content and annealing temperature (Fig. E.5(b) and (c)) [101, 102]. Transmission-Kikuchi diffraction analyses revealed that the grain size is still above the exchange length of bulk fcc-Co [104]. Thus, the coercivity only qualitatively coincides with the random anisotropy model (Fig. E.5(d)). Using the micromagnetic constants of pure Co to explain the measured data fails [105]. Thus, micromagnetic constants of supersaturated solid solutions need to be calculated and are the focus of current research.

Another ferromagnetic-diamagnetic system, which has been investigated, is Fe-Cu. It is very attractive because Fe has a high magnetic moment and low costs [22]. Using different sample preparation methods, it has already been shown that soft magnetic properties with a tunable magnetic hysteresis can be obtained in supersaturated solid solutions [105–109]. The Fe-Cu alloys synthesized by HPT-deformation consisted mainly of fcc-Cu phase with tiny, residual Fe particles [102]. Detailed APT investigations showed that Fe-clusters are present in the as-deformed microstructures. At the same time, Fe is also dissolved in the fcc-Cu grains. The ratio of clustered to dissolved Fe varied as a function of composition, which further changed the magnetic properties as revealed by SQUID magnetometry [102]. In Fig. E.6(a), the DC-magnetization versus applied magnetic field for samples with increasing Fe content measured at 8 K and room temperature are shown. No saturation of the hysteresis is observed even at the highest applied field. The formation of a supersaturated solid solution of Fe in Cu is confirmed by the measured non-zero
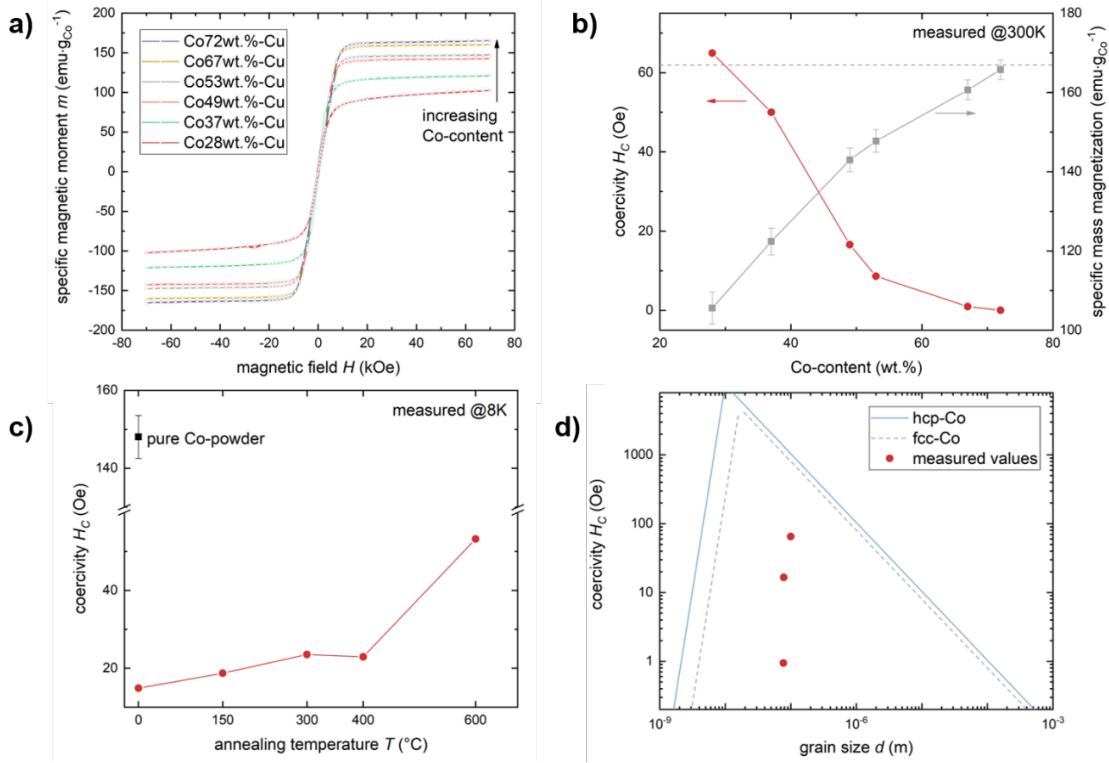
Figure E.5.: (a) Magnetization versus applied field for CoCu samples with different compositions measured at room temperature. (b) Coercivity and magnetization versus Co-content measured at room temperature. (c) Coercivity as function of annealing temperature for Co72 wt.%Cu. (d) Herzer plot using micromagnetic constants of bulk fcc and hcp Co (solid lines) and experimentally obtained values from HPT-deformed CoCu samples. Adapted from Ref. [101].

high-field susceptibility, which is due to a suppression of the ferromagnetic long-range interaction. Coercivities measured in the as-deformed state and its evolution with annealing quantitatively complies with the random anisotropy model similar to the Cu-Co alloys. Normalized zero-field cooling (ZFC) and field-cooling (FC) curves of as-deformed samples as a function of Fe-concentration are plotted in Fig. E.6(b). The Fe25 wt.%-Cu samples showed a typical thermally activated behavior (superparamagnetism due to the residual Fe particles). The Fe14 wt.%-Cu sample displayed splitting of both curves and also a maximum in the FC-curve (at about 50 K). A similar maximum, but no splitting, was observed for Fe7 wt.%-Cu sample. That behavior was correlated to a magnetic frustrated state (spin-glass behavior of diluted Fe), which proved that deformation-induced mixing of Fe and Cu by HPT can be achieved on an atomic scale [110, 111]. In the Fe-Cu sample with medium

Fe content (14 wt.%), the magnetic frustrated state was proven by testing for the dynamic scaling law for spin-glasses [35, 48] and by magnetic-field shifts following the Almeida-Thouless line [52] using frequency dependent AC susceptibility measurements in the as-deformed state and after annealing. Both magnetic phases (frustrated and thermal activated) are still present after annealing at low temperatures (150°C). The coercivity decreases from 128 Oe in the as-deformed state to 55 Oe after annealing at 150°C, which indicates a reduction in residual stresses. During annealing at 250°C, the magnetic frustrated phase vanishes, but larger Fe particles in the microstructure increase the coercivity. After annealing at 500°C, a bulk ferromagnetic behavior was observed, which indicated the formation of multidomain particles confirmed by microstructural investigations [101].
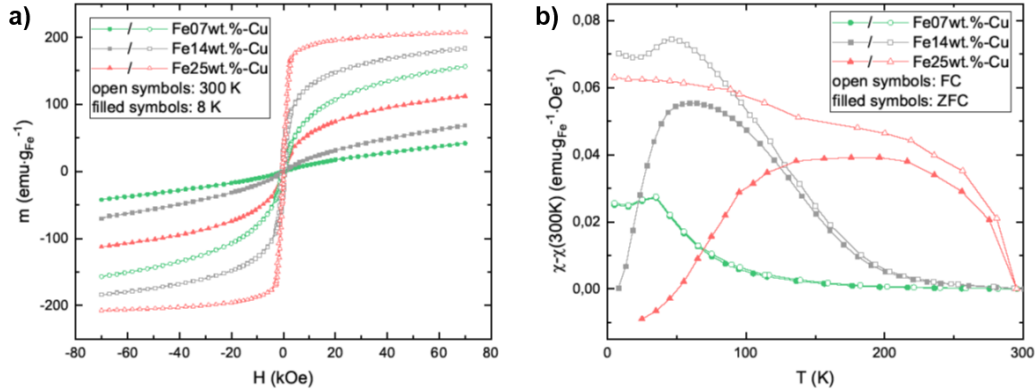
Figure E.6.: (a) Magnetization versus applied field for HPT-deformed FeCu samples measured at room temperature. (b) Normalized ZFC (filled symbols) and FC curves (open symbols) with an applied field H = 50 Oe of as-deformed samples as a function of Fe-content. Adapted from Ref. [102].

The results show that in the HPT-deformed immiscible systems magnetic tunability is possible by changing the chemical composition or by subsequent annealing and semi-hard magnetic properties are reached. To push the limits towards enhanced soft magnetic properties, different Fe-Co ratios are mixed with Cu in Ref. [112] as the addition of Fe can lead to decreasing magnetocrystalline anisotropy and increasing saturation magnetization. Based on findings from binary compositions deformed by HPT, a region in the ternary phase diagram to synthesize homogeneous nanocrystalline supersaturated solid solutions has been identified (Fig. E.7). For samples containing a higher ferromagnetic content, a two-step HPT-deformation process at different temperatures was used. Depending on the ratio of Fe and Co, samples with a high

ferromagnetic content either form a single-phase supersaturated solid solution or a microstructure which consist of bcc- and fcc-phases. Soft magnetic properties were confirmed for large Co-to-Fe-ratios. For example, the coercivity of a Co-rich $Cu_{17}Fe_{11}Co_{72}$ is about 2 Oe at room temperature [113]. This low coercivity might originate from a decreased magnetocrystalline anisotropy due to the addition of Fe and might be further lowered by the formation of the supersaturated solid solution.
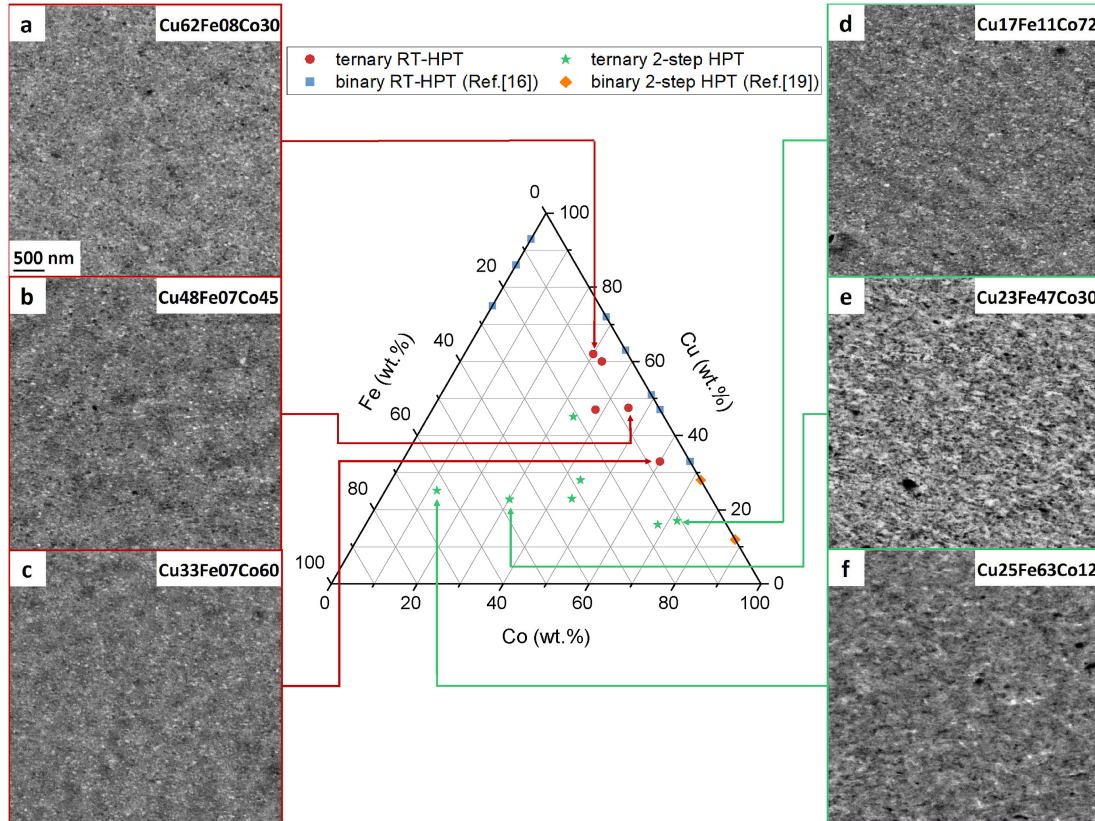
Figure E.7.: The ternary phase diagram with compositions investigated in this study. Images on the left (a)-(c) show SEM micrographs of samples, which are processed by HPT-deformation at room temperature. Images on the right (d)-(f) show SEM micrographs of samples processed by the two-step HPT-deformation process at different temperatures. The scale bar in a) applies to all micrographs. Reprinted from Ref. [112].

Considering application, a further important magnetic property is magnetoresistivity. A giant decrease of resistivity with increasing applied magnetic field, the giant magneto-resistance (GMR) effect, was first observed for very thin layers of alternating ferromagnetic Fe and antiferromagnetic Cr [114, 115]. The GMR phenomenon is not limited to layered systems and can be also found for materials which consist of nanometer-sized ferromagnetic particles dispersed in non-magnetic metallic matrixes ('granular' GMR) [116, 117]. Binary and ternary powder mixtures consisting

of different compositions of elemental Cu, Co, Ni, and Fe were thus processed by HPT-deformation and examined as possible candidates for the granular GMR effect [118–120]. In these studies, it could be shown that it is possible to produce HPT-deformed samples showing GMR behavior at room temperature. The GMR-ratio is small compared to multilayer systems already in application. It is, however, in a similar range to literature values of other materials processed by different methods showing granular GMR [116, 117]. For example, a maximum GMR of $\sim 3.5\%$ was found for a Cu-Co sample with approximately equiatomic fraction of Co and Cu. For the investigated ternary systems, the highest drop in resistivity at room temperature was found in $Cu_{62}Fe_{19}Ni_{19}$ after annealing (2.45% at 1790 kA/m). However, no saturation was measured in any composition and higher magnetic fields or lower measurement temperatures are expected to lead to a stronger GMR effect.

E.4.2. HPT-deformation of powders to obtain hard magnetic materials

In the literature, HPT processing of powders has been successfully used for the production of NdFeB based materials [121, 122]. An amorphous precursor was obtained from crushed melt spun ribbons and was consolidated applying a hydrostatic pressure in the HPT device. During subsequent HPT-deformation, decomposition of $Nd_2Fe_{14}B$ to an amorphous matrix phase with finely dispersed nanocrystalline α-Fe-grains occurs [121]. In Ref. [122], a beneficial (00l) phase texture of $Nd_2Fe_{14}B$ upon HPT-deformation further induced anisotropic magnetic properties and resulted in a maximum energy product of 22.8 MGOe.

Based on $SmCo_5$ hard magnetic powder, it was demonstrated how the different magnetic exchange interactions and magnetic hardening mechanisms (c.f. Fig. E.3) can be successfully implemented by HPT-deformation of powders. Therefore, powder blends of $SmCo_5$ and magnetically different binder phases, i.e., Fe, Ni, Co, Cu, Zn, Sn, and Cr, were applied to HPT-deformation. The microstructures and corresponding hysteresis loops are summarized in Fig. E.8(a) and (b), respectively Fig. 9. The different types of microstructures introduced in Fig. 3 could be well reproduced. A type I magnetic system was obtained using diamagnetic Cu as a binder phase [16]. In preliminary experiments, type II magnets deforming SmCo-based intermetallic powders ($SmCo_5$, Sm_2Co_7, Sm_2Co_{17}) by HPT were fabricated as well. An exchange coupled type III system was prepared using Fe [123] and a type IV ferro-antiferromagnetic

composite is represented by $SmCo_5$+Cr. Unfortunately, an exchange bias for $SmCo_5$ using Cr as binder phase (type IV system) could not be proven yet. Apart from exchange bias samples, the magnetic behavior follows the theoretical prediction. M_s is highest for the Fe containing composition (exchange coupled spring magnet) and lowest for the diamagnetic and antiferromagnetic binder phase. H_c is lowest for the type III sample, containing the lowest amount of $SmCo_5$, while H_c is higher for the refined structure and further increases by adding Cr and Cu. The highest H_c is obtained by the type I system, where Cu is magnetically isolating the refined $SmCo_5$ particles.
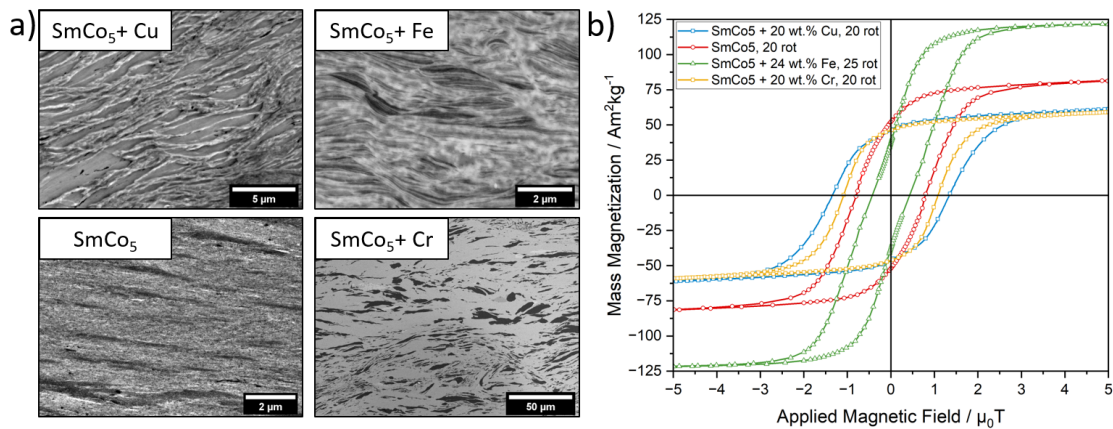
Figure E.8.: (a) BSE images of HPT-deformed samples at a radius of 2 mm. Different $SmCo_5$ based powder blends are used as starting material. (b) Corresponding hysteresis measurements depicted between ± 5 T.

The type I [16] and type III [15, 123] $SmCo_5$ based material systems were investigated in more detail with a focus on the material processing of several chemical compositions and the influence of applied deformation on the microstructure. Staab et al. [16] deformed several samples to different extents, the composite structure was refined and an elongation of the hard magnetic phase particles, separated by Cu was reported. The best processability and simultaneously very good magnetic properties were found using 20 wt.% of Cu as binder phase. Increasing the amount of Cu did not lead to a deterioration of the coercivity but the diamagnetic Cu phase led to a dilution of the total magnetization of the sample. A similar microstructure evolution was apparent for Fe-$SmCo_5$ composites as presented by Weissitsch et al. [123]. Figure E.9(a)-(e) shows BSE images of a RT deformed 47 wt.% Fe-$SmCo_5$ composite at different radii of a single sample. A mainly compression dominated deformation is visible at radius 0 (Fig. 9(a)). With increasing radius, the inhomogeneous structure with separated

phases of Fe (dark contrast) and SmCo$_5$ (bright contrast) remains. However, the distance between the phases decreases and a lamellar morphology, well below 1 µm is found for radius 3 in Fig. E.9(d)-(e). Refined heterophase structures are observed for both material systems [15, 16, 123]. However, if ball milled powders were used, the resulting phase morphology changes drastically depending on the used chemical composition [15].
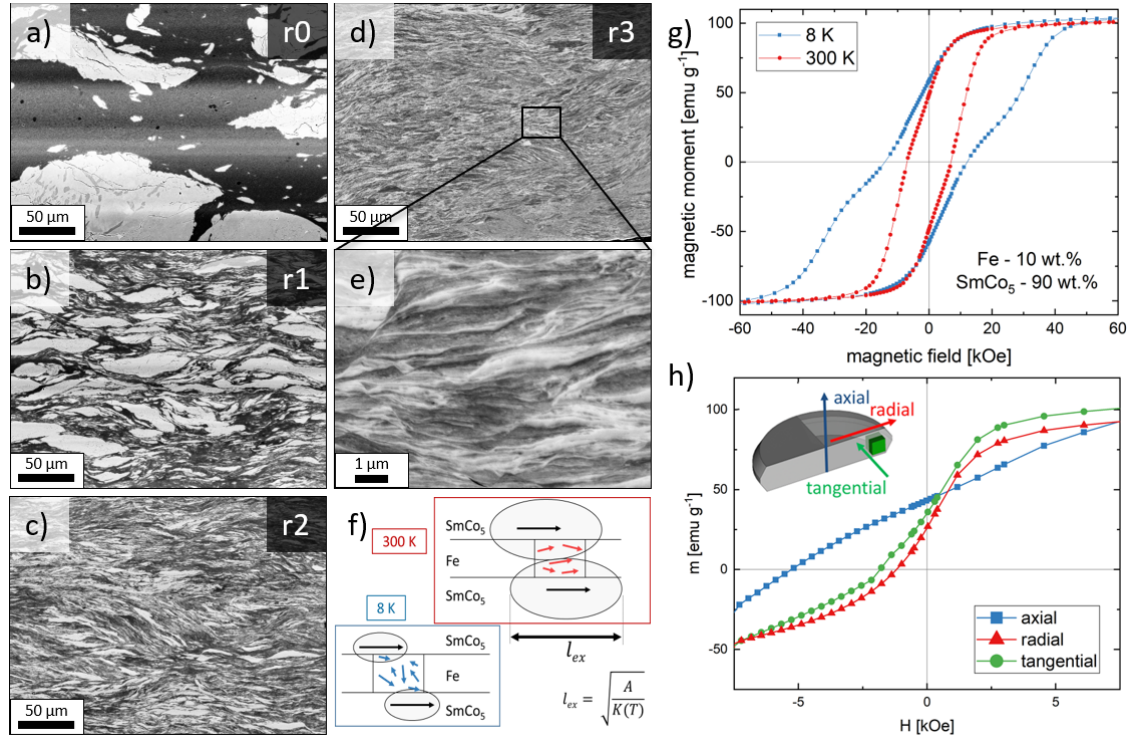
Figure E.9.: (a)-(d) BSE-images of an HPT-deformed 47 wt.% FeSmCo$_5$ composite at different radii. (e) shows the lamellar structure at a higher magnification. The temperature dependent exchange length is schematically shown in (f) with respect to the lamellar morphology. (g) Changing the temperature, allows to switch between coupling and decoupling of soft and hard magnetic composite. (h) Magnetic anisotropic behavior induced by the shear strain through HPT.

As presented in Fig. E.9(g), magnetic hysteresis measurements at different temperatures are performed on a Fe-SmCo$_5$ composite with 10 wt.% Fe and 90 wt.% SmCo$_5$. A different H_c, but also a change of the shape of the hysteresis is visible. An exchange coupled behavior at higher temperatures is found and a decoupled compound with magnetically separated phases (pronounced by the 'knee' apparent in recoil curve) is measured at low temperatures. This effect is due to the lamellar microstructure. The temperature dependency of the magnetocrystalline anisotropy of the SmCo$_5$ phase is

invers proportional to the exchange length, which is decisively responsible if exchange coupling can occur. Therefore, the Fe phase is not completely coupled to the $SmCo_5$ phase, as the decreasing temperature decreases the exchange length (Fig. E.9(f)). Moreover, magnetic anisotropic characteristics (Fig. E.9(h)) measured in directions with respect to the HPT-disc are correlated to a crystallographic texture upon deformation [15]. This is further proven by synchrotron diffraction experiments for both the Fe and the $SmCo_5$ phase. The c-axis of the hexagonal $SmCo_5$ orients in axial HPT-disc direction, while the easy axis of the Fe phase points towards the tangential HPT-disc direction. Also Staab et al. [16] reported an deformation induced texture of the $SmCo_5$-Cu nanocomposites. XRD analyses revealed increasing intensities of reflexes containing c-components whereas the intensity of reflexes which did not contain c-components decreased. In addition to XRD analyses, the magnetic measurements conducted along different sample directions, similar to above described, showed this preferential orientation of the c-axis along the axial direction of the HPT disc as well. This reported texture of the $SmCo_5$ phase, crystallizing in a hexagonal structure ($CaCu_5$-type) [40], is of potential interest since it is one of the main challenges in hard magnetic materials processing. The advantage may be the hexagonal crystal structure of $SmCo_5$ which is plastically more anisotropic compared to fcc or bcc materials resulting in a pronounced basal texture during HPT as reported for Mg [36, 124].
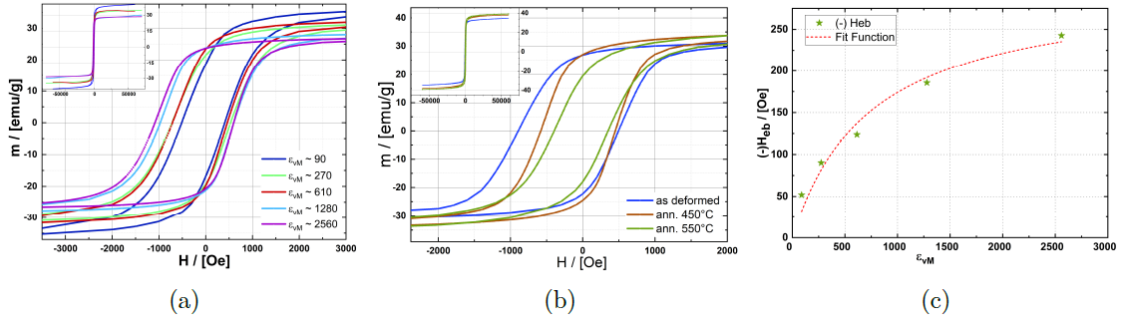
Figure E.10.: (a) Hysteresis loops of a $Fe_{10}Ni_{40}$-NiO_{50} nanocomposite HPT-deformed to different amounts of applied strain measured at 8K. (b) Hysteresis loops of as-deformed and annealed $Fe_{10}Ni_{40}$-NiO_{50} nanocomposites. (c) Measured exchange bias for different amounts of applied strain. Reprinted from Ref. [125].

The coercivity and the squareness of the hysteresis loops can be also enhanced at room temperature in nanocomposites consisting of ferromagnetic and antiferromagnetic components with a Néel temperature, T_N, above room temperature using the exchange bias effect. The enhancement is maximal after field annealing above T_N

[42]. The possibility to achieve an exchange bias was recently reported for another type IV material system, the Fe-NiO system. In a first study, the possibility to synthesize nanocomposites by HPT-deformation consisting of Fe (ferromagnetic) and NiO (antiferromagnetic) phases with a phase ratio of 1:1 was investigated. In Ref. [125], the synthesis of ferromagnetic-antiferromagnetic nanocomposites by HPT was evaluated to a much greater extent by studying also different ratios of ferromagnetic-antiferromagnetic phases (Fe or $Fe_{20}Ni_{80}$ and NiO) and by further investigating the influence on magnetic properties. With rising strain, an increase in exchange bias (H_{eb}) was found which could be related to the microstructural refinement of the nanocomposites. As example, the hysteresis loop of an HPT processed $Fe_{10}Ni_{40}$-NiO_{50} nanocomposite is shown in Fig. E.10(a). Tuning of magnetic properties was further possible by subsequent annealing treatments (Fig. E.10(b)). The fit in Fig. E.10(c) shows a saturation behavior for increasing applied strain for the maximal achievable H_{eb}. Menéndez et al. [126] studied a similar type IV system (Co-NiO). While they differentiate between powder and ball milled powder as starting material prior HPT-deformation, the applied strain was relatively low, resulting in a coarser microstructure and lower H_{eb} values.

Phase transformations using HPT was demonstrated by Lee et al. [82]. They used and compared arc-melted ingots, powders and nano-sized powders during HPT-deformation, as starting materials to induce the $L1_0$-FeNi phase transformation. Several millions of years are required to naturally form $L1_0$-FeNi. However, enhanced diffusion processes due to HPT-induced lattice defects drastically reduces annealing times to a few days, which is stronger pronounced for fine powders. Using HPT processing for Mn-Al-C based permanent magnets is further proposed by Popov et al. [127]. When deforming the γ-phase a strong increase of H_c with increasing radius and thus applied strain is found (from 0.22 T up to 0.58 T). In addition, a stress-driven phase transformation of the metastable γ-phase into the ϵ-phase was reported. They suggested a combination of hot extrusion and HPT to form magnetic anisotropic grains through a textured microstructure and utilize the large structural defect density to foster domain wall pinning.

Weissitsch et al. [128] used the HPT process in combination with annealing treatments to circumvent common processing limits within the MnBi material system. The formation of the hard magnetic α-MnBi phase (medium dark contrast, marked by arrows) is reported after equiatomic MnBi powder blends are HPT compacted and annealed for different times as shown in Fig. E.11(a) and (b). This intermetallic phase
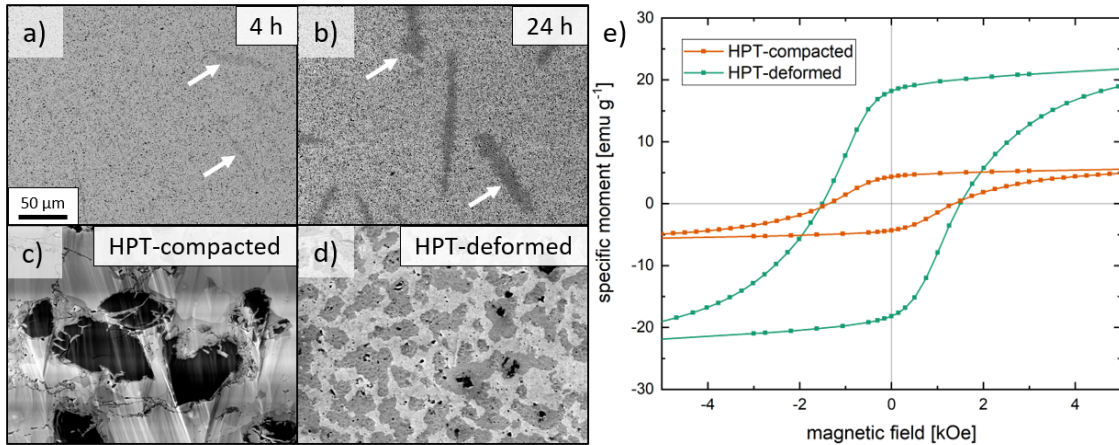
Figure E.11.: HPT-deformed MnBi composite after conventional annealing for (a) 4 h and (b) 24 h showing the ferromagnetic α-MnBi phase formation. This phase formation is enhanced after annealing for 4 h in presence of an external isostatic magnetic field and for higher deformation grades (c)-(d). Corresponding magnetic hysteresis curves are shown in (e).

is a potential candidate to substitute rare-earth based magnets, but its formation is a challenging task. They monitored the phase formation by in-situ synchrotron annealing experiments and found an enhanced number of α-MnBi phase nucleation sites for HPT-deformed samples. The α-MnBi phase formation is further improved when a magnetic field is applied during the annealing treatment. This again is strongly dependent on the deformation history. BSE images of an HPT compacted (Fig. E.11(c)) and deformed (Fig. E.11(d)) sample after the same in-field annealing treatment is shown. The deformed sample, which shows refined Mn particles (dark contrast), also exhibits an extended amount of α-MnBi phase (medium contrast). The saturation magnetization of the composite scales with the existing amount of α-MnBi phase and magnetic SQUID measurements support these results as shown in Fig. E.11(e).

E.5. Summary

HPT-deformation applied to powder blends of magnetic materials has shown a rising interest in recent years. The process enables several advantages such as grain refinement and the production of nanostructured composite materials or supersaturated solid solutions influencing the magnetic properties. Nevertheless, the process is not limited to obtain technically or scientifically relevant soft- and hard magnetic materials.

Reports on superconducting materials show an influence of plastic deformation on the microstructure formation and resulting magnetic properties. Similarities to phase transitions and refined grains are reported [129–134]. Further works on high entropy alloys [135, 136] and shape memory materials are found [137].

The possibilities of the high-pressure torsion process applied to magnetic materials is probably an often under-estimated technique. The opportunities of microstructural tuning (i.e., grain refinement, texture evolution or mechanical alloying processes) are combined with sample sizes exhibiting bulk dimensions. In particular, the chance to choose the starting materials which are not limited to bulk but also any kind of powder blends are feasible, allows a variety of possible microstructures and enables sophisticated pathways for material scientists. Besides the starting material itself, process parameters such as pressure, strain and temperature offer a wide range to tune the microstructure and hence the magnetic properties further. As a result, the HPT process provides a great variety of opportunities to further investigate different material systems interesting for magnetic applications.

Acknowledgement

E.6. References

[1] Kaveh Edalati et al. Influence of dislocation–solute atom interactions and stacking fault energy on grain size of single-phase alloys after severe plastic deformation using high-pressure torsion, *Acta Mater.* **69** (2014), pp. 68–77.
DOI: 10.1016/j.actamat.2014.01.036.

[2] R. Pippan et al. Saturation of Fragmentation During Severe Plastic Deformation, *Annu. Rev. Mater. Res.* **40**, no. 1 (2010), pp. 319–343.
DOI: 10.1146/annurev-matsci-070909-104445.

[3]   Karoline Sophie Kormout, Reinhard Pippan, and Andrea Bachmaier. Deformation-Induced Supersaturation in Immiscible Material Systems during High-Pressure Torsion, *Adv. Eng. Mater.* **19**, no. 4 (2017), p. 1600675.
DOI: 10.1002/adem.201600675.

[4]   A. Bachmaier and R. Pippan. Generation of metallic nanocomposites by severe plastic deformation, *Int. Mater. Rev.* (2013), pp. 41–62.

[5]   Yulia Ivanisenko et al. Evidence of $\alpha \to \omega$ phase transition in titanium after high pressure torsion, *Int. J. Mater. Res.* **99**, no. 1 (2008), pp. 36–41.
DOI: 10.3139/146.101606.

[6]   X. Sauvage, A. Chbihi, and X. Quelennec. Severe plastic deformation and phase transformations, *J. Phys. Conf. Ser.* **240**, no. 1 (2010), p. 012003.
DOI: 10.1088/1742-6596/240/1/012003.

[7]   H. Wang et al. Transformation pathway from alpha to omega and texture evolution in Zr via high-pressure torsion, *Appl. Phys. Lett.* **114**, no. 6 (2019).
DOI: 10.1063/1.5087721.

[8]   Boris B. Straumal et al. Paper presented at "XV International Conference on Electron Microscopy", 15–18 September 2014, Cracow, Poland, *Int. J. Mater. Res.* **106**, no. 7 (2015), pp. 657–664.
DOI: 10.3139/146.111215.

[9]   A. Bachmaier et al. Phase separation of a supersaturated nanocrystalline Cu–Co alloy and its influence on thermal stability, *Acta Materialia* **96** (2015), pp. 269–283.
DOI: 10.1016/j.actamat.2015.05.053.

[10]   Dmitry Gunderov and Vasily Astanin. Influence of HPT Deformation on the Structure and Properties of Amorphous Alloys, *Metals* **10**, no. 3 (2020), p. 415.
DOI: 10.3390/met10030415.

[11]   Kaveh Edalati and Zenji Horita. A review on high-pressure torsion (HPT) from 1935 to 1988, *Mater. Sci. Eng., A* **652** (2016), pp. 325–352.
DOI: 10.1016/j.msea.2015.11.074.

[12]   Anton Hohenwarter et al. Technical parameters affecting grain refinement by high pressure torsion, *Int. J. Mater. Res.* **100**, no. 12 (2009), pp. 1653–1661.
DOI: 10.3139/146.110224.

[13]   Jun Cui et al. Manufacturing Processes for Permanent Magnets: Part I—Sintering and Casting, *JOM* **74**, no. 4 (2022), pp. 1279–1295.
DOI: 10.1007/s11837-022-05156-9.

[14]   Jun Cui et al. Manufacturing Processes for Permanent Magnets: Part II—Bonding and Emerging Methods, *JOM* **74**, no. 6 (2022), pp. 2492–2506.
DOI: 10.1007/s11837-022-05188-1.

[15] Lukas Weissitsch et al. Manufacturing of Textured Bulk Fe-SmCo5 Magnets by Severe Plastic Deformation, *Nanomaterials* **12**, no. 6 (2022), p. 963.
DOI: 10.3390/nano12060963.

[16] Franziska Staab et al. Hard magnetic SmCo5-Cu nanocomposites produced by severe plastic deformation, *Acta Mater.* **246** (2023), p. 118709.
DOI: 10.1016/j.actamat.2023.118709.

[17] Kaveh Edalati et al. Nanomaterials by severe plastic deformation: review of historical developments and recent advances, *Mater. Res. Lett.* (2022), pp. 163–256.

[18] R. Z. Valiev, R. K. Islamgaliev, and I. V. Alexandrov. Bulk nanostructured materials from severe plastic deformation, *Prog. Mater. Sci.* **45**, no. 2 (2000), pp. 103–189.
DOI: 10.1016/S0079-6425(99)00007-9.

[19] Zhi-Rui Wang et al. A Review of Ultrafine-Grained Magnetic Materials Prepared by Using High-Pressure Torsion Method, *Materials* **15**, no. 6 (2022), p. 2129.
DOI: 10.3390/ma15062129.

[20] Andrew B. Kustas, Donald F. Susan, and Todd Monson. Emerging Opportunities in Manufacturing Bulk Soft-Magnetic Alloys for Energy Applications: A Review, *JOM* **74**, no. 4 (2022), pp. 1306–1328.
DOI: 10.1007/s11837-021-05019-9.

[21] Oliver Gutfleisch et al. Magnetic Materials and Devices for the 21st Century: Stronger, Lighter, and More Energy Efficient, *Adv. Mater.* **23**, no. 7 (2011), pp. 821–842.
DOI: 10.1002/adma.201002180.

[22] J. M. D. Coey. Magnetic materials, *J. Alloys Compd.* **326**, no. 1 (2001), pp. 2–6.
DOI: 10.1016/S0925-8388(01)01239-7.

[23] J. M. D. Coey. Hard Magnetic Materials: A Perspective, *IEEE Trans. Magn.* **47**, no. 12 (2011), pp. 4671–4681.
DOI: 10.1109/TMAG.2011.2166975.

[24] H. Kronmüller. Theory of Nucleation Fields in Inhomogeneous Ferromagnets, *Phys. Status Solidi B* **144**, no. 1 (1987), pp. 385–396.
DOI: 10.1002/pssb.2221440134.

[25] Balamurugan Balasubramanian et al. Magnetic nanostructuring and overcoming Brown's paradox to realize extraordinary high-temperature energy products, *Sci. Rep.* **4**, no. 6265 (2014), pp. 1–6.
DOI: 10.1038/srep06265.

[26] R. B. Goldfarb and F. R. Fickett. Units for magnetic properties: *NIST* (1985).

[27] Ralph Skomski. *Simple Models of Magnetism.* Oxford University Press, 2008.
DOI: 10.1093/acprof:oso/9780198570752.001.0001.

[28] H. R. Hilzinger. The influence of planar defects on the coercive field of hard magnetic materials, *Appl. Phys.* **12**, no. 3 (1977), pp. 253–260.
DOI: 10.1007/BF00915199.

[29] F. Bittner et al. The impact of dislocations on coercivity in L10-MnAl, *J. Alloys Compd.* **704** (2017), pp. 528–536.
DOI: 10.1016/j.jallcom.2017.02.028.

[30] H. Kronmüller. "Magnetisierungskurve der Ferromagnetika", *Moderne Probleme der Metallphysik*. Berlin, Germany: Springer, 1966, pp. 24–156.
DOI: 10.1007/978-3-642-87531-1_2.

[31] William Fuller Brown. The Effect of Dislocations on Magnetization Near Saturation, *Phys. Rev.* **60**, no. 2 (1941), pp. 139–147.
DOI: 10.1103/PhysRev.60.139.

[32] H. Kronmüller. The Contribution of Dislocations to the Magnetocrystalline Energy and Their Effect on Rotational Hysteresis Processes, *J. Appl. Phys.* **38**, no. 3 (1967), pp. 1314–1315.
DOI: 10.1063/1.1709599.

[33] J. Fidler, H. Kirchmayer, and P. Skalicky. Pinning of magnetic domain walls at dislocations and precipitates in Co5Sm crystals, *Philos. Mag. B* (2006), pp. 765–780.

[34] D. Goll and H. Kronmüller. High-performance permanent magnets, *Naturwissenschaften* **87**, no. 10 (2000), pp. 423–438.
DOI: 10.1007/s001140050755.

[35] Giselher Herzer. Soft magnetic nanocrystalline materials, *Scr. Metall. Mater.* **33**, no. 10 (1995), pp. 1741–1756.
DOI: 10.1016/0956-716X(95)00397-E.

[36] Han-Joo Lee et al. Evolution in hardness and texture of a ZK60A magnesium alloy processed by high-pressure torsion, *Mater. Sci. Eng., A* **630** (2015), pp. 90–98.
DOI: 10.1016/j.msea.2015.02.011.

[37] K. Hono and H. Sepehri-Amin. Strategy for high-coercivity Nd–Fe–B magnets, *Scr. Mater.* **67**, no. 6 (2012), pp. 530–535.
DOI: 10.1016/j.scriptamat.2012.06.038.

[38] Hao Tang, Mohammad Aref Hasen Mamakhel, and Mogens Christensen. Enhancing the coercivity of SmCo5 magnet through particle size control, *J. Mater. Chem. C* **8**, no. 6 (2020), pp. 2109–2116.
DOI: 10.1039/C9TC06137A.

[39] K. Suzuki et al. Magnetic domains and annealing-induced magnetic anisotropy in nanocrystalline soft magnetic materials, *J. Appl. Phys.* **103**, no. 7 (2008).
DOI: 10.1063/1.2835068.

[40] O. Gutfleisch. Controlling the properties of high energy density permanent magnetic, *J. Phys. D: Appl. Phys.* **33**, no. 17 (2000), R157.
DOI: 10.1088/0022-3727/33/17/201.

[41] E. F. Kneller and R. Hawig. The exchange-spring magnet: a new material principle for permanent magnets, *IEEE Trans. Magn.* **27**, no. 4 (1991), pp. 3588–3560.
DOI: 10.1109/20.102931.

[42] J. Nogués et al. Exchange bias in nanostructures, *Phys. Rep.* **422**, no. 3 (2005), pp. 65–117.
      DOI: 10.1016/j.physrep.2005.08.004.

[43] K. P. Skokov and O. Gutfleisch. Heavy rare earth free, free rare earth and rare earth free
      magnets - Vision and reality, *Scr. Mater.* **154** (2018), pp. 289–294.
      DOI: 10.1016/j.scriptamat.2018.01.032.

[44] R. Grössinger et al. Properties, Benefits, and Application of Nanocrystalline Structures in
      Magnetic Materials, *Adv. Eng. Mater.* **5**, no. 5 (2003), pp. 285–290.
      DOI: 10.1002/adem.200310081.

[45] R. R. Mulyukov R. Z. Valiev and V. V. Ovchinnikov. Direction of a grain-boundary phase in
      submicrometre-grained iron, *Philosophical Magazine Letters* **62**, no. 4 (1990), pp. 253–256.
      DOI: 10.1080/09500839008215131.

[46] Kh Ya Mulyukov, GF Korznikova, and RF Valiev. Microstructure and magnetic properties of
      submicron grained cobalt after large plastic deformation and their variation during annealing,
      physica status solidi (a) **125**, no. 2 (1991), pp. 609–614.
      DOI: 10.1002/pssa.2211250222.

[47] Stephan Scheriau et al. Tailoring the Magnetic Properties of Ferritic Alloys by HPT, *Materials
      Science Forum* **584-586** (2008), pp. 923–928.
      DOI: 10.4028/www.scientific.net/MSF.584-586.923.

[48] S. Scheriau et al. Magnetic characteristics of HPT deformed soft-magnetic materials, *Journal
      of Magnetism and Magnetic Materials* **322**, no. 20 (2010), pp. 2984–2988.
      DOI: 10.1016/j.jmmm.2010.04.032.

[49] Akihide Hosokawa et al. Micostructure and Magnetic Properties in Nanostructured Fe and
      Fe-Based Intermetallics Produced by High-Pressure Torsion, *Materials Transactions* **55**, no.
      8 (2014), pp. 1286–1291.
      DOI: 10.2320/matertrans.M2014119.

[50] Y. Oba et al. Anomalous magnetic anisotropy and magnetic nanostructure in pure Fe induced
      by high-pressure torsion straining, *Physical Review Research* **2**, no. 3 (2020). Publisher:
      American Physical Society, p. 033473.
      DOI: 10.1103/PhysRevResearch.2.033473.

[51] Kaveh Edalati et al. High-pressure torsion of pure cobalt: hcp-fcc phase transformations
      and twinning during severe plastic deformation, *Applied Physics Letters* **102**, no. 18 (2013),
      p. 181902.
      DOI: 10.1063/1.4804273.

[52] Kh. Ya. Mulyokov et al. Magnetic hysteretic properties of submicron grained nickel and their
      variations upon annealing, *Journal of Magnetism and Magnetic Materials* **89**, no. 1 (1990),
      pp. 207–213.
      DOI: 10.1016/0304-8853(90)90728-9.

[53] R. Groessinger et al. Frequency Dependence of the Coercivity of Soft Magnetic Materials, *IEEE Transactions on Magnetics* **48**, no. 4 (2012). Conference Name: IEEE Transactions on Magnetics, pp. 1473–1476.
DOI: 10.1109/TMAG.2011.2174351.

[54] S. Taskaev et al. Influence of Severe Plastic Deformation on Magnetic Properties of Fe48Ni48Zr4, Fe49.5Co16.5B33Ta and Co80Zr16B4 Alloys, *Physics Procedia*. 20th International Conference on Magnetism, ICM 2015 **75** (2015), pp. 1404–1409.
DOI: 10.1016/j.phpro.2015.12.158.

[55] Abdelahad Chbihi et al. Optimization of the Magnetic Properties of FePd Alloys by Severe Plastic Deformation, *Advanced Engineering Materials* **12**, no. 8 (2010). _eprint: https://onlinelibrary.wiley.com/doi/pdf, pp. 708–713.
DOI: 10.1002/adem.200900326.

[56] I Shchetinin et al. "Magnetic properties of nitrides Sm2Fe17 compound after severe plastic deformation by torsion at 77K", *METAL 2019-28th International Conference on Metallurgy and Materials, Conference Proceedings*. 2019, pp. 816–820.

[57] Ping-Zhan Si et al. Phase transformation and enhanced coercivity in B-N-doped MnAl nanocrystalline bulk alloys prepared by high pressure torsion, *AIP Advances* **10**, no. 1 (2020), p. 015320.
DOI: 10.1063/1.5130064.

[58] Ping Zhan Si et al. High Coercivity in MnAl Disc Prepared by Severe Plastic Deformation, *physica status solidi (b)* **257**, no. 3 (2020). _eprint: https://onlinelibrary.wiley.com/doi/pdf/10.1002/pssb.201900356, p. 1900356.
DOI: 10.1002/pssb.201900356.

[59] B. B. Straumal et al. Amorphization of Nd–Fe–B alloy under the action of high-pressure torsion, *Materials Letters* **145** (2015), pp. 63–66.
DOI: 10.1016/j.matlet.2015.01.041.

[60] V. V. Stolyarov et al. Structure evolution and changes in magnetic properties of severe plastic deformed Nd(Pr)–Fe–B alloys during annealing, *Journal of Alloys and Compounds* **281**, no. 1 (1998), pp. 69–71.
DOI: 10.1016/S0925-8388(98)00774-9.

[61] I. S. Tereshina et al. Magnetic hysteresis properties of nanocrystalline (Nd,Ho)-(Fe,Co)-B alloy after melt spinning, severe plastic deformation and subsequent heat treatment, *Journal of Alloys and Compounds* **681** (2016), pp. 555–560.
DOI: 10.1016/j.jallcom.2016.04.228.

[62] B. B. Straumal et al. Amorphization of crystalline phases in the Nd–Fe–B alloy driven by the high-pressure torsion, *Materials Letters* **161** (2015), pp. 735–739.
DOI: 10.1016/j.matlet.2015.09.076.

[63]   A. G. Popov et al. Effect of High-Pressure Torsion Deformation and Subsequent Annealing on Structure and Magnetic Properties of Overquenched Melt-Spun Nd9Fe85B6 Alloy, *Journal of Iron and Steel Research, International* **13** (2006), pp. 160–165.
DOI: 10.1016/S1006-706X(08)60175-2.

[64]   Wei Li et al. Bulk α-Fe/Nd2Fe14B nanocomposite magnets produced by severe plastic deformation combined with thermal annealing, *Journal of Applied Physics* **108**, no. 5 (2010), p. 053901.
DOI: 10.1063/1.3480789.

[65]   Wei Li et al. Nanocrystallization and magnetic properties of amorphous Nd9Fe85B6 subjected to high-pressure torsion deformation upon annealing, *Journal of Applied Physics* **104**, no. 2 (2008), p. 023912.
DOI: 10.1063/1.2959379.

[66]   Wei Li et al. Controllable nanocrystallization in amorphous Nd9Fe85B6 via combined application of severe plastic deformation and thermal annealing, *Applied Physics Letters* **91**, no. 6 (2007), p. 062509.
DOI: 10.1063/1.2768023.

[67]   Hailing Li et al. Phase evolution, microstructure and magnetic properties of bulk α-Fe/Nd2Fe14B nanocomposite magnets prepared by severe plastic deformation and thermal annealing, *Journal of Alloys and Compounds* **651** (2015), pp. 434–439.
DOI: 10.1016/j.jallcom.2015.08.132.

[68]   A. Musiał et al. Tuning of the magnetic properties of Hf2Co11B alloys through a combined high pressure torsion and annealing treatment, *Journal of Alloys and Compounds* **787** (2019), pp. 794–800.
DOI: 10.1016/j.jallcom.2019.02.098.

[69]   Xiaohong Li et al. Controllably Manipulating Three-Dimensional Hybrid Nanostructures for Bulk Nanocomposites with Large Energy Products, *Nano Letters* **17**, no. 5 (2017). Publisher: American Chemical Society, pp. 2985–2993.
DOI: 10.1021/acs.nanolett.7b00264.

[70]   Hailing Li et al. Simultaneously increasing the magnetization and coercivity of bulk nanocomposite magnets via severe plastic deformation, *Applied Physics Letters* **103**, no. 14 (2013), p. 142406.
DOI: 10.1063/1.4824032.

[71]   Hailing Li et al. Tuning the microstructure and magnetic properties of bulk nanocomposite magnets with large strain deformation, *Journal of Magnetism and Magnetic Materials* **425** (2017), pp. 84–89.
DOI: 10.1016/j.jmmm.2016.10.126.

[72]   A. G. Popov et al. High-pressure-torsion deformation of melt-spun Nd9Fe85B6 alloy, *The Physics of Metals and Metallography* **104**, no. 3 (2007), pp. 238–247.
DOI: 10.1134/S0031918X07090050.

[73] A. G. Popov, V. V. Serikov, and N. M. Kleinerman. Thermomagnetic and Mössbauer studies of structural transformations caused in the amorphous Nd9Fe85B5 alloy by severe plastic deformation and annealing, *The Physics of Metals and Metallography* **109**, no. 5 (2010), pp. 505–513.
DOI: 10.1134/S0031918X1005011X.

[74] I. V. Shchetinin et al. Structure and magnetic properties of Sm2Fe17Nx alloys after severe plastic deformation by high pressure torsion, *Materials Letters* **274** (2020), p. 127993.
DOI: 10.1016/j.matlet.2020.127993.

[75] Akihide Hosokawa and Yusuke Hirayama. Cold consolidation and coercivity enhancement in Sm2Fe17N3 magnets by high-pressure torsion, *Scripta Materialia* **226** (2023), p. 115251.
DOI: 10.1016/j.scriptamat.2022.115251.

[76] Maxim Ulyanov et al. Structural properties of Fe49Ni49Ti2 alloy deformed by high pressure torsion, *AIP Advances* **11**, no. 2 (2021), p. 025311.
DOI: 10.1063/9.0000084.

[77] Ulyanov M.n et al. INFLUENCEOF HIGH PRESSURE TORSION ON MAGNETIC PROPERTIES FE50NI50 AND FE49NI49AL2 ALLOYS, *Chelyabinsk Physical and Mathematical Journal* **6**, no. 2 (2021), pp. 255–263.

[78] Sergey V. Taskaev et al. Magnetic Properties of Ternary Fe–Ni–Ti Alloys After Severe Plastic Deformation, *IEEE Magnetics Letters* **11** (2020). Conference Name: IEEE Magnetics Letters, pp. 1–4.
DOI: 10.1109/LMAG.2020.2993133.

[79] M. Kołodziej et al. Structural transformations and magnetic properties of plastically deformed FeNi-based alloys synthesized from meteoritic matter, *Journal of Magnetism and Magnetic Materials* **502** (2020), p. 166577.
DOI: 10.1016/j.jmmm.2020.166577.

[80] Seungwon Lee and Z. Horita. Annealing Behavior of FeNi Alloy Processed by High-Pressure Torsion, *Materials Science Forum* **667-669** (2011). Publisher: Trans Tech Publications Ltd, pp. 313–318.
DOI: 10.4028/www.scientific.net/MSF.667-669.313.

[81] T. Ohtsuki et al. Nanoscale characterization of FeNi alloys processed by high-pressure torsion using photoelectron emission microscope, *Journal of Applied Physics* **114**, no. 14 (2013), p. 143905.
DOI: 10.1063/1.4824372.

[82] Seungwon Lee et al. Formation of FeNi with L10-ordered structure using high-pressure torsion, *Philosophical Magazine Letters* **94**, no. 10 (2014). Publisher: Taylor & Francis _eprint: https://doi.org/10.1080/09500839.2014.955546, pp. 639–646.
DOI: 10.1080/09500839.2014.955546.

[83] M. V. Gorshenkov et al. Magnetic properties of Mn-Al alloy after HPT deformation, *Materials Letters* **272** (2020), p. 127864.
DOI: 10.1016/j.matlet.2020.127864.

[84] A. S. Fortuna, M. V. Gorshenkov, and R. V. Sundeev. The effect of high-pressure torsion on the structure and long-range order of ferromagnetic τ-MnAl alloy, *Materials Letters* **296** (2021), p. 129888.
DOI: 10.1016/j.matlet.2021.129888.

[85] A. S. Fortuna et al. Influence of annealing on the microstructure and magnetic properties of the τ-MnAl alloy deformed by high pressure torsion, *Journal of Alloys and Compounds* **901** (2022), p. 163424.
DOI: 10.1016/j.jallcom.2021.163424.

[86] Yuxiao Jia et al. $L{1}_{0}$ rare-earth-free permanent magnets: The effects of twinning versus dislocations in Mn-Al magnets, *Physical Review Materials* **4**, no. 9 (2020). Publisher: American Physical Society, p. 094402.
DOI: 10.1103/PhysRevMaterials.4.094402.

[87] Yuxiao Jia et al. Roadmap towards optimal magnetic properties in L10-MnAl permanent magnets, *Acta Materialia* **245** (2023), p. 118654.
DOI: 10.1016/j.actamat.2022.118654.

[88] P. W. Bridgman. Effects of High Shearing Stress Combined with High Hydrostatic Pressure, *Physical Review* **48**, no. 10 (1935). Publisher: American Physical Society, pp. 825–847.
DOI: 10.1103/PhysRev.48.825.

[89] P. W. Bridgman. "SHEARING PHENOMENA AT HIGH PRESSURE OF POSSIBLE IMPORTANCE FOR GEOLOGY", *Volume V Collected Experimental Papers, Volume V*. Cambridge, MA and London, England: Harvard University Press, 1964, pp. 3001–3017.
DOI: 10.4159/harvard.9780674287785.c22.

[90] Eun Yoo Yoon et al. Mechanical properties and thermal stability of bulk Cu cold consolidated from atomized powders by high-pressure torsion, *Journal of Materials Science* **47**, no. 22 (2012), pp. 7770–7776.
DOI: 10.1007/s10853-012-6569-x.

[91] A. V. Korznikov et al. Structure and properties of superfine-grained iron compacted out of ultradisperse powder, *Acta Metallurgica et Materialia* **39**, no. 12 (1991), pp. 3193–3197.
DOI: 10.1016/0956-7151(91)90054-5.

[92] A. Bachmaier, A. Hohenwarter, and R. Pippan. New procedure to generate stable nanocrystallites by severe plastic deformation, *Scripta Materialia* **61**, no. 11 (2009), pp. 1016–1019.
DOI: 10.1016/j.scriptamat.2009.08.016.

[93] I. V. Alexandrov et al. Microstructures and properties of nanocomposites obtained through SPTS consolidation of powders, *Metallurgical and Materials Transactions A* **29**, no. 9 (1998), pp. 2253–2260.
DOI: 10.1007/s11661-998-0103-4.

[94] Hongqi Li et al. Strong and ductile nanostructured Cu-carbon nanotube composite, *Applied Physics Letters* **95**, no. 7 (2009), p. 071907.
DOI: 10.1063/1.3211921.

[95] M. Wurmshuber et al. Ultrafine-grained Tungsten by High-Pressure Torsion – Bulk precursor versus powder processing route, *IOP Conference Series: Materials Science and Engineering* **580**, no. 1 (2019). Publisher: IOP Publishing, p. 012051.
DOI: 10.1088/1757-899X/580/1/012051.

[96] Martin Stückler et al. Oxide-stabilized microstructure of severe plastically deformed CuCo alloys, *Journal of Alloys and Compounds* **901** (2022), p. 163616.
DOI: 10.1016/j.jallcom.2022.163616.

[97] Lukas Weissitsch et al. Processing of Nanostructured Bulk Fe-Cr Alloys by Severe Plastic Deformation, *Materials Science Forum* **1016** (2021). Conference Name: International Conference on Processing & Manufacturing of Advanced Materials: Processing, Fabrication, Properties, Applications Publisher: Trans Tech Publications Ltd, pp. 1603–1610.
DOI: 10.4028/www.scientific.net/MSF.1016.1603.

[98] Kaveh Edalati. Review on Recent Advancements in Severe Plastic Deformation of Oxides by High-Pressure Torsion (HPT), *Advanced Engineering Materials* **21**, no. 1 (2019). _eprint: https://onlinelibrary.wiley.com/doi/pdf/10.1002/adem.201800272, p. 1800272.
DOI: 10.1002/adem.201800272.

[99] Martin Stückler et al. Magnetic Binary Supersaturated Solid Solutions Processed by Severe Plastic Deformation, *Nanomaterials* **9**, no. 1 (2019). Number: 1 Publisher: Multidisciplinary Digital Publishing Institute, p. 6.
DOI: 10.3390/nano9010006.

[100] A. Bachmaier et al. Tailoring the magnetic properties of nanocrystalline Cu-Co alloys prepared by high-pressure torsion and isothermal annealing, *Journal of Alloys and Compounds* **725** (2017), pp. 744–749.
DOI: 10.1016/j.jallcom.2017.07.200.

[101] Martin Stückler et al. Intermixing of Fe and Cu on the atomic scale by high-pressure torsion as revealed by DC- and AC-SQUID susceptometry and atom probe tomography, *Acta Materialia* **196** (2020), pp. 210–219.
DOI: 10.1016/j.actamat.2020.06.035.

[102] Martin Stückler et al. Magnetic dilution by severe plastic deformation, *AIP Advances* **10**, no. 1 (2020), p. 015210.
DOI: 10.1063/1.5128058.

[103] J. R. Childress and C. L. Chien. Reentrant magnetic behavior in fcc Co-Cu alloys, *Physical Review B* **43**, no. 10 (1991). Publisher: American Physical Society, pp. 8089–8093.
DOI: 10.1103/PhysRevB.43.8089.

[104] Helmut Kronmüller and Manfred Fähnle. *Micromagnetism and the Microstructure of Ferromagnetic Solids.* Publication Title: Micromagnetism and the Microstructure of Ferromagnetic Solids ADS Bibcode: 2003mmfs.book.....K. 2003. 448 pp.

[105] T. D. Shen, R. B. Schwarz, and J. D. Thompson. Soft magnetism in mechanically alloyed nanocrystalline materials, *Physical Review B* **72**, no. 1 (2005). Publisher: American Physical Society, p. 014431.
DOI: 10.1103/PhysRevB.72.014431.

[106] R. Moreno et al. Temperature-dependent exchange stiffness and domain wall width in Co, *Physical Review B* **94**, no. 10 (2016). Publisher: American Physical Society, p. 104433.
DOI: 10.1103/PhysRevB.94.104433.

[107] C. L. Chien et al. Magnetic properties of ${\mathrm{Fe}}_{\mathit{x}}$$${\mathrm{Cu}}_{100\mathrm{\ens}}\mathit{x}}$ solid solutions, *Physical Review B* **33**, no. 5 (1986). Publisher: American Physical Society, pp. 3247–3250.
DOI: 10.1103/PhysRevB.33.3247.

[108] P. Crespo et al. Magnetic and structural properties of as-milled and heat-treated bcc-Fe70Cu30 alloy, *Journal of Magnetism and Magnetic Materials* **150**, no. 3 (1995), pp. 409–416.
DOI: 10.1016/0304-8853(95)00280-4.

[109] T. Ambrose, A. Gavrin, and C. L. Chien. Magnetic properties of metastable fcc Fe-Cu alloys prepared by high energy ball milling, *Journal of Magnetism and Magnetic Materials* **124**, no. 1 (1993), pp. 15–19.
DOI: 10.1016/0304-8853(93)90063-8.

[110] Oldřich Schneeweiss et al. Magnetic properties of the CrMnFeCoNi high-entropy alloy, *Physical Review B* **96**, no. 1 (2017). Publisher: American Physical Society, p. 014437.
DOI: 10.1103/PhysRevB.96.014437.

[111] C. L. Chien et al. Magnetic Percolation in New Crystalline FCC Fe-Cu Alloys, *MRS Online Proceedings Library* **80**, no. 1 (1986), pp. 395–400.
DOI: 10.1557/PROC-80-395.

[112] Martin Stückler et al. Sampling the Cu–Fe–Co phase diagram by severe plastic deformation for enhanced soft magnetic properties, *Journal of Materials Research and Technology* **12** (2021), pp. 1235–1242.
DOI: 10.1016/j.jmrt.2021.03.073.

[113] Martin Stückler et al. In situ AC-hysteresis measurements of SPD-processed Cu20(Fe15Co85)80, *AIP Advances* **11**, no. 1 (2021), p. 015033.
DOI: 10.1063/9.0000009.

[114] G. Binasch et al. Enhanced magnetoresistance in layered magnetic structures with antiferromagnetic interlayer exchange, *Physical Review B* **39**, no. 7 (1989). Publisher: American Physical Society, pp. 4828–4830.
DOI: 10.1103/PhysRevB.39.4828.

[115] M. N. Baibich et al. Giant Magnetoresistance of (001)Fe/(001)Cr Magnetic Superlattices, *Physical Review Letters* **61**, no. 21 (1988). Publisher: American Physical Society, pp. 2472–2475.
DOI: 10.1103/PhysRevLett.61.2472.

[116]   John Q. Xiao, J. Samuel Jiang, and C. L. Chien. Giant magnetoresistance in nonmultilayer magnetic systems, *Physical Review Letters* **68**, no. 25 (1992). Publisher: American Physical Society, pp. 3749–3752.
DOI: 10.1103/PhysRevLett.68.3749.

[117]   A. E. Berkowitz et al. Giant magnetoresistance in heterogeneous Cu-Co alloys, *Physical Review Letters* **68**, no. 25 (1992). Publisher: American Physical Society, pp. 3745–3748.
DOI: 10.1103/PhysRevLett.68.3745.

[118]   Stefan Wurster et al. Tuneable Magneto-Resistance by Severe Plastic Deformation, *Metals* **9**, no. 11 (2019). Number: 11 Publisher: Multidisciplinary Digital Publishing Institute, p. 1188.
DOI: 10.3390/met9111188.

[119]   Stefan Wurster et al. Microstructural Changes Influencing the Magnetoresistive Behavior of Bulk Nanocrystalline Materials, *Applied Sciences* **10**, no. 15 (2020). Number: 15 Publisher: Multidisciplinary Digital Publishing Institute, p. 5094.
DOI: 10.3390/app10155094.

[120]   M. Kasalo et al. Magnetoresistive behaviour of ternary Cu-based materials processed by high-pressure torsion, *IOP Conference Series: Materials Science and Engineering* **1249**, no. 1 (2022). Publisher: IOP Publishing, p. 012047.
DOI: 10.1088/1757-899X/1249/1/012047.

[121]   D.V. Gunderov et al. "Phase Transformation in Crystalline and Amorphous Rapidly Quenched Nd-Fe-B Alloys under SPD", *Nanomaterials by Severe Plastic Deformation*. John Wiley & Sons, Ltd, 2004, pp. 165–169.
DOI: https://doi.org/10.1002/3527602461.ch3i. eprint: https://onlinelibrary.wiley.com/doi/pdf/10.1002/3527602461.ch3i.

[122]   Fuchen Hou et al. Evolution of microstructures and magnetic properties in bulk Nd-Fe-Cu-B nanocomposites prepared by high pressure thermal deformation, *Journal of Magnetism and Magnetic Materials* **499** (2020), p. 166271.
DOI: 10.1016/j.jmmm.2019.166271.

[123]   Lukas Weissitsch et al. Strain Induced Anisotropic Magnetic Behaviour and Exchange Coupling Effect in Fe-SmCo5 Permanent Magnets Generated by High Pressure Torsion, *Crystals* **10**, no. 11 (2020). Number: 11 Publisher: Multidisciplinary Digital Publishing Institute, p. 1026.
DOI: 10.3390/cryst10111026.

[124]   Bartlomiej J. Bonarski et al. Texture Evolution of Magnesium Single Crystals Deformed by High-Pressure Torsion, *Materials Science Forum* **584-586** (2008). Publisher: Trans Tech Publications Ltd, pp. 263–268.
DOI: 10.4028/www.scientific.net/MSF.584-586.263.

[125]   Michael Zawodzki et al. Exchange Bias Demonstrated in Bulk Nanocomposites Processed by High-Pressure Torsion, *Nanomaterials* **13**, no. 2 (2023). Number: 2 Publisher: Multidisciplinary Digital Publishing Institute, p. 344.
DOI: 10.3390/nano13020344.

[126] E. Menéndez et al. Cold compaction of metal–ceramic (ferromagnetic–antiferromagnetic) composites using high pressure torsion, *Journal of Alloys and Compounds.* Proceedings of the 12th International Symposium on Metastable and Nano-Materials (ISMANAM-2005) **434-435** (2007), pp. 505–508.
DOI: 10.1016/j.jallcom.2006.08.142.

[127] Vladimir V. Popov et al. Microstructure and magnetic properties of Mn-Al-C permanent magnets produced by various techniques, *Manufacturing Review* **8** (2021). Publisher: EDP Sciences, p. 10.
DOI: 10.1051/mfreview/2021008.

[128] Lukas Weissitsch et al. Synthesis of hard magnetic α-MnBi phase by high pressure torsion and field assisted annealing, *Journal of Magnetism and Magnetic Materials* **584** (2023), p. 171082.
DOI: 10.1016/j.jmmm.2023.171082.

[129] V. A. Beloshenko and V. V. Chishko. Deformation-heat treatment of Nb-Ti superconductors using severe plastic deformation methods, *The Physics of Metals and Metallography* **114**, no. 12 (2013), pp. 992–1002.
DOI: 10.1134/S0031918X13090032.

[130] Kaveh Edalati et al. High strength and superconductivity in nanostructured niobium–titanium alloy by high-pressure torsion and annealing: Significance of elemental decomposition and supersaturation, *Acta Materialia* **80** (2014), pp. 149–158.
DOI: 10.1016/j.actamat.2014.07.065.

[131] Masaki Mito et al. Large enhancement of superconducting transition temperature in single-element superconducting rhenium by shear strain, *Scientific Reports* **6**, no. 1 (2016). Number: 1 Publisher: Nature Publishing Group, p. 36337.
DOI: 10.1038/srep36337.

[132] Terukazu Nishizaki et al. Superconducting properties in bulk nanostructured niobium prepared by high-pressure torsion, *Physica C: Superconductivity.* New3SC-9 **493** (2013), pp. 132–135.
DOI: 10.1016/j.physc.2013.03.046.

[133] M. J. R. Sandim et al. Size effects on the magnetic properties of Cu–Nb nanofilamentary wires processed by severe plastic deformation, *Superconductor Science and Technology* **19**, no. 12 (2006), p. 1233.
DOI: 10.1088/0953-2048/19/12/002.

[134] M. Ullrich et al. High temperature deformation of Bridgman melt-textured YBCO, *Materials Science and Engineering: B* **53**, no. 1 (1998), pp. 143–148.
DOI: 10.1016/S0921-5107(97)00317-6.

[135] Wenqian Wu et al. Dual mechanisms of grain refinement in a FeCoCrNi high-entropy alloy processed by high-pressure torsion, *Scientific Reports* **7**, no. 1 (2017). Number: 1 Publisher: Nature Publishing Group, p. 46720.
DOI: 10.1038/srep46720.

[136]   Natalia Shkodich et al. Effect of High-Pressure Torsion on the Microstructure and Magnetic Properties of Nanocrystalline CoCrFeNiGax (x = 0.5, 1.0) High Entropy Alloys, *Materials* **15**, no. 20 (2022). Number: 20 Publisher: Multidisciplinary Digital Publishing Institute, p. 7214. DOI: 10.3390/ma15207214.

[137]   R. Chulist et al. Microstructure and texture in Ni50Mn29Ga21 deformed by high-pressure torsion, *Scripta Materialia* **62**, no. 9 (2010), pp. 650–653. DOI: 10.1016/j.scriptamat.2010.01.016.

Synthesis of hard magnetic α-MnBi phase by high pressure torsion and field assisted annealing

Lukas Weissitsch[a], Stefan Wurster[a], Martin Stückler[a,$\diamond$], T. Müller[b,♣], Heinz Krenn[c], Reinhard Pippan[a] and Andrea Bachmaier[a]

[a] *Erich Schmid Institute of Materials Science, Austrian Academy of Sciences, Jahnstraße 12, 8700 Leoben, Austria*

[b] *Deutsches Elektronen Synchrotron (DESY), 22607 Hamburg, Germany*

[c] *Institute of Physics, University of Graz, Universitätsplatz 5, 8010 Graz, Austria*

$\diamond$ *Current address: TDK Electronics GmbH & Co OG, 8530 Deutschlandsberg, Austria*

♣ *Current address: Anton Paar GmbH, Anton-Paar-Str. 20, 8054 Graz, Austria*

Abstract

Bulk composites using powder blends of Mn and Bi with equal atomic ratios are consolidated and severely deformed by high-pressure torsion (HPT). Subsequent annealing treatments lead to the formation of the ferromagnetic and rare-earth free hard magnetic α-MnBi phase. The initial phase formation is studied by in-situ high-energy XRD annealing experiments showing a beneficial influence of HPT-deformation on the amount of α-MnBi. The nucleation sites are strongly increased, thus the volumetric α-MnBi phase content exceeds 50 vol.%. A lower HPT-pressure of 2 GPa is found to be preferred over 5 GPa to obtain high α-MnBi contents. Annealing is done with or without applying an external magnetic field. Additionally, influences of the HPT-induced shear deformation are discussed and correlated with preferred diffusion path ways fostering the formation of anisotropic α-MnBi phase.

F. Synthesis of hard magnetic α-MnBi phase by HPT and field assisted annealing

Keywords: Plastic deformation; Magnetic properties; in-situ High-energy X-ray diffraction; diffusion; phase nucleation and growth; anisotropic magnetic properties

Figure F.0.: Graphical Abstract

F.1. Introduction

For several decades, the MnBi system has attracted the attention of researchers. Since the 1950's, the magnetic properties of this material system have been studied, fostering possible applications as a permanent magnet material [1, 2]. The equilibrium phase diagram has been constantly improved [1, 3–5]. Nowadays, phase transitions and their crystal structures are widely understood [6, 7]. Recent research interest focuses on the intermetallic and ferromagnetic low-temperature phase of equiatomic composition, denoted as the 'α-MnBi phase', which exhibits exceptional hard magnetic properties. A rare and interesting phenomenon is the positive temperature coefficient of intrinsic coercivity for temperatures $T < 500\,\text{K}$ [8, 9], originating in a large and peaking magnetocrystalline anisotropy of about $2.2\,\text{MJ/m}^3$ above $400\,\text{K}$ [6, 10, 11]. Thus, this material is particularly interesting as a permanent magnet for high-temperature applications.

However, two drawbacks are known: first, the low saturation magnetization (M_s) of hard magnetic materials, which is about 79 emu/g for α-MnBi [12]. This could be circumvented if exchange coupling between the hard magnetic α-MnBi phase and a soft magnetic material is induced. Second, processing the α-MnBi phase in sufficient quantities is a challenging task. Thus, the main goal of this work is to show that a comparatively easy process of severe plastic deformation by high-pressure torsion (HPT), in concatenation with an adequate subsequent annealing step, can be used to process large quantities of α-MnBi.

The current roadmap of fabricating MnBi-based permanent magnets starts with the formation of a high-purity α-MnBi phase in the form of an alloy or powder, which then has to be reprocessed to form bulk materials, usually referred to as a top-down approach. A very effective way is to utilize rapid cooling processes and subsequent annealing procedures. Several studies show the presence of α-MnBi phase in materials after arc-melting [8, 13, 14] or melt spinning [15–17], which are then ground, milled, magnetically separated, and compacted. Maintaining good magnetic properties during such consolidation processes is challenging and a task on its own [18]. Sometimes, this includes the alignment of the powders in a magnetic field or the alloying of additional elements to obtain a dense (anisotropic) green body [19, 20]. At this stage of processing, materials possess strongly refined particle sizes within the range down to the single domain size (about 250 nm [21]). A subsequent proper annealing treatment allows the formation of the high temperature β-MnBi phase, which is transferred upon slow cooling and a peritectic transition, to the α-MnBi phase [4, 11, 15, 22, 23]. Such a procedure significantly increases the amount of the desired phase, already showing incredible results up to 98 wt% α-MnBi content. However, for industrial utilization, a high demand for a simplified processing route exists.

For this, a bottom-up technique is implemented, where the starting materials can be powders and one directly obtains a bulk material. To generate the desired α-MnBi phase, HPT, a severe plastic deformation method, is introduced herein. HPT-deformation allows obtaining large sample sizes with dimensions of several millimeters up to centimeters, whereas the microstructure simultaneously features particle and grain sizes in the range between micrometers to tens of nanometers [24]. As starting materials, bulk materials, or any powder blends, which can be also consolidated in an inert gas atmosphere, are convenient. To compare this technique with other deformation processes, the applied shear strain γ is often converted to the von Mises equivalent strain ε, which is based on the equivalence of deformation energy and

F. Synthesis of hard magnetic α-MnBi phase by HPT and field assisted annealing

described by [25]

$$\varepsilon = \frac{\gamma}{\sqrt{3}} = \frac{1}{\sqrt{3}} \cdot \frac{2\pi r}{t} n,$$

where r is the radial distance of the analyzed part of the sample to the HPT rotation axis, t the thickness of the cylindrical specimen in the axial direction, and n the number of applied revolutions. Very large amounts of deformation can easily be applied, as the shear strain is directly proportional to the number of revolutions. HPT usually leads to a shear texture and a pronounced grain refinement, yet in principle, a broad variety of microstructural morphologies can be obtained [26]. The possibility to combine completely different processing steps, inter alia, powder compaction (equivalent to sintering), grain refinement, and texturing is notable and will open new opportunities in the production of MnBi permanent magnets. The main drawback of HPT is the limited sample size, although upscaling is possible [27]. However, HPT is the easiest way to study the influence of high applied strains, and the results can be adapted for more continuous and industrially relevant manufacturing designs [28].

In this study, we first discuss the influence of HPT-processing parameters (e.g., applied pressure, amount of applied strain) on the formation of the α-MnBi phase during subsequent annealing. The α-MnBi phase formation is monitored by scanning electron microscopy (SEM) as well as by high energy X-ray diffraction (HEXRD) in-situ annealing experiments using synchrotron-radiation. In the second part, the annealing procedure is further improved applying a vacuum and magnetic field environment while annealing. The influence of the direction of applied magnetic field with respect to the HPT-induced microstructural texture is extensively studied by SQUID magnetometry. The thorough investigation of the large parameter space provides sound knowledge on influences of processing steps on the α-MnBi phase formation which further allows setting the magnetic properties by tuning the process accordingly.

F.2. Experimental

F.2.1. Sample preparation

Binary powder blends with an equal atomic ratio are mixed using conventional high purity powders (Mn: Alfa Aesar 99.95% - 325 mesh; Bi: Alfa Aesar 99.999% - 200 mesh). Ball milling of the powder blends is done by using an air-cooled planetary ball mill (Retsch PM400), with a 1:20 powder-to-ball ratio at 300 rpm and a total

milling time up to 4 h. To prevent heat development inside the jar, the milling process is interrupted every 60 min for at least 30 min. To prevent oxidation, the powder handling, ball-milling as well as the consolidation process is carried out in an Ar-atmosphere. The powder blends are hydrostatically consolidated in the HPT device; these samples will herein be denoted as HPT-compacted. Further samples are subsequently HPT-deformed at a nominal pressure of 2 or 5 GPa for 30 revolutions and at room temperature (RT) using a rotation speed of ~ 0.6 rpm supported by high-pressure air cooling to avoid a temperature increase through inner friction. In the second part of this study, the development of an even simpler process is intended, utilizing powder blends without previous ball-milling. The powders are HPT-compacted and deformed by applying 10 revolutions at a nominal pressure of 2 GPa at RT by 0.6 rpm and high-pressure air cooling. To study the α-MnBi phase formation with respect to the HPT-induced textured microstructure of Bi, an additional Bi sample is processed from Bi-granules (HMW Hauner 99.99% < 5 mm) and deformed by 25 revolutions at a nominal pressure of 2 GPa.

F.2.2. Annealing treatments

Quarters or eighths of HPT-deformed samples are conventionally annealed (CA) under ambient conditions at 230 °C with dwell times between 4 h and 120 h. The specimens are wrapped in a protective foil before the isothermal treatment. After the annealing process, they are quenched in ethanol.

For in-situ HEXRD experiments, quarters of HPT samples are investigated by heating them with an in-situ heating stage (THMS600 Linkam, Tadworth, United Kingdom), entailing a custom-made sample holder to mount the samples inside an Ar-flushed chamber, suppressing the formation of oxides. The specimens are heated with a heating rate of 2 °Cs^{-1}, isothermally held at 240 °C for 3 h followed by furnace cooling down below 40 °C. The lattice parameter change of a reference Cu specimen upon the same annealing treatment settings is used to calibrate the recorded temperature measured by a thermocouple mounted in the heating plate underneath the sample.

The Magnetic field assisted Vacuum Annealing (MVA) procedure is realized by a custom-made vacuum chamber fitting into the homogeneous field region provided by the conical pole pieces (diameter of 176 mm) of an electromagnet (Type B-E 30, Bruker), operated at a constant magnetic field of 2 T. Within the vacuum chamber, two copper blocks, each containing a cartridge heating element (Keller, Ihne & Tesch

F. Synthesis of hard magnetic α-MnBi phase by HPT and field assisted annealing

Ges. m.b.H.; HHP, $\varnothing 10 \times$ L50 mm, 100 W) are positioned. These blocks embrace an especially designed copper specimen holder. Fig. F.1a) shows a photograph of parts of the specimen holder on the upper left and a schematic representation of the described vacuum set-up. The specimen holder hosts up to eight halved HPT discs (drawn in green), which are heated by the direct heat transfer through the copper stock. A thermocouple is mounted next to the specimens allowing monitoring the constancy of the temperature, which is set to 240 °C for all MVA experiments. The applied external magnetic field is recorded using a Hall-probe (Model 475 DSP, Lakeshore), placed next to the vacuum chamber.

The applied shear strain during HPT-deformation is known to induce a crystallographic alignment (texture), which accordingly influences the magnetic properties [29]. Therefore, the applied field direction during MVA with respect to the HPT-disc orientations is expected to have an impact on the α-MnBi formation. For this reason, the sample holder allows a perpendicular and parallel mount of the sample axis in regard to the applied magnetic field. As depicted in the schematics (Fig. F.1b)), the applied external field (H-field) penetrates the HPT-disc, allowing extracting pieces, which are field annealed parallel to their axial, tangential, or radial HPT-disc direction. In the following, these samples are denoted as B_{ax}, B_{tan}, and B_{rad}, respectively.

F.2.3. Microstructural characterization

The microstructure is investigated using a SEM (LEO 1525, Carl Zeiss Microscopy GmbH), where images are recorded in backscattered electron (BSE) mode in tangential HPT-disc orientation. Electron backscatter diffraction (EBSD) examination is performed with a Bruker e$^-$-Flash^{FS} detector and for chemical analysis, energy dispersive X-ray spectroscopy (EDX; XFlash 6|60 device, Bruker) is applied. X-ray diffraction measurements (XRD; Bruker Phaser D2, Co-K$_\alpha$-radiation) are applied to the plane surface with the diffraction vector in the axial direction of the HPT-disc. References for expected peak positions are taken from the Crystallography Open Database (Mn: COD 9011108, Bi: COD 9008576, α-MnBi: COD 9008899) [30]. Hardness measurements (Micromet 5104, Buehler) are performed in the tangential HPT-disc direction on the polished sample with an indentation load of 50–100 g. The sample's density is determined by a balance (Sartorius Secura225D-1S) and a density determination kit (Sartorius YDK03), applying the principle of Archimedes. The density of the reference medium (soapy water, $\rho = 0.997105 \, \mathrm{g/cm^3}$) is measured using
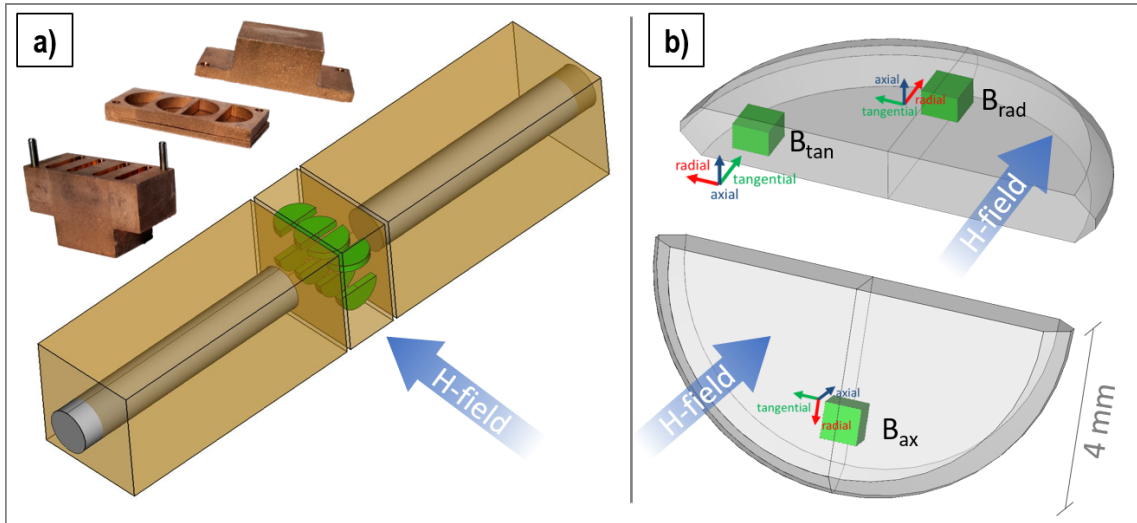
Figure F.1.: a) Schematic representation of the vacuum annealing construction. Two heating elements are embedded in copper blocks, heating the sample holder (photograph on upper left) by direct contact. The samples (illustrated in green) can be mounted in two different orientations (parallel and perpendicular to the applied external field). b) The external applied field penetrates the sample in three different directions with respect to the hpt-disc orientation (radial, tangential, axial). Within one sample, three pieces for SQUID measurements with different field annealing directions are obtained.

a reference volume (10 cm^3).

Magnetic results are obtained by a SQUID-magnetometer (Quantum Design MPMS-XL-7, Quantum Design, Inc., San Diego, CA, USA) operated with the manufacturer's software MPMSMultiVu Application (version 1.54). All hysteresis loops are measured between ±65 kOe. Synchrotron high-energy X-ray diffraction (HEXRD) experiments are performed in transmission mode, parallel to the axial HPT-disc direction, at the beamline P21.2 at PETRA III (DESY, Hamburg, Germany) [31]. The spot size is set to $200 \times 200\,\mu m^2$, and a photon energy of 60 keV is used. Wide-angle X-ray scattering (WAXS) diffraction patterns are recorded by two Varex XRD 4343 CT flat panel detectors at 0.2 Hz during the in-situ annealing treatment. The experimental setup is calibrated using LaB6, and 2D patterns are azimuthally integrated using PyFAI [32].

F.3. Results

F.3.1. Influence of pressure and HPT-deformation on α-MnBi formation

A highly uniform Mn and Bi phase distribution is required to focus on the characteristics of the α-MnBi phase formation, which is realized by ball milling of the powder blends. To monitor the ball milling process, the milling process is interrupted every 60 min and measured by XRD. The XRD patterns are shown in Fig. F.2 wherein the position for theoretical reference peaks of Mn, Bi, and the α-MnBi phases are indicated by vertical lines. The diffraction patterns reveal peak broadening within the first two hours, but no further significant changes regarding phase evolution, peak intensity changes, or peak broadening up to 4 h milling time are visible. Thus, after 4 h, a steady state seems to be well established, and this powder is used for further experiments.
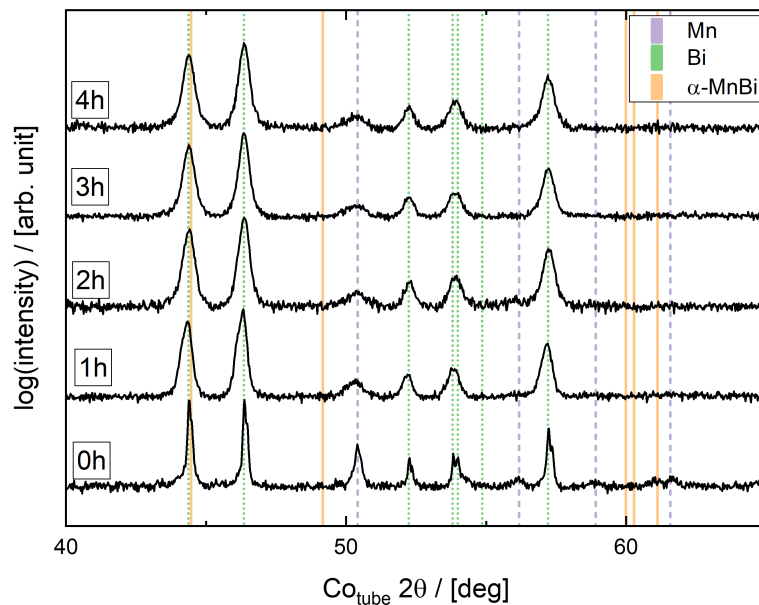
Figure F.2.: XRD measurements of a MnBi powder blend after ball milling for different times. Peak broadening stagnates after 2 h of milling time. No α-MnBi phase formation is detected.

To separate the influence of HPT-consolidation and HPT-deformation on the α-MnBi phase formation, further experiments are performed on compacted powder blends, whereby one sample is compacted at 2 GPa and another one at 5 GPa. The compacted samples are cut and suspended for annealing treatments at 230 °C in

ambient conditions for different times. BSE images recorded in the tangential HPT-disc direction are presented in Fig. F.3. The samples compacted at 2 GPa and 5 GPa are shown in the first and second columns, respectively, while the annealing time increases from top to bottom. In the as-compacted state (labeled with 0 h), a microstructure with homogeneously dispersed Mn particles is found. After 4 h of annealing, a contrast change of the 2 GPa compacted sample indicates the formation of a new phase (marked by arrows).

When annealing for 24 h, this phase appears as cigar-shaped silhouettes for both samples. However, larger, but fewer "cigar-regions" are found for the 2 GPa sample compared to the 5 GPa sample. EDX mapping of a part of one of these "cigar-regions" (shown in the last row of Fig. F.3) reveal an equally strong and coeval appearance of Mn (orange) and Bi (green). Quantitative analysis gives an indication for the presence of the α-MnBi phase, but small Mn particles being present within the analyzed volume impede accurate quantification. The uniform distribution of Mn and Bi does not prevail outside these "cigar-regions", where a strict distinction between the two phases is present. In addition, indentation hardness also revealed differences between the new forming phase (66 ± 3 HV) and the surrounding matrix (40 ± 2 HV).

Unexpectedly, the α-MnBi phase starts to vanish after annealing for 48 h. This behavior is stronger pronounced for the 2 GPa sample and in addition, the morphology of the sample surface changes, as an oxide layer is formed. Confirmed by EDX measurements (see Figure Supplementary F.1), mainly Mn-oxide formation occurs and the development of this layer inversely scales with the visible amount of α-MnBi phase.

To investigate the α-MnBi phase formation in more detail, in-situ annealing HEXRD experiments are conducted for samples processed with different applied pressure (2 GPa and 5 GPa) and strain (HPT-compacted and HPT-deformed to 30 turns). Integrated intensity plots of every measurement during the complete annealing experiment for all four samples are shown in Fig. F.4.

The {220} Mn peak is found in all recorded spectra and the α-MnBi phase forms in each performed experiment. For all samples, the {101} α-MnBi peak is visible at the end of the annealing treatment but arises after different times. After about 200 s, the {101} α-MnBi peak is visible for both HPT-deformed samples. For the compacted samples, the same peak requires more time to emerge and arises after roughly 2000 s and 5000 s for 2 GPa and 5 GPa, respectively. This is more difficult to identify for the
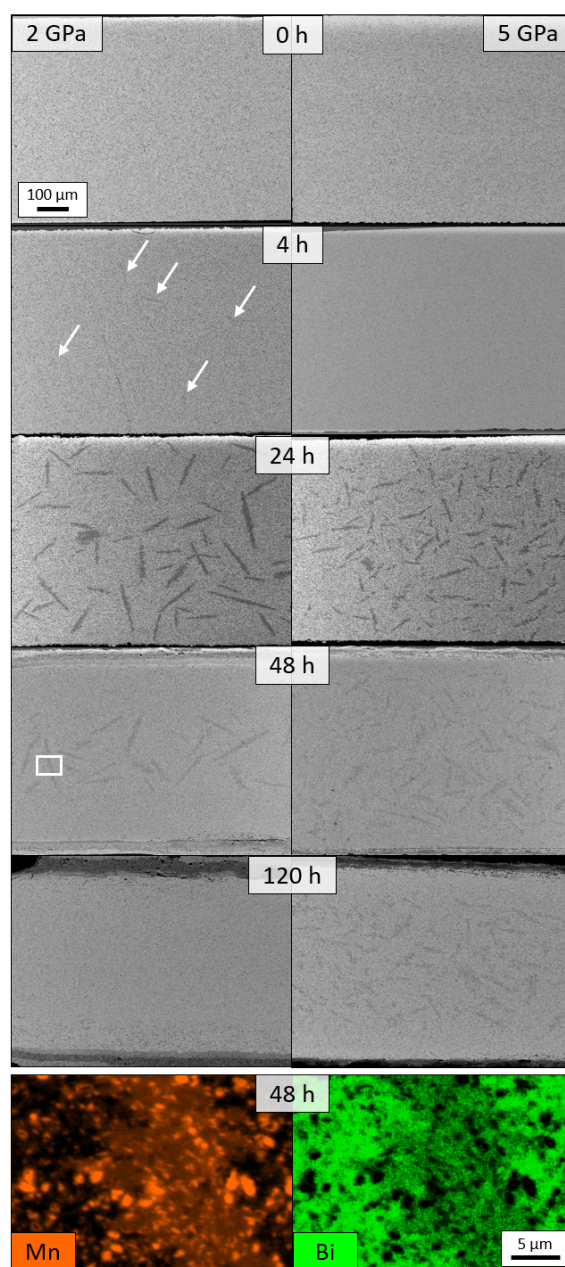
Figure F.3.: BSE images of HPT-compacted MnBi powder blends, compacted at 2 GPa or 5 GPa (left and right column) and annealed under ambient conditions for different times at 230 °C. The last row shows a magnified region of the 2 GPa and 48 h annealed state (white-rimed rectangle), where the distribution of Mn and Bi is visualized by the EDX signal. The cross-sections are recorded in tangential HPT-disc direction, with the axial direction pointing vertically.

5 GPa compacted sample, as an additional peak appears at a slightly lower q-value, which is most likely dedicated to the formation of an oxide which forms faster than the {101} α-MnBi peak. An additional {002} α-MnBi peak is only visible for the 5 GPa compacted sample.

To better understand the observed intensities, sections of the first (initial state = as-processed sample; first row) as well as the last diffractogram of the in-situ annealing experiment (annealed for 3 h; second row) are shown in Fig. F.5. Due to the chosen experimental setup, only a section of the Debye-Scherrer rings is recorded. For the compacted samples, bright spots (exemplarily marked by arrows) indicate the α-MnBi phase formation. For the deformed samples continuous lines with lower intensities at the same diffraction angles confirm the existence of the α-MnBi phase. Diffraction images recorded after 24 h annealing (last row in Fig. F.5), which was performed ex-situ, again show bright spots for compacted samples and continuous rings with low intensity for deformed samples. These differences prove a larger number of differently oriented α-MnBi crystallites in the HPT deformed samples. Furthermore, crystallographic texture is present in the as-processed samples (in particular after HPT-deformation has been applied) as can be seen by the non-homogeneous intensity distribution along the Debye-Scherrer rings.

F.3.2. Influence of magnetic field assisted annealing on the α-MnBi phase formation

Processing of the α-MnBi phase is further improved by MVA, and simplified by using powder blends without ball-milling and a maximum HPT-pressure of 2 GPa. 2 GPa was chosen, as α-MnBi phase formation is faster in this case according to the in-situ HEXRD annealing results. Fig. F.6 shows hysteresis loops of an HPT-compacted and HPT-deformed sample after MVA at 2 T for 4 h, both annealed tangentially (B_{tan} c.f. Fig. F.1b)). The samples are measured between $\pm$ 65 kOe at 300 K. Values for M_s are acquired by linearly extrapolating the magnetization above 35 kOe against H^{-1} and determining the intercept at $M(H^{-1}) = 0$ [33, 34]. For the compacted and MVA-treated sample (triangle, brown curve), an M_s of 9.89 emu/g is found. The deformed sample shows an M_s of 33.92 emu/g at 300 K measurement temperature (cube, green curve) and an M_s of 36.12 emu/g at 10 K (empty cube, blue curve). The coercivity H_c slightly increases from 1.38 kOe to 1.58 kOe for HPT-compacted and HPT-deformed samples, respectively. The H_c of the latter one significantly decreases
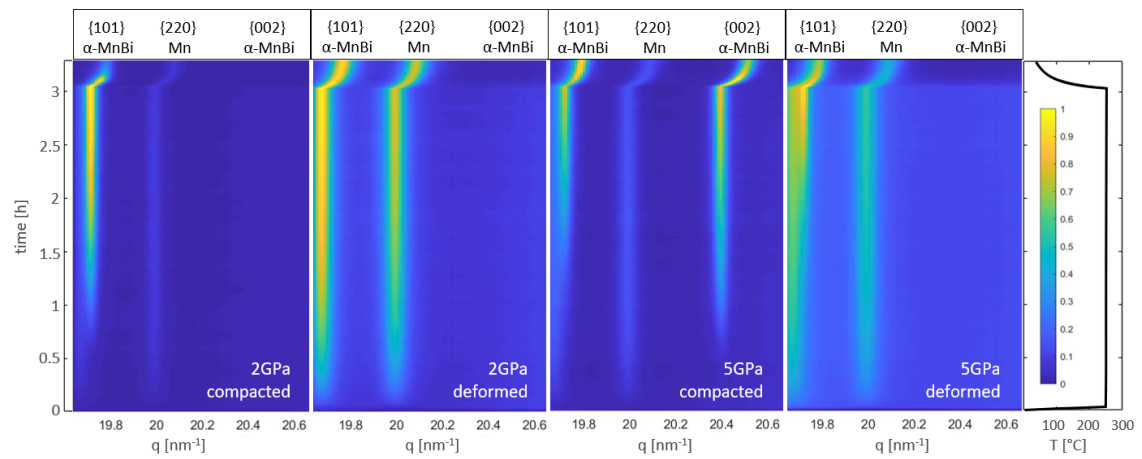
Figure F.4.: Intensity plots of in-situ HEXRD annealing experiments. Four samples, compacted and deformed by 30 revolutions at 2 and 5 GPa are depicted. On the right, the corresponding temperature profile and an intensity scale bar are plotted. The peak intensities are normalized within the presented figures to the respective most intense peak. The q-range is limited to a small representative fraction of the measured q-range, which includes peaks from the relevant phases, to facilitate visual comparison.

Figure F.5.: Selected area detector diffraction patterns of the HEXRD annealing experiments. Tiny spots with high intensities (arrows) are visible for the HPT-compacted samples, while continuous lines with low intensities are found at the same diffraction angle for the HPT-deformed samples. Both of them correspond to the forming α-MnBi phase. The color scheme refers to the normalized intensity of the diffraction pattern.

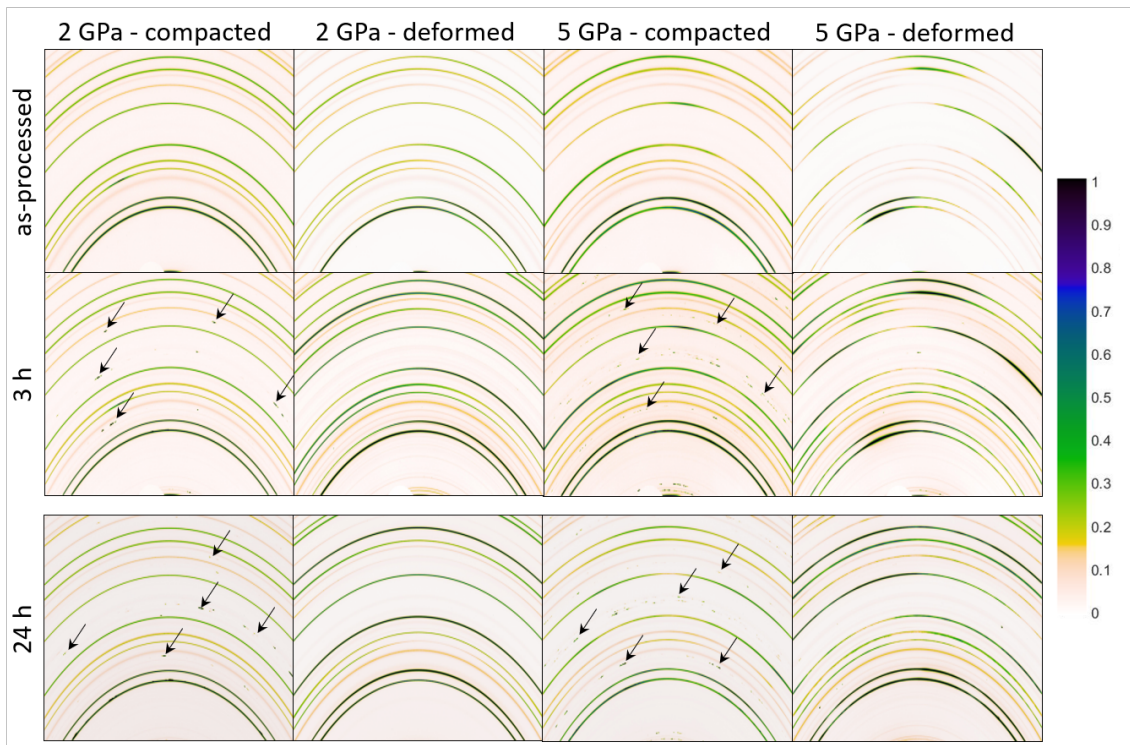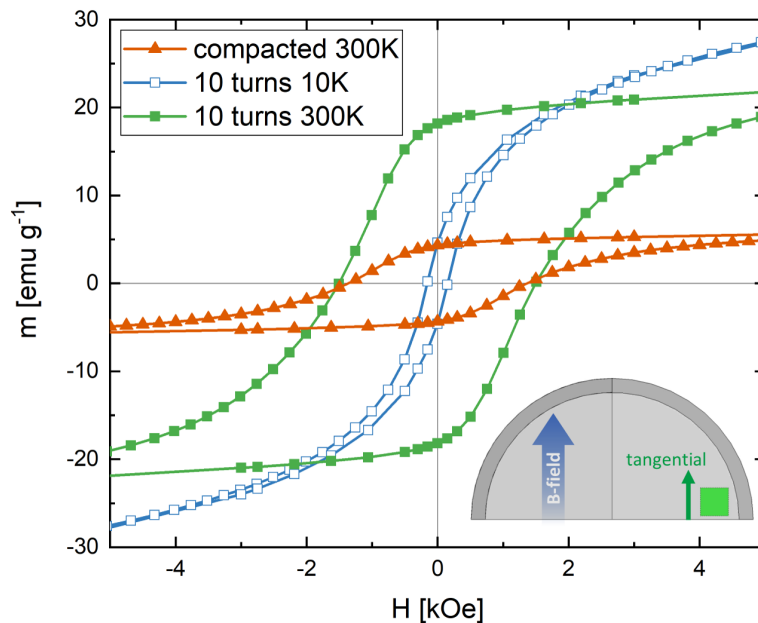Figure F.6.: SQUID magnetometry hysteresis loops of magnetic field assisted vacuum annealed HPT-compacted and HPT-deformed samples. Comparing both processing routes (compaction vs. deformation) M_s substantially rised for the HPT-deformed sample. Hc is reduced for the HPT-deformed sample if measured at 10 K, verifying the existing α-MnBi phase.

by one order of magnitude to 0.16 kOe, if measured at 10 K.

BSE images with different magnifications of the HPT-compacted and HPT-deformed samples after MVA are shown in Fig. F.7. The images are recorded in tangential viewing direction with respect to the HPT-disc. It can be seen, that the α-MnBi phase (medium atomic number (Z), medium grey regions) preferentially forms around existing Mn particles (low Z, dark regions). Larger Mn particles and a lower α-MnBi phase fraction is recognized for the HPT-compacted sample. The Bi phase (high Z, bright regions) of the deformed sample still exhibits grain sizes below 1 μm (see Fig. F.7f)) although the composite material is annealed for 4 h at a homologous temperature of $T_{h,Bi} = 0.89$.

The increased occurrence of the α-MnBi phase formation after HPT-deformation and subsequent MVA is further supported by XRD measurements (Fig. F.8). The halved HPT-discs are MVA-treated with a field direction applied perpendicular (blue lines, B_{ax}) and parallel (red lines, $B_{tan,rad}$) to the HPT-shear deformation. The curves are normalized with respect to the most intense Bi peak at $2\theta = 31.65°$. Dotted lines represent the HPT-compacted and continuous lines the HPT-deformed sample. In

HPT-compacted   HPT-deformed
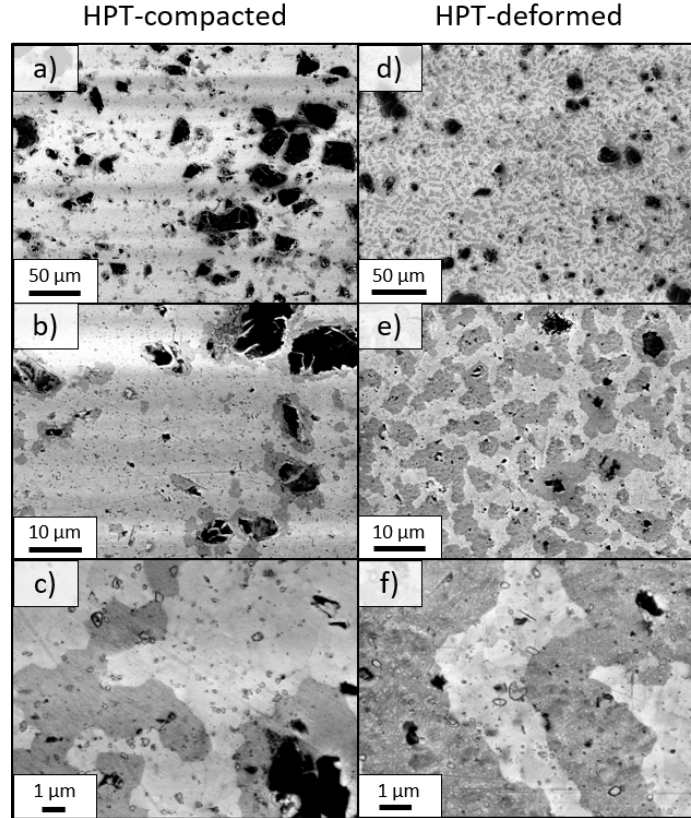
Figure F.7.: BSE images with different magnifications of an HPT-compacted sample after MVA a)-c) and an HPT-deformed (10 revolutions) sample after MVA d)-f).

general, pronounced α-MnBi peaks are visible for HPT-deformed sample, whereas the compacted sample exhibits weaker intensities.

These XRD measurements show a strong improvement of α-MnBi phase formation after HPT-deformation and MVA. Thus, magnetic measurements are conducted to an HPT-deformed sample (10 revolutions, 2GPa) after MVA for 4 h. The induced texture, which is introduced by HPT, and the direction of MVA are set in correlation with the magnetic properties. To do so, three samples (B_{ax}, B_{rad}, and B_{tan}, compare Fig. F.1b)) are measured by SQUID magnetometry. After measuring one hysteresis loop, the sample is demagnetized thus, the remanence M_r is minimized before the applied measurement field direction is rotated for the next measurement. All principal directions with respect to the HPT-disc (axial, radial, tangential) were aligned with the magnetic field and they are denoted as M_{ax}, M_{rad}, and M_{tan}. This is schematically indicated in Fig. F.9, where the MVA field direction is shown as a blue arrow and the samples are highlighted (green cubes) within the HPT-disc. The resulting nine
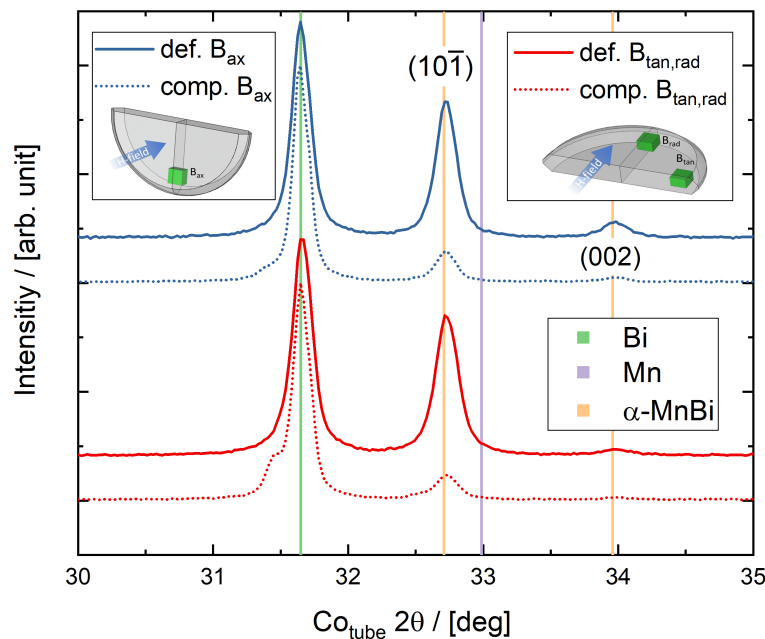
Figure F.8.: X-ray diffraction patterns of HPT-compacted (dotted lines) and HPT-deformed (continuous lines) after magnetic field assisted vacuum annealing. The magnetic field is applied perpendicular (blue lines, B_{ax}) and parallel (red lines, $B_{tan,rad}$) to the shear deformation. A tiny peak slightly lower to the Bi peak is assigned to a forming oxide, but only for the compacted sample.

hysteresis loops are shown in detail as well as complete loops in Fig. F.9. The corresponding magnetic properties are summarized in Table 1.

Table F.1.: Magnetic properties of hysteresis loops presented in Fig. F.9. Samples with different MVA directions are measured in three perpendicular measurement field directions. The corresponding coercivity H_c, saturation magnetization M_s, remnant magnetization M_r and the squareness ratio M_r/M_s are listed.

MVA direction	SQUID direction	H_c [kOe]	M_s [emu g^{-1}]	M_r [emu g^{-1}]	M_r/M_s
B_{ax}	M_{ax}	1.52	33.5	10.5	0.31
B_{ax}	M_{rad}	1.69	35.0	10.9	0.31
B_{ax}	M_{tan}	1.69	33.1	12.7	0.38
B_{rad}	M_{ax}	1.69	33.0	8.7	0.26
B_{rad}	M_{rad}	1.59	34.3	11.2	0.33
B_{rad}	M_{tan}	1.37	33.4	15.1	0.45
B_{tan}	M_{ax}	1.96	35.2	9.1	0.26
B_{tan}	M_{rad}	1.84	35.1	11.1	0.32
B_{tan}	M_{tan}	1.52	33.9	18.1	0.53
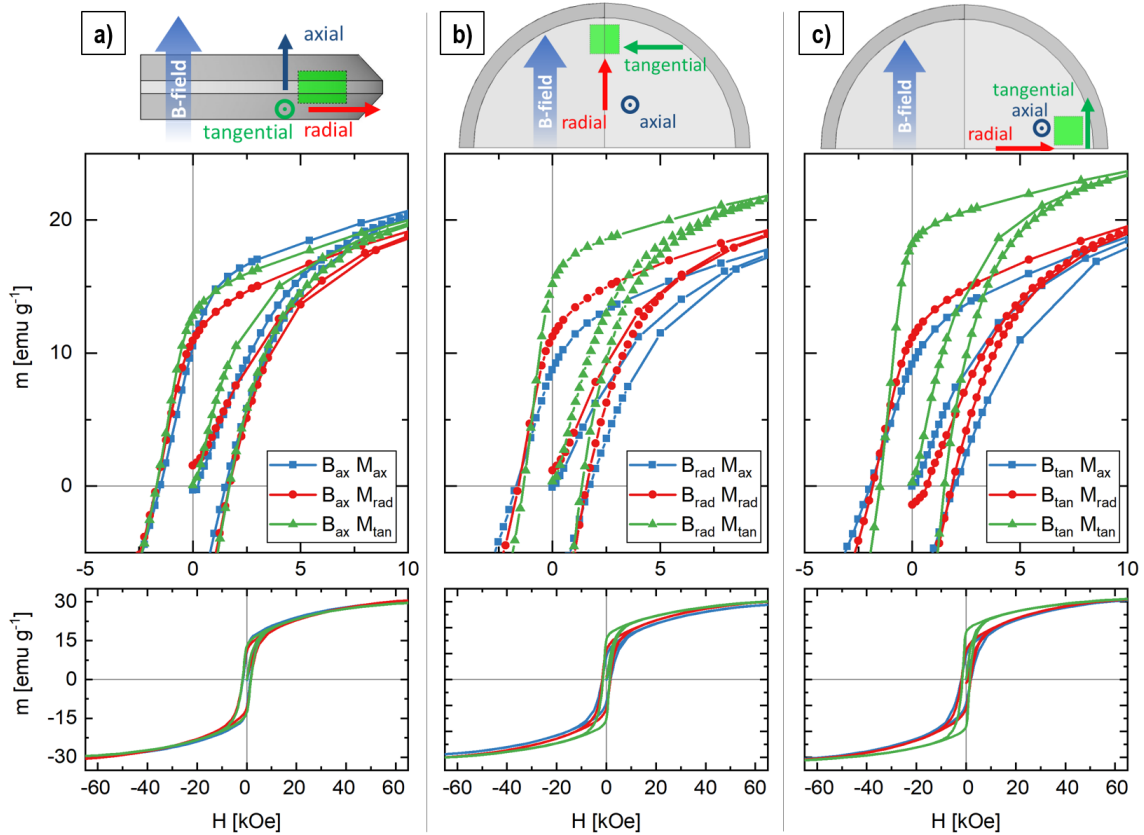
Figure F.9.: Hysteresis loops of an HPT-deformed sample after MVA treatment. Cut pieces (green cubes in scheme) undergo the MVA with field direction applied parallel to the a) axial b) radial and c) tangential HPT-disc direction. Sections as well as the complete hysteresis loops are presented.

F.4. Discussion

F.4.1. Influence of pressure and HPT-deformation on α-MnBi formation

Similarities between HPT-deformation and ball milling are known. In particular, if applied to a single-phase metallic material, the microstructure is generally refined. Although it is possible to induce very high amounts of strain by extensive milling times or by HPT-deformation, the refinement and resulting grain sizes are limited as a steady-state regime is reached [27, 35–37]. By combining both techniques, it is possible to add beneficial advantages, e.g., ball milling allows forming a homogeneously powder blend of refined Mn and Bi particles, and subsequent HPT-deformation leads to a completely dense bulk material. Therefore, highly uniform samples are processed

enabling to profoundly study influences of HPT processing on the α-MnBi formation.

The milling process is often performed with a surfactant meant to further decrease the particle size. However, in a recent study, milling of arc melted ingots within an Ar-gas atmosphere was found to be beneficial for the α-MnBi phase [13, 38–40]. Therefore, the milling process was executed in Ar-atmosphere. The obtained XRD spectra (Fig. F.2) show peak broadening at the beginning of the milling process but do not show any significant changes after 2 h. This is explained by the difference in volumetric content of Mn (17 vol%) and Bi (83 vol%), to obtain the intended equal atomic ratio. The volumetric excess of the ductile Bi is conceived to cover the Mn particles and hinders their further refinement while the kinetic energy is absorbed by the higher plasticity of the Bi phase. A similar behavior upon ball milling of ductile-brittle material systems is already reported [41–43]. BSE images (not shown) of the 4 h milled powder blend reveal a homogeneous dispersion of Mn particles, which are reduced from 44 μm to sizes below 1 μm, enclosed by a Bi matrix. The major part of Mn particle refinement is expected to occur during the first 2 h of milling, yet a homogeneous distribution of Mn particles and sizes within a Bi matrix is assured by all means after 4 h of milling.

An influence of the applied pressure during HPT-compaction is found for the α-MnBi phase formation. A faster phase formation is detected for the 2 GPa sample, as already after 4 h annealing contrast changes in cigar-shaped regions are found, see Fig. F.3. After 24 h annealing time, for both samples, the α-MnBi phase evolved. This is confirmed by EDX measurements (see Fig. F.3) and hardness measurements. The measured hardness values for the α-MnBi phase (66 ± 3 HV) are lower than previously reported 109 ± 15 HV [44], however, the microstructure is not comparable. A hardness value similar to the literature is expected when the ratio of α-MnBi phase increases, or nanoindentation would have been performed directly at the existing α-MnBi phase. Interestingly, the α-MnBi phase fraction does not increase with further increased annealing times; rather, it vanishes. Again, this process is faster for the 2 GPa sample, but also the development of an oxide layer on its surface is found (see Supplementary). The preferred formation of an oxide can be explained by the enthalpy of formation, which shows a much lower value for Mn-oxides (and therefore a more stable bond) compared to the α-MnBi phase [45, 46]. Furthermore, the dissolution of already existing α-MnBi phases could be driven by an increased Mn diffusion to the sample surface. At least for thin films, a high migration of Mn atoms in Bi is already reported [47]. On the other hand, in the case of O diffusion, the pronounced oxygen

F. Synthesis of hard magnetic α-MnBi phase by HPT and field assisted annealing

sensitivity of the α-MnBi phase is already described by Cui et al. [48]. However, for the sample compacted at 5 GPa, a similar but decelerated behavior is observed. When applying 5 GPa, the pressure–temperature diagram for pure Bi shows at least two phase transitions [49], which might also occur during the loading and unloading pressure within the compaction process in the current study. As the only difference between the samples is the compaction pressure, probably these phase transitions influence the diffusion of Mn or O in the Bi matrix, even though the pressure is not applied during annealing. A profound understanding of the mentioned diffusion processes requires further studies. In any case, an exposure to oxygen was avoided for all further experiments in this work.

The HEXRD results (Fig. F.4) confirm that the α-MnBi phase (represented by the {101} α-MnBi peak, the most intensive peak for polycrystalline powder) is formed for all investigated samples but again at different formation velocities. Verifying the previous results from ex-situ annealing treatments, an accelerated phase formation is found for the 2 GPa HPT-compacted sample compared to the 5 GPa one, requiring about 2000 s and 5000 s to form, respectively. This behavior is even improved further, when HPT-deformed samples are annealed, requiring about 200 s for the {101} α-MnBi peak to form. This can be explained by enhanced diffusion processes, as already known for materials obtained by severe plastic deformation [50, 51]. We will discuss this topic in more detail later on. It is more difficult to understand the relative intensities within the presented figures. Based on the crystal structure (COD: 9011108 [30]), the intensity of the {220} Mn-peak is about 2.4 % of the most pronounced Mn-peak ({411} at $q = 29.9\,\mathrm{nm^{-1}}$) in an isotropic polycrystalline sample. Although being present in all spectra, the {220} signal is low. Yet due to the normalization to the maximum peak value ({002} α-MnBi for 5 GPa HPT-compacted and {101} α-MnBi else) of every given image in Fig. F.4, it appears with a different intensity. This is because the {101} α-MnBi peak grows to a different extend during annealing and this also explains the seemingly increased background signal for both HPT-deformed samples. However, at first sight, an analysis of the diffraction pattern did not show a clear correlation between peak intensities and processing routes.

It appears that the integrated intensities and thus the supposed amount of α-MnBi phase strongly depend on the phase formation characteristics. When we compare the 2D-detector recordings of the 3 h state with the as-processed state in Fig. F.5, bright spots evolve midst the beforehand existing Mn and Bi rings for both compacted samples. At exactly the same diffraction angles where bright spots are visible, continuous lines

are found for the HPT-deformed samples. Consequently, the α-MnBi phase forms in larger crystallites within the HPT-compacted samples (few, larger grains), whereas the HPT-deformed samples show a more homogeneously distributed nucleation behavior, which seems to be independent of the pressure applied. When the samples are annealed for 24 h and measured ex-situ by HEXRD, as shown in the third row of Fig. F.5, no changes regarding the number of nucleation sites are detected as indicated by a similar number of α-MnBi spots in the diffraction patterns. Besides the conclusions on the differences in nucleation behavior, the different appearance of α-MnBi in the diffraction patterns of HPT-compacted and HPT-deformed samples also has consequences on the interpretability of the peak intensities. Since the integrated intensities for the HPT-compacted samples originate from very few high-intensity spots of large α-MnBi crystallites and the presence or absence of a single crystallite with measurable orientation has a huge effect, these intensities are not used for conclusions about phase fractions due to the enormous statistical error. This is also illustrated by the fact that the {002} α-MnBi peak for the 5 GPa compacted sample is higher than in any other measurement but is based on a single crystallite with accidentally beneficial orientation.

The statistics of these experiments is given by the diffraction volume and the size of the crystallites. The samples are measured with a minimum thickness of about 500 μm for HPT-deformed samples and about 800 μm for compacted samples, at a spot size of 200x200 μm^2. Comparing to the 4 h and 24 h images in Fig. F.3, several α-MnBi phase regions are expected to exist in this interaction volume. Moreover, when the annealing times are increased, the number of detected α-MnBi phase spots is barely increased, showing that grain growth is preferred over nucleation at this stage. It is also possible to distinguish between the different compaction pressures, as for the 5 GPa compacted sample a higher number of α-MnBi phase spots is visible similar to the higher number of "cigar-shaped" regions in SEM (compare to Fig. F.3). HPT-deformation seems to be beneficial as the continuous Debye-Scherrer rings indicate a considerably higher density of α-MnBi phase nucleation sites. Diffusion mechanisms are the key aspect for the α-MnBi phase to form. The annealing temperature in the experiments is constantly kept below the eutectic temperature of 265 °C [52, 53], which is relatively low for diffusion processes. However, the high defect density induced by plastic deformation could enhance the inter-diffusion process of Mn and Bi, as such behavior is already reported for Ni [54–56]. Additionally, this phase forms almost directly after the heat treatment starts further sustaining this argument.

F. Synthesis of hard magnetic α-MnBi phase by HPT and field assisted annealing

Consequently, the most important findings from these measurements are as follows:

- A combination of ball milling, HPT, and annealing leads to α-MnBi phase formation.

- HPT-deformation prior to annealing treatments drastically enhances the number of α-MnBi phase nucleation sites.

- Diffusion processes as the most decisive phase formation parameter are correlated to the defect density.

- Long-time annealing at ambient conditions adversely affects the α-MnBi phase formation.

- α-MnBi grain growth is preferred over nucleation, at least for HPT-compacted samples.

- HPT-processing at 2 GPa yields a higher α-MnBi phase fraction than at 5 GPa.

F.4.2. Influence of magnetic field assisted annealing on the α-MnBi phase formation

In the second part of this study, the α-MnBi phase formation is further studied. In this part, the high defect density is solely applied by HPT without ball milling, and the heat treatment is combined with an additional magnetic field. As stated in the introduction, a commercial use of MnBi based permanent magnets is mainly barred by the inability to manufacture large quantities of bulk α-MnBi phase. In addition, porosity often is a limiting factor for magnetic properties when starting with powders. However, HPT-processing of metallic powders leads to completely dense materials. The measured density for the HPT-compacted $(8.778 \pm 0.223 \, \text{g/cm}^3)$ is lower compared to the HPT-deformed $(9.421 \pm 0.221 \, \text{g/cm}^3)$ sample. The density value of the compacted powder sample is in good agreement with the calculated value of $8.625 \, \text{g/cm}^3$ using theoretical values and a medium composition. The higher density for the HPT-deformed sample could indicate a preferred Mn particle transport towards the HPT-disc edge during deformation, thus leading to a higher Bi content. However, a significant porosity of HPT treated samples is excluded. To increase the α-MnBi volume fraction, it is necessary to raise the number of nucleation sites and additionally accelerate phase growth. A beneficial influence of magnetic field annealing on α-MnBi phase formation was already mentioned in 1958 [57], although its origin

is not fully understood until today. It is stated that field annealing increases the Zeeman energy affecting the critical radius of nuclei. Furthermore, a decrease of free energy for the α-MnBi phase formation is reported to result in a negative formation enthalpy and an enhanced nucleation rate [22, 23]. The resulting localized reaction heat is believed to be responsible for Mn and Bi particles partially melting. Thus, a rotation of crystallites occurs leading to a textured and anisotropic phase formation if a magnetic field is applied [15, 58, 59]. Moreover, the huge magnetocrystalline anisotropy of about $2.2 \, \text{MJ/m}^3$ at the annealing temperature (herein 240°*C*) seems to affect the recrystallization process (including nucleation and grain growth) [6, 10], and analogies to strain-induced recrystallization can be drawn [59, 60]. In general, magnetic field annealing of a Mn-Bi composite leads to an enhanced α-MnBi phase volume fraction and grain alignment (texture formation) [15, 23, 58, 61], which is also supported by the results of the current study.

The volume fraction of α-MnBi can be calculated with the measured saturation magnetization M_s as it is proportional to the α-MnBi fraction, considering the theoretical M_s of 79 emu/g [9, 12]. Therefore, we can estimate the volume content by using the calculated M_s value of Fig. F.6 and the theoretical value [12]. The amount of α-MnBi phase in the HPT-compacted sample after MVA equals a content of 12%. Only by deforming the sample prior to MVA, the volume fraction increases above 50% ($M_s = 33.92$ emu/g), indicating a higher number of nucleation sites. Except for the applied strain, no differences between HPT-compacted and HPT-deformed samples shown in Fig. F.6 are present. The higher strain leads to a higher number of small Mn particles, increasing the size of Mn and Bi interfaces. Furthermore, the microstructural defect density ρ is increased, which is related to the critical nucleation radius $r_c = 2\gamma p$. γ is the specific grain boundary energy, and p is the driving force, whereby p is directly proportional to ρ [62]. Therefore, r_c is lowered with increasing ρ. Consequently, a larger phase interface and high ρ - both tunable by HPT - enhances the α-MnBi phase formation. This is supported by the measured hysteresis loops and by BSE images presented in Fig. F.7.

The H_c of the hysteresis loops (Fig. F.6) is strongly decreased when measured at lower temperatures, another strong indication for the presence of the α-MnBi phase due to its positive temperature coefficient of intrinsic coercivity [8, 9]. The H_c measured at 300 K of the HPT-compacted and HPT-deformed sample are comparable: 1.38 kOe and 1.58 kOe, respectively. However, lower values can be found in the literature after similar field annealing measurements. For example, Gabay et al. [15] found

an H_c of 0.6 kOe. Compressed MnBi powder blends in a study of Mitsui et al. [58] attain an H_c of 0.8 kOe. Thus, HPT-deformation has a beneficial effect on magnetic properties. Magnetic hardening by grain refinement is well known and it is thought to mainly contribute to a change of H_c of the α-MnBi phase particles [63–65]. This is imposingly demonstrated by Mitsui et al. [22], where magnetic field annealing leads not only to an enhanced volume of α-MnBi phase but also to a decreased H_c due to an increased grain size after annealing. Based on the phenomenologically described expression $H_c = H_a \left(1 - \frac{\delta}{D}\right)^n$ [65], the α-MnBi phase of the HPT-deformed samples show crystallite sizes D of about 0.7 μm, whereby δ is the Bloch wall width (7 nm), H_a the theoretical limit of H_c at $D \approx \delta$ (40 kOe), and an exponent n (0.7) is used [10, 65]. For such crystallite sizes, a large H_c (> 10 kOe) could be expected [48, 66].

Based on the above introduced expression for H_c, two different samples (HPT-compacted and HPT-deformed) only exhibit a similar H_c if the crystallite size is similar. Combining this information with the higher amount of α-MnBi phase fraction present for the HPT-deformed sample, this further supports our results obtained from HEXRD, where HPT-deformation increases the number of α-MnBi nucleation sites. Accordingly, it is noted that magnetic properties are mainly influenced during the initial annealing process (regarding magnetic field annealing procedures), and changes stagnate for increased annealing times [15, 22, 60, 67].

Concluding, primarily effects of α-MnBi phase formation are due to the enhanced nucleation behavior after HPT-deformation and higher amounts of defects. Additionally, the reduced grain size of the Mn-Bi composite after HPT, thus enlarged grain boundary volume and defect density, favors grain boundary diffusion and facilitates phase formation [54–56]. The resulting α-MnBi crystallite sizes seem to be small and independent of previous HPT-deformation.

F.4.3. HPT-induced magnetic anisotropy

HPT-deformation often induces texture in metallic materials [68]. For hard magnetic SmCo$_5$ composites, which were HPT-deformed, a textured microstructure and, as a result, anisotropic magnetic behavior is reported [29, 69]. Thus, an influence of differently aligned MVAs in combination with the crystallographic texture of the HPT-deformed MnBi sample is expected. However, the XRD measurements on the B$_{ax}$ and B$_{tan,rad}$ annealed samples (Fig. F.8) reveal similar texture for the Bi phase after MVA for differently applied field directions, since the intensities of all Bi peaks

are similar in the two samples. Due to the low peak intensities of Mn, an analysis of this phase is omitted. However, differences are found for the α-MnBi peaks of the HPT-deformed sample. For the B_{ax} anneal, the (002) and (004) planes, and for the $B_{tan,rad}$ anneal, the (110) plane are more pronounced, respectively. This fits with recently reported findings, where the c-axis of the α-MnBi phase tends to form parallel to the applied magnetic field [59, 61, 70–72].

Based on SQUID measurements, a detailed investigation of magnetic properties is presented in Fig. F.9, and corresponding magnetic parameters are summarized in Table 1. In general, a higher remnant magnetization M_r indicates an increased amount of crystallographically aligned grains [59, 61]. The M_s value slightly differs between 33.0 emu/g and 35.2 emu/g. Thus, the α-MnBi phase content varies between 41.8% and 44.6%. Therefore, the amount of forming α-MnBi phase is not affected by different MVA directions; though, magnetic properties, e.g., H_c and M_r, are influenced. Further commenting on the differences of the α-MnBi phase content, which can occur if α-MnBi phase particles of sizes in the range of a quasi-single domain regime, exhibiting a high H_c, are not completely demagnetized between the presented M_{ax}, M_{tan}, and M_{rad} measurements. Therefore, the sample exhibits residual magnetic fields when it is rotated. This could be circumvented if magnetic measurement fields would be applied at higher magnetic fields, which is not possible using the current device.

For the B_{ax} sample (Fig. F.9a)), the measured values for H_c and M_r show an isotropic magnetic behavior of the α-MnBi phase. In contrast, H_c and M_r change for the B_{rad} sample (Fig. F.9b)) as a function of the SQUID measuring field direction. Similar behavior is observed for the B_{tan} sample (Fig. F.9c)), which shows the largest differences. If the α-MnBi phase formation would be only dependent on the direction of the applied magnetic field during MVA, one would expect hysteresis loops where the easy and hard axis of the α-MnBi phase can be correlated to the MVA field. This is already reported and explained due to a partially melting of the surrounding Bi and an enabled rotation of the α-MnBi grains [15, 23, 58, 61]. However, this is clearly not the case for our samples as the M_r value does not follow the applied field directions. Thus, a significant influence of the applied shear deformation during HPT-deformation is presumed. The squareness ratio M_r/M_s (presented in Table 1) is a frequently used measure for the degree of texture, thus the anisotropic magnetic behavior. It is highest when the measuring field direction is applied in the tangential HPT-disc direction (anisotropic) and lowest for the axial direction (isotropic), a valid observation for all field annealing directions. This observation is assumed to originate

F. Synthesis of hard magnetic α-MnBi phase by HPT and field assisted annealing

in the shear-deformed microstructure, entailing a preferred orientation for the forming α-MnBi phase. For thin films, the α-MnBi grains are reported to preferably align their c-axis parallel to the Bi c-axis [67, 73]. As the Bi phase is the one that is easily accessible by microstructural investigations and to check if the α-MnBi phase formation correlates with a preexisting texture of the MnBi composite prior annealing, a pure Bi sample is processed by HPT-deformation (RT, 25 rotations, 2 GPa). The performed EBSD scans are recorded in the tangential HPT-disc viewing direction. Exemplarily an inverse pole figure map is presented in Fig. F.10a) and a pole figure obtained from several scans is shown in Fig. F.10b). The radial and tangential HPT-disc directions point in horizontal and vertical direction, while the axial HPT-disc direction points perpendicular to the paper plane. A largely identical orientation of the Bi grains is visible, with the c-axis of the Bi crystals pointing parallel to the axial HPT-disc direction. Assuming the same texture in the composite sample, the α-MnBi grains should be perfectly aligned when the MVA field is applied parallel to the crystallographic textured Bi, thus the axial HPT-disc direction. Yet, such a behavior is not observed by our measurements for the B_{ax} sample.

This clearly shows the importance of diffusion processes on α-MnBi formation enabled by HPT-deformation. The initial phase nucleation is assumed to happen at Mn and Bi particle interfaces [23]. Diffusion processes in solids prefer to occur along grain boundaries rather through the interiors of crystals. An enhanced grain boundary diffusion is known for HPT materials [54–56] and found for polycrystalline Bi [74], as well as Mn diffusion in Bi thin films [47]. Moreover, in slightly different experiments, we obtained similar results as Borsup et al. [66] where a rapid and incredibly extensive diffusion of molten Bi in polycrystalline Mn is found (see Figure Supplementary F.2).

The highest magnetic anisotropy is found for B_{tan}. If grain boundaries are aligned parallel to the MVA field (compare to Fig. 10a), the forming phase could preferably grow along this direction (as mass transport is relieved) and simultaneously form textured grains. Additionally, one should think about the textured Bi-matrix. The surface normal of the preferred (001) slip plane [75] is parallel to the c-axis, allowing dislocation pathways within the shear-plane. Therefore, so-called short circuit or pipe diffusion [76] is directed within the shear plane, additionally enhancing diffusion processes in the mentioned plane. The formation of a textured α-MnBi phase upon MVA seems to be facilitated by diffusion processes in the shear-plane, whereas α-MnBi crystallite growth upon MVA in axial HPT-disc direction, thus normal to the dislocation pathways and grain boundaries, is suppressed. Thereby, the direction of
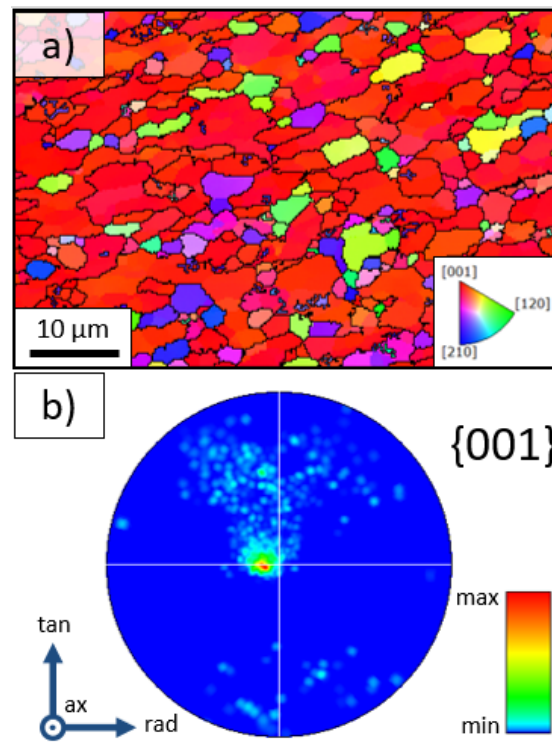
Figure F.10.: a) inverse pole figure map and b) corresponding pole figure for the {001} plane obtained from EBSD scans on HPT-deformed pure Bi sample (RT, 25 rotations, 2 GPa). For the pole figure, the radial and tangential HPT-disc directions point in horizontal and vertical direction. The axial direction points perpendicular to the paper plane. The maximum intensity in the pole figure correlates to the axial HPT-disc direction.

applied MVA can be used to tune the grade of anisotropy of hard magnetic properties within the HPT-processed sample.

F.5. Conclusion

In this work, we successfully produced the ferromagnetic α-MnBi phase for the first time by applying severe plastic deformation using HPT and a subsequent thermal processing step. The influence of applied pressure by HPT changes the rate of the α-MnBi phase formation, as well as its decomposition if annealed at atmosphere. The initial phase nucleation and formation is studied by means of in-situ HEXRD annealing and it is found that the α-MnBi phase forms shortly after beginning of the heat treatment for HPT-deformed samples. This process depends on the applied pressure and is slower for HPT-compacted samples without severe deformation, thus

lower microstructural defects. Most importantly, a correlation between higher α-MnBi phase nucleation sites and applied HPT-deformation is found, further revealing that upon annealing α-MnBi phase growth is preferred over nucleation at least for the HPT-compacted samples. By applying magnetic field assisted vacuum annealing (MVA) to HPT-processed samples, the α-MnBi phase formation is enhanced. HPT-compacted and HPT-deformed samples show similar coercivities, thus similar α-MnBi grain sizes, but a differing saturation magnetization as the α-MnBi phase reaches a higher volume fraction (>50 vol%) for the HPT-deformed one. Our results point towards the importance of diffusion processes for the α-MnBi phase formation. The diffusion is enhanced for samples with higher defect densities (HPT-deformed compared to HPTcompacted) and influenced by the shear deformation induced, refined grain boundary structure. This further provides the possibility to form anisotropic hard magnets. Summarized, the α-MnBi phase formation is best for HPT-deformed and MVA samples, where the applied annealing field is parallel to the HPT shear direction.

Declaration of Competing Interest: The authors declare that they have no known competing financial interests or personal relationships that could have appeared to influence the work reported in this paper.

Data Availability: Data will be made available on request.

Acknowledgements

F.6. References

[1]   N. Makino. A Review of Studies on the Permanent Magnet, *Tetsu-to-Hagane* **44** (1958), pp. 1217–1224.
      DOI: 10.2355/tetsutohagane1955.44.10_1217.

[2] E. W. Lee and L. F. Bates. Nature, **272** (1978), pp. 568–568.
     DOI: 10.1038/272568a0.

[3] T. Chen. Contribution to the equilibrium phase diagram of the Mn–Bi system near MnBi,
     Journal of Applied Physics **45** (1974), pp. 2358–2360.
     DOI: 10.1063/1.1663594.

[4] K. Oikawa et al. Thermodynamic Assessment of the Bi-Mn System, *Mater. Trans.* **52** (2011),
     pp. 2032–2039.
     DOI: 10.2320/matertrans.M2011229.

[5] Y. Mitsui et al. Thermodynamic assessment for the Bi–Mn binary phase diagram in high
     magnetic fields, *Journal of Alloys and Compounds* **577** (2013), pp. 315–319.
     DOI: 10.1016/j.jallcom.2013.05.198.

[6] J. Cui et al. Current progress and future challenges in rare-earth-free permanent magnets,
     Acta Materialia **158** (2018), pp. 118–137.
     DOI: 10.1016/j.actamat.2018.07.049.

[7] D. T. Zhang et al. Crystal structure and magnetic properties of MnxBi100-x (x=48, 50, 55 and
     60) compounds, *Journal of Magnetism and Magnetic Materials* **324** (2012), pp. 1887–1890.
     DOI: 10.1016/j.jmmm.2012.01.017.

[8] J. Cui et al. Thermal stability of MnBi magnetic materials, *J. Phys.: Condens. Matter* **26**
     (2014), p. 064212.
     DOI: 10.1088/0953-8984/26/6/064212.

[9] J.B. Yang et al. Anisotropic nanocrystalline MnBi with high coercivity at high temperature,
     Appl. Phys. Lett. **99** (2011), p. 082505.
     DOI: 10.1063/1.3630001.

[10] X. Guo et al. Magnetic properties of MnBi prepared by rapid solidification, *Phys. Rev. B* **46**
     (1992), pp. 14578–14582.
     DOI: 10.1103/PhysRevB.46.14578.

[11] T. Chen and W. Stutius. The phase transformation and physical properties of the MnBi and
     Mn1.08Bi compounds, *IEEE Transactions on Magnetics* **10** (1974), pp. 581–586.
     DOI: 10.1109/TMAG.1974.1058367.

[12] J. Park et al. Electronic Structure and Maximum Energy Product of MnBi, *Metals* **4** (2014),
     pp. 455–464.
     DOI: 10.3390/met4030455.

[13] N.M. Lam et al. Fabrication of Mn-Bi Nanoparticles by High Energy Ball Milling, *Mater.
     Trans.* **56** (2015), pp. 1394–1398.
     DOI: 10.2320/matertrans.MA201577.

[14] N.V. Rama Rao et al. Fabrication of anisotropic MnBi nanoparticles by mechanochemical
     process, *Journal of Alloys and Compounds* **586** (2014), pp. 349–352.
     DOI: 10.1016/j.jallcom.2013.10.067.

[15]   A.M. Gabay, G.C. Hadjipanayis, and J. Cui. New anisotropic MnBi permanent magnets by field-annealing of compacted melt-spun alloys modified with Mg and Sb, *Journal of Magnetism and Magnetic Materials* **495** (2020), p. 165860.
DOI: 10.1016/j.jmmm.2019.165860.

[16]   A.M. Gabay, G.C. Hadjipanayis, and J. Cui. Effect of Sb substitution on crystal structure, texture and hard magnetic properties of melt-spun MnBi alloys, *Journal of Alloys and Compounds* **792** (2019), pp. 77–86.
DOI: 10.1016/j.jallcom.2019.03.407.

[17]   Y.B. Yang et al. Temperature dependences of structure and coercivity for melt-spun MnBi compound, *Journal of Magnetism and Magnetic Materials* **330** (2013), pp. 106–110.
DOI: 10.1016/j.jmmm.2012.10.046.

[18]   W. Tang et al. Engineering microstructure to improve coercivity of bulk MnBi magnet, *Journal of Magnetism and Magnetic Materials* **563** (2022), p. 169912.
DOI: 10.1016/j.jmmm.2022.169912.

[19]   P. Kainzbauer et al. The Ternary Bi-Mn-Sb Phase Diagram and the Crystal Structure of the Ternary τ Phase Bi0.8MnSb0.2, *J. Phase Equilib. Diffus.* **40** (2019), pp. 462–481.
DOI: 10.1007/s11669-019-00719-x.

[20]   S. Lu et al. Effect of Mg content on the microstructure and magnetic properties of rare-earth-free MnBi alloys, *Journal of Magnetism and Magnetic Materials* **570** (2023), p. 170499.
DOI: 10.1016/j.jmmm.2023.170499.

[21]   H. Kronmüller, J.B. Yang, and D. Goll. Micromagnetic analysis of the hardening mechanisms of nanocrystalline MnBi and nanopatterned FePt intermetallic compounds, *J. Phys.: Condens. Matter* **26** (2014), p. 064210.
DOI: 10.1088/0953-8984/26/6/064210.

[22]   Y. Mitsui et al. Reactive sintering process of ferromagnetic MnBi under high magnetic fields, *Journal of Magnetism and Magnetic Materials* **453** (2018), pp. 231–235.
DOI: 10.1016/j.jmmm.2018.01.026.

[23]   D. Miyazaki et al. Enhancement of the Phase Formation Rate during In-Field Solid-Phase Reactive Sintering of Mn-Bi, *Mater. Trans.* **58** (2017), pp. 720–723.
DOI: 10.2320/matertrans.MBW201609.

[24]   Z. Horita et al. Severe Plastic Deformation under High Pressure: Upsizing Sample Dimensions, *Mater. Trans.* **61** (2020), pp. 1177–1190.
DOI: 10.2320/matertrans.MT-M2020074.

[25]   H.P. Stüwe. Equivalent Strains in Severe Plastic Deformation, *Adv. Eng. Mater.* **5** (2003), pp. 291–295.
DOI: 10.1002/adem.200310085.

[26] K.S. Kormout, R. Pippan, and A. Bachmaier. Deformation-Induced Supersaturation in Immiscible Material Systems during High-Pressure Torsion: Deformation-Induced Supersaturation, *Adv. Eng. Mater.* **19** (2017), p. 1600675.
DOI: 10.1002/adem.201600675.

[27] A. Hohenwarter et al. Technical parameters affecting grain refinement by high pressure torsion, *International Journal of Materials Research* **100** (2009), pp. 1653–1661.
DOI: 10.3139/146.110224.

[28] G. Faraji and H. Torabzadeh. An Overview on the Continuous Severe Plastic Deformation Methods, *Mater. Trans.* **60** (2019), pp. 1316–1330.
DOI: 10.2320/matertrans.MF201905.

[29] L. Weissitsch et al. Manufacturing of Textured Bulk Fe-SmCo5 Magnets by Severe Plastic Deformation, *Nanomaterials* **12** (2022), p. 963.
DOI: 10.3390/nano12060963.

[30] S. Gražulis et al. Crystallography Open Database (COD): an open-access collection of crystal structures and platform for world-wide collaboration, *Nucleic Acids Research* **40** (2012), pp. D420–D427.
DOI: 10.1093/nar/gkr900.

[31] Z. Hegedüs et al. Imaging modalities at the Swedish Materials Science beamline at PETRA III, *IOP Conf. Ser.: Mater. Sci. Eng.* **580** (2019), p. 012032.
DOI: 10.1088/1757-899X/580/1/012032.

[32] G. Ashiotis et al. The fast azimuthal integration Python library: pyFAI, *J Appl Crystallogr.* **48** (2015), pp. 510–519.
DOI: 10.1107/S1600576715004306.

[33] C.P. Bean and I.S. Jacobs. Magnetic Granulometry and Super-Paramagnetism, *Journal of Applied Physics* **27** (1956), pp. 1448–1452.
DOI: 10.1063/1.1722287.

[34] D.-X. Chen et al. Size determination of superparamagnetic nanoparticles from magnetization curve, *Journal of Applied Physics* **105** (2009), p. 083924.
DOI: 10.1063/1.3117512.

[35] R. Pippan et al. Saturation of Fragmentation During Severe Plastic Deformation, *Annu. Rev. Mater. Res.* **40** (2010), pp. 319–343.
DOI: 10.1146/annurev-matsci-070909-104445.

[36] O. Renk and R. Pippan. Saturation of Grain Refinement during Severe Plastic Deformation of Single Phase Materials: Reconsiderations, Current Status and Open Questions, *Mater. Trans.* **60** (2019), pp. 1270–1282.
DOI: 10.2320/matertrans.MF201918.

[37] C. Knieke, M. Sommer, and W. Peukert. Identifying the apparent and true grinding limit, *Powder Technology* **195** (2009), pp. 25–30.
DOI: 10.1016/j.powtec.2009.05.007.

[38] H.-R. Shen et al. Microstructure and magnetic properties of anisotropic Mn-Bi powder prepared by low energy ball milling assisted with polyvinylpyrrolidone, *Journal of Magnetism and Magnetic Materials* **551** (2022), p. 169108.
DOI: 10.1016/j.jmmm.2022.169108.

[39] K. Kanari et al. Processing of magnetically anisotropic MnBi particles by surfactant assisted ball milling, *Journal of Magnetism and Magnetic Materials* **426** (2017), pp. 691–697.
DOI: 10.1016/j.jmmm.2016.10.141.

[40] J. Cao et al. Microstructure and magnetic properties of MnBi alloys with high coercivity and significant anisotropy prepared by surfactant assisted ball milling, *Journal of Magnetism and Magnetic Materials* **473** (2019), pp. 505–510.
DOI: 10.1016/j.jmmm.2018.10.052.

[41] M. Abareshi, S.M. Zebarjad, and E.K. Goharshadi. Study of the morphology and granulometry of polyethylene-clay nanocomposite powders, *J Vinyl Addit Technol.* **16** (2010), pp. 90–97.
DOI: 10.1002/vnl.20217.

[42] M.S. El-Eskandarany. *Mechanical alloying for fabrication of advanced engineering materials.* Norwich, N.Y: Noyes Publications, 2001.

[43] R. Taherzadeh Mousavian et al. Fabrication of aluminum matrix composites reinforced with nano- to micrometer-sized SiC particles, *Materials & Design* **89** (2016), pp. 58–70.
DOI: 10.1016/j.matdes.2015.09.130.

[44] X. Jiang et al. Mechanical and electrical properties of low temperature phase MnBi, *Journal of Applied Physics* **119** (2016), p. 033903.
DOI: 10.1063/1.4939811.

[45] C.P. Wang et al. Thermodynamic assessments of the Bi–U and Bi–Mn systems, *Journal of Nuclear Materials* **412** (2011), pp. 66–71.
DOI: 10.1016/j.jnucmat.2011.02.021.

[46] K.T. Jacob et al. Thermodynamic Data for Mn3O4, Mn2O3 and MnO2, *High Temperature Materials and Processes* **30** (2011).
DOI: 10.1515/htmp.2011.069.

[47] Y. Iwama, U. Mizutani, and F. Humphrey. Formation process of MnBi thin films, *IEEE Trans. Magn.* **8** (1972), pp. 487–489.
DOI: 10.1109/TMAG.1972.1067370.

[48] J. Cui et al. Effect of composition and heat treatment on MnBi magnetic materials, *Acta Materialia* **79** (2014), pp. 374–381.
DOI: 10.1016/j.actamat.2014.07.034.

[49] H.-Y. Chen et al. Phase transition of solid bismuth under high pressure, *Chinese Phys. B* **25** (2016), p. 108103.
DOI: 10.1088/1674-1056/25/10/108103.

[50] K. Oh-ishi et al. High-pressure torsion for enhanced atomic diffusion and promoting solid-state reactions in the aluminum–copper system, *Acta Materialia* **61** (2013), pp. 3482–3489.
DOI: 10.1016/j.actamat.2013.02.042.

[51] B.B. Straumal et al. Accelerated Diffusion and Phase Transformations in Co–Cu Alloys Driven by the Severe Plastic Deformation, *Mater. Trans.* **53** (2012), pp. 63–71.
DOI: 10.2320/matertrans.MD201111.

[52] R.G. Pirich. Gravitationally Induced Convection During Directional Solidification of off-Eutectic Mn-Bi Alloys, *MRS Proc.* **9** (1981), p. 593.
DOI: 10.1557/PROC-9-593.

[53] H. Okamoto. Supplemental Literature Review of Binary Phase Diagrams: Ag-Co, Ag-Er, Ag-Pd, B-Ce, Bi-La, Bi-Mn, Cu-Ge, Cu-Tm, Er-Y, Gd-Tl, H-La, and Hg-Te, *J. Phase Equilib. Diffus.* **36** (2015), pp. 10–21.
DOI: 10.1007/s11669-014-0341-7.

[54] Yu.R. Kolobov et al. Grain boundary diffusion characteristics of nanostructured nickel, *Scripta Materialia* **44** (2001), pp. 873–878.
DOI: 10.1016/S1359-6462(00)00699-0.

[55] G. Wilde and S. Divinski. Grain Boundaries and Diffusion Phenomena in Severely Deformed Materials, *Mater. Trans.* **60** (2019), pp. 1302–1315.
DOI: 10.2320/matertrans.MF201934.

[56] M.D. Baró et al. DIFFUSION AND RELATED PHENOMENA IN BULK NANOSTRUC-TURED MATERIALS, (n.d.), p. 43.

[57] O.L. Boothby, D.H. Wenny, and E.E. Thomas. Recrystallization of MnBi Induced by a Magnetic Field, *Journal of Applied Physics* **29** (1958), pp. 353–353.
DOI: 10.1063/1.1723130.

[58] Y. Mitsui et al. Magnetic-field-induced enhancement for synthesizing ferromagnetic MnBi phase by solid-state reaction sintering, *Journal of Alloys and Compounds* **615** (2014), pp. 131–134.
DOI: 10.1016/j.jallcom.2014.06.131.

[59] H. Yasuda et al. Formation of Crystallographically Aligned BiMn Grains by Semi-solid Processing of Rapidly Solidified Bi-Mn Alloys under a Magnetic Field, *Mater. Trans.* **44** (2003), pp. 2207–2212.
DOI: 10.2320/matertrans.44.2207.

[60] T. Chen and W.E. Stutius. Magnetic-field-induced recrystallization in MnBi, *Journal of Applied Physics* **45** (1974), pp. 4622–4625.
DOI: 10.1063/1.1663100.

[61] W.Y. Zhang et al. Grain alignment due to magnetic-field annealing in MnBi:Bi nanocomposites, *J. Phys. D: Appl. Phys.* **49** (2016), p. 455002.
DOI: 10.1088/0022-3727/49/45/455002.

[62] G. Gottstein. *Materialwissenschaft und Werkstofftechnik.* Berlin, Heidelberg: Springer, 2014. DOI: 10.1007/978-3-642-36603-1.

[63] K. Kobayashi, R. Skomski, and J.M.D. Coey. Dependence of coercivity on particle size in SmzFe17N 3 powders, *Journal of Alloys and Compounds* (1995).

[64] V. Ly et al. Low-temperature phase MnBi compound: A potential candidate for rare-earth free permanent magnets, *Journal of Alloys and Compounds* **615** (2014), S285–S290. DOI: 10.1016/j.jallcom.2014.01.120.

[65] K. Suzuki et al. Spin reorientation transition and hard magnetic properties of MnBi intermetallic compound, *Journal of Applied Physics* **111** (2012), 07E303. DOI: 10.1063/1.3670505.

[66] J. Borsup et al. Formation and magnetic properties of low-temperature phase manganese bismuth prepared by low-temperature liquid phase sintering in vacuum, *Journal of Magnetism and Magnetic Materials* **544** (2022), p. 168661. DOI: 10.1016/j.jmmm.2021.168661.

[67] W.K. Unger and M. Stolz. Growth of MnBi Films on Mica, (1971).

[68] S. Suwas and S. Mondal. Texture Evolution in Severe Plastic Deformation Processes, *Mater. Trans.* **60** (2019), pp. 1457–1471. DOI: 10.2320/matertrans.MF201933.

[69] F. Staab et al. Hard Magnetic SmCo 5-Cu Nanocomposites Produced by Severe Plastic Deformation, (2022). DOI: 10.2139/ssrn.4263460.

[70] K. Kang, L.H. Lewis, and A.R. Moodenbaugh. Alignment and analyses of MnBi/Bi nanostructures, *Appl. Phys. Lett.* **87** (2005), p. 062505. DOI: 10.1063/1.2008368.

[71] Z. Ren et al. The segregated structure of MnBi in Bi–Mn alloy solidified under a high magnetic field, *Materials Letters* **58** (2004), pp. 3405–3409. DOI: 10.1016/j.matlet.2004.04.021.

[72] P.Z. Si et al. Magnetic-field-enhanced reactive synthesis of MnBi from Mn nanoparticles, *Journal of Magnetism and Magnetic Materials* **476** (2019), pp. 243–247. DOI: 10.1016/j.jmmm.2018.12.077.

[73] W.K. Unger and H. Harms. Grain size of MnBi films, *Appl. Phys.* **2** (1973), pp. 191–196. DOI: 10.1007/BF00884210.

[74] W.P. Ellis and N.H. Nachtrieb. Anomalous Self-Diffusion in Solid Bismuth: The Trapping Mechanism, *Journal of Applied Physics* **40** (1969), pp. 472–476. DOI: 10.1063/1.1657422.

[75] Y. Yanaka et al. Plastic Deformation Behavior and Mechanism of Bismuth Single Crystals in Principal Axes, *Mater. Trans.* **57** (2016), pp. 819–823. DOI: 10.2320/matertrans.MD201503.

[76]   A.L. Ruoff and R.W. Balluffi. Strain-Enhanced Diffusion in Metals. II. Dislocation and Grain-Boundary Short-Circuiting Models, *Journal of Applied Physics* **34** (1963), pp. 1848–1853. DOI: 10.1063/1.1729698.

F.7. Appendix of Paper F

Supplementary data

Supplementary data to this article can be found online at https://doi.org/10.1016/j.jmmm.2023.171082.
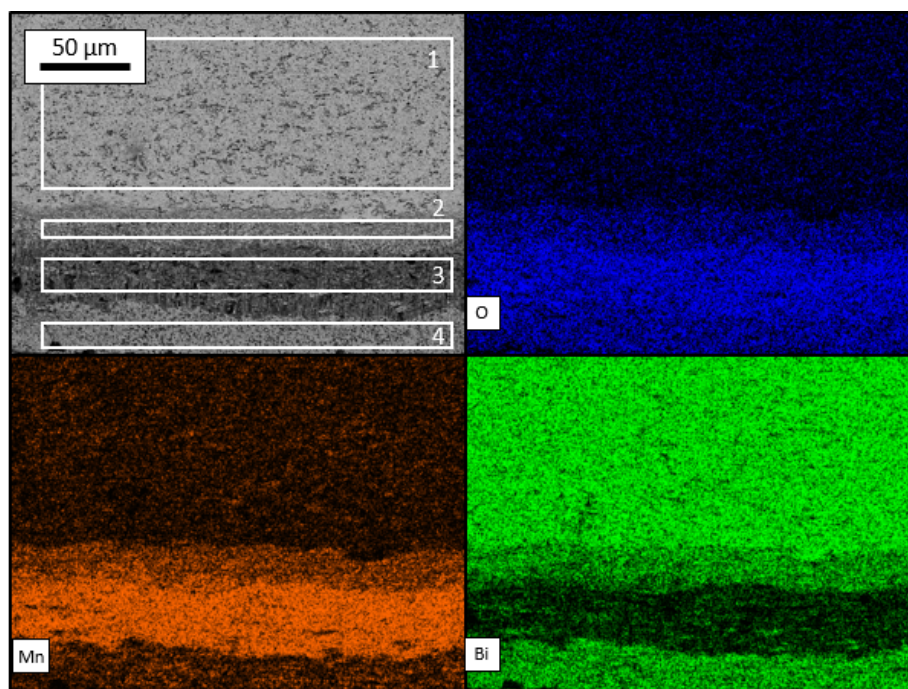

Figure Supplementary F.1.: Secondary electron image and corresponding energy dispersive X-ray spectroscopy mapping analysis of an MnBi composite after 120 h conventional annealing at 230 °C. The images are recorded in tangential HPT-disc direction on the HPT-disc edge with the surface normal (axial HPT-disc direction) pointing downwards. The color intensity of each graph is correlated to their relative occurrence on the map. The chemical compositions for the marked regions and the entire map are summarized in Table Supplementary 1.

Table Supplementary F.1.: Chemical composition obtained from EDX analysis.

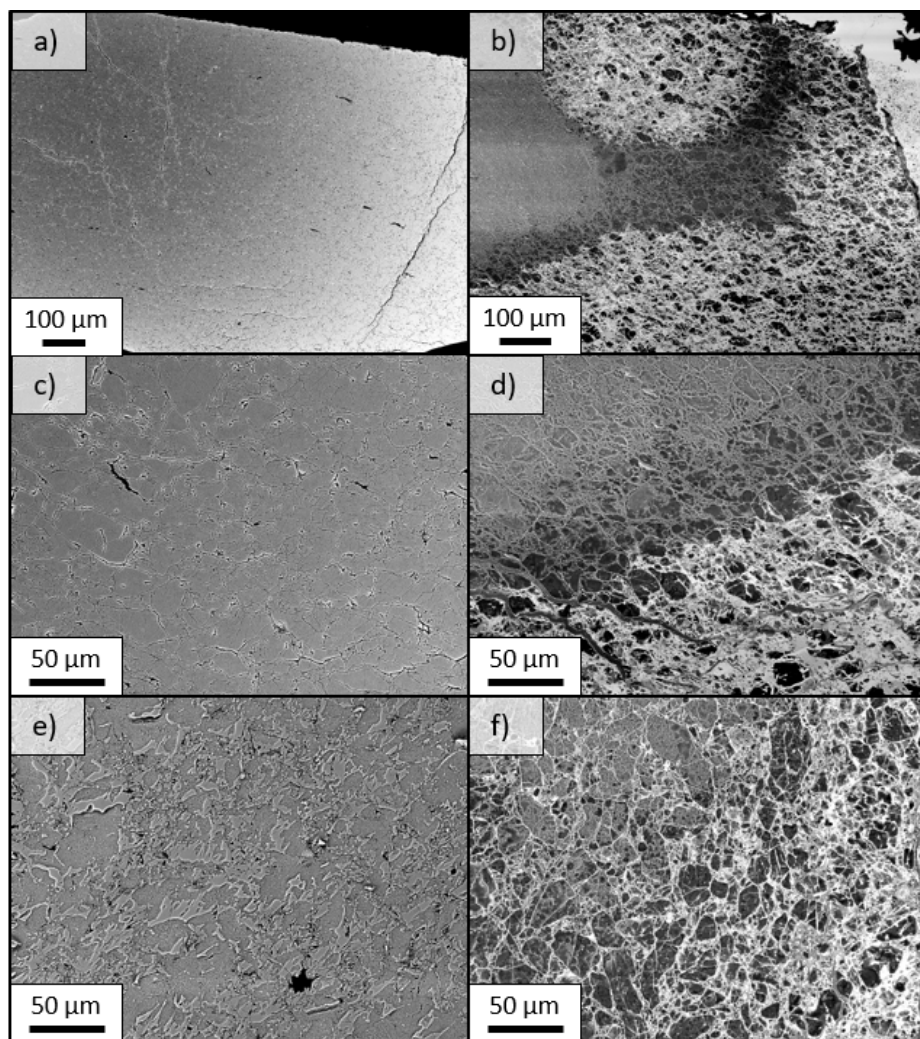|	Mn [at. %]	Bi [at. %]	O [at. %]
total map	29,4	24,3	46,3
area 1	24,1	46,1	29,8
area 2	34,6	18,4	47,0
area 3	41,3	6,5	52,3
area 4	21,6	18,9	59,5

Figure Supplementary F.2.: BSE images of an HPT-deformed a) and c) and an HPT-compacted e) sample. Without any further pretreatment, the same samples were immersed into molten Bi at 410°C for 4 h b), d) and f). The Bi phase diffuses inside the bulk material, along the Mn grain boundaries for several 100 μm.